Hybrid Metallic Nanostructures for Bio and Analytical Applications

by

Nafiseh Moghimi

A thesis
presented to the University of Waterloo
in fulfillment of the
thesis requirement for the degree of
Doctor of Philosophy
in
Chemistry

Waterloo, Ontario, Canada, 2014

AUTHOR'S DECLARATION

Abstract

Different hybrid nanoparticles (NPs), including FeM (M=Ni, Au, Pt, Pd) and Fe-biomolecules (biomolecule=glucose oxidase, p53p protein), have been synthesized by a surfactant-free, single-step electrochemical method. FeNi bimetallic NP systems have been chosen as the starting point of the present study. Shape evolution and phase transformation of FeNi NPs obtained by changing their composition is demonstrated. It has been shown that the shape evolution of NPs from concave cube to truncated sphere occurs concurrently with the phase transformation from bcc to fcc. In-situ formation of a very thin Ni-doped FeOOH outer layer and $NiFe_2O_4$ intermediate layer on the skin of the NPs is observed, the latter of which passivates the surface and dramatically enhances the air stability. Furthermore, bimetallic FeNi concave nanocubes with high Miller index planes have been obtained through controlled triggering of the different growth modes of Fe and Ni. Taking advantage of the higher activity of the high-index planes, mono-dispersed concave nanocages have been fabricated by introducing a material-independent electroleaching process. With the high-index facets exposed, these concave nanocubes and nanocages are found to be 10 and 100-fold, respectively, more active toward electrochemical detection of 4-aminophenol than cuboctahedrons which provides a label-free sensing approach to monitoring toxins in water and pharmaceutical wastes. In addition, the shape-dependent magnetic properties of a bimetallic system have been studied for FeNi NPs with well-defined concave cubic and octahedron shapes. The alloy composition was chosen to be close to that of Invar FeNi alloys (35% Ni content) but with concurrent presence of both bcc and fcc phases, in order to investigate the role of phase combination in controlling the magnetic properties. The role of the two phases in governing the magnetic properties has also been studied for both bulk and nanoalloys by large-scale density function theory (DFT) calculations using Vienna Ab-initio Simulation Package (VASP, Version 5.2), which provides a new complementary approach to understanding the magnetic properties of alloy materials.

To extend the aforementioned method to other hybrid and bimetallic systems, FePt NPs with different compositions ($Fe_{25}Pt_{75}$, $Fe_{30}Pt_{70}$, $Fe_{35}Pt_{65}$) have been synthesized and their chemical sensing investigated for the electro-oxidation of vitamin C. The FePt alloy NPs are found to be superior catalysts for vitamin C electro-oxidation than Pt NPs and are significantly more selective for the detection of vitamin C against other common interference species, including dopamine, citric acid, uric acid, glucose, and NaCl. Enhancement in sensor performance can be attributed to the increase in specific surface area due to reduction of nanocrystallite size and to modification in the Pt electronic structure as a result of nanoalloying. We also synthesize bimetallic FeAu, FePd, and AuPt NPs and investigate their electrochemical properties for As(III) detection. The synergistic effect of alloying with Fe leads to better performance for Fe-noble metal NPs (Au, Pt, Pd) than pristine noble metal NPs (without Fe alloying), with the best performance found for FePt NPs. The selectivity of the sensor has also been tested in the presence of a large amount of Cu(II), acting as the most detrimental interfering ion for As detection.

The versatility of the method for hybridization of different components is demonstrated by synthesizing size-specific hybrid NPs based on Fe-biomolecules. We have chosen an anticancer peptide (p53p, MW 1.8 kDa) and an common enzyme (glucose oxidase, MW 160 kDa) as model molecules to illustrate the versatility of the method towards different types of molecules over a large size range. We show that the electrostatic interaction for complex formation of metal hydroxide ion with the partially charged side of the biomolecule in the solution is the key to hybridization of metal-biomolecule materials to form complexes as the building blocks. These hybrid NPs with controllable sizes ranging from 30 nm to 3.5 μm are found to exhibit superparamagnetic behavior, which is a big challenge for particles in this size regime. As an example of greatly improved properties and functionality of the new hybrid material, in-vitro toxicity assessment of Fe-glucose oxidase hybrid NPs shows no adverse effect, while the Fe-p53p hybrid NPs are found to selectively bind to cancer cells. The present work therefore definitely demonstrates the general applicability of the hybridization method for synthesis of metallic hybrid NPs with magnetic properties for different applications, including chemical sensing, magnetic resonance imaging contrast agents, and targeted drug delivery carriers.

Acknowledgements

I would like to express my deepest gratitude to my PhD supervisor Prof. Kam Tong Leung for his invaluable support throughout this project. He gave me the opportunity to be a part of the Waterloo Advanced Technology Laboratory (WATLabs) family and opened the door that lead to the fascinating world of science and technology in front of me. I would also like to thank my advisory committee members, Dr. Juewen Liu, Dr. Mark Pritzker, and Dr. Dan Thomas for their insightful comments, suggestions and valuable feedback on the work.

It is a pleasure to thank our science and electronic shop people; Harmen Vander Heide, Peter Kessel, Jacek Szubra, Zhenwen Wang and Krunomir Dvorski for helping me every time I faced any technical problem. Their brilliance has always led me to come back to my experiments by solving problems I have encountered with. I am also grateful to Dr. Jalil Assoud and Dr. Steven Forsey for their help and advice in solid state chemistry and organic chemistry. I acknowledge Dr. Zhengding Su and Dr. John Honek because of their help and support in using their equipment for bio test and providing the cancer drug materials. I am thankful to Apraku Donkor and Dr. Shirley Tang, for their help and collaborations in the biochemistry part of the thesis. I would also thank Mehdi Rahimi and Dr. Holger group for their comments in electrochemistry experiments and XRD analysis. I am grateful to Dr. Jason Li (Asylum Inc.) for assistance with the AFM experiments

I acknowledge the Waterloo Institute for Nanotechnology for the Graduate Research Fellowship to support my research in Nanotechnology and National Council of Canada. I am gratefully acknowledges Dr. Mamata Mohapatra for her unwaiveing support and willingness to help and give helpful suggestions during the past years.

I am truly thankful to my colleagues and group members, Samad Bazargan, Avisek Chatterjee, Debabrata Pradhan, Nina Heinig, Marwa Abdellah, Bahareh Rahsepar, Joseph Palathinkal , Saurabh Srivastava and Lei Zhao for their tremendous support and enthusiasm.

Last but not least, I express my heartfelt gratitude to my parents, my siblings and spouse for their love has always been with me and has given me the energy to reach my goals. I am proud of you and you have a big share in what I have achieved.

Table of Contents

List of Figures

List of Tables

Chapter 1

Introduction

1.1 Hybrid Nanoparticles

Nanotechnology has recently attracted much attention in analytical and biochemistry because of the application of a wide variety of nanomaterials, especially nanoparticles (NPs), in analytical methods. NPs are very interesting because they constitute a new type of material with properties that are very different from those of individual atoms and molecules or bulk matter. NPs have a much larger surface area to volume ratio (or specific surface area) than their bulk counterpart, which along with quantum size effects forms the basis of their unique physicochemical properties.

Metallic clusters or NPs have attracted much recent attention[1] because of their extremely small size and their potential usefulness in a wide range of catalytic, [2,3] information-storage and magnetic, [4–6] biomedical,[7] and optical and electronic applications.[8,9,10] Hybrid or multifunctional NPs constructed from more than one component have also attracted increased interest due to their additional functionalities.[11–14] The term "hybrid NP" is commonly used to describe a discrete multi-component NP, which includes multi-metallic systems and alloy NPs.[10] These components could be two (or three) metals, or a metal and an organic or biomolecule, or a metal and metal oxide. A number of important considerations motivate the combination of more than one component together to make a composite NP. For instance, the surface chemical properties particle can be modified by coating with a second material to improve colloidal stability or resistance to oxidation.[10] New synergetic effects can be created upon alloy formation of two metals. Additional functionality may also be introduced into a NP in bio-applications, for instance, by attaching an antibody for biological targeting application. Many different possible types and morphologies of hybrid NPs exist, some of which are showed schematically in Figure 1.1.[10]

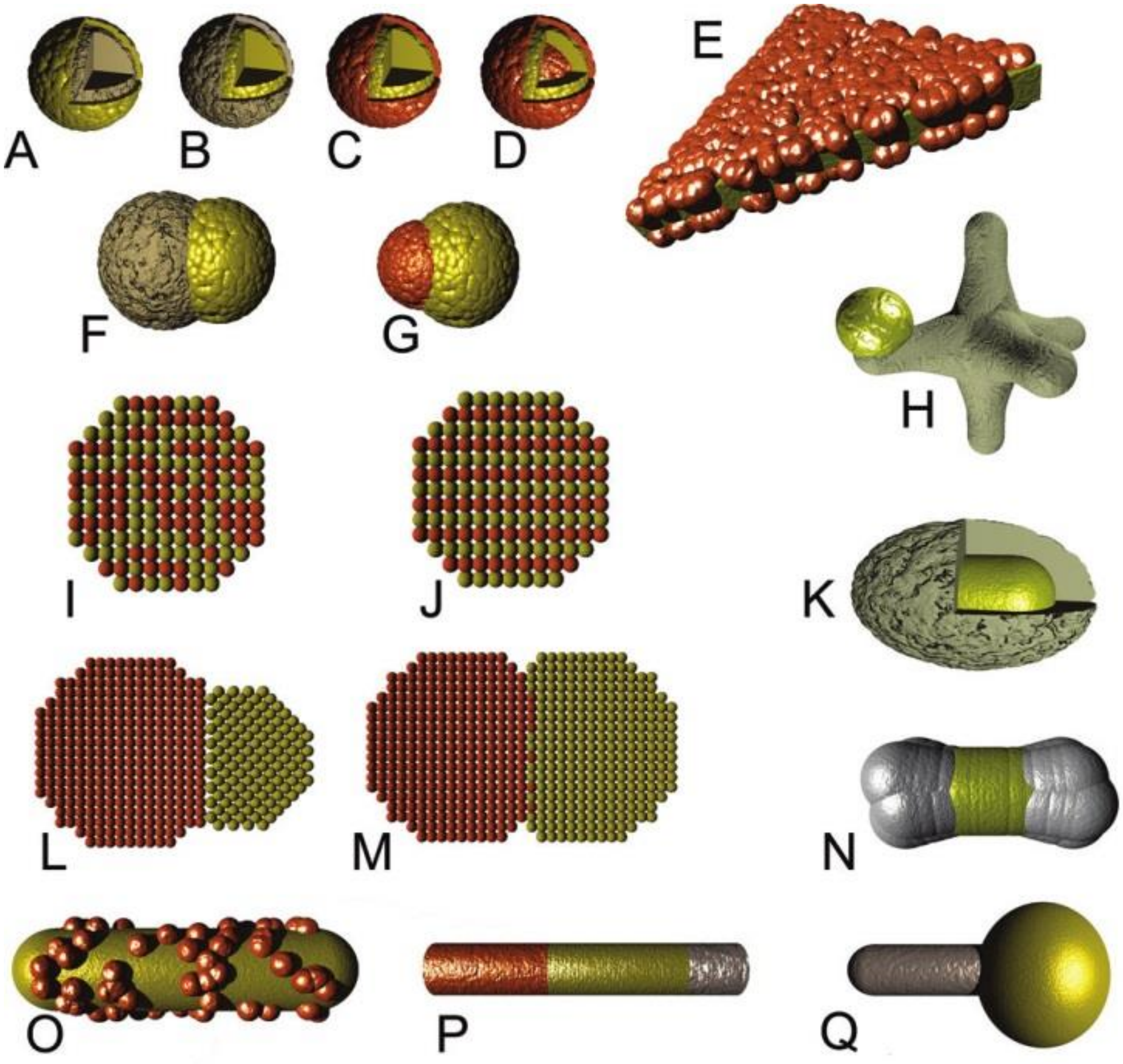

Figure 1.1 Examples of hybrid nanoparticles (NPs): (a) dielectric@metal core-shell, (b) metal@dielectric core-shell, (c) metal@metal coreshell, (d) metal@metal@metal core-shell, (e) metallic nanotriangle with overcoat of second metal, (f) heterodimer composed of dielectric and metal parts, (g) heterodimer composed of two different metal parts, (h) semiconductor crystal with attached metal nanosphere, (i) cross section through alloy metal NP showing disordered nature of atomic occupancies, (j) cross section through NP composed of an intermetallic compound showing ordered atomic occupancy, (k) metal nanorods coated in a thick shell of dielectric, (l) dimer with incoherent crystalline interface between the parts, (m) dimer with coherent interface between the parts, (n) nanorods with overgrowth of another metal at the rod ends, (o) nanorods with a sparse overgrowth of a second metal, (p) segmented nanowires or nanowire composed of two or more elements, and (q) “nanotadpole”.[10*]

---

[*] Reprinted with permission from: Cortie, M. B. and McDonagh, A. M., Chem. Rev. 111, 3713–35 (2011). Copyright (2011) by the American Chemical Society.

Bimetallic NPs are a unique class of materials that show a combination of properties associated but sometimes very different with the two metals components. In many cases, their specific physical and chemical properties are greatly enhanced owing to a synergistic effect.[15,16] Based on the mixing pattern (also known as chemical ordering), bimetallic NPs can be divided into three main types:[9] Core-shell segregated alloy NPs (Figure 1.2a) consist of a core of one type of atom (A) surrounded by a shell of another type of atom (B), though there may be some mixing between the core and the shell at their interface ($A_{core}B_{shell}$). Segregated alloy NPs or heterostructures[1] (Figure 1.2b) consist of A and B subclusters, which may share a mixed interface (left) or may only have a small number of A-B bonds (right). A more common type of alloy NPs is the mixed A-B alloy NPs (Figure 1.2c), which may be either ordered (left) or randomly mixed (i.e., a solid solution, right). Randomly mixed alloy NPs are what have often been referred to as "alloy" NPs in the literature. The intermixed pattern is common to many systems. Multishell alloy NPs (Figure 1.2d) may contain layered or onion-like alternating -A-B-A- shells. Metastable structures of this type were suggested for the growth of Cu-Ag, Ni-Ag and Pd-Ag NPs in computer simulations studies.[17,18,19] Bimetallic alloy NPs (A_mB_n) can be generated with a variety of controlled size (m + n) and composition (m/n).

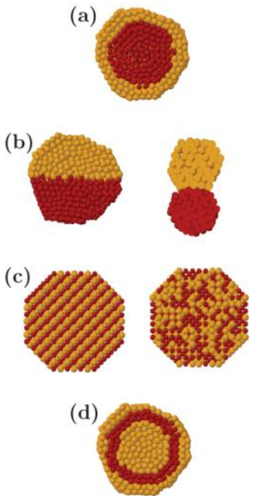

Figure 1.2 Cross-sectional schematic representation of nanoparticless of possible mixing patterns: (a) core-shell, (b) subcluster segregated, (c) mixed, and (d) three shell.[9†]

[†] Reprinted with permission from: Ferrando, R., Jellinek, J. & Johnston, R. L., Chem. Rev. 108, 845–910 (2008). Copyright (2008) by the American Chemical Society.

Among all the bimetallic NPs, bimetallic alloy NPs are among the most important nanomaterials because of their applications in numerous catalytic reactions, including catalytic reforming reactions, pollution control, and alcohol oxidation.[20–25] Increase in solid solubility of alloy components with decreasing particle size is one of the prominent effects. The "alloy" properties of these NPs are found to depend not only on their relative compositions and crystal structures, but also on their sizes and shapes.[26] Alloy NPs can be generated in a variety of media, including as-born in NP beams, growth in colloidal solutions, immobilized on surfaces, or inside pores. These alloy NPs are particularly interesting because their chemical and physical properties may be tuned by varying the composition and atomic ordering as well as the size and shape of the NPs. Indeed, alloy NPs may display not only magic-number sizes but also magic compositions, i.e., compositions at which the alloy NPs exhibit special stability or other enhanced properties.[9]

Alloy NPs may also be classified as "free"/"bare" or "passivated"/"coated", depending on whether the surface of the NP is stabilized by surfactant molecules or ligands.[9] Free/bare NPs are usually produced in a molecular beam or the gas phase, while passivated NPs can be generated in both the solution and gas phases. Alloy NPs may also be "supported" on surfaces or inside porous materials. One challenge in studying bare metal NPs is that it could be difficult to isolate and handle them. To enable the investigation of near-uniformly sized NPs and to exploit NP properties in device applications, it is necessary to protect them with a shell. NPs can also be deposited from a solution onto a (conductive) substrate or from the gas phase onto any substrate such as graphite, silicon, or an inorganic oxide. For applications in which NPs need to be immobilized on a surface (e.g. sensing), synthesis methods for supported NPs are more appropriate.

1.2 Methods for preparation

Different methods can be used for making hybrid NPs, including bimetallic and alloy NPs. In this section, we summarize the synthetic techniques that are commonly used to prepare hybrid NPs consisting of two components. These synthetic principles can be extended to produce more complex, multicomponent structures, if desired. Our focus is on thecombination of metallic components but some of the methods can also be used for synthesis of metal-semiconductor or metal-oxide hybrid NPs.

1.2.1 Chemical Reduction

A colloidal metal particle consists of a metallic core surrounded by a ligand shell. Colloidal metallic particles can be produced by chemical reduction of metal salts dissolved in an appropriate solvent in the presence of surfactants (e.g., citrate, alkylthiols, thioethers) or polymeric ligands (e.g., polyvinylpyrrolidone or PVP), which passivate the NP surface.[27] First published by Faraday in 1857,[28] this approach was further developed and standardized by Turkevich in 1950s,[29] who also proposed a mechanism for the formation of colloidal NPs which involves stepwise nucleation, growth and agglomeration. Modern analytical experiments have essentially validated this mechanism, which makes use of "seed" particles (<1 nm in diameter) as nuclei for further growth ("ripening").[30]

1.2.1.1 Co-reduction

The coprecipitation method is a one-step method that produces hybrid particles by simultaneous nucleation and growth. Solution conditions are chosen to enable both components to precipitate simultaneously. If the two components nucleate heterogeneously on each other, then a homogeneous composite particle will form.[31,32] In the case of metallic components, however, the coprecipitation does not usually occur because the redox potential for each reduction reaction is different. This leads to the more noble element being reduced first followed by the other element. This can be overcome by using a very strong reductant such as borohydride, so that reduction occurs so rapidly that the usual galvanic processes do not occur to a significant extent.[10] The order of deposition can be changed if the reduction is conducted in the presence of a ligand (surfactant) that bonds more strongly to the metal with the higher redox potential. Another way of making bimetallic particles is reduction of the co-complexes, that contain both metal species.[9]

1.2.1.2 Successive reduction

Atoms of one metal can be deposited onto an as-prepared NP of another metal via the so-called "seed-germ" process introduced by Schmid and coworkers.[31] In this method, as-prepared NP (seed) with active surfaces undergoes a second reduction step in the presence of salts of the other metal. The seed is usually produced separately by some appropriate method, such as nucleation and growth by reduction, pH change of a solution, or pyrolysis of an appropriate precursor.[10] The reaction environment is then changed so that a second component can precipitate onto the first component. The second component will often nucleate and grow on the first component to produce the composite NPs, because heterogeneous nucleation is generally more favorable than homogeneous nucleation.[33,34]

1.2.2 Synthesis by galvanic replacement

This method has two separate steps, in which a NP of a moderately active metal, such as Ag or Co, of appropriate shape and size is first produced, and then a solution of a more noble metal such as Au is introduced. The more noble metal precipitates onto and begins to consume the more active core material by galvanic displacement. If the process is allowed to proceed to completion, the product could be a hollow, single-phase NP of the second component[10] (Figure 1.3). If the process is stopped before completion, a hybrid core-shell or alloy NP is produced. Generally, the more noble metal precipitates on the outside of the core NP but in some cases an inversion could occur. For instance, when Au is reacting with InAs NPs, Au diffuses rapidly to the interior of the InAs NPs to form a well-defined core, while a shell of amorphous InAs or In_2O_3 forms on the Au core.[35]

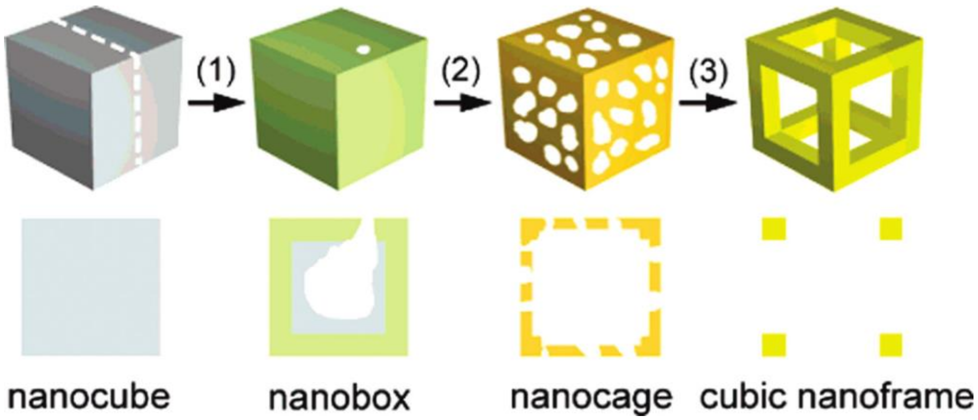

Figure 1.3 Perspective diagram (top) and cross sectional view (bottom) of the process of galvanic displacement of Au for Ag, which is used to convert a template to alloy boxes or cages, or even a hollow frame.[36‡]

1.2.3 Template growth

Physical vapour deposition can be used to produce NPs of triangular or semishell.[37] Hybrid NPs can be produced by changing the composition in the sputter targets. In solution, a

---

[‡] Reprinted with permission from: Lu, X.; Au, L.; McLellan, J.; Li, Z.-Y.; Marquez, M.; Xia, Y., Nano Lett. 7, 1764 (2007). Copyright (2008) by the American Chemical Society.

porous alumina template is generally used to prepare hybrid NPs by successive addition of metals, such as Au followed by Pt using appropriate salt solutions. To obtain free hybrid nanocylinders or nanowires, the template is then dissolved by electrolysis and nanostructures are produced.[38,39]

1.2.4 Radiolysis and sonochemical synthesis

In the radiolytic method, γ-ray irradiation of water leads to solvated electrons and these electrons reduce the metal ions, and the subsequent coalescence of metals results in NPs.[9] In the case of two metals, the more noble metal is reduced preferentially. Formation of core-shell or alloy NPs is possibledepending on the relative concentrations of the two metals, rate of radiolysis (which depends on the γ-ray dosage), rate of inter-ion electron transfer and nature of the ligands coordinated to the metal ions.[9,40]

In sonochemical synthesis, high-intensity ultrasound is used to irradiate on aqueous solution of metal ions. In this method, formation of a core-shell structure is influenced by the sonochemical experimental conditions: effective stirring, microjet stream and shock wave.[41] Kan et al. have shown that successive deposition is more effective than simultaneous deposition for sonogeneration of core-shell Au-Pd alloy NPs.[42]

1.2.5 Molecular beams and ion implantation

Synthesis of NPs by molecular beams is generally applicable using metal NP sources of the gas condensation type. These include the following:[9,43–45]

- Laser vaporization: For synthesis of bimetallic NPs, a powerful incident laser beam is used to vaporize or ablate single alloy targets (in the form of rods, discs or pallets), mixed metallic powders, or two monometallic targets.
- Pulsed arc NP ion source: Mono or bimetallic target is used and the vaporization occurs by passing an intense electrical discharge.
- Ion sputtering: Bombarding a metal target with high-energy inert gas ions (generally Kr^+ or Xe^+) with bombardment energies in the range of 10-30 keV and currents of ~10 mA are required to produce NPs.
- Magnetron sputtering: By applying either a DC or a RF potential, argon plasma is illuminated onto a target and confined by a magnetic field (generated in a magnetron). Ar^+ ions in the plasma are then accelerated onto the target and sputter it.

After the atoms are generated in the gas phase, condensation of NPs can be achieved by letting the metal vapors collide with a cold inert carrier gas and/or expansion through a nozzle.[46] In addition, sequential implantation of two different metal ions has been used to generate implanted bimetallic NPs. For example, generation of solid-solution Ag-Au, Cu-Pd, and Cu-Au alloy NPs by ion implantation in silica using metallic ion beams with energies of approximately 100 keV has been demonstrated.[47]

1.2.6 Electrochemical synthesis

Electrochemical synthesis is one of the most versatile methods of generating mono and bimetallic NPs in solution. Bimetallic PdNi, FeCo, and FeNi NPs have been prepared using two sacrificial bulk metallic anodes in a single electrolysis cell.[48] Bimetallic NPs of the less soluble metals as anode, such as Pt, Rh, Ru, and Mo, can be produced by reducing their salts at the cathode electrochemically. Core-shell layered bimetallic NPs such as Pt core and Pd shell[49] can also be produced by electrochemical deposition methods. In electrochemical synthesis, the more reactive metals are used as the reducing agents for the more noble metals, e.g., the Fe^{2+}/ Fe^0 couple has an electrode standard potential E_0 of –0.45 V (wrt SHE), while that for $[PdCl_4]^{2-}/Pd^0$ is +0.59 V. Pd-coated Fe NPs have been generated in this way.[50]

We briefly compare different synthesis methods of hybrid NPs with the electrochemical method, and explain why we have chosen this method for synthesis of hybrid NPs in the present work. Wet chemical methods conducted at room temperature have been used to produce amorphous alloy NPs by reverse micelle synthesis and microemulsion process,[51] while crystalline NPs can be produced in various aqueous and nonaqueous media by, borohydride reduction and hydrazine reduction of Fe and Ni inorganic salts for example.[52] However, it is very difficult to obtain a narrow size distribution of NPs with these room-temperature methods, making it necessary to perform the synthesis at a higher temperature (above 300°C) in the presence of surfactants.[53] Although surfactants can also stabilize the dispersion of NPs and prevent their aggregation, incorporation of bulky or strongly binding surfactants in the NPs can affect their properties, sometimes in an undesirable way. Dry synthesis methods, such as arc discharge,[54] hydrogen plasma reaction[55] and reduction of $FeCl_2$ and $NiCl_2$ vapours in the presence of H_2,[56] can produce spherical NPs or powders. However, the product obtained often agglomerate into NPs or chains due to their magnetic interactions. This makes generation and study of uniformly dispersed, individually separated NPs challenging. Electrochemical methods have the advantage of producing NPs with a uniform spatial distribution without agglomeration, which therefore provides the maximum exposed surface for electro-catalysis without any additional step. Electrodeposition usually results in highly crystalline NPs with a very thin oxide-shell that is formed in-situ in the synthesis. This oxide shell can sometimes serve as a protective layer from further oxidation and make the hybrid NPs stable in air. Electrodeposition can also be performed in a mild solution (close to neutral pH) at room or low temperature (4°C), which is highly desirable for hybridization of metal-biomolecules. For sensor applications that require supported NPs, the electrochemical method does not require additional steps for electrode preparation.

1.3 Fe-M Nanostructures

As for bulk alloys, a very wide range of combinations and compositions are possible for alloy NPs. Driven by the need for low-cost soft magnets,[57,58] catalysts,[59] and biosensors,[60] the study of bimetallic (and trimetallic) transition metal-based NPs has become a very important research area. In particular, the use of bimetallic NPs, such as Ni, Fe, and Co in combination with noble metals, can decrease the content of expensive noble metals, thereby producing low-cost, affordable catalysts. Being an essential trace element, Fe meets the requirements for application in the human body. Fe-based soft alloys are used for their high magnetic flux density. They are also offer interesting mechanical, electrochemical and biological properties. In this section, we provide a few examples of hybrid NPs reported in the recent literature, with emphasis on those containing transition metal (or oxide) components. In particular, we focus on experimental studies of hybrid NPs that show improved magnetic properties, enhanced chemical sensing performance and air/gas stability.

Improved magnetic properties: FeNi is one of the most well-known systems for its interesting magnetic properties. Their properties are very different, in some cases, from the single metals Fe and Ni. In the nano-size regime, FeNi nanostructures with different shapes exhibit different magnetic properties. For instance, the coercivity of FeNi alloy nanowires and nanotubes shows disparate behaviour according to a report by Zhang et al.[61] FeNi alloy nanowires and nanotubes were produced in the pores of anodized aluminum oxide templates by direct current electrodeposition at different potentials. The observed differences in coercivity were attributed to differences in the grain size and distinctive structures of FeNi nanowires and nanotubes.[61] Figure 1.4 shows the SEM and TEM images of the template, FeNi nanowires and nanotubes so produced, together with their magnetic hysteresis loops.

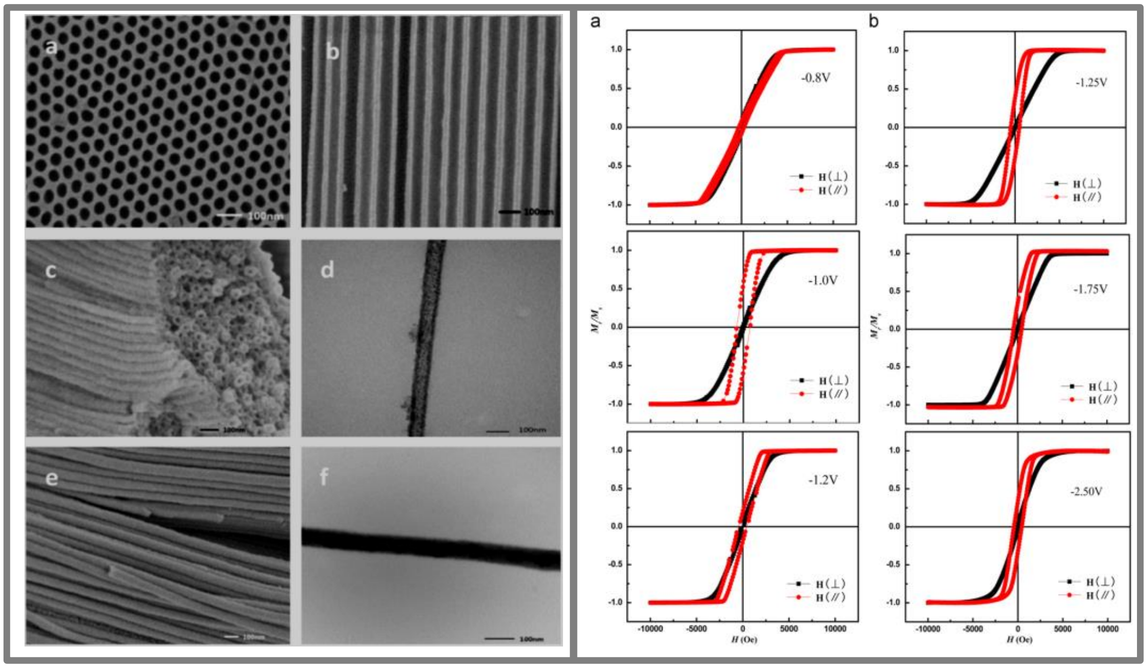

Figure 1.4 Left panel: Scanning electron microscopy images of (a) the surface and (b) cross-section of anodized aluminum oxide template, (c) FeNi alloy nanotubes and (e) nanowires; and corresponding transmission electron microscopy images of (d) FeNi alloy nanotubes and (f) nanowires. Right panel: Magnetic hysteresis loops of FeNi alloy (a) nanowires and (b) nanotubes with different ratios. The red dots denote results for the field applied parallel to axis and the black dots denote that for field applied perpendicular to axis.[61][§]

Another example of enhancement in magnetic properties due to alloying involves nanofibers composed of Co and Ni, which have been prepared by electrospinning. The prepared CoNi nanofibers revealed better magnetic properties compared to those of Co-doped Ni and pristine Ni nanofibers and so have the potential for use as nickel-based soft magnetic materials.[62] Figure 1.5 shows the scanning electron microscopy (SEM) images of nanofibers with their magnetic hysteresis loop.

[§] Reprinted with permission from: Zhang, X. Zhang, Zhang, H., Wu, T., Li, Z., Zhang, Z., Sun, H., J. Magn. Magn. Mater. 331, 162–167 (2013). Copyright (2013) by the Elsevier.

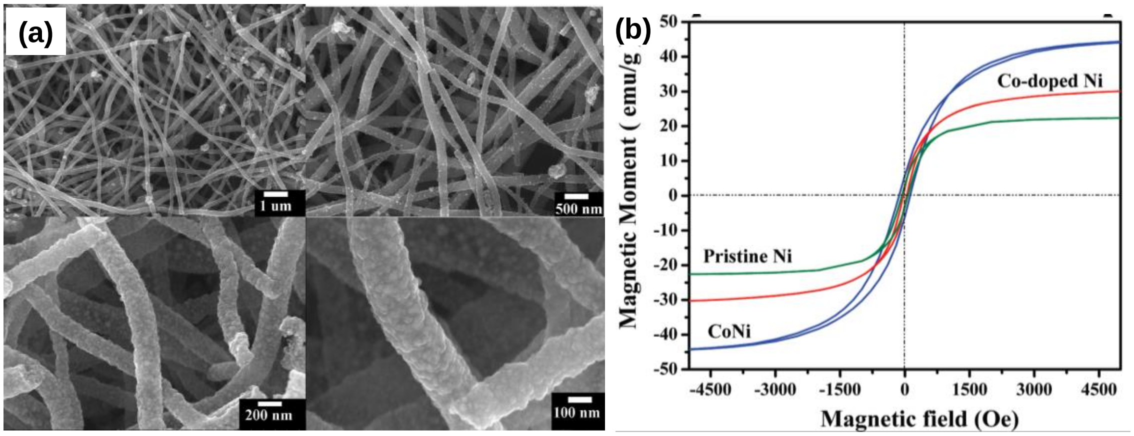

Figure 1.5 (a) Scanning electron microscopy images at different magnifications of electrospun NiAc/CoAc/PVA nanofiber mats; (b) magnetic properties of CoNi nanofibers compared with those for Co-doped Ni and pristine Ni nanofibers.[62][**]

Catalysis and chemical sensing: Detection of chemical and biological agents plays a fundamental role in biomedical and environmental sciences.[63] Nanomaterials with their unique physicochemical properties have great potential for use in new recognition and transduction processes for chemical and biological sensors, and improving the signal-to-noise ratio by miniaturization of the sensor elements. [63] Alloying or hybridization can enhance the chemical activity of nanomaterial even more. For instance, $PtFe_x$ NPs provide more active sites for methanol oxidation compared to Pt NPs.[64] Similar improvement has been observed in Pd_xNi_y bimetallic NPs (with Pd-to-Ni atomic ratios of 2:1, 3:2 and 1:1) for formic acid oxidation.[65] The peak current obtained using Pd_3Ni_2 catalysts for formic acid oxidation was found to be about three times higher than that using Pd catalysts, both supported on multiwalled carbon nanotubes.

An interesting synergistic property has been reported by Jiang and Xu. They showed that their Pt–Ni bimetallic nanocatalysts exhibit excellent catalytic activity for the decomposition of hydrous hydrazine, producing hydrogen with a 100% selectivity at room temperature, while the corresponding single-component Ni and Pt counterparts were found to be totally inactive to this reaction.[16] The last example is FePt NPs with chemically disordered face-centered cubic (fcc) structure, in which Fe and Pt atoms are positioned randomly in the lattice. The results show that intermetallic FePt NPs are much better catalysts for the oxygen reduction reaction.[66]

[**] Reprinted with permission from: Barakat, N. a. M.; Khalil, K. a.; Mahmoud, I. H.; Kanjwal, M. a.; Sheikh, F. a.; Kim, H. Y., J. Phys. Chem. C, 114, 15589–15593(2010). Copyright (2010) by the American Chemical Society.

Stability: Because of their small size and high specific surface area, nanoparticles are usually very active and can be easily oxidized or reacted. Maintaining their stability and a long shelf-life is therefore a big challenge for most NPs and most of their preparation methods. Hybridization can sometimes be used to overcome these challenges. As an example, Markova et al. reported air-stable magnetic bimetallic FeAg NPs, which exhibit antibacterial and antifungal activities against a variety of microorganisms, including disease-causing pathogens. They showed that the formation of a Fe_3O_4/γ-FeOOH double shell on a "redox" active zero-valent iron surface is responsible for its high air stability.[67] Figure 1.6 shows a schematic illustration of the bimetallic FeAg nanoparticles and their corresponding SEM image and X-ray elemental maps. Furthermore, Liu et al. reported PtFe bimetallic NPs with various architectures, including PtFe random alloys, Pt_3Fe/Pt core-shell, Pt_3Fe intermetallic, and Pt/Fe_xO_y core-shell-like NPs, which are stable toward CO/H_2. Both the alloy and core-shell nanoparticles show a lower onset potential for the electro-oxidation of CO/H_2 than that of pure Pt.[68]

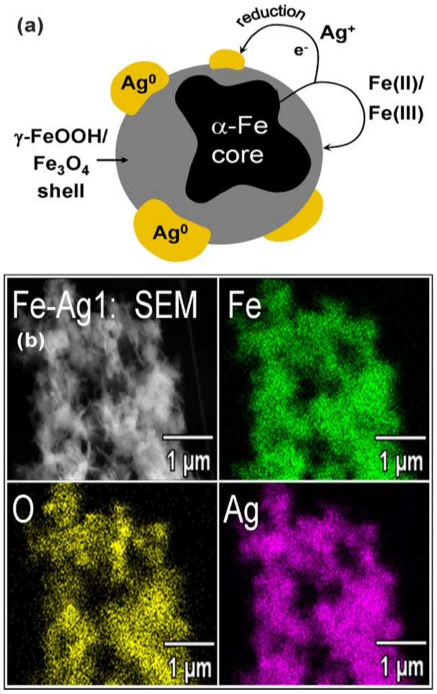

Figure 1.6 (a) Schematic illustration of bimetallic FeAg nanoparticles and (b) their scanning electron microscopy (SEM) image and Fe, O and Ag X-ray elemental mapssilver (Ag)) of Fe−A.[67††]

[††] Reprinted with permission from: Markova, Z.; Siskova, K. M.; Filip, J.; Cuda, J.; Kolar, M.; Safarova, K.; Medrik, I.; Zboril, R., Enviromental Sci. Technol. 47, 5285–5293(2013). Copyright (2013) by the American Chemical Society.

1.4 Scope of Thesis

Hybrid nanostructures offer additional functionalities compared to pristine NPs. In the present work, we develop a hybridization method using electrochemical amperometry to synthesize hybrid metallic NPs. A series of detailed studies are performed to establish and optimize the synthesis methods and to understand the underlying growth mechanisms of different hybrid NPs, including bimetallic Fe-M (M=Ni, Au, Pt, Pd) NPs and Fe-biomolecule (glucose oxidase, p53p protein). Using several electrochemical methods, we fabricate NPs with well-defined composition, shape and size by varying electrolytes, deposition potentials and bath temperature. Our objectives are two-fold: (a) to develop fundamental understanding of their structure-property relations through manipulation of the growth parameters, and (b) to exploit the novel properties of these hybrid NPs for sensing, analytical and biological applications.

After a brief introduction to hybrid nanoparticles and their synthesis methodologies (Chapter 1) and a description of the experimental setup and characterization techniques used in this work (Chapter 2), we present the results of four different studies on hybrid nanoparticles. In Chapter 3, we report the controlled electrochemical synthesis of FeNi NPs with different shape, composition, phase combination and sensing and magnetic properties by careful variation of experimental parameters. We demonstrate a direct correlation between the FeNi NP composition their shape and phase transformation by detailed X-ray diffraction and transmission electron microscopy analyses. We further show that our method provides a simple approach to synthesize FeNi concave nanocubes and nanocages, the shapes of which are not thermodynamically favorable. The concave shape can be obtained through controlled triggering of different growth kinetics of Fe and Ni. Our kinetic studies show that upon reaching a minimal size of 45-50 nm, thermodynamically driven growth switches to kinetically driven growth. We report enhancement in air-stability, chemical activity and shape-dependent magnetic properties for these FeNi NPs due to the synergistic properties introduced by hybridization. We also provide a large-scale computation study based on density functional theory (DFT) in order to investigate the effect of the crystalline phase combination on the magnetic properties of these FeNi alloys.

The enhancement in chemical sensing observed for FeNi NPs inspired us to explore the possibility of improving the chemical sensing for vitamin C (Chapter 4) and arsenic (Chapter 5) by synthesis of Fe-noble metal NPs. In Chapter 5, we extend our hybridization method to the synthesis of FeM (M=Au, Pt, Pd) NPs and show the versatility of this method for obtaining different bimetallic systems. FePt NPs are found to notably enhance the sensitivity and selectivity toward detection of vitamin C, in comparison to Pt NPs, due to reduction of the over-potential for vitamin C oxidation as a result of alloying. The selectivity of the FePt sensor has also been greatly enhanced even in the presence of other common interfering species, including dopamine, citric acid, uric acid, glucose and NaCl. X-ray photoelectron spectroscopy reveals changes in the electronic structure of FePt NPs from that of pristine NPs, which could provide a mechanism for the observed enhancement in the electro-oxidation of vitamin C. Similar effect is also observed for arsenic detection (Chapter 5).

Chapter 6 introduces a breakthrough approach in making a new class of bio-nanomaterials by hybridization of Fe and biomolecule (i.e., glucose oxidase and p53p protein). These hybrid NPs are obtained in-situ by using Fe-biomolecule complexes as the building blocks. To illustrate the versatility of this hybridization method, we have chosen an anticancer peptide (p53p) and an enzyme (glucose oxidase), with vastly different structures and different sizes. Advanced three-dimensional characterization by multi-cross sectional focused ion beam scanning electron microscopy, along with state-of-the-art secondary ion mass spectroscopy chemical imaging, confirms the hybrid nature of these NPs. These results also demonstrate the importance of these three-dimensional characterization methods for investigation of integrated nanostructures such as hybrid NPs. We further propose a “stone-and-mortar” structural model for these hybrid NPs, in which Fe nanocrystallites are “stuck” together by biomolecules. We also observe extraordinary superparamagnetic behavior of these hybrid NPs in the large-size regime (30-3500 nm). This synergetic property is the result of isolating Fe nanocrystallites inside the NP by the biomolecules. As a good demonstration of using these hybrid NPs in bio-applications, we test the biocompatibility and selective binding of Fe-biomolecule NPs for targeted drug delivery and for use as magnetic resonance imaging contrast agents. In particular, Fe-enzyme NPs are found to exhibit no detrimental effects on cell growth of very delicate cells (i.e. human hepatoma cells), which make them bio-friendly and an excellent contrast agent for magnetic resonance imaging (that requires cell-friendly and magnetic nanoparticles). On the other hand, Fe-p53p NPs are found to selectively bind to Mdm2 and MdmX, which are over-expressed in nearly 50% of cancers and inhibit p53p anticancer activity, providing a promising anticancer therapeutic drug.

The present work not only introduces a new strategy of direct incorporation of two components (metal-metal and metal-biomolecule) into a hybrid structure, but also demonstrates the advantages in tuning the resulting properties for applications, including label-free chemical sensing of toxins in water and pharmaceutical waste, targeted drug delivery and contrast enhancement for magnetic resonance imaging.

Chapter 2

Experimental Details

In this chapter we summarize the experimental techniques that are used for synthesis and characterization of hybrid nanoparticles (NPs). A brief description of each of the relevant methods follows.

2.1 Electrochemical Methods for Synthesis and Characterization

2.1.1 Electrochemical techniques for synthesis

Electrochemical deposition of hybrid NPs is often conducted in a freshly prepared deoxygenated electrolyte solution by using amperometry potentiostatically versus a reference electrode such as Ag/AgCl for an appropriate amount of deposition time. Amperometry is a powerful technique in which a current is measured as a function of either time or applied electrode potential. Potentiostatic amperometry corresponds to amperometry conducted with the electrode potential kept constant while time is varied. Electrode potentials at which the metal ions are reduced to their respective zero-valent metals are applied. For instance, the applied potential for Fe or Ni is –1.4 V, while that for Pt or Pd is –1.2V and that for Au is –0.8 V (all vs Ag/AgCl). The applied potential is chosen to be sufficiently positive relative to –1.6 V to avoid excessive hydrogen evolution. The electrolyte provides the main source of metal ions for the preparation of hybrid NPs, while supporting electrolyte is used to increase the conductivity of the primary electrolyte solution. Deposition temperature and pH are two important factors and are selected on a case by case, which is discussed in the experimental part of each chapter.

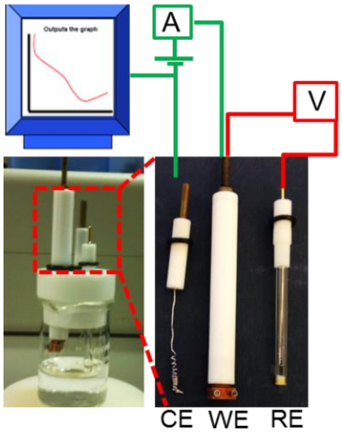

Figure 2.1 A 3-electrode electrochemical station with working electrode (WE), Ag/AgCl reference electrode (RE) and Pt counter electrode (CE).

2.1.2 Electrochemical techniques for analysis

2.1.2.1 Cyclic Voltammetry, Square Wave Voltammetry and Differential Pulse Voltammetry

For the characterization and particularly sensing application, a number of electrochemical methods have been used. They are mostly based on voltammetry. Voltammetry itself is a form of amperometry, in which the current is measured as a function of the potential applied to the electrode. Different voltammetric techniques are performed based on how the potential is varied as a function of time. In cyclic voltammetry, the potential is increased linearly from an initial potential to a final potential (as defined in the measurement). The potential is then reversed and sweep in the opposite direction until it reaches the initial potential value. The sweep rate is an important parameter in cyclic voltammetry and it usually lies between 5 mV/s and 1 V/s. The sweep rate is one of the most important variables in voltammetry, because it controls the time scale of the experiment.[69]

Square wave voltammetry (SWV) is a frequency-dependent electrochemical technique, in which the waveform of the applied potential is discontinuous rather than linear. The waveform is a superimposition of a square wave potential on a staircase potential, which results in higher sensitivity than the staircase potential alone.[70] Figure 2.2 shows the schematic of the potential profile (waveform) in SWV.

The current is sampled at the start and the end of each pulse and the current difference between these two measurements is plotted against the staircase potential in a square wave voltammogram. The reduction or oxidation of species is measured as a peak or trough.[71] Differential pulse voltammetry (DPV) can be considered a derivative of linear or staircase voltammetry but the potential waveform consists of small pulses (with constant amplitude) that superimpose on a staircase waveform. DPV and SWV are similar techniques, but in SWV equal time is spent at the potential of the ramped baseline and that of the superimposed pulse.

In this work, we usually used cyclic voltammetry (CV) for initial investigation of the species in the solution. As will be shown in Chapter 3, we compare the CV voltagrams of FeNi NP electrodes in PBS solution with and without 4-aminophenol. From the differences in the CV profiles we could conclude FeNi electrodes are sensitive to the presence of 4-aminophenol. A similar investigation is applied for vitamin C (Chapter 4) and arsenic (Chapter 5). We also used CV for electroleaching of FeNi NPs to obtain concave nanocages. SWV and DPV are used for more accurate measurement of the sensing properties of trace amounts of arsenic in solution. The calibration plot for this sensor as obtained by these methods is presented in Chapter 5.

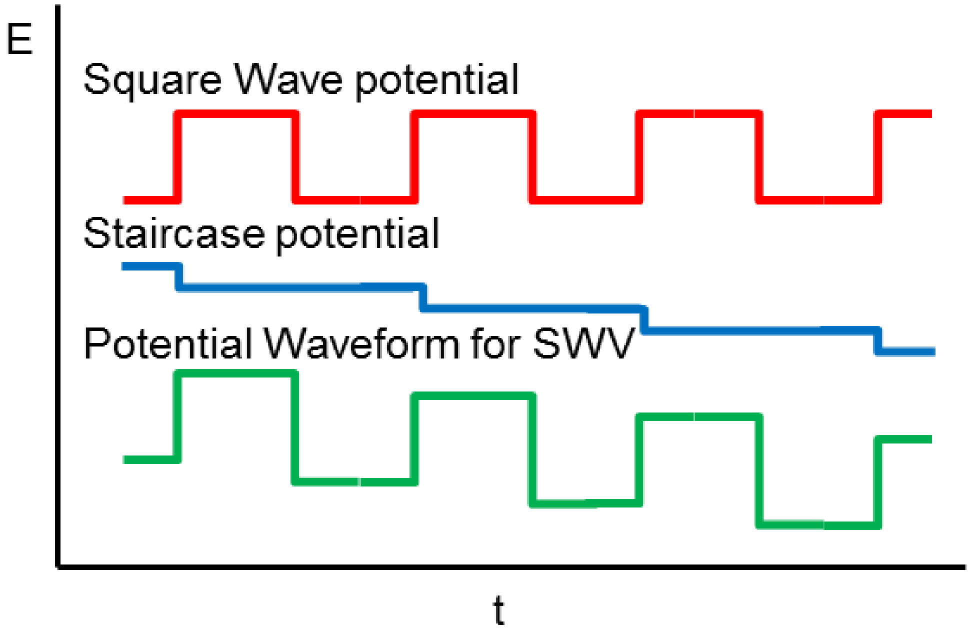

Figure 2.2 The potential waveform for square wave voltammetry.

2.1.2.2 Chronoamperometry

In chronoamperometry, the potential of the working electrode is stepped and the resulting current resulting from faradic processes at the electrode (caused by the potential step) is monitored as a function of time. Due to electron transfer, the faradaic current decays as described in the Cottrell equation:

$$I = nFAC_0D^{1/2}\pi^{-1/2}t^{-1/2}$$

where n is the number of electrons participating in the oxidation or reduction reaction, F is the Faraday constant, A is area of the electrode, D is the diffusion coefficient and C_0 is the initial concentration (bulk) of electrolyte. We apply chronoamperometry in Chapter 3 to obtain the electroactive surface area of FeNi NP electrodes using the Cottrell equation. By applying a step potential sufficiently enough than the oxidation peak of cyanide in $K_3Fe(CN)_6$ solution, we plot the I-t (current vs time) and could obtain A, the electroactive area of the electrode.

2.2 Characterization by Scanning Electron Microscopy (SEM), Helium Ion Microscopy (HIM) and Transmission Electron Microscopy (TEM)

To investigate growth mechanisms, structure-property relations and shape-dependent properties, we have used different electron and ion microscopic techniques to image the surface and structure of hybrid nanoparticles (NPs). Scanning electron microscopy (SEM) is one of the main tools used for this purpose. In SEM, an accelerated beam of electrons is focused on the sample with a typical spot size of 1 nm and the image is obtained with an appropriate detector by scanning this fast electron beam on the sample. Figure 2.3 shows the LEO FESEM 1530 microscope, which is equipped with a field-emission source and an acceleration voltage up to 25 kV and has been used for the bulk of the present work. This microscope is equipped with in-lens and out-of-lens SE detectors for secondary electron imaging and a Centaurus detector (manufactured by K.E. Developments Ltd.) for backscattered electron imaging. Moreover, it also houses an EDAX energy-dispersive X-ray (EDX) analysis system, which provides elemental identification based on detection of X-ray emission at element-specific characteristic photon energies from the sample upon excitation by the high-energy electron beam. The X-ray emission spectra so obtained can also be used for quantifying the composition of the elements in the sample through the intensities of their characteristic X-ray emission lines. The SEM system also contains various other optional detectors, including a cathode-luminescence detector and a scanning transmission electron microscopy (STEM) detector, which have only been used occasionally in the present work.

The principles and applications of helium ion microscopy (HIM) are very similar to SEM. In HIM, the source, image contrast mechanism and the interaction of helium ion beam with the sample are, however, quite different from those of the electron beam. By finely regulating the helium pressure in the vicinity of the source (a needle-shaped single crystal), the amount of positively charged helium ions from the apex atoms of ionization disc can be easily controlled, and the helium ions so produced can be accelerated and collimated by adjusting the aperture, focus or extracting voltage. A helium ion source is long-lasting and provides intense ion currents from a volume no larger than a single atom (less than 1 Å). The resulting ion beam has a remarkable brightness of 4×10^{-9} A/cm^2/sr (at an extraction voltage of 25 kV) with a small energy spread ($\Delta E/E \sim 3\times10^{-5}$). The small energy spread of the helium ions (< 1 eV) minimizes the chromatic aberrations. After impinging on the sample surface, the helium ion beam generates secondary electrons, in addition to scattered helium ions and atoms. The secondary electrons so produced can then be used to generate an image of the surface. The principal advantages of HIM compared to SEM are that the ions do not suffer from diffraction limitation, because the larger mass of the helium ions (compared to electrons) gives rise to a smaller de Broglie wavelength. The helium ion beam therefore in effect provides a finer probe on the sample. Furthermore, the yield of secondary ions per incident particles is greater in HIM, which permits faster image acquisition with a better signal-to-noise ratio for a given incident particle dosage.[72] Furthermore, the interaction volume of the helium beam near the surface can be considerably smaller than that of an SEM, which makes HIM more surface-sensitive.[73]

Figure 2.4 shows the Zeiss ORION Plus HIM used for the present work. Introduction of a He gas at a very low flow rate (by changing the pressure from 10^{-9} to 10^{-7} Torr) leads to formation of an intense He^+ ion beam upon field ionization at a high positive bias (~ 25 kV) of a cryogenically cooled atomically sharp tip (W). Upon appropriate in-situ construction of the emitter tip, a trimer of the tip is obtained and the He^+ ions created at one of the three atoms in the trimer are accelerated and focused through the ion optics column. The focused He^+ beam is then directed and scanned across the sample to produce secondary electrons. These secondary electrons are detected using an Everhart-Thornley detector, while the Rutherford backscattered ions are detected using a microchannel plate detector. Similar to the electron beam detectors in the SEM, secondary electron imaging provides both the surface morphology and electron density information, while the backscattered ion imaging offers image contrast based on the atomic number of the elements.

Transmission electron microscopy (TEM) measurements have been performed by using a JOEL 2010F microscope at McMaster University and more recently a Zeiss Libra 200 microscope on the UW campus, both operated at 200 kV. TEM has been used for crystal structure characterization, phase determination and identification of the surface planes of the individual nanostructures. Unlike the aforementioned SEM and HIM studies that have been all carried out by myself, the TEM measurements were performed with the help of an operator. For some experiments, the samples were prepared by using focused ion beam microscopy to obtain an appropriate sample thickness, before carrying out the TEM measurement. More details about TEM sample preparation will be given in individual chapters (e.g Chapter 3).

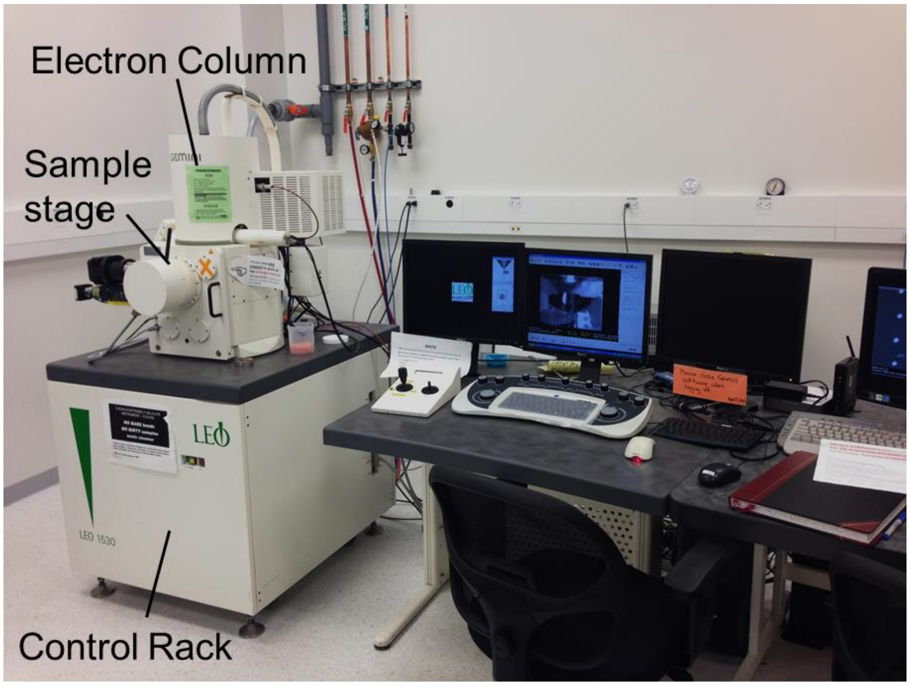

Figure 2.3 Photograph of the LEO FESEM 1530 field-emission scanning electron microscope (SEM), equipped with secondary electron in-lens and out-of-lens (SE2) detectors, and backscattered electron detector (BSD) and an EDAX energy-dispersive X-ray analysis system.

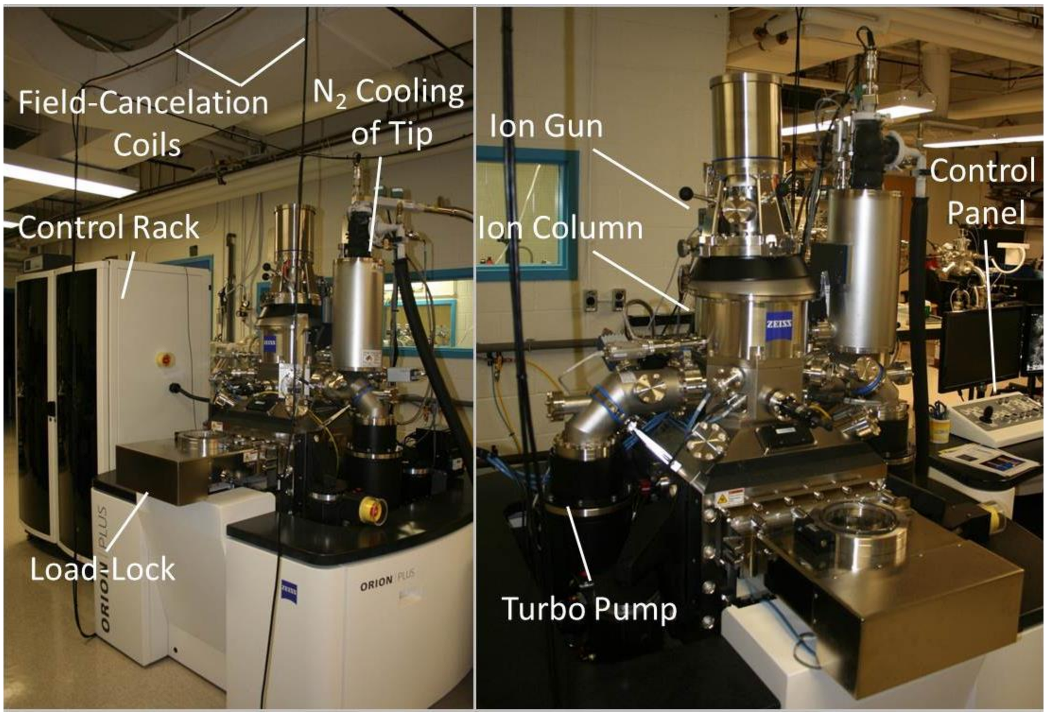

Figure 2.4 Photograph of a Zeiss Orion Plus helium ion microscope. Left: The control, data acquisition and field-isolation electronics and the microscope itself. Right: A closer look at the ion-column and the sample chamber equipped with secondary electron and backscattered ion detectors.

2.3 Characterization by X-ray Photoelectron Spectroscopy (XPS) and Secondary Ion Mass Spectrometry (SIMS)

2.3.1 XPS Chemical-State Composition Analysis

X-ray photoelectron spectroscopy has been performed on as-prepared hybrid NPs before and after the sensing experiments, in order to examine their chemical states and the corresponding composition profile and to investigate any changes before and after the sensing process. XPS spectra collected as a function of sputtering depth have also been used to understand the composition change in the depth direction in the near-surface region of the hybrid NPs. The instrument used for these measurements is a Thermo-VG Scientific ESCALab 250 Microprobe (Figure 2.5), which is equipped with a monochromatic Al Kα X-ray source (1486.6 eV) operated at a typical energy resolution of 0.4-0.5 eV full-width-at-half-maximum. The photoejected electrons from the atomic core-levels or the valence band of the material as a result of monochromated X-ray illumination are produced from the very top surface region of the sample (with a typical electron escape depth of less than 10 nm). The kinetic energy of these photoelectrons is analyzed by using a hemispherical analyzer and can be used to determine the corresponding binding energy (given a known incident X-ray photon energy) using the Einstein equation.[74] When compared with the appropriate standards, the binding energy contains chemical shift information about the local chemical environments.

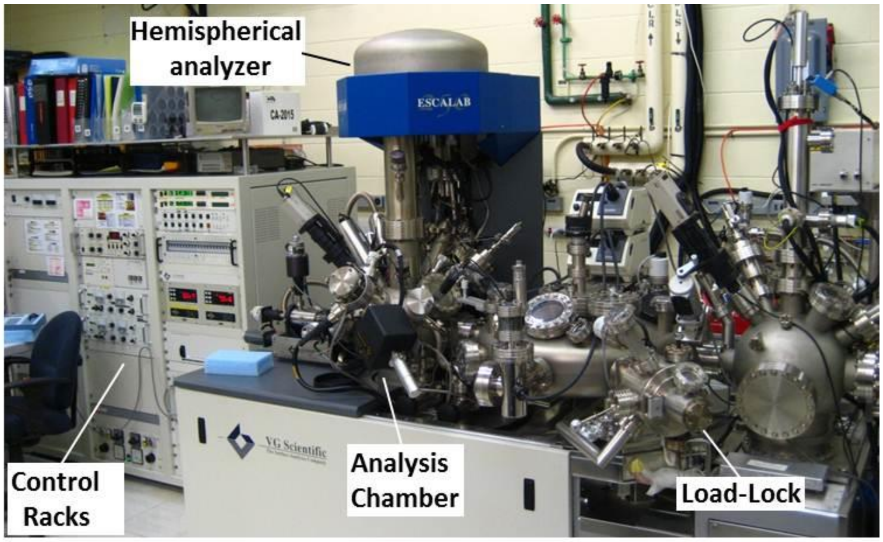

Figure 2.5 Photograph of the Thermo-VG Scientific ESCALab 250 Microprobe used for chemical analysis of the hybrid nanoparticles.

2.3.2 SIMS Chemical Mapping

Time-of-flight secondary ion mass spectrometry (TOF-SIMS) is a surface analysis technique that can produce high resolution chemical images in three dimensions. Coupled with a recently introduced Argon cluster sputtering ion source technology, SIMS is now capable of analysing soft materials and biological materials.[75] In this technique, a focused high energy primary ion beam (1–40 keV) is used to bombard the sample surface, which causes emission of secondary ions. An ion image based on the time-of-flight of the secondary ions is then produced by rastering the primary ion beam across the sample surface. The TOF detection scheme also offers parallel detection of multiple species, ideal for the analysis of complex biological samples.

In the ION-TOF SIMS-5 system (Figure 2.6), the Bi^{3+} analysis or primary ion source positioned at 45° to the sample was operated at 30 keV beam energy with a 0.4 pA beam current and a 100 μs pulse width. Secondary ions were electrostatically directed to the TOF analyser by biasing the sample stage at 2.5 kV with the extraction lens set at 4.5 kV at an opposite polarity. Appropriate secondary ions were collected over a rastered sampling area of 100×100 μm^2 to obtain a 2D map. The sample could also be sputtered with a O^{2+} ion beam or an Argon cluster ion beam (each generated from a separate sputtering ion source) alternating with the Bi^{3+} primary ion beam to remove the sample layer by layer at a well-defined sputtering rate. The 2D maps were collected as a function of sputtering depth to obtain the depth profiles and construct the corresponding 3D images of the components.

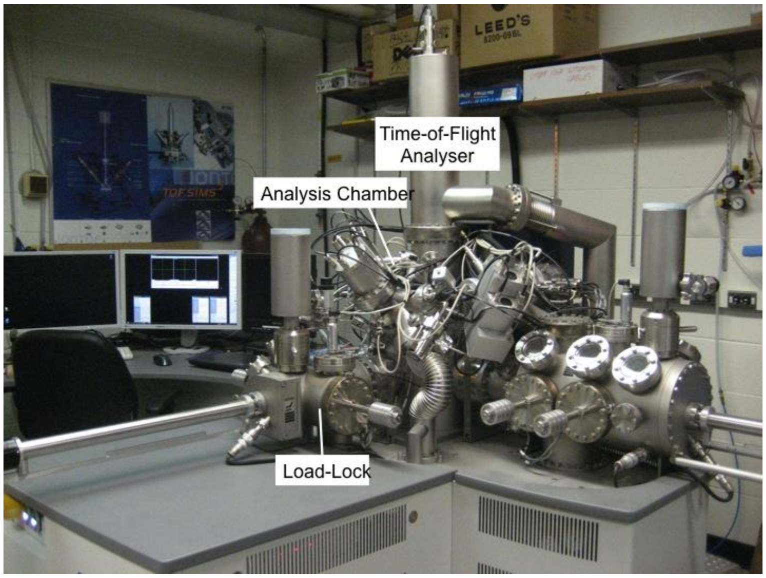

Figure 2.6 Photograph of ION-TOF SIMS-5 system used for chemical analysis of hybrid nanoparticles.

2.4 Characterization by X-ray Diffraction

Figure 2.7 shows a Panalytical X'pert Pro MRD X-ray diffractometer used for determining the average crystalline structure of the hybrid nanoparticles reported in the present work. Different optics and diffraction geometries available are for this system. Since the NPs produced in this study are very small and well separated on the substrate, the amount of available sample for analysis is usually very low. The signal strength from these NPs is therefore usually very weak and the signal is dominated by the substrate (e.g. Si). In order to concentrate the signal coming from the NPs, glancing incidence X-ray diffraction (GIXRD) technique is used to examine the crystal structure of these hybrid NPs. In the GIXRD method, the detector is swept over the 2θ angle with the incidence angle (ω) of the X-ray beam kept at a very shallow angle (close to the critical angle of the sample). Because the incidence angle is below the critical angle, an evanescent wave is formed. This evanescent wave only penetrates into a thin layer (less than 100 nm) and travels on the surface of the sample, which leads to an enhanced interaction of the X-ray beam with the nanostructured layer on the surface of the substrate.[76] As a result, the intensity of the signal collected from the surface layer that contains the hybrid NPs increases significantly. For this purpose, a parallel beam geometry with an X-ray mirror on the incident beam side and a parallel-plate collimator on the diffracted beam side is used. This configuration allows GIXRD measurements at a typical incidence angle of 0.5° for most samples.

To analyze the grain size, we conducted Scherrer analysis. The Scherrer formula used for calculating the average crystallite size is given by:

$$\text{Crystallite size} = \frac{K \times \lambda}{(B_{Observed} - B_{Instrument}) \times Cos(\theta)} \text{ ,}$$

where K is the shape factor of the nanocrystallites, λ is the wavelength of the X-ray used for obtaining the diffraction pattern, θ is the peak position, B_{Observed} is the peak width (FWHM) of the most intense XRD peak of the sample, and $B_{\text{Instrument}}$ is the peak width observed for the standard stress-free sample. The latter arises due to instrumental effects. For the X-ray optics used in our GIXRD system the observed $B_{\text{Instrument}}$ is $B_{\text{Instrument}}$=0.40° (or 0.0022 rad).

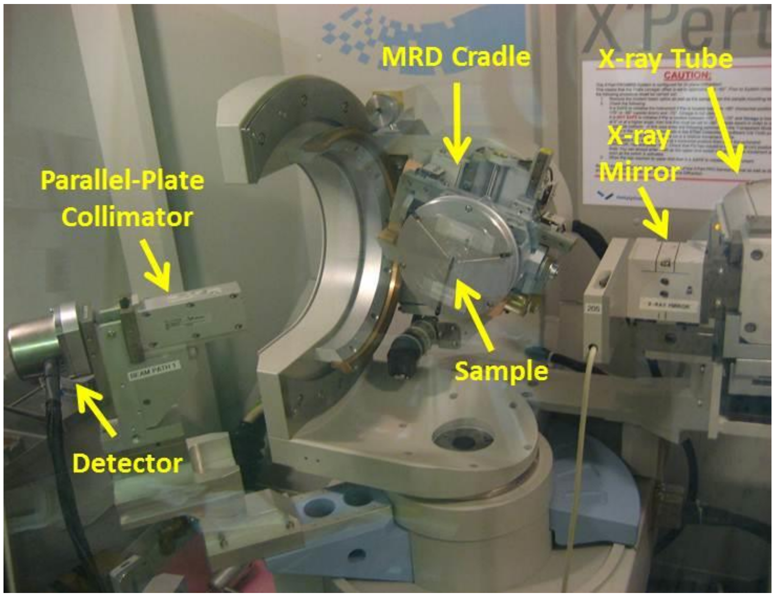

Figure 2.7 Photograph of the Panalytical X'pert Pro MRD X-ray diffractometer used for crystal structure characterization of the hybrid nanoparticles. The instrument is set up in the parallel beam geometry with an X-ray mirror and a parallel plate collimator used for the incident and diffracted beam optics, respectively.

2.5 Measurement of Magnetic Properties

A Quantum Design DynaCool Physical Property Measurement System (PPMS) is used to characterize the physical and magnetic properties of hybrid NPs (Figure 2.8a). In this instrument, the magnetic field can be varied from 0 to ± 9 Tesla (90 kOe), while the sample temperature can be changed from 1.9 to 400 K. The DynaCool PPMS system employs a single two-stage pulse tube cryo-refrigerator (Cryomech) to generate liquid helium from bottled helium to cool both the superconducting magnet and the temperature control system. The DynaCool also provides a low vibration environment for sample measurements.

For more sensitive measurements of magnetic properties of samples over a broad range of temperature and magnetic field, a EverCool Quantum Design Magnetic Property Measurement System (MPMS) was used. (Figure 2.8b) The Vibrating Sample Magnetometer (VSM), with the Cryomech cryofrigerator, is used to perform extremely sensitive magnetic measurements with superconducting pickup coils and a Superconducting Quantum Interference Device (SQUID).

The MPMS SQUID VSM utilizes a superconducting magnet (a solenoid of superconducting wire) to subject samples to magnetic fields up to 7 Tesla (70 kOe). The SQUID and magnet must both be cooled with liquid helium. Liquid helium is also used to cool the sample chamber, providing temperature control of samples from 400 K down to 1.8 K. No particular sample preparation is needed. However, the sample should be smaller than a maximum size 5×5 mm^2 to be put inside the bore of the magnet and the sample is appropriately positioned such that the sample vibration occurs in the homogeneous part of the magnetic field.

In this work, both PPMS and SQUID experiments are used to obtain hysteresis loops (magnetization vs applied field) and temperature dependent magnetic moments (from 4 K to room temperature or upper) in Chapter 3 and Chapter 6. Since hybrid NPs were supported on Si substrate, we used a Si sample with the same size was used for the background deduction.

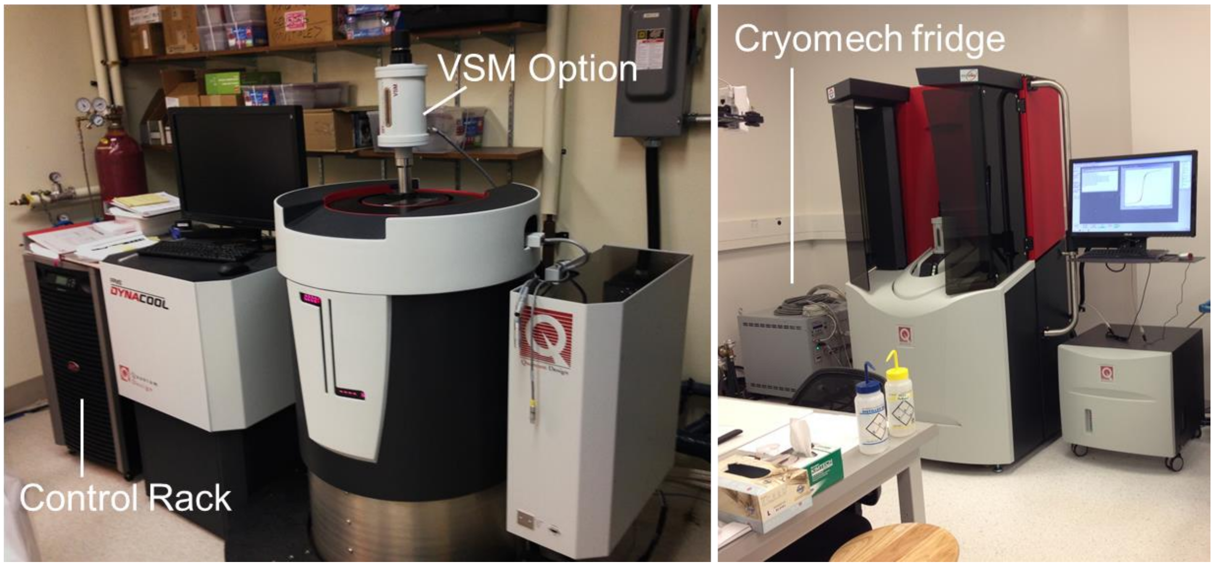

Figure 2.8 (a) Photograph of the computer, pump cabinet and cryostat of the Quantum Design Dynacool physical property measurement system. (b) General setup for Superconducting Quantum Interference Device (SQUID) for magnetic properties measurements for hybrid NPs by Quantum Design Magnetic Property Measurement System (MPMS)-VSM system.

Chapter 3

FeNi Metallic Hybrid NPs

3.1 Phase-induced Shape Evolution of FeNi Nanoalloys and their Air Stability by In-situ Surface Passivation‡‡

3.1.1 Introduction

Development of bimetallic or trimetallic nanostructured materials, particularly alloy or core-shell nanoparticles (NPs), have attracted much recent attention because of their novel catalytic,[2,3] magnetic,[4–6] and optical properties,[9,10] which can be significantly different from those of their constituent single-metallic materials. The "alloy" properties of these nanoalloys are found to depend not only on their relative compositions and crystal structures, but also on their sizes and shapes.[26] Driven by the need for low-cost soft magnets,[57,58] catalysts,[59] and biosensors,[60] the study of bimetallic and trimetallic Fe-based nanoparticles (e.g., FeNi, FeCo, FeCONi, FeNiZn) has become a very important research area. As one of the most widely used magnetic materials, FeNi alloys have been synthesized by a variety of methods that usually produce spherical NPs over a large size range (10–500 nm). In wet chemical methods conducted at room temperature, amorphous alloy NPs can be obtained by a reverse micelle synthesis and microemulsion process,[51] while crystalline NPs can be produced in various aqueous and nonaqueous media by borohydride reduction and hydrazine reduction of Fe and Ni inorganic salts.[52] However, it is very difficult to obtain a narrow size distribution of NPs with these room-temperature methods, making it necessary to perform the synthesis at a higher temperature (above 300°C) in the presence of surfactants.[53] Although surfactants can stabilize the dispersion of NPs and prevent their aggregation, the presence of bulky or strongly binding surfactants at the NP surface often affects their properties, sometimes in an undesirable way. In dry synthesis methods, such as arc discharge,[54] hydrogen plasma reaction,[55] and reduction of $FeCl_2$ and $NiCl_2$ vapours in the presence of H_2,[56] the spherical NPs or powders so obtained often agglomerate into clusters or chains due to their magnetic interactions. This makes the study and application of

---

‡‡ This section is made from one of my publications: N. Moghimi, S. Bazargan, D. Pradhan, K. T. Leung, J. Phys. Chem. C, 2013, 117 (9), pp 4852–4858. Copyright (2013) by the American Chemical Society.

uniformly dispersed, individually separated NPs challenging.

Besides these difficulties in the synthesis of FeNi alloy nanoparticles with desirable shape, size and spatial distribution, the easy oxidation of these NPs in air is a serious problem. Air-stability is one the greatest challenges in the synthesis and applications of magnetic metals (Fe-based materials) and becomes more serious when it comes to the nano-size regime because the metallic nanoparticles have a great affinity for oxygen and immediately oxidize in air even at room temperature. Since the magnetic properties change (usually lower) with oxidation of these magnetic nanoparticles, efforts are made to keep them stable in air. This further complicates the synthesis methods with the need for an additional surface passivation step including coating with metal oxides[77,78] or encapsulation in polymers,[79] carbon nanotubes[80] and silica shells.[81] To date, only a few shape-controlled alloy NPs, mostly platinum alloys, have been made by using capping reagents, surfactants, diols or gas reducing agents.[82]

Furthermore, despite the large number of studies on the role of alloy components in modifying the structural and other properties of alloy NPs, no study on the role of the second metal in the shape evolution of alloy NPs have been reported. In the present work, we present the first surfactant-free, single-step, electrochemical deposition (ECD) technique to synthesize air-stable FeNi alloy NPs with different shapes and a narrow size distribution uniformly dispersed on a Si substrate at room temperature. We further demonstrate, that the shape evolution of these NPs from Fe-rich concave cubes to Ni-rich truncated spheres is correlated with their concurrent phase transformation from bcc (pure Fe phase) to fcc (pure Ni phase). Since the spatial uniformity and size distribution of these NPs deposited on the substrate depend on the type of nucleation (i.e. progressive or instantaneous), we show that the introduction of Ni^{2+} to the Fe^{2+} electrolyte can be used to change the type of nucleation from progressive to instantaneous, resulting in uniform deposition. As a side benefit of the present preparation method, formation of Ni-doped Fe oxides on top of the NPs in-situ also passivates the surfaces and results in remarkably air-stable NPs.

3.1.2 Materials and Methods

FeNi alloy NPs are prepared by electrodeposition (ECD) on a H-terminated Si(100) substrate in a three-electrode cell workstation (CH Instruments 660A). Silicon chips (15×2.5 mm^2, 0.4 mm thick), precut from a Si(100) wafer (p-type, B-doped, with a resistivity of 0.01-

0.02 Ω-cm), cleaned using the RCA method[83] and H-terminated by dipping in an aqueous HF (2%) solution, are used as the working electrode. A standard Ag/AgCl reference electrode is used while a Pt wire is used as the counter electrode. The electrolyte consists of different concentrations of Fe^{2+} and Ni^{2+} solutions prepared by dissolving $FeCl_2{\cdot}6H_2O$ and $NiCl_2{\cdot}6H_2O$ salts (Aldrich, 99%) in doubly distilled water, with a 200 mM H_3BO_3 solution used as a supporting electrolyte. In a freshly prepared deoxygenated electrolyte solution, ECD is obtained by amperometry for an appropriate deposition time potentiostatically at −1.4 V vs. Ag/AgCl, at which potential Fe^{2+} and Ni^{2+} are reduced to their respective metals. A Deposition potential −1.4 V (vs. Ag/AgCl) is chosen as the optimum potential because non-homogeneous deposition occurs at −1.2 V and excessive hydrogen evolution at −1.6 V. The surface morphology of the NPs so prepared is characterized by field-emission scanning electron microscopy (SEM) in a LEO FE-SEM 1530 microscope. Crystal structures are determined by glancing-incidence X-ray diffraction (GIXRD) in a PANalytical X'Pert Pro MRD diffractometr with Cu-Kα (1.542 Å) radiation at an incidence angle of 0.5˚. These data are correlated with the local nanostructures and elemental compositions determined by transmission electron microscopy (TEM) in a JEOL 2010F STEM and FEI Tecnai F20 TEM systems, both operating at 200 kV. Chemical-state composition of the nanoalloys are analyzed as a function of Ar ion sputtering time by depth-profiling X-ray photoelectron spectroscopy (XPS) in a Thermo-VG Scientific ESCALab 250 microprobe with a monochromatic Al Kα radiation (1486.6 eV), operated with a typical energy resolution of 0.4-0.5 full width at half-maximum.

3.1.3 Results and discussion

Nanoparticles are deposited on a H-terminated Si(100) substrate by amperometry potentiostatically at −1.4 V vs. Ag/AgCl in a three-electrode cell. The electrolyte is made up of $FeCl_2$ and $NiCl_2$ solutions of different concentrations, with 200 mM boric acid as the supporting electrolyte. The pH of the solutions is 3.5. Two series of co-ECD experiments are performed by varying one of the MCl_2 concentrations (M = Fe or Ni) while keeping the other concentration fixed at 5 mM.

Figure 3.1 compares the SEM images of pristine Fe and Ni NPs, prepared by separate ECD in 35 mM of their respective chloride solutions, with those of FeNi alloy NPs prepared by co-ECD for 20 s. Each electrolyte is designated by FeX:NiY, where X and Y correspond to the concentrations in mM of $FeCl_2$ and $NiCl_2$ solutions, respectively. The corresponding Ni at. % and the respective Ni mole fraction of the electrolyte are summarized in Table 3.1. For ECD in Fe35, cubic Fe NPs are observed together with bigger NP clusters with a broad size distribution, which suggests progressive nucleation in the growth mechanism of these Fe NPs. By introducing Ni^{2+} as a second component into the Fe^{2+} solution, the average size of the cubic NPs in the Fe30:Ni5 solution becomes larger but with reduced clustering (Figure 3.1, left column; Table 3.1). This suggests that the nucleation has changed from a progressive to instantaneous mechanism which results in a more uniform deposition and a narrower size distribution. The nature of nucleation of metals on a surface greatly depends on the substrate, concentration of metal ions in the electrolyte and applied potential. The current density I as a function of time t for instantaneous nucleation followed by diffusion-limited growth generally is given by the relation:[84]

$$\frac{I^2}{I_m^2} = \frac{1.9542}{t/t_m}\{1 - \exp[-1.2564(t/t_m)]\}^2$$

while that for progressive nucleation obeys the equation:

$$\frac{I^2}{I_m^2} = \frac{1.2254}{t/t_m}\{1 - \exp[-2.3367(t/t_m)^2]\}^2$$

where t_m corresponds to the time when the maximum current density I_m is reached. Figure 3.2 shows the square of the normalized current density (I/I_m) as a function of the normalized time (t/t_m) for FeNi deposition on a Si substrate at a constant applied potential of –1.4 V (vs Ag/AgCl). The experimental data for pristine Ni and FeNi alloy NPs are found to be in excellent agreement with the instantaneous growth relation, while that for pristine Fe NPs follows the progressive growth relation.

By keeping the $NiCl_2$ concentration constant at 5 mM while reducing the $FeCl_2$ concentration, the average size of the cubic NPs has decreased with the corresponding size distribution becoming notably narrower. On the other hand, ECD in Ni35 produces more uniform deposition of considerably larger spherical NPs and a narrower size distribution, which suggests an instantaneous growth mechanism. By introducing Fe^{2+} as a second component into the Ni^{2+} solution, the average size of the spherical NPs becomes notably smaller (Figure 3.1, center column; Table 3.1). As the electrolyte becomes Ni-rich, the morphology changes to truncated spheres. The distorted nanospheres become more and more faceted, along with the emergence of some truncated cubes, truncated octahedron and other distorted cubes, as the Ni^{2+}

concentration approaches the Fe^{2+} concentration. The corresponding size distribution plots for NPs obtained from Fe10:Ni5 and Fe5:Ni10 solutions are shown in Figure 3.1. The size distribution of the concave cubic samples (e.g., Fe10:Ni5) is found to be narrower than that of the truncated spherical samples (e.g. Fe5:Ni10) (Figure 3.2, bottom center), which is likely due to the well-defined shape of the nanocubes.

The high-magnification SEM images, shown in Figure 3.1 (right panel), illustrate the shape evolution of FeNi nanoalloys with increasing Ni content. When the concentration of Fe^{2+} is more than that of Ni^{2+} in the electrolyte, the dominant shape follows the cubic shape of the pristine Fe NP. Adding Ni atoms into the Fe host system changes the regular cubic shape to concave cubic, which is more obvious at 31 at. % Ni (Fe10:Ni5). As the relative Ni^{2+} electrolyte concentration increases, the edges of the nanocubes appear to have an increasing concave curvature, giving rise to pointy corners without forming spherical shape characteristic of the Ni NPs. For the electrolyte with equal Fe^{2+} and Ni^{2+} concentrations (Fe5:Ni5), an indentation at the center of a cubic face is clearly observed (Figure 3.1, right column). As the electrolyte becomes Ni-rich, the morphology changes to truncated spherical, following the spherical morphology of the pristine Ni NP, with the introduction of facets into the spherical shape due to the presence of Fe.

Table 3.1 Atomic percentage of Ni obtained by EDX, average size, phase combination and lattice constants deduced by XRD for FeNi alloy NPs obtained from FeX:NiY electrolytes (with the corresponding Ni mole fraction). Pure Fe (Fe35) and Ni (Ni35) nanoparticles are included as references.

FeX:NiY (X, Y in mM)	**Ni mole fraction (%) in electrolyte**	**Ni content (at. %) obtained by EDX**	**Average size (nm)**	**Phase[a]**	**Lattice constant (Å)**
Fe35	0	0	56 with clusters	bcc	2.864 ± 6
Fe30:Ni5	14	11	78 ± 8	bcc	2.866 ± 6
Fe15:Ni5	25	22	70 ± 5	76% bcc + 24% fcc	2.867 ± 6 3.583 ± 8
Fe10:Ni5	33	31	63 ± 3	61% bcc + 39% fcc	2.867 ± 6 3.587 ± 8
Fe5:Ni5	50	47	62 ± 2	43% bcc + 57% fcc	2.866 ± 6 3.572 ± 8
Fe5:Ni10	67	64	58 ± 2	fcc	3.544 ± 8
Fe5:Ni15	75	73	93± 5	fcc	3.539 ± 8
Fe5:Ni30	86	81	100 ± 6	fcc	3.529 ± 8
Ni35	100	100	163 ± 7	fcc	3.525 ± 8

[a] For nanoalloy with a mixture of two phases, the relative amounts for bcc and fcc phases are obtained by using a nonlinear least-squares optimization peak-fitting software.

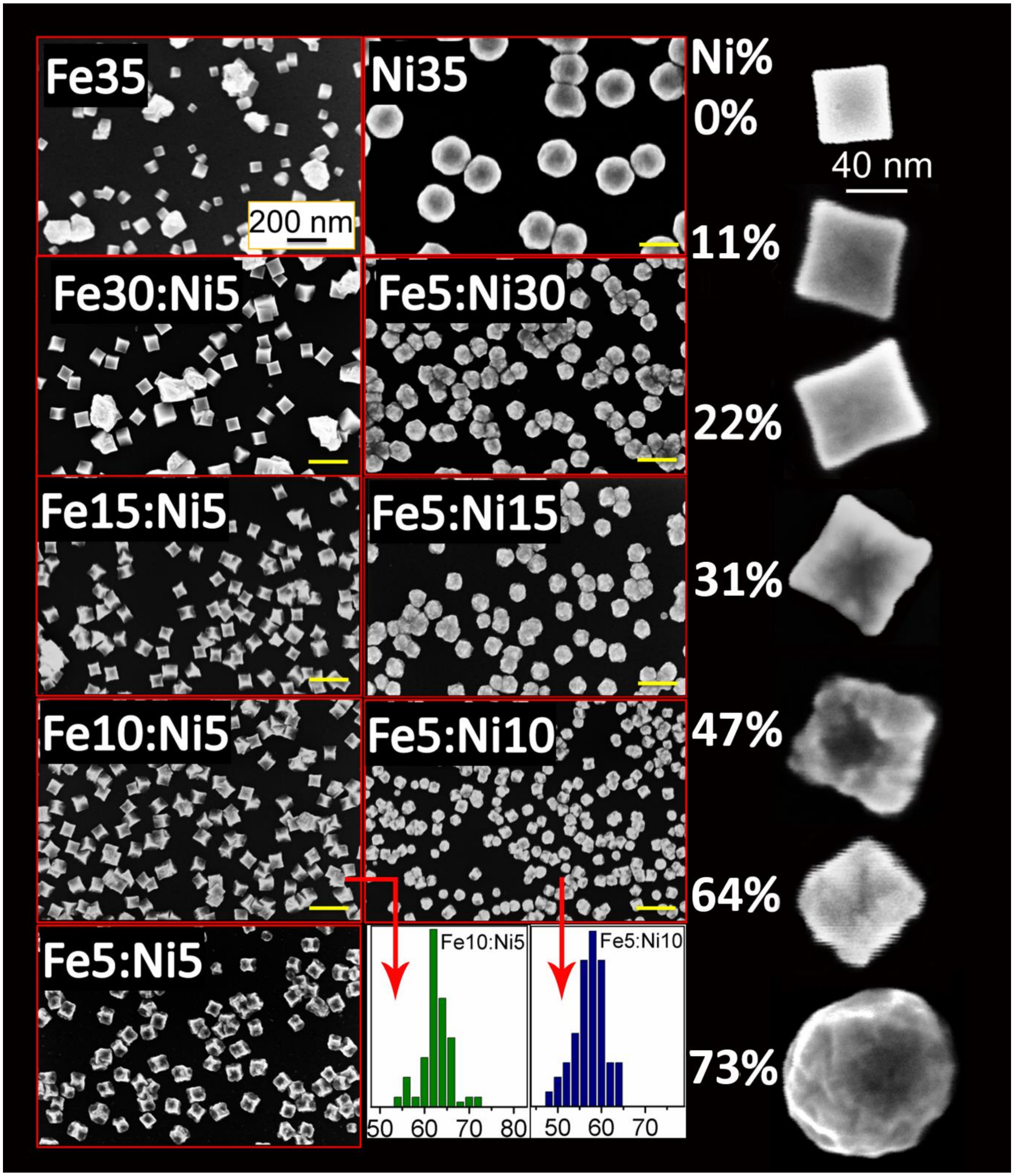

Figure 3.1 SEM images of FeNi alloy nanoparticles electrodeposited on a H-Si(100) substrate at −1.4 V (vs Ag/AgCl) for 20 s in different FeX:NiY solutions, where X and Y correspond to the concentrations in mM of $FeCl_2$ and $NiCl_2$, respectively. Center bottom panel presents the corresponding particle size distributions for Fe10:Ni5 and Fe5:Ni10. Right panel shows the high-magnification SEM images of FeNi alloy NPs for Ni at. % (as determined by EDX) of 0% (Fe35), 11% (Fe30:Ni5), 22% (Fe15:Ni5), 31% (Fe10:Ni5), 47% (Fe5:Ni5), 64% (Fe5:Ni10), and 73% (Fe5:Ni15).

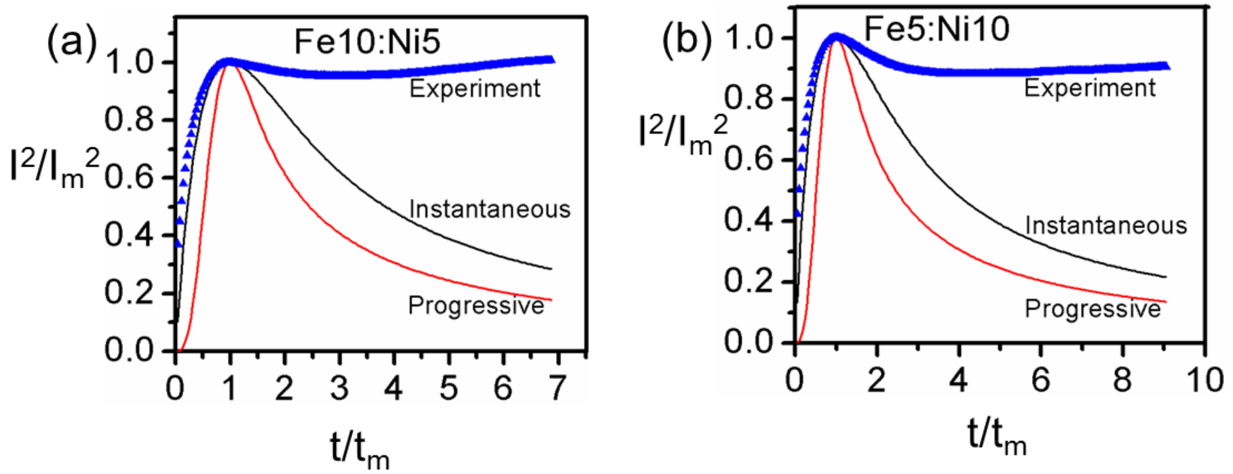

Figure 3.2 Comparison of square of the normalized current density (I/I_m) as a function of the normalized time (t/t_m) for (a) FeNi alloy concave nanocubes obtained in 10 mM $FeCl_2$ and 5 mM $NiCl_2$, and (b) FeNi alloy truncated nanospheres obtained in 5 mM $FeCl_2$ and 10 mM $NiCl_2$, on Si substrate by amperometry potentiostatically at –1.4 V (vs Ag/AgCl). These data are compared with calculated curves for instantaneous nucleation and progressive nucleation as described by Equations 1 and 2, respectively.

Although phase transformation from bcc to fcc as a function of Ni atomic content has been observed in FeNi bulk alloys[85,86] and ultrafine FeNi particles,[55,56] the connection between this phase transformation and the shape of NPs remains unclear. We investigate the shape evolution of FeNi alloy NPs from concave cubic to truncated spherical with increasing Ni atomic content by glancing-incidence XRD for FeNi alloy NPs obtained by co-ECD in different electrolytes. No diffraction patterns of pure metallic Fe or Ni (and their oxides) are observed, which indicates the absence of segregated metal NPs. The region of 2θ = 50-60° contains mainly diffraction features of the Si(100) substrate and is therefore not shown. (Figure 3.3) For NPs obtained with the Fe30:Ni5 electrolyte, the most intense diffraction peak, (110), is shifted to a lower 2θ value, indicating lattice expansion as a result of alloy formation in the bcc phase region of the FeNi alloy phase diagram.[87]

Increasing the relative Ni content to 22 at. % with Fe15:Ni5 (Table 3.1) introduces a new set of features corresponding to the fcc phase of the FeNi alloy. With further increase in the relative Ni content to 31 at. % (Fe10:Ni5) and 47 at. % (Fe5:Ni5), the diffraction features for the fcc alloy phase are found to shift to a higher 2θ value, which indicates lattice contraction due to the gradual inclusion of the smaller “guest” Ni atoms into the lattice of the larger “host” Fe atoms. The increase in the relative Ni content also appears to reduce the intensities of the bcc diffraction peaks without affecting their 2θ locations. (Figure 3.3) For NPs obtained with the Fe5:Ni5 electrolyte, the fcc alloy phase becomes more dominant than the bcc alloy phase, with the (111) feature of the fcc phase becoming the most prominent while the diffraction features for the bcc phase greatly diminished in intensity. Further increase in the Ni content from 47 at. % (Fe5:Ni5) to 64 at. % (Fe5:Ni10), 73 at. % (Fe5:Ni15), and 81 at. % (Fe5:Ni30) (Table 3.1) produces a single set of diffraction features corresponding to the fcc phase of FeNi alloy. These features are also found to be shifting toward a higher 2θ, converging to the diffraction pattern of the Ni fcc phase (Ni35).

Concave cubic structures are formed when the fcc unit cells are introduced as the guest to the main bcc host phase (from Fe15:Ni5 to Fe5:Ni5). When the phase transition from bcc to fcc is complete (Fe5:Ni10), the final shape of NPs is found to switch from concave cubic to truncated spherical. Of particular interest is that the concave cubic shape becomes most obvious (Figure 3.1, right panel), when the relative concentrations of Fe and Ni are the same in the electrolyte (Fe5:Ni5) and the amounts of bcc and fcc phases are almost equal (Table 3.1, Figure 3.3). The deep indentations in the concave faces of NPs obtained from Fe5:Ni5 have become filled in, converting the NPs to more spherical, as the Ni content increases into the Ni-rich regime (Figure 3.1, right panel). XRD patterns of the NPs obtained in different stages of the growth (i.e. with different deposition times) from Fe5:Ni5 show the initial formation of bcc phase and the subsequent growth of the fcc unit cells in the bcc host lattice, which lead to the concave cubic shape similar to that found for the Fe-rich alloy NPs. (Figure 3.4) It therefore confirms that even when both phases are present in equal amounts, the final shape of NPs is governed by the Fe host crystal structure.

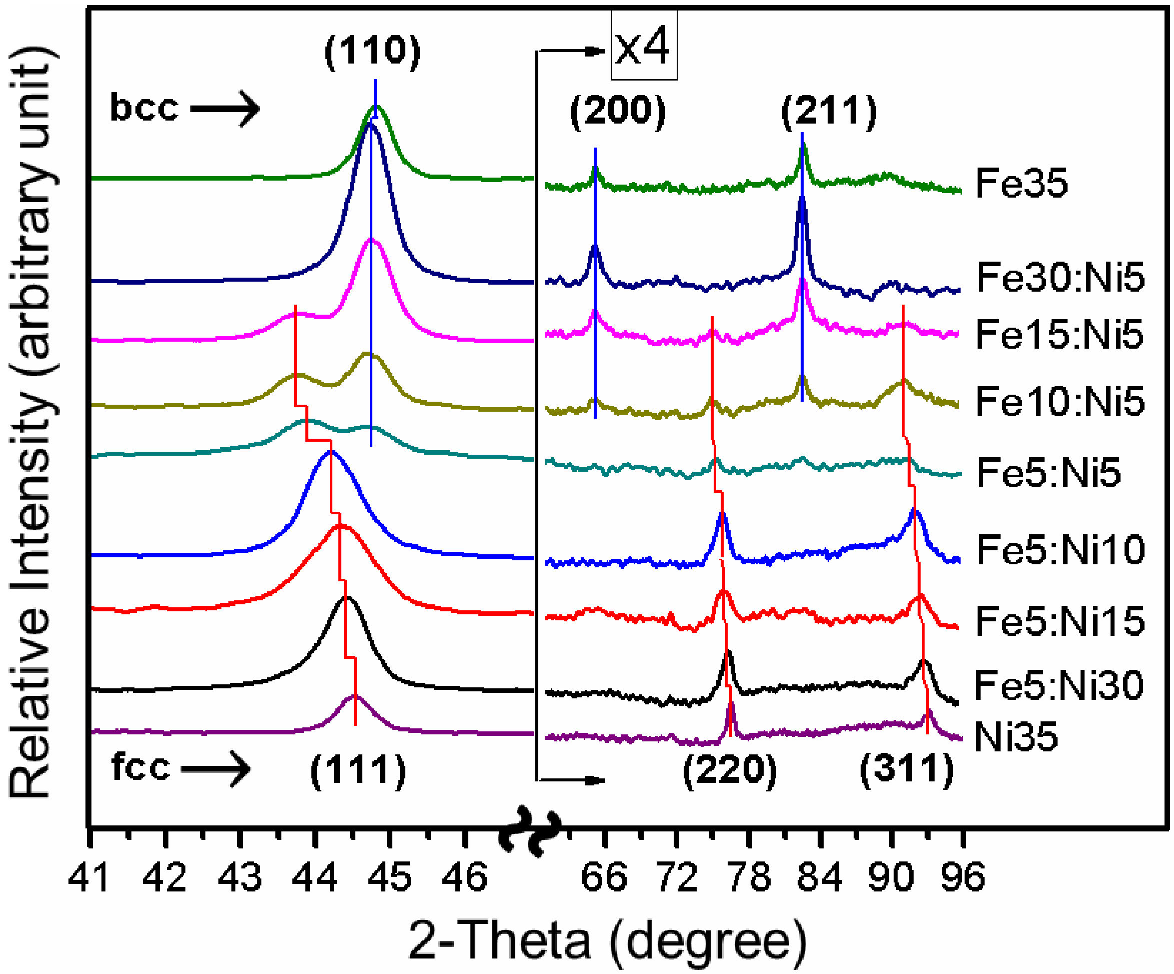

Figure 3.3 Glancing-incidence XRD patterns of FeNi alloy nanoparticles electrodeposited on a H-Si(100) substrate at –1.4 V (vs Ag/AgCl) for 20 s in different FeX:NiY solutions, where X and Y correspond to the concentrations of $FeCl_2$ and $NiCl_2$ in mM, respectively.

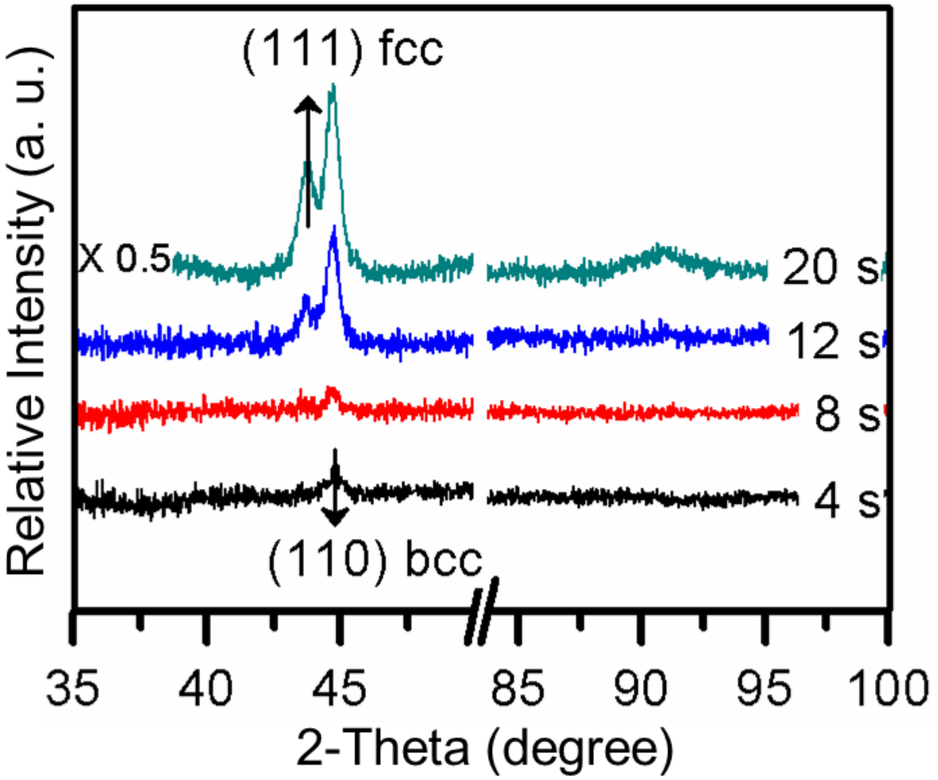

Figure 3.4 Glancing-incidence XRD patterns of NPs obtained in Fe5:Ni5 electrolyte with total deposition time of 4 s, 8 s, 12 s, and 20 s, illustrating the different stages of growth.

To confirm alloy formation and the absence of segregated Fe or Ni NPs or domains inside the NPs, we collect XPS spectra of the Fe 2p and Ni 2p regions as a function of sputtering depth. To identify the peak locations and the corresponding chemical shifts, we have fitted the spectra with Gaussian-Lorentzian lineshapes using the CasaXPS program, after appropriate correction with the Shirley background. To remove the carbonaceous layer commonly found due to sample handling in air, we perform Ar sputtering of the as-prepared samples for 10 s. The resulting chemical-state compositions for typical FeNi alloy concave nanocubes and truncated nanospheres are compared with those of pure Fe and Ni NPs in Figure 3.5 (also after 10 s of sputtering), respectively. Compared to the pristine Ni NPs, the Ni $2p_{3/2}$ peaks at 852.9 eV has a discernible shift of 0.3 eV toward higher binding energies for alloy nanocubes, while no obvious differences in the Fe $2p_{3/2}$ peak position from the pristine Fe NPs is observed (Figure 3.5a and 3.5b). On the other hand, for the FeNi nanospheres, the metallic Fe $2p_{3/2}$ peak exhibits a 0.3 eV binding energy shift to a higher binding energy and the Ni $2p_{3/2}$ peak location does not change (Figure 3.5e and 3.5f). The peaks at 855.6 eV and 709.6 eV are related to the Ni and Fe oxides, respectively, in a thin oxide shell of the alloy NP, which are removed completely after 190 s sputtering. Continued sputtering to 1030 s for both nanocubes and nanospheres reduces the metallic Fe and Ni features, with the emergence of a new Fe $2p_{3/2}$ feature at 707.2 eV and a new Ni $2p_{3/2}$ feature at 853.6 eV attributable to Fe silicide and Ni silicide respectively.[74,88] It should be noted that the Si 2p peak remains unchanged at 99.4 eV because of the overwhelming contribution from bulk silicon (not shown). The broad peak at 712.2 eV found after 70 s of sputtering and remained up to 1390 s of sputtering in FeNi nanospheres (Figure 3.5f) corresponds to the Ni $L_3M_{23}M_{45}$ Auger transition.[74] The presence of detectable Ni Auger feature for the FeNi nanospheres and not the FeNi nanocubes confirms the higher Ni content in the former.

According to the charge transfer theory for transition metal alloys,[89] we calculate the partial charge transfers, ΔZ_A, for Fe (Ni) to be 0.17 (0.34) per atom in the nanocubes and 0.34 (0.17) per atom in the nanospheres using the following relation:

$$\Delta Z_A = 1.2\,(1 - C_A)\,\Delta\varphi^*,$$

where $\Delta\varphi^*$ is the difference in electronegativities of the metals, and C_A is the concentration of metal A. The smaller partial charge transfers for Fe 2p (Ni 2p) in Fe-rich (Ni-rich) alloy NPs also explain the lack of discernible binding energy shift in XPS spectra. The lack of a discernible binding energy shift for Fe in the nanocubes and for Ni in the nanospheres could be due to the weak electron transfer and/or to the strong photopeak from the majority metal in the nanocubes (Fe) and nanospheres (Ni), respectively, that overwhelms any weak feature corresponding to the alloy peak.

The O 1s feature at 530.0 eV (Figure 3.5c) corresponds to O^{-2} species which includes very close-lying FeO, NiO and/or $NiFe_2O_4$ features. [90,91] Similarly, the feature at 531.5 eV corresponds to OH^- which is from contributions of $Ni(OH)_2$ and/or FeOOH. [90,92] The remaining O 1s feature at 532.4 eV can be assigned primarily to SiO_x from the bare substrate region not covered by NPs. The O 1s features are reduced dramatically (by over 60%) upon just 70 s of sputtering and more gradually upon further sputtering, which confirms the removal of the thin oxide skin on the nanocubes and subsequent SiO_x removal on the rest of the substrate. In particular, the O 1s feature at 531.5 is found to be removed first, and this is followed by the depletion of feature at 530.0 eV. This implies the possibility of two oxide region with different composition.

In the valence band spectra for the as-deposited FeNi concave nanocubes (Figure 3.5d) and truncated nanospheres (Figure 3.5h), the electron density of states is found to be broadly distributed between 0 and 4 eV, with significant intensity at the Fermi level characteristic of a metal. The valence band maximum for FeNi nanocubes (Figure 3.5d) located at 1.2 eV is 0.2 eV higher than that for pristine Fe NPs (Figure 3.6d, bottom trace), which is in good accord with the spectrum of invar FeNi alloy.[93] The valence band spectra of the FeNi nanospheres (Figure 3.5h) exhibit a sharper density of states distribution than nanocubes (Figure 3.5d) and more closely resemble to that of the pristine Ni NPs (Figure 3.5h, bottom trace). No discernible shift of the valence band maximum in the as-deposited nanospheres and upon sputtering to 430 s occurs. Sputtering nanocubes and nanospheres for 1390 s exposes the feature at 2.6 eV, which can be attributed to the hybridised Fe 3d-Si 2p or Ni 3d-Si 3p states, [94] similar to the M-Si 3s features (M=Ni, Co) reported by Tersoff. [95] The strong peak at 9.1 eV that becomes more intense with increasing sputtering time corresponds to Ar 3p feature of implanted Ar as a result of sputtering.

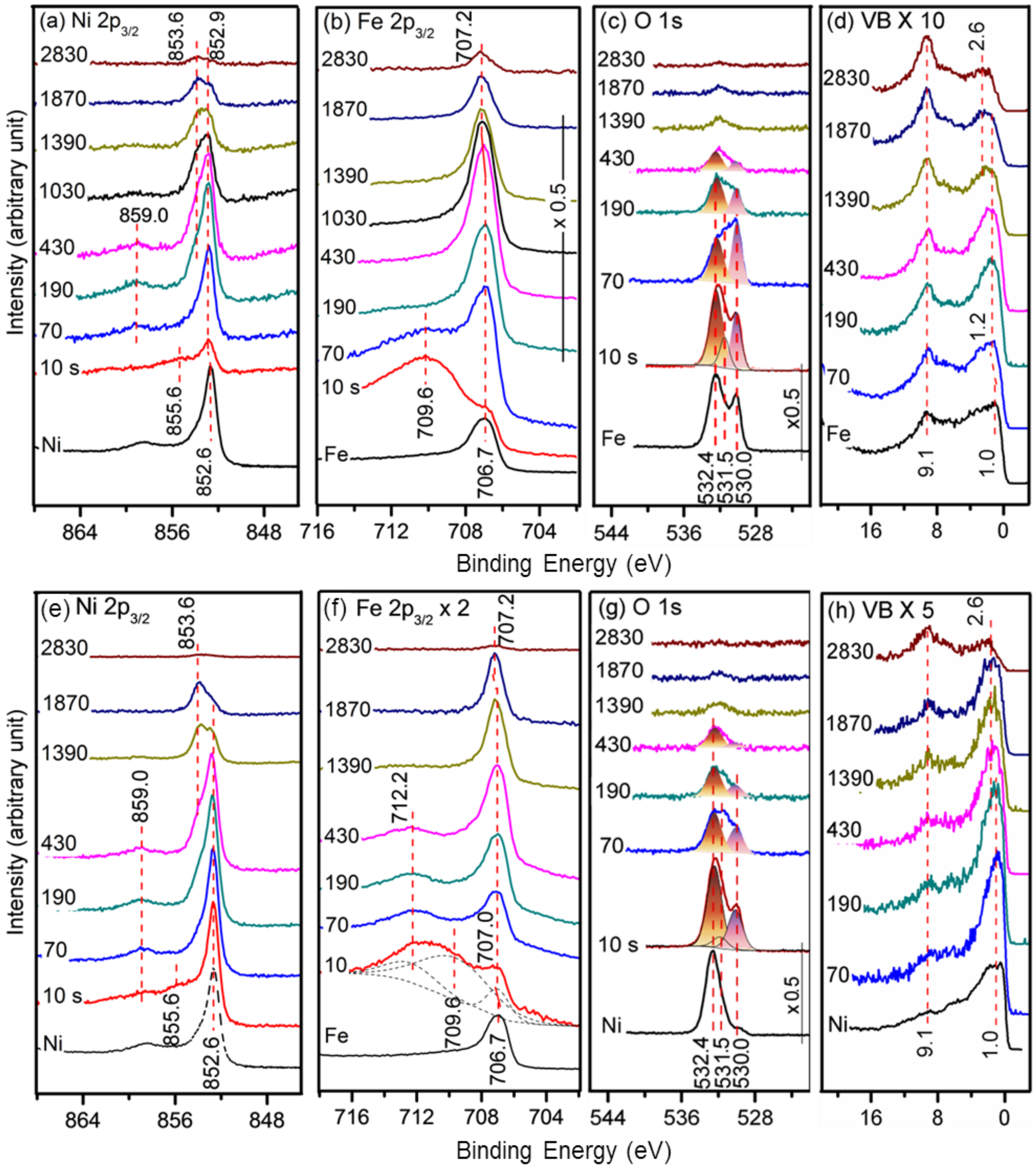

Figure 3.5 XPS spectra of (a, e) Ni 2p, (b, f) Fe 2p, (c, g) O1s, and (d, h) valence band (VB) regions for FeNi alloy nanocubes as-electrodeposited on H-Si(100) in Fe10:Ni5 (upper panels) and nanospheres obtained in Fe5:Ni10 electrolyte (lower panels), and upon sputtering for 10 s, 70 s, 190 s, 430 s, 1390 s, 1870 s, and 2830 s. The corresponding Ni 2p (a, e) and VB spectra (h) for pristine Ni nanoparticles obtained in Ni35 and Fe 2p (b, f) and VB spectra (d) for pristine Fe nanoparticles obtained in Fe35 are also shown for comparison.

Figures 3.6a and 3.6b show the corresponding depth profiles for Fe $2p_{3/2}$ peaks for the alloy at 706.7 eV and 707.0 eV and Fe-silicide at 707.2 eV, the Ni $2p_{3/2}$ peaks for the alloy at 852.6 eV and 852.9 eV and Ni-silicide at 853.6 eV, and the O 1s peaks for all oxides at 530.0 eV and 531.5 eV for the nanocubes and nanospheres, respectively. For nanocubes (Figure 3.6a), the metal silicide features begin to emerge upon sputtering for ~1000 s, which marks the interface between the NP and the Si substrate. On the other hand, the metal oxide features are found to be removed rapidly after brief initial sputtering for 70 s and completely removed after 430 s of sputtering, indicating a thin oxide shell.

Between the oxide shell and the NP-Si interface, we identify the alloy core region, in which the Fe alloy profile is higher than the Ni alloy profile due to the higher Fe content in the Fe10:Ni5 electrolyte. More importantly, the relative intensities of the Fe and Ni alloy features are found to be changing gradually inside this alloy core region, which suggests the presence of a Fe relative composition gradient increasing toward the interface. For the nanospheres (Figure 3.6b), the Ni silicide feature emerges after 900 s of sputtering while the weaker Fe silicide feature occurs after ~1800 s. The oxide features are found to be totally removed after just 190 s of sputtering. These trends indicate the presence of a similar metal silicide region and a metal oxide shell region. Furthermore, a metal alloy core region is also observed, with the Ni alloy profile lying higher than the Fe alloy profile due to the higher Ni content resulting from deposition in the Fe5:Ni10 electrolyte. Interestingly, the weaker Fe alloy profile is found to cross over the stronger Ni alloy profile at ~1000 s of sputtering. Despite the Ni-rich composition of the alloy nanospheres, the gradual change in the relative composition of Fe in the alloy core region leads to a higher Fe alloy composition at the NP-Si interface. This suggests faster Fe nucleation than Ni nucleation, leading to a Fe-rich nucleus, during the initial stage of alloy NP formation.

TEM-EDX linescans across a typical nanocube (Figure 3.6c) and a nanosphere (Figure 3.6d) also confirm the corresponding XPS depth profiles shown in Figure 3.6a and 3.6b. The similarity between the XPS depth profile and the corresponding TEM-EDX profile shows that both the nanocubes (Figure 3.6a vs 3.6c) and nanospheres (Figure 3.6b vs 3.6d) are highly homogenous in composition. From both XPS depth profiling and TEM linescans can be observed that despite the difference in shape, both nanocubes and nanospheres exhibit an alloy-core oxide-shell structure. Depending on the electrolyte composition, the alloy core can be either Fe-rich or

Ni-rich at the core region with a gradual composition change extending into the Fe-rich nucleus. From the O 1s depth profile, we estimate the thickness of the oxide shell to be 5.3 nm, using the sputtering rate of 0.74 nm/min obtained for this sample determined from a profilometry. This thickness is found to be in good agreement with the thickness (~6 nm) obtained from a line scan of the corresponding TEM-EDX data (not shown). Schematic diagrams illustrating the respective compositions of the FeNi alloy nanocube and nanosphere are presented in Figure 3.6e and 3.6f.

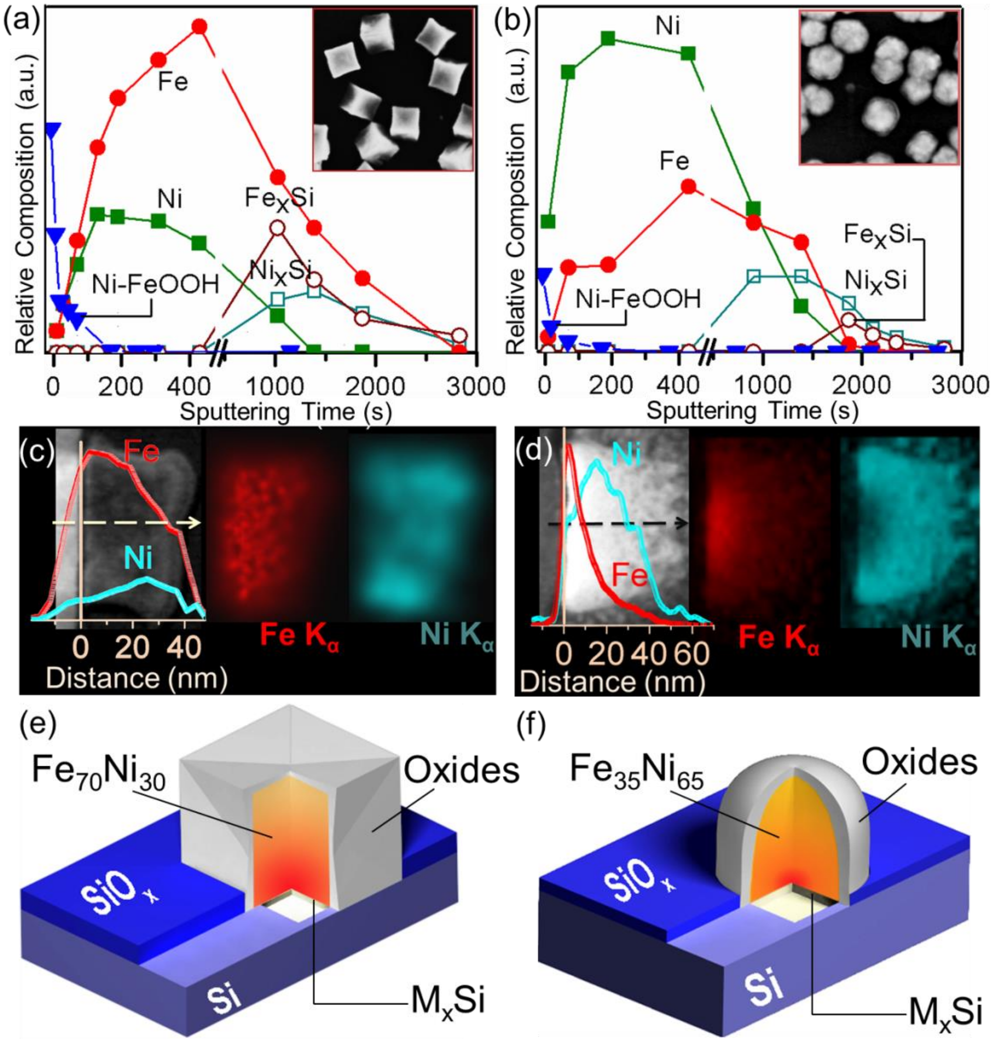

Figure 3.6 Depth profiles of Fe $2p_{3/2}$ features for alloy at 706.7 eV and 707.0 eV and Fe silicides at 707.2 eV, and Ni $2p_{3/2}$ features for alloy at 852.6 eV and 852.9 eV and Ni silicides at 853.6 eV for (a) FeNi alloy concave nanocubes obtained from a Fe10:Ni5 electrolyte and (b) FeNi alloy truncated nanospheres obtained from a Fe5:Ni10 electrolyte. (c) and (d) show EDX line scans and EDX-TEM mapping of a typical concave nanocube and nanosphere. Schematic models of a FeNi (e) nanocube and (f) a nanosphere as inferred from depth-profiling XPS and TEM data. Both FeNi alloy cores are also covered by an oxide shell (consisting of Ni-doped FeOOH and $NiFe_2O_4$) supported on the Si substrate with a metal silicide (M_xSi) interface.

To investigate the nature of the oxide shell, we show in Figure 3.7a the Fe $2p_{3/2}$ and Ni $2p_{3/2}$ spectra for the FeNi concave nanocubes as-prepared from a Fe10:Ni5 electrolyte and upon Ar^+ sputtering for 10 s and 40 s. The Fe $2p_{3/2}$ peak at 710.3 eV can be attributed to FeOOH, in accord with the 710.7 eV position found in our reference sample (not shown) and the literature.[90] The small difference could be due to Ni incorporation in the oxide shell, and is consistent with the Ni $2p_{3/2}$ oxide peak at 855.6 eV. As the electrolytes consist of $FeCl_2$ and $NiCl_2$, and given the formation of β-FeOOH in the chloride solution,[96] Ni^{2+} could be doped into the β-FeOOH structure in the presence of Cl^-.[97] After sputtering for 40 s, the Fe $2p_{3/2}$ peak (at 710.3 eV) is found to shift to a lower binding energy with appearance of a small shoulder, revealing the presence of an intermediate oxide layer attributable to $NiFe_2O_4$.[98] Formation of an intermediate $NiFe_2O_4$ layer has also been observed in steel alloys.[99] The oxide shell therefore consists of Ni-doped FeOOH in the outer shell and $NiFe_2O_4$ in the inner shell. A proposed growth mechanism of the oxide shell is given in the following:

Immediately after stopping the applied potential, the as-formed Fe nanoparticle undergoes oxidation in the acidic solution:

1. $Fe \rightarrow Fe^{2+} + 2e^-$

Furthermore, the following redox reaction could also occur in the presence of water:[100]

2. $4Fe^{2+} + O_2 \rightarrow 4Fe^{3+} + 2O^{2-}$

The Fe^{2+} ion then undergoes further reactions to form FeOH (ad) (Reactions 3, 4) and $Fe(OH)_2$ (Reaction 5), the latter of which could further dehydrate to FeO (Reaction 6).

3. $Fe^{2+} + OH^- \rightarrow FeOH^+$
4. $FeOH^+ + e^- \rightarrow FeOH\ (ad)$
5. $Fe^{2+} + 2H_2O \rightleftharpoons Fe(OH)_2 + 2H^+$
6. $Fe(OH)_2 \rightleftharpoons FeO + H_2O$

Fe^{3+} can go onto form of $Fe(OH)_3$ (Reaction 7), followed by dehydration to FeO(OH) (Reaction 8) and to Fe_2O_3 (Reaction 9).

7. $Fe^{3+} + 3H_2O \rightleftharpoons Fe(OH)_3 + 3H^+$
8. $Fe(OH)_3 \rightleftharpoons FeO(OH) + H_2O$

9. $2\,FeO(OH) \rightleftharpoons Fe_2O_3 + H_2O$

For the as-formed Ni, reactions similar to (1), (3-6) could also occur.

10. $Ni \rightarrow Ni^{2+} + 2\,e^{-}$

11. $Ni^{2+} + OH^{-} \rightarrow NiOH^{+}$

12. $NiOH^{+} + e^{-} \rightarrow NiOH$ (ad)

13. $Ni^{2+} + 2\,H_2O \rightleftharpoons Ni(OH)_2 + 2\,H^{+}$

14. $Ni(OH)_2 \rightleftharpoons NiO + H_2O$

In the acidic solution and the presence of Ni^{2+}, Fe^{2+} can also be oxidized to ferrite:[101]

15. $(3-x)\ Fe(OH)_2 + x\ Ni(OH)_2 + O_2 \rightleftharpoons Fe_{3-x}\,Ni_x\,O_4 + 4\,H_2O$

where $0 < x < 1$. When the amount of dissolved oxygen is low, Fe(II)-containing products (FeO and Fe_3O_4) are favored. The presence of Ni^{2+} ions facilitates ferrite formation. Similar formation of Ni ferities as an intermediate layer has also been reported for rust formation in an oxidizing atmosphere.[99] As the formation of the adsorbed MOH (M = Fe or Ni) is the rate-determining step and the number of adsorption sites is limited on the nanoparticle surface, the concentration of FeOH (ad) is overwhelmingly higher than that of NiOH (ad) because the adsorption rate for $FeOH^{+}$ is considerably larger than that for $Ni(OH)^{+}$.[92] This effectively leads to the formation of a Ni-doped FeO(OH)-rich film on the nanoparticle surface.[102]

One of the great challenges in synthesizing magnetic materials, such as Fe, Ni, Co and their alloys, particularly in the nanoscale is their very high air activity and easy oxidization. To protect the metallic nanoparticles from oxidation, an additional step of coating the NP with transition-metal oxides,[77,78] or encapsulation in polymers,[79] carbon nanotubes[80] and silica shells[81] is often required. In the present work, the oxide layer formed in-situ on the FeNi NPs in the co-ECD eliminates the need for such an extra step. From their corresponding TEM-EDX linescans and XPS depth-profile data, we estimate this oxide layer to be 6 nm thick for concave nanocubes and ~5 nm thick for truncated nanospheres, with the majority of the NPs (~ 95 vol. %) remaining as metallic. To evaluate the resistance of these NPs to oxidation in air, the samples were placed in an air environment with 80% relative humidity at room temperature for 60 days. No diffraction peak attributable to oxides in XRD and less than 5% increase in the amount of oxygen as measured by EDX is observed for both NPs. More precisely, the change in magnetization saturation and coercivity of nanoparticles can reflect changes in the metallic portion also changes in nature of material. We have used this technique to investigate if any further oxidation occurs after long exposure of the nanoparticles to the air. The magnetization saturation obtained from SQUID hysteresis loops is found to decrease only by just 0.8% in the concave nanocubes and 1.2% in the truncated nanospheres which is comparable to the experimental uncertainty of the measurement. Therefore, no significant change in the magnetization saturation is observed. Similarly, almost no change in coercivity of both the concave nanocubes and truncated nanospheres is observed. These data demonstrate that effectively no metallic part of NPs has been converted to oxide. All of these data therefore support the remarkable air stability of these NPs (Figure 3.7b). The presence of Ni-incorporated FeOOH, along with the denser intermediate layer of $NiFe_2O_4$, on the NPs inhibit oxidation of NPs in air, which is in good agreement with the anti-corrosive properties of Ni-doped FeOOH and of the $NiFe_2O_4$ protective layer in steel alloys.[97,99]

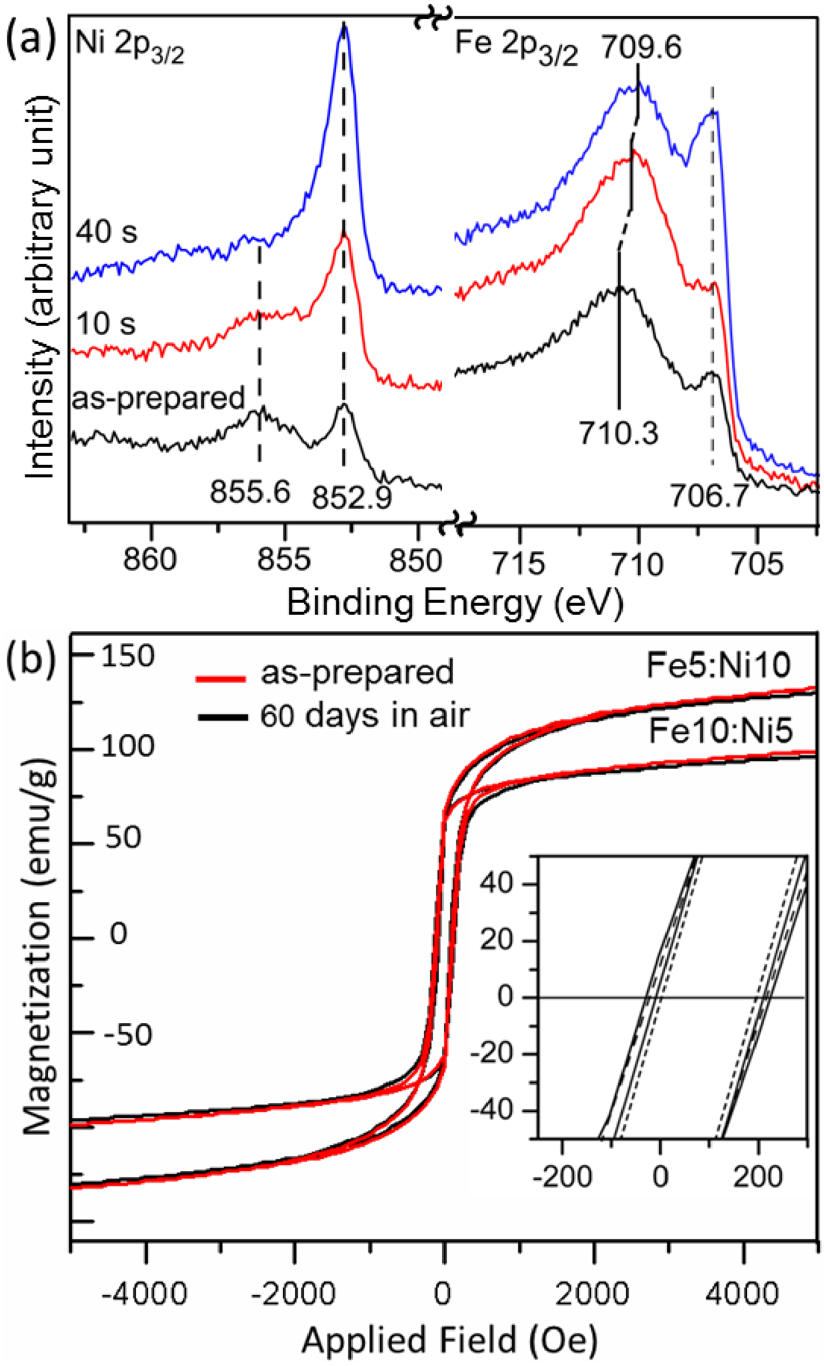

Figure 3.7 (a) Fe $2p_{3/2}$ and Ni $2p_{3/2}$ spectra for the as-prepared nanoparticles from Fe10:Ni5 electrolyte and sputtered by Ar^+ for 10 s and 40 s; (b) Magnetization hysteresis loops measured at room temperature and coercivity (inset) for samples as-prepared from Fe10:Ni5 and Fe5:Ni10 electrolytes (solid lines) and upon exposure to the humid air (80 % relative humidity) for 60 days (dash line).

3.1.4 Summary

In the present work, near mono-size FeNi alloy NPs were obtained by a single-step co-electrodeposition method with a good control on shape, structure and composition. By changing the Fe:Ni ratio, we can obtain different compositions and shapes ranging from concave cubic Fe-rich alloy NPs to truncated spherical Ni-rich alloy NPs. In the initial growth stage, FeNi alloy formation follows instantaneous nucleation unlike pure Fe, which follows progressive nucleation. This leads to a very narrow size distribution and little clustering during NP growth. We study the effect of addition of a second metal to a host metal lattice on changing the final shape of the resulting bimetallic NP system, and demonstrate the important role of phase transformation in the shape evolution of FeNi NPs from concave cubic to truncated spherical shape. XPS depth profiling and elemental TEM linscans show the presence of Fe-rich nucleus for both nanocubes and nanospheres particles and a composition gradient inside the NPs where Fe content gradually decreases from the Si interface towards the oxide surface and modifies the surface function. Depending on the electrolyte composition, the alloy core can be either Fe-rich or Ni-rich in the core region. A thin protective oxide layer consisting of a Ni-doped FeOOH outer layer and $NiFe_2O_4$ intermediate layer can be obtained in-situ over the entire metallic core, which provides effective corrosion protection. This study provides new insight into the use of guest metal in a host system as a parameter to control the shape of bimetallic or alloy nanoparticles.

3.2 Bimetallic FeNi Concave Nanocubes and Nanocages[§§]

3.2.1 Introduction

Shape-dependent physico-chemical properties of nanostructured materials are widely explored for advanced applications. A variety of growth methods have been used to control the shape of nanostructures of mostly noble metals in order to enhance their catalytic activity.[103–108] These methods commonly produce nanostructures with convex shapes enclosed by low-index {100}, {110} and {111} facets as a result of minimization of the surface energies.[103,106] Due to their high surface energies, high-index facets usually grow faster than the other facets, leaving them out of the exposed faces of the final shape during crystal growth.[109,110] Furthermore, the high densities of atomic steps, ledges, kinks and dangling bonds present in these high-index facets lead to their high activity. As the exposed crystalline faces of nanomaterial have strong influence on both reactivity and selectivity, it is therefore desirable to have high-index facets. To date, only a few methods have been reported for producing nanostructures with high-index surfaces and they can be categorized into two common approaches. One such approach involves the use of external agents such as surfactants, reducing agents or stabilizers for enforcing the preferred growth orientations.[109,111–115] However, these external agents upon covering the pristine surfaces of the nanostructures invariably reduce the surface activity, often due to incomplete removal used in post-processing. The other approach involves carving the concave nanostructures by removing materials from the as-prepared convex nanoparticles (NPs) by different procedures, including electrochemical pulses,[110,116] and galvanic replacement reaction.[117] These material removal methods, however, suffer from the need for multiple steps in the synthesis, with the NPs prepared beforehand as the starting materials.

As cuboid nanostructures are enclosed by {100} and {110} facets, concave cubes with their high index planes are generally rare. For non-noble metals, it has not been possible to make concave nanostructures with previous methods due to their inherently high reactivity. In a recent study, we show that the morphologies of nanostructures of a bimetallic system obtained by electrochemical method greatly depend on the ratio of starting materials.[118] Here, we demonstrate that it is possible to produce FeNi concave nanocubes using a one-step, surfactant-

---

[§§] This section is made from one of my publications: N. Moghimi, M. Abdellah, J. P. Thomas, M. Mohapatra, K. T. Leung, J. Am. Chem. Soc., Communication, 2013, 135 (30), pp 10958–10961. Copyright (2013) by the American Chemical Society.

free electrochemical method by manipulating the growth kinetics involving a bimetallic system. The advantage of high reactive facets is explored further by developing nanocages with preferential etching in the center of concave cube through an electroleaching process, thereby introducing a new approach for synthesizing concave nanocages. Electro-catalytic activities of concave nanocubes and nanocages are also evaluated by electro-oxidation of 4-aminophenol (4-AP) as a model chemical sensing reaction. It should be noted that 4-AP is an important organic compound that can be used for E. coli detection and as an intermediate or degradation product in the synthesis of paracetamol in pharmaceutical industry. While Fe and Fe-based bimetallic nanoparticles are widely studied and used for groundwater remediation of contamination involving chlorinated and nitroaromatic organic compounds [20,119–121] and toxic metal ions (As, Cd, Cr, and Pb) [122,123] no report is available on using these NPs for sensing toxic contamination in the water. The present work therefore not only introduces two novel synthesis methods for producing these concave nanostructures but also offers new active nanomaterials for label-free sensing applications in monitoring toxins in water and pharmaceutical wastes.

3.2.2 Material and Methods

Concave nanostructures are rare because of their thermodynamically unfavorable shapes. Here, we prepare bimetallic FeNi concave nanocubes with high Miller index planes through controlled triggering of different growth kinetics of Fe and Ni.

FeNi concave nanocubes are obtained by electrodeposition of two metal ions (Fe^{2+}, and Ni^{2+}) at room temperature using amperometry for 20 s at –1.4 V (vs Ag/AgCl) in electrolytes of 5 mM $NiCl_2$ mixed with 15 mM, 10 mM and 5 mM $FeCl_2$, all with 200 mM H_3BO_3 as the supporting electrolyte. By changing the Fe/Ni ratio different compositions of FeNi nanoparticles has been obtained. The Ni contents of nanocubes obtained in the three electrolytes as determined by Energy Dispersive X-ray Spectroscopy are in good accord with the respective relative Ni% of the electrolytes.

The FeNi cuboctahedrons are prepared at 4 °C by amperometry for 30 s at –1.4 V (vs Ag/AgCl) in an electrolyte of 1.5 mM $NiCl_2$ and 1.5 mM $FeCl_2$, with the supporting electrolyte consisting of 100 mM H_3BO_3 and 50 mM $NaClO_4$. Since H_3BO_3 can form complex with $NiOH^+$ [124] and slow down the kinetics of the Ni growth, we could manipulate the kinetics of the system to obtain different shape by reducing the concentration of boric acid and increasing the conductivity of solution by $NaClO_4$. Reducing the total concentration of Fe^{2+} and Ni^{2+} in the solution and reducing deposition temperature to 4 ℃ could also slow down the growth kinetics.

3.2.3 Results and Discussion

Figure 3.8a-3.8c shows typical SEM images of the nanocubes obtained from three electrolytes of different relative Ni compositions by amperometry at 25 °C. These FeNi concave nanocubes all exhibit narrow size distributions with average sizes of 59 nm, 63 nm, and 80 nm for Ni contents of 22%, 31%, and 47%, respectively. Increasing the Ni content to 47% appears to increase the concavity of the nanocubes (Figure 3.8c). For electrolytes with greater than 50%Ni, the NPs become truncated spheres. Detailed discussion about the shape evolution of FeNi nanoparticles obtained in electrolytes with different %Ni contents is given elsewhere.[118]

To characterize the concavity of the FeNi nanocubes, we index the surface facets by cross-sectional TEM. Using a focused ion beam (FIB) to cut a 50 nm thick lamella of typical FeNi concave NPs (with 47% Ni content) on a Si substrate, we obtain a high-resolution TEM image of the cross section of a single concave cube along the [001] direction (Figure 3.8d), with the corresponding diffraction pattern shown in Figure 3.8e.

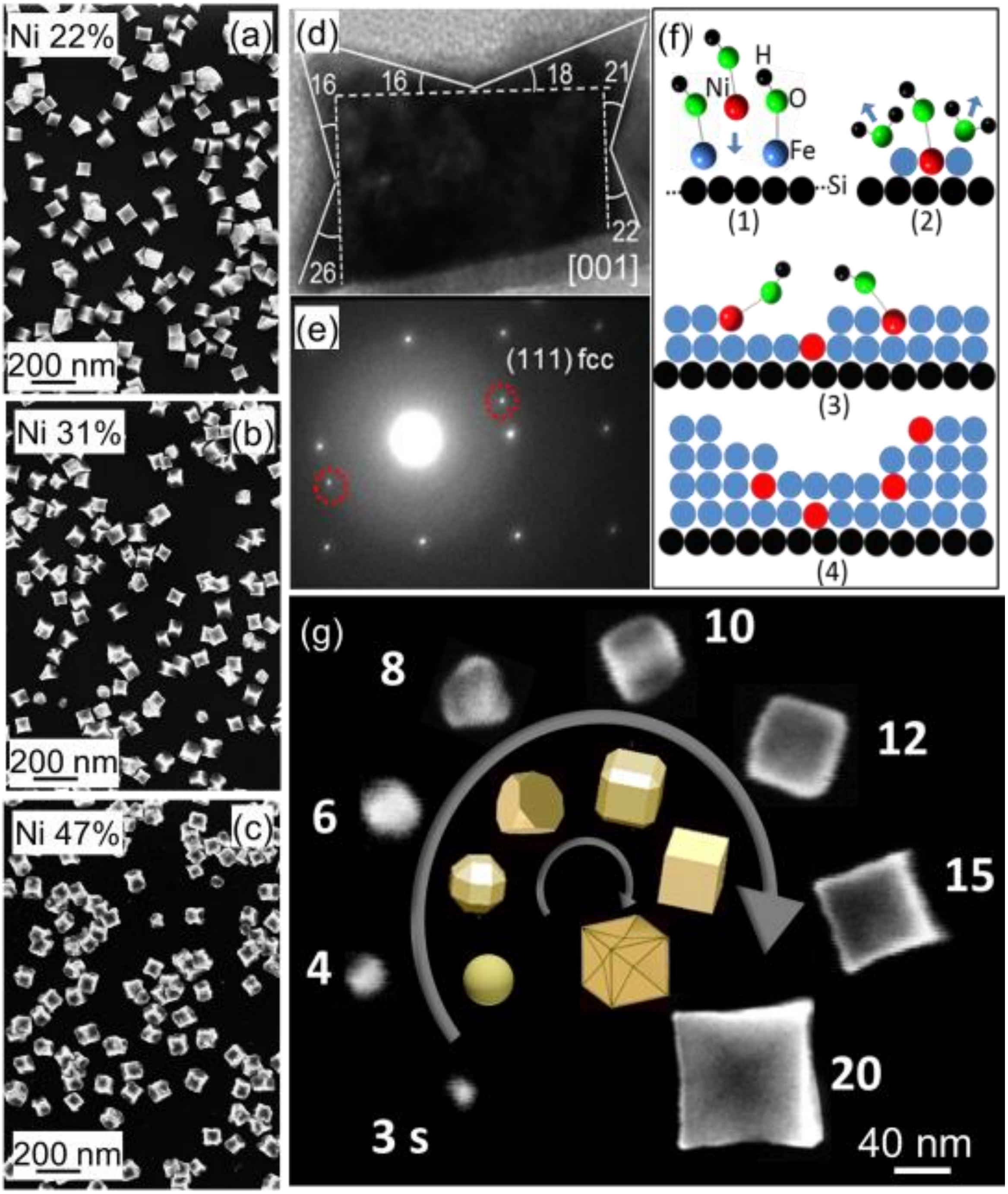

Figure 3.8 SEM images of concave nanocubes with different Ni content: (a) 22%, (b) 31%, and (c) 47%. (d) HR-TEM image of a FeNi concave nanocube with 47% Ni content, and (e) the corresponding electron diffraction pattern projected from the [001] axis, with circles marking the fcc spots in a bcc pattern. (f) Schematic diagram illustrating a plausible mechanism for the formation of higher index facets on a concave nanocube, which involves (1) selective adsorption of FeOH+ over NiOH+, (2) faster reduction of FeOH+ than NiOH+, (3) and (4) formation of step or kink defects and ultimately higher index planes. (g) SEM images of typical nanoparticles with 47% Ni content with increasing deposition time from 3 s to 20 s.

The observed diffraction pattern corresponds to the bcc FeNi pattern overlapping with the FeNi fcc pattern (points marked by red circles), which shows that these NPs are in the mixed-phase region of the FeNi phase diagram.[118] By measuring the angles of the surface planes between the concave cube and a perfect cube and comparing them with those of an ideal concave cube (Figure 3.9), we conclude that the surface of the concave nanocube is mainly enclosed by the {720} facets, along with some other high-index facets such as {520}, {730}, and {310}. The ideal concave cube angel and their relationships with the Millers indexes are in the following:

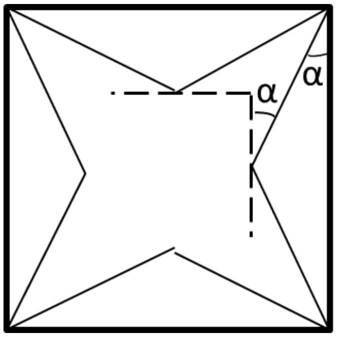

{hkl}	α
{610}	9.5
{510}	11.3
{410}	14.0
{720}	15.9
{310}	18.4
{830}	20.6
{520}	21.8
{730}	23.2

Figure 3.9 Theoretical relationship between the interfacial angles and high-index facets for an ideal concave cube.[115]

Thermodynamically, high-index facets, with their higher surface energies, are expected to grow faster than low-index facets, which generally result in their disappearance during crystal growth. The present formation of concave nanocubes with their high-index facets exposed is therefore a kinetically driven process. Since pristine Fe NPs obtained under similar electrochemical deposition conditions have a well-defined cubic shape (Figure 3.10), the concavity of the FeNi nanocubes is caused by the presence of Ni.

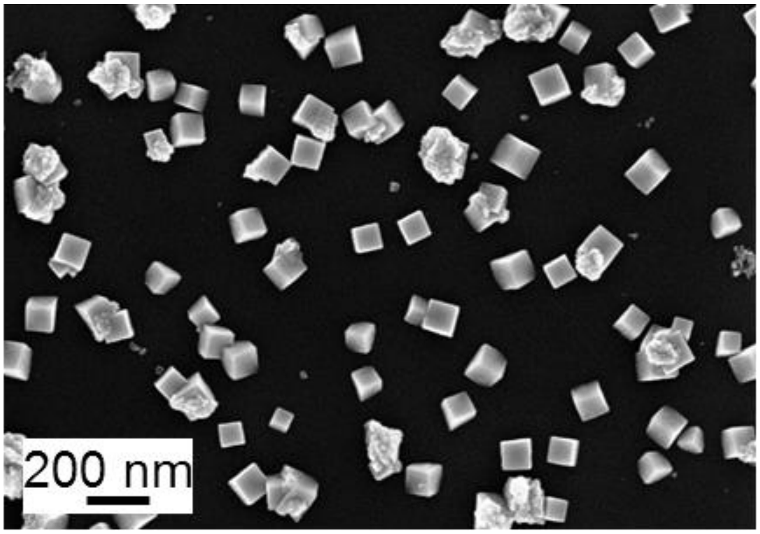

Figure 3.10 SEM images of pristine Fe nanoparticles with well-defined cubic shape obtained in 5 mM $FeCl_2$ and H_3BO_3.

To investigate how Ni changes the Fe NPs from cubic to concave cubic shape in the absence of any surfactants or capping agents, we examine the role of kinetics in the formation mechanism in the present method. Electrochemical reduction of the Fe-group metal ions (M^{2+}) starts with the formation of MOH^+ in the aqueous solution.[125] The MOH^+ ion then undergoes adsorption onto the substrate surface, followed by reduction to metal (M):[92]

$$MOH^+_{(aq)} \rightarrow MOH^+_{(ads)} \qquad \text{(reaction 1, rate constant } k_1\text{)}$$

$$MOH^+_{(ads)} + H^+ + 2e^- \rightarrow M + H_2O \qquad \text{(reaction 2, rate constant } k_2\text{)}$$

Following the law of mass action, the adsorption rate depends on the concentration of M^{2+} and the amount of free adsorption sites with rate constant k_1, while the reduction rate depends on the surface coverage of MOH^+ with rate constant k_2.[92] The early electroplating work on FeNi bulk alloy films has shown higher adsorption and reduction rates for $FeOH^+$ than the corresponding rates for $NiOH^+$.[92] We therefore conclude that in the present case the adsorbed $NiOH^+$ ions are most likely surrounded by adsorbed $FeOH^+$ ions in the first adlayer upon reaction 1. This is then followed by reduction of $FeOH^+$ to Fe that occurs first at the $FeOH^+$ rich perimeter of the adlayer upon reaction 2. The slower reduction of the adsorbed $NiOH^+$ inside the perimeter of the adlayer would cause disruption to the growth of the (100) plane, creating step or kink defects. The next incoming ions, i.e. $FeOH^+$ or $NiOH^+$, would therefore adsorb preferentially onto the defect sites, forming the higher index planes (Figure 3.8f). The presence of Cl^- and Ni^{2+} ions increases the reduction rate of Fe ions, and leads to more kinetically favored (as opposed to thermodynamically favored) growth of particles with higher-energy surface facets. This was also observed in the formation of concave Au nanocubes when the rate of reduction of Au ions was enhanced by increasing the ascorbic acid concentration.[113]

To investigate the conditions under which kinetics becomes dominant over thermodynamics, we perform electrodeposition of FeNi NPs in an electrolyte of 5 mM $NiCl_2$ and 5 mM $FeCl_2$ with different deposition time from 3 s to 20 s. Figure 3.8g shows that the FeNi NPs have undergone significant morphological change, from sphere to truncated cube to cube and finally to concave cube, with increasing deposition time.

Given that the shape of a NP is obtained by minimizing the energy of formation, a NP embryo must initially exist as a sphere because the surface area to volume ratio of a sphere (with the smallest critical radius) is the smallest.[126,127] Depending on the crystalline nature of the metal, non-spherical shapes can develop due to different surface energies of the exposed crystalline planes. For a NP of a particular shape, the critical radius (r*) is inversely proportional to the shape factor, ξ: [127]

$$r^* = 2(\gamma/\Delta Gv)(1/\xi^2)$$

where γ is the surface energy and ΔGv is the volumetric energy. As a result, each shape would require a specific minimal size to become thermodynamically stable. As the sphere ($\xi = 1$) continues to grow, the next stable shapes are truncated cube ($\xi = 0.922$) and cube ($\xi = 0.898$), because the surface energies for the exposed corners are generally greater than those of the edges, which are in turn greater than those of the surface planes. In accord with our observations, after the cubic shape has been stabilized upon reaching the minimal size of 45–50 nm, only then would the aforementioned kinetics driven mechanism become apparent. This kinetic effect therefore leads to stabilization of the thermodynamically unfavorable concave cubic shape.

With the presence of high-index facets, concave nanocubes should have higher chemical activities than nanoparticles with low-index facets such as cuboctahedron. To demonstrate the superior reactivity of these FeNi concave nanocubes, we synthesize FeNi cuboctahedrons with similar %Ni content and similar size but with convex surfaces, and we compare their electrochemical properties. Figure 3.11a shows the SEM image of the resulting FeNi cuboctahedrons with a similar average size (75 nm) to the concave nanocubes (Figure 3.8c), obtained by amperometry at 4 °C. The corresponding %Ni content as determined by EDX of the former (49%) is also found to be similar to the latter (47%). Using these two samples (i.e, FeNi concave nanocubes and cuboctahedrons deposited on Si substrates) as the working electrodes in a three electrode cell (with a Pt wire and Ag/AgCl as the counter and reference electrodes, respectively), we perform chronoamperometry in a solution of 10 mM phosphate buffer saline (PBS) with pH 7 and 1 mM $K_3Fe(CN)_6$, in order to determine the electroactive surface areas for both samples. From the cyclic voltammograms of FeNi concave nanocubes in PBS solutions with and without $K_3Fe(CN)_6$ (Figure 3.11b), the oxidation peak of cyanide is found to be located at 370 mV (vs Ag/AgCl). For our chronoamperometric measurements, we therefore select a step potential of 600 mV to be sufficiently higher than the oxidation peak of cyanide. The cyclic voltammograms (CVs) of cuboctahedrons are found to be similar to those of concave nanocubes. From the resulting I-t (current vs time) data, the electroactive area (A) can be obtained from the slope of the I vs $t^{-1/2}$ plots shown in Figure 3.11c using the Cottrell equation:

$$I = nFAC_0D^{1/2}\pi^{-1/2}t^{-1/2}$$

where n is the number of electrons participating in the oxidation or reduction, F is the Faraday constant, D is the diffusion coefficient and C_0 is the initial concentration of $K_3Fe(CN)_6$. The mass-normalized electroactive surface area of concave nanocube electrode is found to be 6.7 m^2g^{-1}, which is over thrice that of cuboctahedron electrode (2.1 m^2g^{-1}). This result therefore demonstrates the significantly higher reactivity of concave nanocubes than nanocubes with convex surfaces.

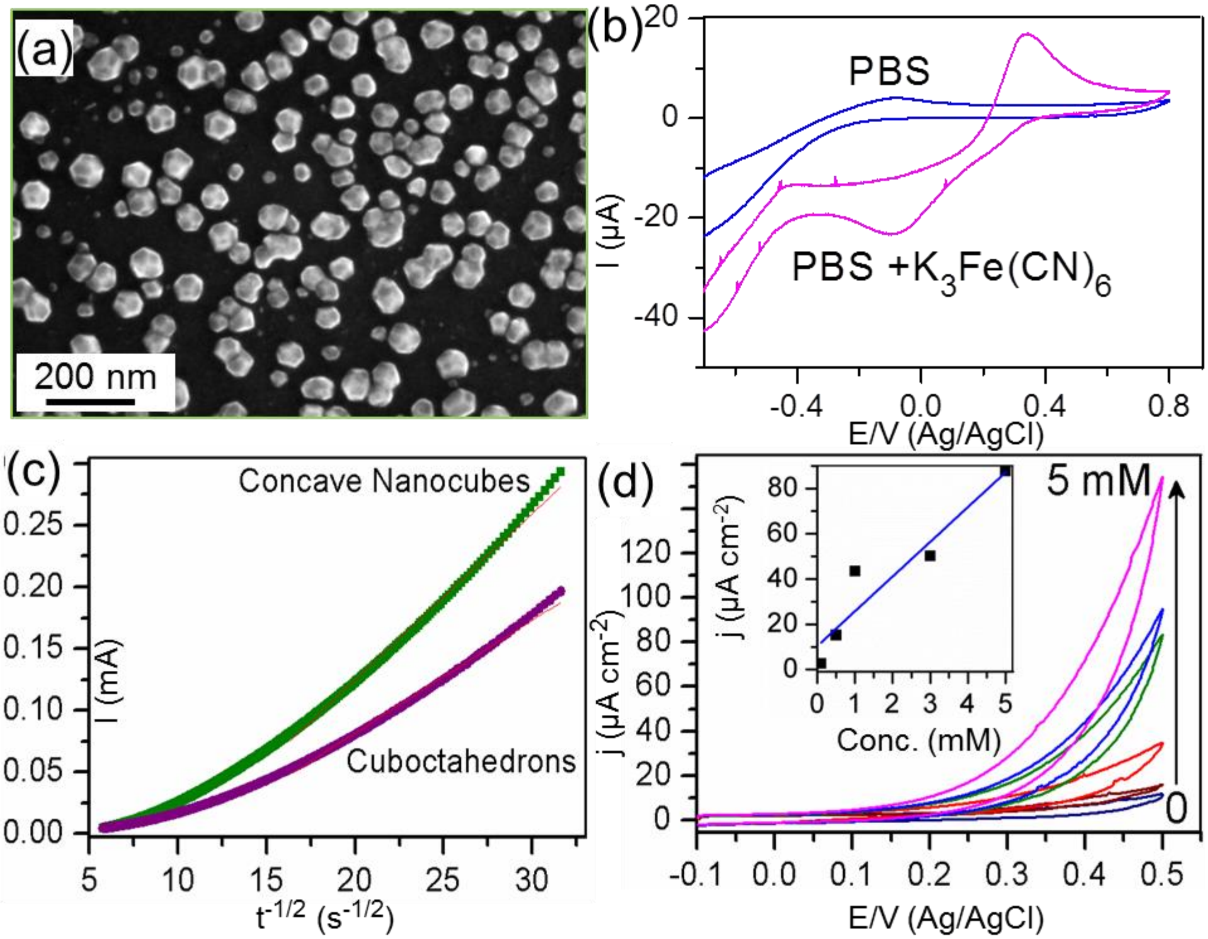

Figure 3.11 (a) SEM images of cuboctahedrons electrodeposited at 4 °C, (b) CV curves of FeNi concave nanocubes in 10 mM PBS with and without 1 mM $K_3Fe(CN)_6$. (c) Cottrell plot obtained by chronoamperometery using FeNi concave nanocubes and cuboctahedrons as the working electrodes. (d) CV curves in different concentrations of 4-aminophenol (with a scan rate of 50 mV s^{-1}). Inset shows the linear relationship between current and concentration.

The high reactivity of these FeNi concave nanocubes opens up new opportunities for sensing biotoxins [e.g. E-coli] for water remediation and for monitoring drug synthesis [e.g., paracetamol] in pharmaceutical industry by electrochemical detection of 4-aminophenol (4-AP). 4-AP is an important "indicator molecule", because it is produced by hydrolysis of 4-aminophenyle-β-D-galactopyranoside by the enzyme β-galactosidase of E-coli[128] and it is an intermediate or degradation product in drug synthesis.[129,130] Figure 3.11d shows the CV curves of FeNi concave nanocubes (with 47% Ni content) in a 10 mM PBS solution (pH=7) in the presence of different concentrations of 4-AP. No change in the shape of concave nanocubes is observed after 20 cycles (Figure 3.12).

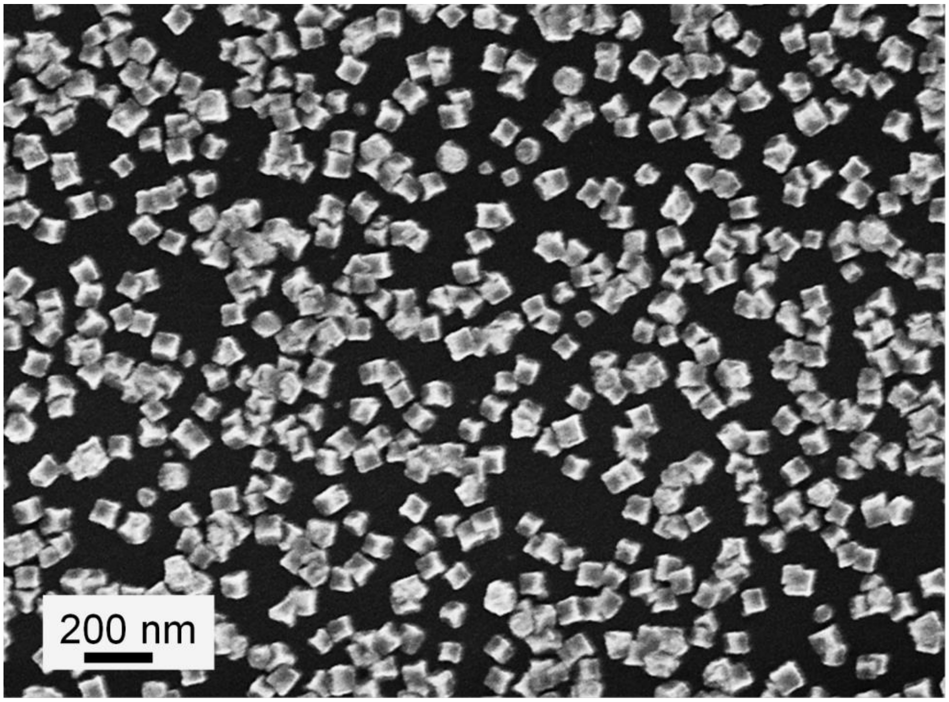

Figure 3.12 SEM images of FeNi concave cubes after 4-aminophenol detection for 20 cycles.

Evidently, increasing the 4-AP concentration from 0.1 mM to 5 mM leads to a higher oxidation current. A linear relation is obtained between the current signal (arbitrarily selected at 0.45 V vs Ag/AgCl) and the 4-AP concentration (Figure 3.11d, inset). (A potential 0.45 V is chosen because it is sufficiently high and close to the oxidation peak potential. The choice of this potential does not affect the relative performance among the NPs considered here.) Furthermore, the oxidation current obtained for the FeNi concave nanocubes at 0.45 V vs Ag/AgCl for 5 mM 4-AP is 10 times greater than that for the FeNi cuboctahedrons (Figure 3.13), again confirming the higher reactivity of the concave nanocubes.

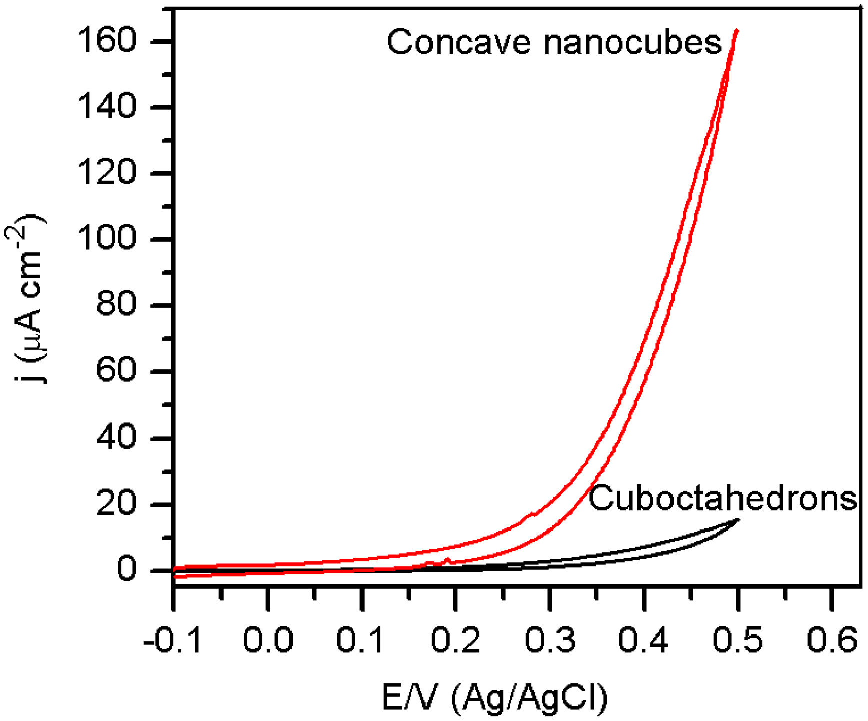

Figure 3.13 CV curves of FeNi concave nanocubes and cuboctahedrons in the presence of 5 mM 4-aminophenol in 10 mM PBS (pH 7).

Among the other 4-AP sensing studies by HPLC or spectrophotometry analysis, electrochemical detection has attracted a lot of recent attention because of its fast response and high sensitivity. Our result therefore shows an excellent performance for FeNi concave nanocubes with a sensitivity of 153 μA cm^{-2} mM^{-1} to 4-AP detection, in comparison with other detection systems including, e.g., graphene-chitosan or graphene-polyaniline composites with sensitivities of 33 and 177 μA cm^{-2} mM^{-1}, respectively.[129,131]

To increase the concavity of the nanocubes further and systematically, we introduce a controlled electroleaching process by applying cyclic voltammetry from –0.1 V to 0.5 V (vs Ag/AgCl) in a 10 mB PBS solution with pH = 3. By controlling the number of CV scans, we could increase the concavity and eventually hollow out the interior of the nanocubes, producing concave nanocages. Figure 3.14 show the SEM images of the concave nanocages obtained after 1, 2 and 3 CV cycles. Material dissolution starts at the center of the concave face because it is expected to have the highest strain and therefore highest chemical potential.[132] Leaching continues to the edges until the center of the nanoparticle is completely hollowed out. In contrast, electroleaching on the cuboctahedrons results in the removal of the exterior surfaces, producing smaller cuboctahedrons with no sign of cage formation (Figure 3.15).

It should be noted that metallic nanocages have been traditionally prepared by first depositing thin shells of a metal on polymer or silica beads and then followed by removal of the beads by calcination or wet chemical etching, [133–135] or by galvanic replacement reaction between Ag nanostructures and a less reactive metal such as Au, Pt, or Pd compounds. [136–140] The present synthesis of nanocages is therefore simple and does not have previously reported problems, including difficulty in removing the colloidal templates, poorly defined composition [141,142] and unwanted coupling in dealloying.[36] We also perform the aforementioned reactivity test on these concave nanocages by measuring the oxidation current of 5 mM 4-AP in PBS (pH = 7) as a function of etching cycles. Remarkably, the concave nanocages obtained after the first CV cycle exhibit over 10-fold enhancement in the current density measured at 0.45 V relative to concave nanocubes and over 100-fold enhancement when compared to the cuboctahedrons.

Even after the second and third cycles, this enhancement in the current density for the concave nanocages remains to be significant, i.e. 5 and 2.4 times that for concave nanocubes, respectively (Figure 3.14d, inset). The remarkable enhancement found for the concave nanocages is due to addition of high (and higher) index planes in the cavities of the nanocages and higher active surface areas. The reduction in enhancement with repeated CV cycles is likely caused by desolation of higher index planes and reduction in the active surface areas. The respective sensitivity and limit of detection are estimated to be 376 $\mu A\ mM^{-1}\ cm^{-2}$and 0.3 μM for the nanocages after the first CV cycle, which confirms their high detection sensitivity compared to other sensors. [129–131]

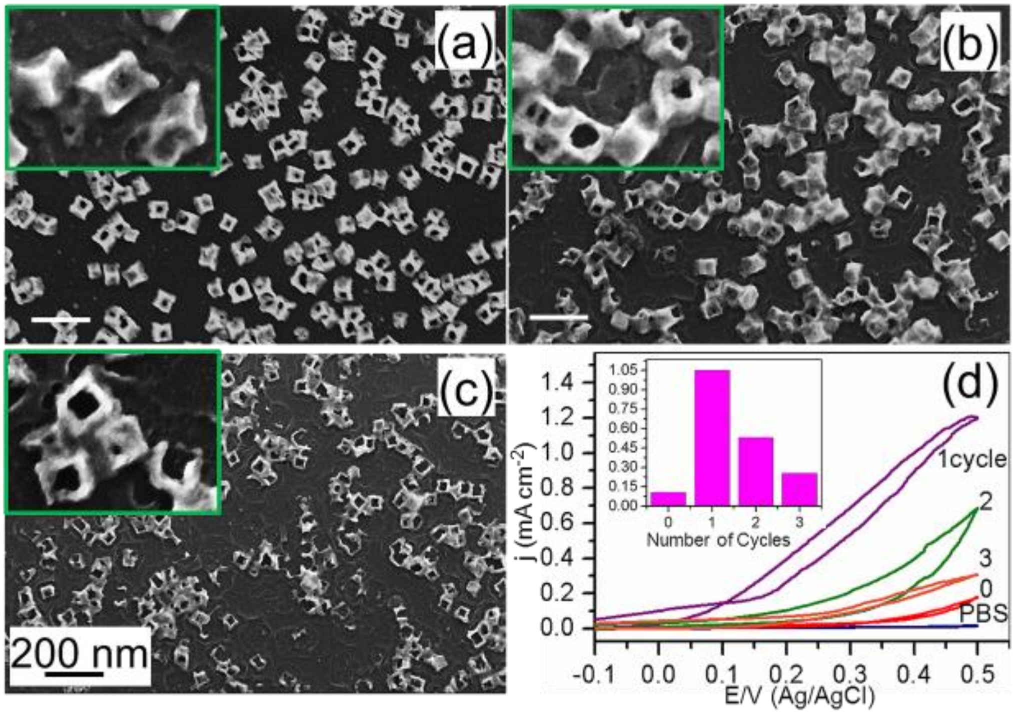

Figure 3.14 (a-c) SEM images of FeNi nanocages obtained by 1, 2, and 3 CV cycles in a 10 mM PBS solution with pH 3 and scan rate of 50 mV s^{-1}, (d) CV curves of concave nanocubes (with zero etching cycle) and the aforementioned concave nanocages in 5 mM 4-aminophenol in PBS (pH=7). Inset shows the corresponding current density measured at 0.45 V (vs Ag/AgCl) for concave nanocubes with different numbers of CV cycles.

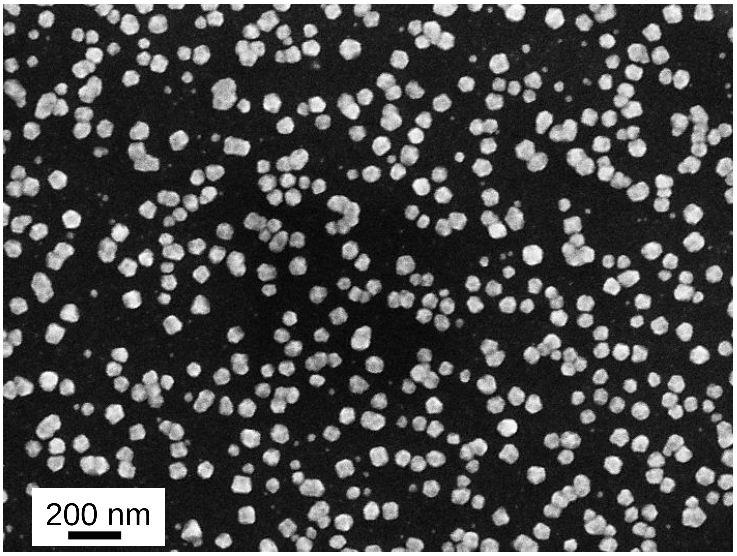

Figure 3.15 SEM images of FeNi cuboctahedron after etching in PBS with pH 3.

3.2.4 Summary

FeNi concave nanocubes and concave nanocages with high-index facets have been obtained by manipulating the kinetics of NP growth using a bimetallic system and by an electroleaching process. These FeNi concave nanocubes and nanocages exhibit remarkably high electro-activities (with over 10 and 100 fold enhancement, respectively) for the detection of 4-aminophenol, when compared with FeNi cuboctahedrons with convex surfaces, making them one of the most electro-active nanostructures reported to date. We therefore demonstrate for the first time that the present electroleaching method is a novel approach to synthesize cage-like nanostructures. FeNi concave nanocages, with their hollow interiors and tunable cavity size, can be used not only as an exceptional sensor in a mild environment close to neutral pH but also for encapsulation and chemical trapping. Since etching is driven by the high activity of the high-index planes located at the cavity, the present method of producing nanocages is therefore material independent and can be extended to any concave nanostructures.

3.3 Shape dependent magnetic properties of FeNi NPs[***]

3.3.1 Introduction

Studying shape-dependent magnetic properties of nanoparticles (NPs) offers rich insights to the fundamentals of magnetism in the nanoscale regime. As an important benchmark bimetallic magnetic system, the FeNi alloy system has been the subject of several theoretical and experimental investigations. This system is particularly intriguing because FeNi alloys such as Invar, Elinvar, and Permalloy exhibit notably different properties depending on their compositions. These alloys are not just interesting to basic research, but they also provide important practical applications. The phase diagram of FeNi alloy exhibits three distinct regions (bcc, fcc, and bcc + fcc), which also make them a fascinating bimetallic material system for experimental and theoretical studies from the crystallography perspective. At room temperature, coexistence of the bcc and fcc phases are observed when the Ni content is between 5% and 72%,[143] the range of which appears to depend on the method of preparation. For instance, the two-phase coexistence is found to occur at 15-34% Ni for alloys obtained by ball milling,[144] while thermal evaporation[145] and sputtering[146] produce alloys with a narrower %Ni range. Interestingly, this range is found to be wider when the size of the alloy is in the nanoscale regime.[85,118,147]

Magnetic properties of FeNi alloys as a function of composition has been studied over the entire range in both bulk and nano alloys.[85,118,144–151] In most of the studies reported to date, the FeNi alloy was found to exhibit a single-crystalline phase for each composition, i.e. either bcc or fcc. In the few studies[144–146,149,151] when the alloy was obtained in the mixed-phase region, the percentage of each phase was not reported, which suggests that its importance has likely not been realized. For both bulk and nanosize, magnetic properties for FeNi alloys with a specific composition but a different combination of bcc and fcc phases have yet to be reported. In practice, when two phases coexist, the relative amount/percentage so obtained appears also to depend on the preparation method. Indeed, there is an acute need for studies on the role of different two-phase combination in their magnetic properties. These studies are obviously very challenging to theory and experiment, because it has not been possible to make alloys with the

---

[***] This section is made from one of my publications: N. Moghimi, F. R. Rahsepar, S. Srivastava, N. Heinig, K. T. Leung, J. Mater. Chem. C, 2014, 2, 6370-6375. Copyright (2014) by the Royal Society of Chemistry.

same composition but with different two-phase combinations using a single method until now. By taking advantage of the unique nanoscale properties, we synthesize here $Fe_{63}Ni_{37}$ alloy NPs with two distinct shapes (but the same composition), for which the combination of fcc and bcc phases in the mixed-phase region are different. This shape-dependent effect potentially provides a new control to the properties of an alloy with a specific composition. The in-situ oxide nano-shell that covers the surface of NPs[118] will protect them against oxidation. We also provide the first investigation of the role of two-phase combinations in governing the magnetic properties in both bulk and nanoalloys using large-scale Density Function Theory (DFT) calculations.

Another important point to note here is that although there a few studies on the shape-dependent magnetic properties of pure oxide nanoparticles of single metals (e.g. magnetite, ferrites) have been reported,[152,153] no investigation on shape-dependent magnetic properties of bimetallic materials, including FeNi alloys or other transition metal combinations have appeared due to the challenges in the synthesis of bimetallic NPs with different shapes due to their inherent reactivities and easy oxidation. This work therefore provides the first experimental study of the effect of particle shape on the magnetic properties of FeNi alloy NPs.

3.3.2 Materials and Methods

Concave cube (CC) and cuboctahedron (COh) NPs were prepared by co-electrodeposition of Fe and Ni on a H-terminated Si(100) substrate in a three-electrode cell by potentiostatic amperometry at −1.4 V vs. Ag/AgCl. A silicon chip (15×2.5 mm^2, 0.4 mm thick), precut from a Si(100) wafer (p-type, B-doped, with a resistivity of 0.01-0.02 Ω-cm), was used as the working electrode, after it has been cleaned by using the RCA method[83] and further H-terminated by dipping in an aqueous HF (2%) solution. A standard Ag/AgCl electrode was used as the reference electrode while a Pt wire was used as the counter electrode. For CC NPs, we used an electrolyte solution consisted of 5 mM $FeCl_2$ and 5 mM $NiCl_2$ in 200 mM H_3BO_3 (used as the supporting electrolyte) and carried out the electrodeposition at room temperature. For COh NPs, electrodeposition was performed at 4 °C in a solution of 2.5 mM $FeCl_2$ and 1.25 mM $NiCl_2$ in 100 mM H_3BO_3 and 50 mM $NaClO_4$ (the latter two were used as the supporting electrolytes).

3.3.3 Results and Discussion

Electrodeposition was carried out for 20 s and 30 s to obtain, respectively, the CC and COh NPs (with average sizes of 75 and 70 nm, respectively) shown in Figure 3.16. The indentation (and the concavity) in the CC NPs indicates that the surfaces of the NPs are made up of high-index planes discussed in more detail elsewhere.[154] The corresponding alloy composition for both CC and COh NPs, as determined by Energy-Dispersive X-ray (EDX) analysis (to ±1 % accuracy), is found to be Fe$_{63}$Ni$_{37}$, which is confirmed by lattice parameter measurements using x-ray Diffraction (XRD).[155] Glancing-incidence XRD patterns of both CC NPs and COh NPs shown in Figure 3.16c indicate alloy formation with mixed fcc and bcc phases. The respective phase percentages are obtained by peak-fitting the most intense fcc(111) and bcc(110) features, after appropriate normalization of the two patterns to the fitted areas of the respective bcc(110) features. The respective amounts of fcc and bcc phases are found to be 37% and 63% for CC NPs and 48% and 52% for COh NPs (Table 3.2). It should be noted that the average size in Table 3.2 corresponds to the average diameter for spherical NPs or to the average side length for cubic NPs obtained by image processing software. The grain size corresponds to the size of a crystallite (or grain) as estimated from the full width at half maximum of the most intense XRD peak by using the Scherrer equation. Within the accuracy of our measurements, the lattice constants for the fcc and bcc phases are essentially the same for both shapes (2.862 ± 6 Å for bcc for both CC and COh NPs, and 3.578 Å and 3.589 ± 8 Å for fcc for CC and COh NPs, respectively).

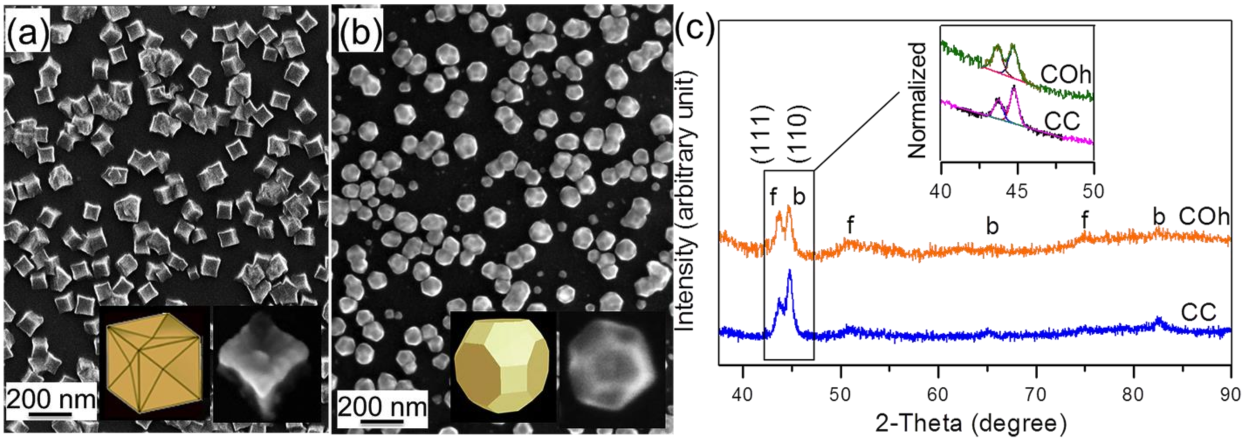

Figure 3.16 SEM images of (a) concave cube (CC), and (b) cuboctahedron (COh) nanoparticles (NPs), with their corresponding higher magnification images and schematic diagrams shown in insets, and (c) glancing-incidence XRD patterns for CC and COh NPs. The peaks for the fcc and bcc phases are marked by “f” and “b”, respectively, with the inset depicting the most intense peaks for CC and COh NPs normalized to their respective bcc(110) peaks.

Table 3.2 Physical parameters of concave cube (CC) and cuboctahedron (COh) nanoparticles with the same composition of $Fe_{63}Ni_{37}$.

$Fe_{63}Ni_{37}$ Shape	Average Size (nm)	Grain Size (nm)	Lattice Constant (Å)	bcc (%)	fcc (%)	Ms (emu/g)	Coercivity (Oe)
CC	75 ± 1	35 ± 1	fcc: 3.578 ± 8 bcc: 2.862 ± 6	63	37	85	100
COh	70 ± 1	22 ± 1	fcc: 3.589 ± 8 bcc: 2.862 ± 6	52	48	40	188

To investigate the local magnetic moments of the CC and COh NPs, we employ high-resolution magnetic force microscopy (MFM), using probe tips with low moments (< 400 Oe) to minimize the perturbation of the sample by the magnetic field from the tip. Figure 3.17 shows the topographic and magnetic force gradient images of the as-prepared CC and COh NPs (i.e. without pre-magnetization before the experiments). Evidently, CC NPs exhibit alternating bright and dark contrast among adjacent NPs, while COh NPs show dark contrasts for most of the neighboring particles. This suggests a lower coercivity for a CC NP as its moment could flip more easily than a COh NP. It is important to emphasize that the observed difference in local magnetic properties is due to differences in the shape and in the relative amounts of fcc and bcc components and not to the relative composition of Fe and Ni as the latter is the same ($Fe_{63}Ni_{37}$) for both CC and COh NPs.

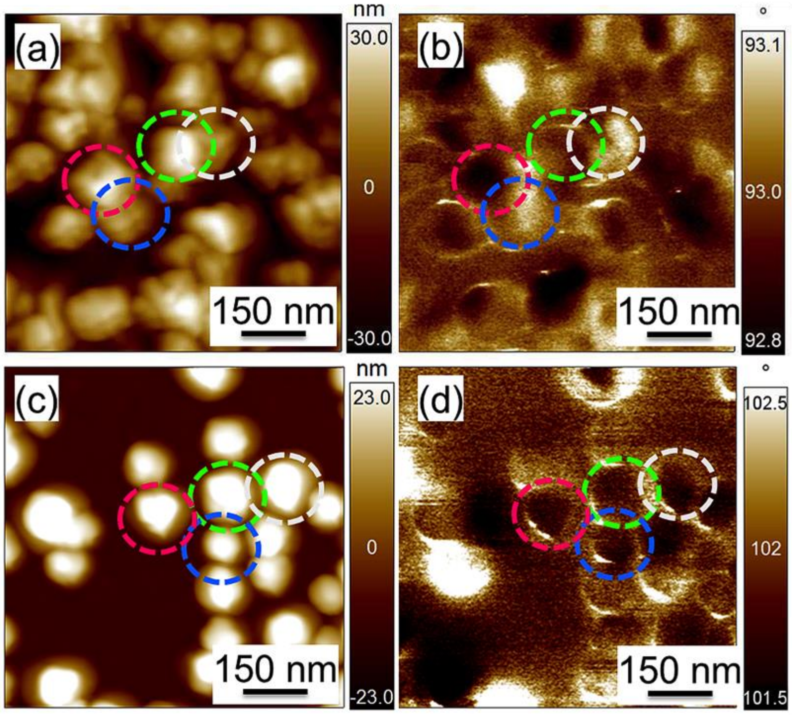

Figure 3.17 Topographic (left) and magnetic force images (right) of (a), (b) concave cubic (CC) and (c), (d) cuboctahedron (COh) $Fe_{63}Ni_{37}$ nanoparticles collected at room temperature.

In Figure 3.18a, we compare the corresponding hysteresis loops for the $Fe_{63}Ni_{37}$ CC and COh NPs. A notably higher maximum magnetization at 0.5 T is found for the CC NPs (85 emu/g) than the magnetic saturation for COh NPs (40 emu/g), while the coercivity for the CC NPs (100 Oe) is smaller than that for the COh NPs (188 Oe) (Table 3.2), as expected from our MFM results. From Figure 3.18a, it is clear that the magnetization of the CC sample is not saturating at the maximum applied field (0.5 T) at 300 K. This residual amount of unsaturation and a well-defined coercivity suggest the presence of a mixed phase of both ferromagnetism and superparamagnetism in the NPs. The maximum magnetization value for CC NPs is smaller than that reported for bulk $Fe_{63}Ni_{37}$ alloy[148–150,156] but is comparable to those found for FeNi alloy NPs reported earlier.[55,80] The M_S value for COh NPs observed here is therefore lower than the FeNi NPs (with the same composition).[55,80] In order to compare with the earlier work and with our own VASP calculations (discussed below), we estimate the moment per atom, μ, using the equation: $\mu = (M_{VSM} \times W) / (\mu B \times N_A \times m)$, where M_{VSM} is the saturated magnetic moment or maximum magnetic moment obtained from VSM measurement, W is the molecular weight, μB is Bohr magneton, N_A is Avogadro number, and m is the mass of the sample. We obtain μ to be 0.95 μB/atom for CC and 0.40 μB/atom for COh NPs.

The hysteresis loop of the CC sample is characterized by a relatively large value for the ratio of the magnetic remanence (Mr) to M_{VSM} (0.52) and a nearly steep reversal of magnetization while that of the COh sample is characterized by a small Mr/M_{VSM} value (0.15) and a gradual change of magnetization to saturation. The large Mr/M_{VSM} value for CC NPs indicates that the particles consist of randomly oriented equiaxial grains with cubic magnetocrystalline anisotropy.[157] On the other hand, the smaller Mr/M_{VSM} value (less than 0.5) found for the COh NPs indicates that the grains inside the particles have magnetostatic interactions.[157] The larger Mr/M_{VSM} value for CC NPs compared to COh NPs is related to the increasing shape/magnetocrystalline anisotropy of the synthesized NPs due to a larger number of atoms with more missing coordination atoms. This difference in the remanence and shape of the MH curves, which shows a different magnetic behaviour, is due to differences in the shape and in the relative amounts of fcc and bcc components, as also illustrated in their MFM results.

Figure 3.18b shows the temperature dependence of the magnetization at an applied field of 100 Oe for the CC and COh NPs after undergoing zero-field-cooled (ZFC) and field-cooled (FC) processes between 5 K and 325 K. The COh NPs signal is scaled up 20 times for better illustration. An irreversible magnetic behavior, indicative of a large thermal irreversibility, is observed for both CC and COh NPs in the entire temperature range. For CC NPs, the ZFC magnetization increases with increasing temperature rapidly in the 5-30 K range and more slowly in the 30–200 K range and then decreases by a small amount upon increasing the temperature to 325 K. The relatively sharp increase of ZFC magnetization found in 5-30 K could be due to some small grains inside the NPs with the blocking temperature falling in this temperature range.[158] On the other hand, increasing the temperature for COh NPs results in increasing ZFC magnetization over the entire temperature range (5-325 K) with the rapid change in the 5-30 K range. As no obvious maximum is observed in the ZFC magnetization from Figure 3.18b, the blocking temperature should be above 325 K in a field of 100 Oe. The decreasing tendency of ZFC curve for CC NPs up to 325 K can be due to the presence of superparamagnetism and ferromagnetism phases in the NPs as has been observed in the magnetization curve (Figure 3.18a). Since no obvious peak in the ZFC magnetization curves of COh NPs is observed, these NPs exhibit typical ferromagnetic behavior without any blocking temperature below 300 K. To confirm this result and to obtain some qualitative information about the magnetic behavior of these NPs, we show the temperature derivative curves of the differences between FC and ZFC magnetizations for the CC and COh NPs (Figure 3.18c). The trend for this derivative curve is the same as that for the temperature derivative of the remanent magnetization.[159] The peak observed at 17 K for both CC and COh NPs represents a low-temperature, frozen, disordered magnetic state. The presence of this magnetic state therefore confirms ferromagnetic behavior for both CC and COh NPs and is consistent with that found in other non-relaxing (quasi-static) ferromagnetic materials (including Fe/Fe oxide and Ni/Ni oxide NPs) reported elsewhere.[159,160]

To account for the notable differences in M_S and coercivity of CC and COh NPs, we consider three plausible contributing factors: (1) particle or grain size, (2) surface anisotropy in different shapes, and (3) ratio of the amounts of bcc to fcc phases. Earlier studies have shown that the saturation magnetization is very sensitive to the size of the NPs[161,162] or the grain size in thin films, with larger particles or grains exhibiting higher saturation magnetization.[163,164] We therefore expect that the CC NPs with a slightly larger particle size and larger grain size should show larger saturation magnetization than COh NPs. Furthermore, missing coordinating atoms around surface metal cations could lead to surface magnetic disorder and pinning. The surface anisotropy becomes lower whenever the coordination symmetry of the surface metal cations is more similar to that of the metal cations in the core of the NP.[165] For ferrite NPs, the surface anisotropy has been reported to be much smaller in cubic nanocrystals than that in spheres. This is likely because the curved topology of spherical nanocrystals could lead to more surface metal cations with less symmetric coordination and to more missing coordinating atoms than the flat surfaces of cubic nanocrystals.[152] Since these missing coordinating atoms and the surface anisotropy can change the coercivity,[166–168] the coercivity should follow the ordering: cube < octahedron cube < concave cube < sphere. Although both concave cube and octahedron may have the same number of facets, the number of atoms is higher on the surface of the concave cube because of its higher index facets with more missing coordinating atoms. However, the saturation magnetization and remanent magnetization are independent of the surface anisotropy, as previously reported for $CoFe_2O_4$ and γ–Fe_2O_3 NPs with different shapes.[152,169] Furthermore, in the size range of our NPs (i.e. 70-75 nm), the surface atoms only represent less than 10% of the total number of atoms. Surface anisotropy therefore cannot account for the observed difference in M_S for CC and COh NPs.

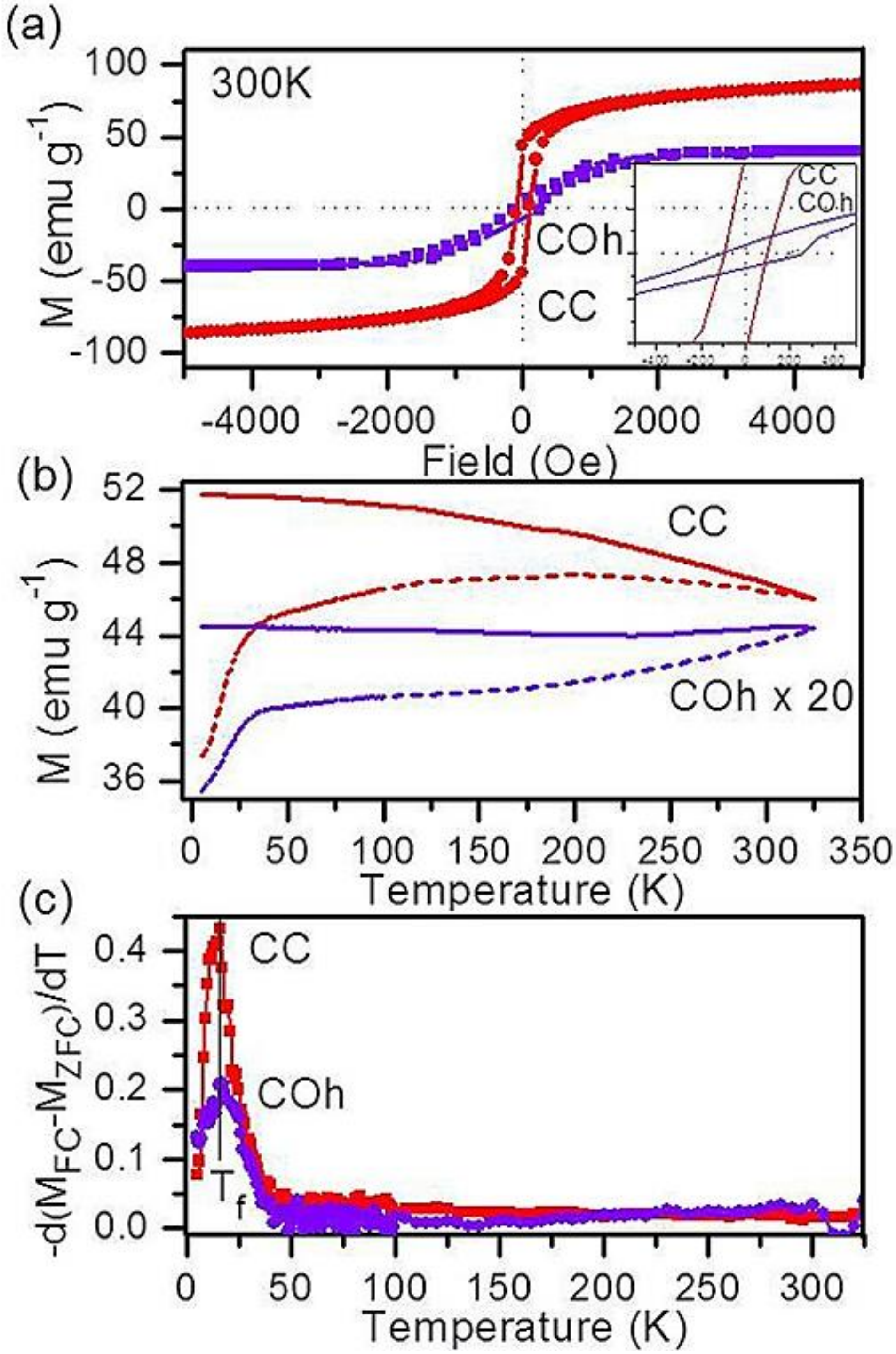

Figure 3.18 (a) Hysteresis loops obtained at room temperature for both concave cube (CC) and cuboctahedron (COh) nanoparticles, with an expanded view over the –500 to 500 Oe range shown in inset, (b) zero-field cooled (ZFC, dashed lines) and field-cooled (FC, solid lines) magnetization (M) curves in the presence of 100 Oe external field, (c) temperature derivative curves of the difference between FC and ZFC moments as functions of temperature.

To evaluate the role of the ratio of the amounts of bcc to fcc phases on the magnetic behavior of NPs, we perform Density Function Theory (DFT) calculation[170] using the Vienna Ab-initio Simulation Package (VASP, Version 5.2)[171] with the MedeA platform (Materials Design). According to the lattice parameters, the fcc phase has a chemical composition close to that of the alloy itself. The bcc phase must also have nearly the same composition as the alloy according to the earlier X-ray lattice parameter measurements on alloys with similar chemical compositions of bcc and fcc phases. [172,173] We therefore construct bcc lattices with super-cells of 256 atoms for ordered structure and of 108 atoms for disordered structure, all with the closest composition to $Fe_{63}Ni_{37}$ composition (where X and Y in the Fe_XNi_Y notation correspond to atom % and not the actual numbers of atoms of Fe and Ni, respectively). For fcc lattices, super-cells of 128 atoms for both ordered and disordered structures are used. The ordered structures are obtained by repeating smaller unit cells to construct the super-cell. For example, the super-cell of 256 atoms for bcc is made up of Fe5Ni3 unit cells (where A and B in the FeANiB notation correspond to the numbers of Fe and Ni atoms, respectively, in the small cell), while the super-cell of 108 atoms for fcc is made up of Fe11Ni7 unit cells. For disordered structures, the atoms are randomly placed in the structure, and the respective super-cell does not contain any repeating structure inside and therefore no smaller unit cells. For example, the super-cell of 108 atoms for the disordered fcc structure is made up of Fe67Ni41. Furthermore, we have also tested several other different initial disordered arrangements and obtained their optimized disordered structures, the cohesive energies of which are found to be similar. This result is also consistent with our observation using super-cells containing the same number of atoms (e.g. 128) but in different volumes for the disordered structures. Our objective here is to use the results obtained for these single-phase crystalline super-cells (i.e. bcc or fcc) to deduce the properties of the NPs with two-phase combinations. We employ the projector-augmented wave (PAW) method and the exchange correlation with the generalized gradient approximation by the Perdew, Burke, and Ernzerhof (PBE-GGA)[174] for structure optimization and magnetic moment calculation (assuming the periodic boundary conditions). The wavefunctions are expanded in a plane wave basis with energy cutoffs of 267.88 eV for Fe and of 269.53 eV for Ni. The surface Brillouin zone was sampled at the Γ point with k-point spacing of 0.5 $Å^{-1}$. The geometries have been optimized by relaxing all atoms until the forces are less than 20 meV/Å, with the energy convergence of the self-consistent-field set to 1.0×10^{-3} eV and Methfessel-Paxton smearing set to 0.2 eV, while keeping the cell constants for the crystal fixed. Since structure optimization by relaxing the lattice parameters has been found to change the original crystal structure (phase and symmetry), we have therefore not included lattice parameter relaxation in the optimization. Given that we constructed super-cells using the pre-defined crystal structures in VASP, the appropriate periodic boundary conditions have been used during structure optimization. The spin-orbit combined magnetic and Vosko-Wilk-Nusair spin-interpolation methods[175] have been employed for the total moment calculations.

The DFT calculations have produced optimized atomic arrangements in the bcc and fcc unit cells with ordered and disordered structures. According to the cohesive energies, the most stable configurations are (Fe11Ni7)×6 and (Fe5Ni3)×16 for the fcc and bcc ordered structures, respectively, and Fe67Ni41 and Fe79Ni49 for the respective fcc and bcc disordered structures. In Figure 3.19a, we summarize the calculated cohesive energies of these super-cells along with their optimized structures, which indicate their relative ease of formation. From the total moments calculated for the optimized super-cell structures, we estimate the moment per atom for each structure. As an independent check of the VASP accuracy, we obtain, in separate calculations, the magnetic moments of a pristine Fe and a pristine Ni super-cells and compare these values [2.2 μB/atom for Fe and 0.6 μB/atom for Ni] with the respective experimental moments for these elements reported in the literature.[148,151] Excellent agreement is found for both Fe and Ni, confirming the high accuracy of our VASP calculations. We also compare the VASP results for the single-phase fcc and bcc $Fe_{63}Ni_{37}$ super-cells in ordered and disordered structures with the experimental values obtained for bulk alloys reported in the literature.[156,176,177] Figure 3.19b shows the experimental M_S values obtained for fcc and bcc alloys in the region of Invar alloy (i.e. 30-38 Ni%) reported in the literature and the calculated magnetic moments for ordered and disordered bcc and fcc unit cells by VASP. In Figure 3.19b, the upper horizontal line and lower horizontal line mark the moments for ordered bcc and disordered fcc, respectively, which correspond to the more stable configurations with less positive cohesive energies for the bcc and fcc lattices (shown in Figure 3.19a). Evidently, the VASP results are very close to the experimental literature values. It should, however, be noted that the amounts of fcc and bcc phases are not indicated in the previous reports, and as explained below this information is important because it could account for the observed discrepancy. By combining different percentages of bcc and fcc unit cells, we could obtain the total magnetic moment of the two-phase structure over the entire range from pure bcc phase to pure fcc phase. Figure 3.19c shows that the calculated total magnetic moment could vary from 1.87 μB/atom for pure bcc phase to 1.15 μB/atom for pure fcc phase. This therefore confirms that the total magnetic moments obtained for alloys with two phases strongly depend on their phase combination. This is the first report on the role of phase combination on the magnetic moment of the alloy, which could be used to explain the differences in M_S values found for FeNi alloys with the same composition reported in the literature. For our case with the bcc-to-fcc combinations of 63% to 37% for CC NPs and of 52% to 48% for COh NPs, this difference (0.1 μB/atom, Figure 3.19c) is found to be quite significant. It should be noted this difference is also expected to be larger in the nano-regime because of the larger defect sites, boundary effects and surface effects.

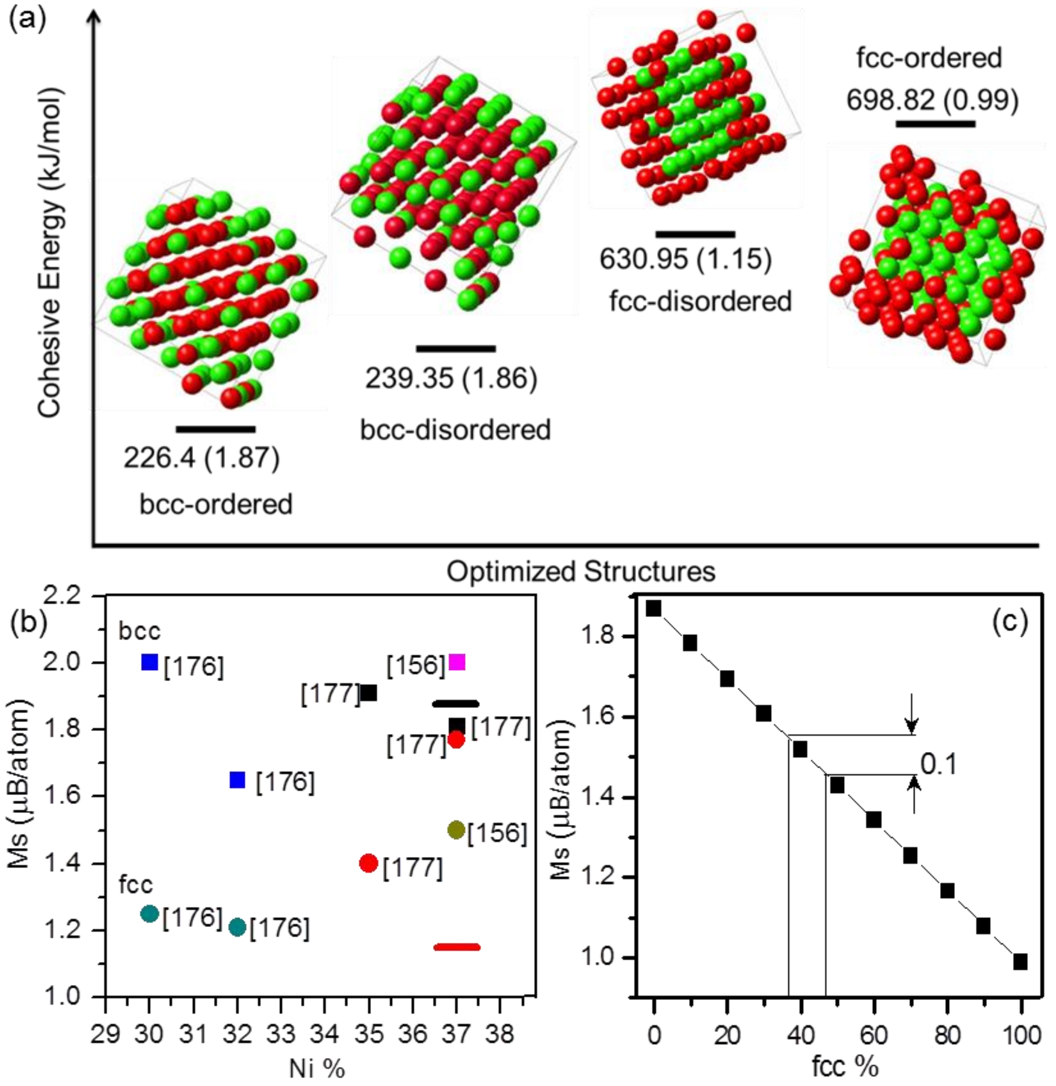

Figure 3.19 (a) Optimized ordered and disordered structures and the corresponding cohesive energies (in unit of kJ/mol, not drawn to scale) and total moment (in parentheses, and in unit of μB/atom) for the most stable $Fe_{63}Ni_{37}$ super cells, (b) comparison of experimental magnetic saturation M_S obtained for bcc (squares) and fcc unit cells (circles) for bulk alloys [Refs. 156, 176, 177] with the VASP results (upper horizontal line for bcc, lower horizontal line for fcc). (c) variation of total moment as a function of fcc unit cells in different combination of bcc to fcc phases.

3.3.4 Summary

In conclusion, the magnetic properties of well-defined concave cubic and cuboctahedron nanoparticles with the same composition but different shape and two-phase combination have been investigated by detailed magnetization experiments and VASP calculations. We show that these NPs with the specific shapes and two-phase combinations but the same composition could be easily produced on Si(100) by electrochemical deposition using appropriate electrolytes. The saturation magnetization and coercivity are found to be different for CC and COh NPs that has been correlated to the surface anisotropy and different two-phase combinations of bcc and fcc phases inside the nanoparticles. A large-scale VASP computational study of the role of different two-phase combinations at a particular composition of FeNi alloys has also been carried out. These calculations offer new insights into magnetic properties of both bulk and nanoalloys consisting of two crystalline phases and can be used to explain the observed differences. In addition to the particle shape, the two-phase combination could therefore provide an important parameter and must be considered in further controlling the magnetic properties of bimetallic alloy nanoparticles.

Chapter 4

FePt Alloy Nanoparticles for Biosensing: Enhancement of Vitamin C Sensor Performance and Selectivity by Nanoalloying[†††]

4.1 Introduction

L-ascorbic acid (AA) or vitamin C is a powerful antioxidant present in food and beverages and often used as a chemical marker for evaluating food deterioration, product quality and freshness.[178,179] Furthermore, AA can help to promote healthy cell development, iron absorption and normal tissue growth, which play significant roles in proper functioning of human metabolism, central nervous and renal systems.[180,181] However, an overdose of AA can cause chemical conversion to oxalate, which contributes to a rise of the oxalate level in urine and results in the development of kidney stones in the long term.[182,183] Precise quantification of AA is therefore of great importance to the food industry and human health. Several methods, including fluorometry and flow injection analysis,[184–187] spectrophotometry and chromatography,[188–190] have been employed to detect and quantify AA in food, biological fluids and pharmaceutical products. However, some of these methods are time-consuming, costly, or in need of specially trained operators. The UV spectrophotometric methods suffer from the interference from almost all kinds of organic compounds due to their absorption in the UV region of interest. On the other hand, visible spectrophotometric methods based on the oxidation of AA with a chromogenic redox reagent are affected by simultaneous oxidation of other phenolic antioxidants.[191] Furthermore, some of the aforementioned methods are based on the reduction properties of AA and are also prone to interferences by other coexisting chemicals with similar reduction properties.[192] Among these methods, electrochemical techniques have attracted much attention because of their numerous advantages, including rapid response, low cost, high sensitivity, simplicity, easy-to-miniaturize instrumentation and compatibility with in-vivo detection.[182,192,193]

In the electrochemical methods, AA is oxidized on bare electrodes (e.g., Pt, Au, or C) and the extent of electro-oxidation can be characterized by measuring the anodic current at an

---

[†††] This section is made from one of my publications: N. Moghimi, K. T. Leung, Anal. Chem., 2013, 85 (12), pp 5974–5980. Copyright (2013) American Chemical Society.

appropriate oxidation potential. However, direct electro-oxidation of AA on bare electrodes is irreversible and usually requires a high overpotential, which could result in electrode fouling. Furthermore, electroactive species, such as dopamine, uric acid and glucose, are found to have oxidation potentials rather close to that of AA. As these species often coexist with AA, they introduce interference signals that cannot be easily separated.[193] To improve the selectivity of electrochemical sensors, it has been proposed that the oxidation potential of AA should be lowered by modifying the electrode with catalysts. Screening suitable catalysts with both high activity and selectivity is therefore not only of scientific significance, but also beneficial to the aforementioned practical applications. Because metallic nanoparticles (NPs), especially noble metal NPs, provide a high electrochemically active surface area, they are ideal catalysts for analytes that have sluggish redox processes.[194,195] They can also act as the active component for effectively accelerating the electron transfer between the electrode and the analyte, which leads to a rapid current response and a reduced overpotential for the electrochemical reactions.[196–198] For AA detection, only a few studies on using noble metal films or nanostructures have been reported, including electrodes modified by Au[199–201] or Pd[192,196,202] nanostructures to obtain a more rapid response and to increase selectivity by lowering the oxidation potential of AA. However, these methods have multiple steps, and most have low sensitivity and a short linear range of detection.

Of the noble metal catalysts, Pt NPs have been extensively used in the enhancement of electrochemical sensing of a variety of biomolecules,[203] including glucose,[204,205] DNA[206] and cholestrol.[207] Numerous efforts have been devoted to the optimization of the existing Pt NP catalysts and to the design of new lower-cost catalysts with minimal Pt content by incorporating other metal components.[66,208,209] To date, these studies have focused primarily on fuel-cell applications[208,210,211] and none on biosensing. Of the Pt NP catalysts used for fuel-cell applications, the best efficiency has been obtained with a Pt content above 60% while noticeably poorer performance is found with a Pt content below 25%. Here, we electrochemically deposit FePt alloy NPs of different Pt content directly on the surface of electrode and investigate the performance enhancement relative to Pt NPs. By keeping the Pt content near the optimal value found for catalyst applications (60-80%), we not only introduce synergistic properties due to the modification to the Pt electronic structures in this alloy NP system, but also reduce material cost by employing Fe as the second metal. Our results show significant improvements in the sensitivity, detection limit, and range of linear response, higher signal-to-noise performance in neutral pH operating environment, and greatly enhanced selectivity to interference species including dopamine, uric acid, citric acid, glucose and NaCl. This simple synthetic approach to producing bimetallic alloys can be extended to other binary metallic systems as new materials for biosensing.

4.2 Experimental Details

4.2.1 Materials

The chemicals (all analytical grade) for the electrodeposition experiments ($FeCl_2$, H_2PtCl_6, and H_3BO_3) and the sensing experiments (ascorbic acid, dopamine, uric acid, citric acid, glucose, and NaCl) were purchased from Sigma-Aldrich and used as received unless stated otherwise. The phosphate buffer saline solution (PBS, 0.1 M Na_2HPO_4-NaH_2PO_4-KCl, pH 7.2) was prepared from a PBS tablet (Sigma). One-side polished Si(100) wafers (p-type, B-doped, with a resistivity of 0.01-0.02 Ω-cm) were purchased from Siegert Wafer GmbH and used as substrates.

4.2.2 Apparatus

All electrochemical experiments were performed in a three-electrode cell workstation (CH Instruments 660A). The Si chips (15×2.5 mm^2, 0.4 mm thick, precut from the Si(100) wafer) were cleaned using the RCA method[83] H-terminated by dipping in an aqueous HF (2%) solution and used as the working electrode for both FePt deposition and sensor applications. The as-prepared electrode was dried and stored in a N_2 atmosphere at room temperature when not in use. A standard Ag/AgCl electrode and a Pt wire were used as the reference and counter electrodes, respectively.

The surface morphology of the NPs was characterized by a field-emission scanning electron microscope (Zeiss Ultra Plus). Crystal structures were determined by glancing-incidence X-ray diffraction (GIXRD) in a PANalytical X'Pert Pro MRD diffractometer with Cu-Kα (1.542 Å) radiation at an incidence angle of 0.5°. These data are correlated with the local nanostructures and elemental compositions determined by transmission electron microscope (Zeiss Libra 200MC TEM system) operating at 200 kV. Chemical-state compositions of the NPs were analyzed by X-ray photoelectron spectroscopy (XPS) in a Thermo-VG Scientific ESCALab

250 microprobe with a monochromatic Al Kα X-ray source (1486.6 eV), operated with a typical energy resolution of 0.4-0.5 full width at half-maximum.

4.2.3 Single-step electrode preparation of Pt and FePt NPs, and electrochemical sensing

FePt alloy NPs with different compositions were prepared by potentiostatic amperometry on a Si substrate in a deoxygenated electrolyte containing 1 mM H_2PtCl_4 and 200 mM boric acid and different concentrations of $FeCl_2$. In order to obtain a homogeneous, uniform NP deposit at a particular FePt alloy composition on the H-terminated Si(100) substrate, we varied the deposition potential from –0.8 to –1.6 V (vs Ag/AgCl). Between –0.8 and –1.0 V, the resulting NPs consisted only of Pt and no Fe. At –1.1 V and –1.2 V, NPs with the desired alloy composition were obtained with a uniform coverage. For potential more negative than –1.2 V, the coverage was found to be less uniform, and at –1.4 V a black precipitate began to appear in the solution. We have therefore chosen an applied potential of –1.1 V (vs Ag/AgCl) as the deposition potential for preparing the FePt alloy NPs.

For the purpose of comparison, Pt NPs and Fe NPs were prepared using the same conditions in the same electrolyte without $FeCl_2$ and $H_2PtCl_{6,}$ respectively. After the deposition, the samples were washed by filtered deionized water (18 MΩ cm) and stored in a N_2 atmosphere at room temperature until use. This method has the advantage of producing NPs with a uniform spatial distribution without agglomeration, which therefore provides the maximal exposed surface for electro-catalysis without any additional step. For electrochemical sensing using the as-prepared NP-coated electrode, cyclic voltammetry was carried out in quiescent solutions of bimolecular analyte in a PBS solution at a scan rate of 50 mV s^{-1}. Magnetic stirring was used throughout the amperometric measurements where sample injections were performed after stabilization of the baseline unless stated otherwise. The electrode was vigorously rinsed with deionized water after each measurement.

4.3 Results and Discussion

4.3.1 Characterization of FePt NPs

Three different sets of FePt alloy NPs are prepared by electrodeposition for 60 s in 1 mM H_2PtCl_4 and $FeCl_2$ with three different concentrations (1 mM, 5 mM and 10 mM).

The SEM images shown in Figure 4.1 reveal spherical NPs with average sizes of 97, 102, and 107 nm, respectively, while EDX analysis shows $Fe_{25}Pt_{75}$, $Fe_{30}Pt_{70}$, and $Fe_{35}Pt_{65}$ as their respective compositions. These FePt alloy NPs all appear to have a rough surface and consist of grains of a few nanometers in size. Changing the deposition time from 3 s to 60 s produces FePt NPs with average size from 10 to 100 nm, with the corresponding electrode surface coverage increasing from 5 % to 40 %. The GlXRD patterns for all three samples show typical fcc patterns of an FePt alloy without any observed features corresponding to segregated bcc Fe or fcc Pt. The GIXRD pattern for $Fe_{25}Pt_{75}$ NPs, shown in Figure 4.1, reveals small shifts in the peaks to a higher angle relative to Pt fcc. For the most intense (111) peak, the observed 0.5° shift indicates a 1.0 % contraction of the fcc lattice of the $Fe_{25}Pt_{75}$ alloy NPs (from 3.911 Å for Pt fcc lattice) due to the substitution of Pt atoms with Fe atoms in the cubic lattice. Similar shifts in the (111) peak by different amounts have also been observed for the $Fe_{30}Pt_{70}$ and $Fe_{35}Pt_{65}$ alloy NPs (Figure 4.1, inset), which indicates a respective lattice contraction of 1.2 % and 1.5 %. Using the widths of the respective (111) peak, we estimate the grain size to be 7 nm, 7 nm and 9 nm for $Fe_{25}Pt_{75}$, $Fe_{30}Pt_{70}$, and $Fe_{35}Pt_{65}$ NPs, respectively, by the Scherrer analysis. Figure 4.1 also shows the STEM image of a typical $Fe_{25}Pt_{75}$ NP and its corresponding Fe and Pt elemental maps obtained by EDX analysis. The uniform distributions of both Fe and Pt elements in the elemental maps of the NP show mixed alloy formation, with a self-organized Pt-enriched region on the surface as indicated by the linescans.

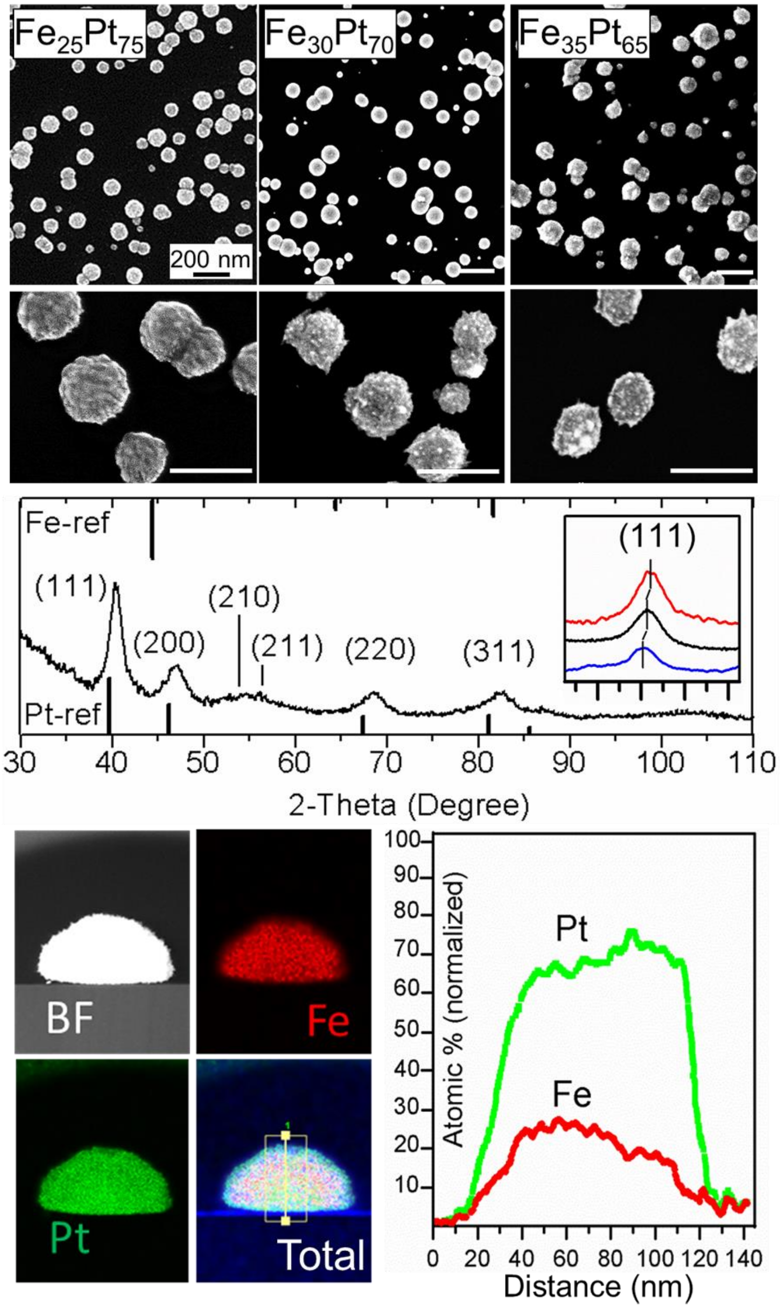

Figure 4.1 Top panel: SEM images of FePt alloy NPs with three different compositions, $Fe_{25}Pt_{75}$, $Fe_{30}Pt_{70}$, and $Fe_{35}Pt_{65}$, obtained from amperometry at –1.1 V vs Ag/AgCl for 60 s deposition (scale bars show 200 nm). Middle panel: Comparison of the GIXRD pattern of $Fe_{25}Pt_{75}$ alloy NPs with the reference patterns for Fe bcc (PDF2 01-085-1410) and Pt fcc (PDF2 004-0802), with the shift in the (111) peaks for $Fe_{25}Pt_{75}$, $Fe_{30}Pt_{70}$, and $Fe_{35}Pt_{65}$ NPs shown in the inset (bottom to the top). Bottom panel: Bright-field (BF) STEM image of a typical $Fe_{25}Pt_{75}$ NP and its corresponding Fe and Pt EDX elemental maps and linescans along the NP (from the surface through the NP).

4.3.2 Sensor Properties[‡‡‡]

To investigate the role of alloying in the electro-catalytic activities of FePt alloy NPs, we study the electro-oxidation of AA by cyclic voltammetry (CV) and potentiostatic amperometry. Figure 4.2a shows the CV curves acquired at a sweep rate of 50 mV s^{-1} in a solution of 10 mM PBS with and without 1 mM AA using a bare Si electrode and electrodes electrodeposited with pristine Fe NPs, pristine Pt NPs and $Fe_{30}Pt_{70}$ alloy NPs. Evidently, the bare Si electrode and Fe-NP electrode both do not exhibit any current response in the presence of AA. On the other hand, the Pt-NP electrode shows a discernibly stronger anodic response to the presence of AA than the Fe-NP electrode but a much weaker response when compared to the alloy-NP electrode. For the alloy-NP electrode, the anodic peak observed at +0.54 V is attributed to the electro-oxidation of AA. Figure 4.2b compares the CV curves obtained in the solution of 10 mM PBS and 1 mM AA for all electrodes including those of FePt NPs with different compositions. The highest anodic peak current density (at +0.54 V) is found for the $Fe_{30}Pt_{70}$-NP electrode, with the anodic response following the order: $Fe_{30}Pt_{70} > Fe_{25}Pt_{75} > Fe_{35}Pt_{65} > Pt > Fe$. Given that the $Fe_{30}Pt_{70}$-NP electrode provides the best electro-catalytic performance among the alloy and pristine NPs studied in the present work, all the subsequent tests are performed using this electrode.

[‡‡‡] In this chapter, we have used the American sign convention, i.e. the cathodic current is positive.

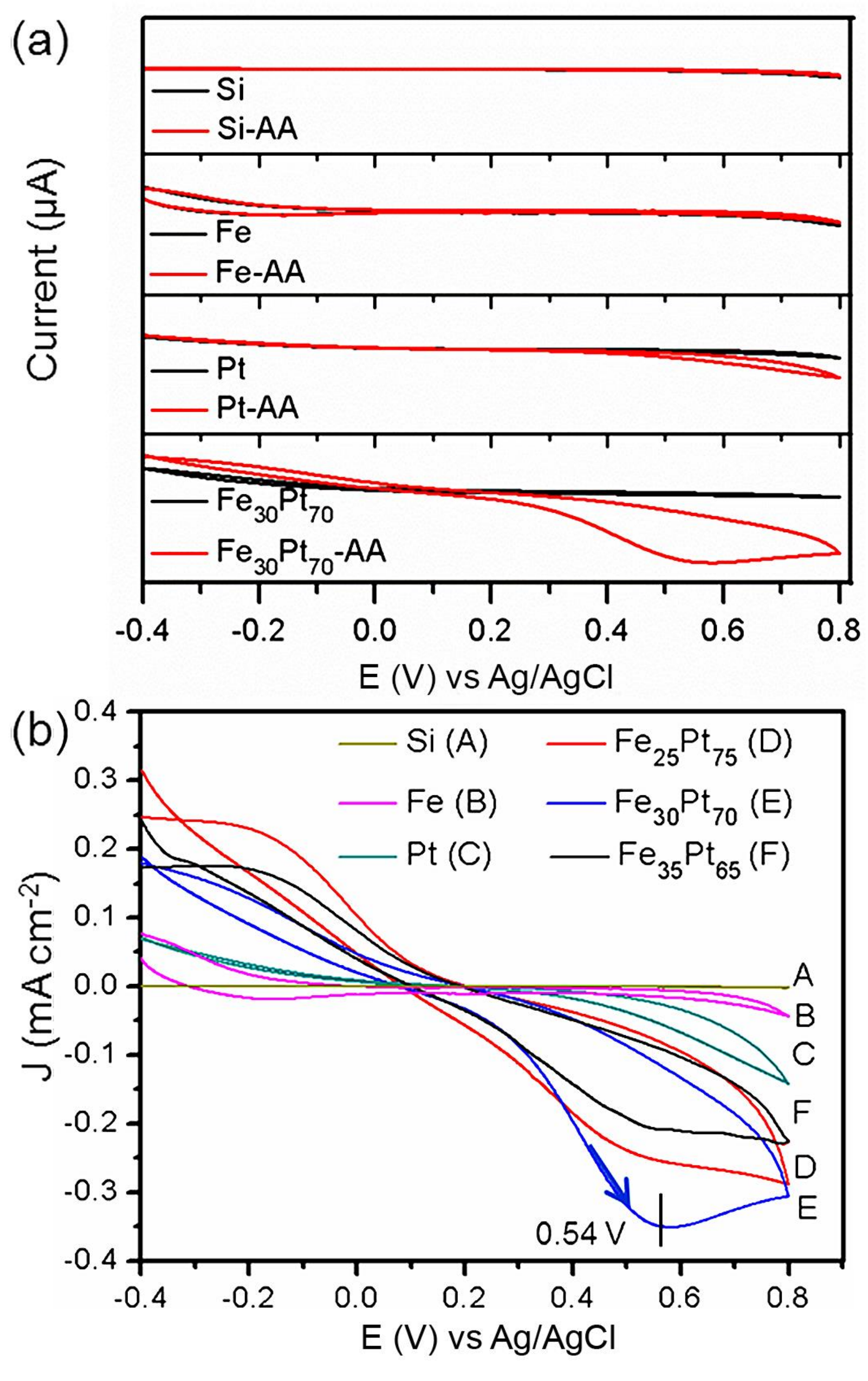

Figure 4.2 (a) Cyclic voltammograms of a bare Si electrode, and electrodes electrodeposited with pristine Fe nanoparticles (NPs), pristine Pt NPs and $Fe_{30}Pt_{70}$ alloy NPs, all in a 10 mM PBS solution without and with 1 mM ascorbic acid (AA). (b) Cyclic voltammograms of Si electrode, electrodes with Fe NPs, Pt NPs, and $Fe_{25}Pt_{75}$, $Fe_{30}Pt_{70}$, and $Fe_{35}Pt_{65}$ alloy NPs in a 10 mM PBS solution with 1 mM ascorbic acid (AA). Scan rate is 50 mVs^{-1}.

In order to investigate the variation of the anodic peak current (measured at +0.54 V) with increasing AA concentration, we perform CV measurements of the $Fe_{30}Pt_{70}$-NP electrode in PBS solutions with increasing AA concentrations at a fixed sweep rate (50 mV s^{-1}) and the result is shown in Figure 4.3a. The anodic peak current density, J, is found to depend linearly on the AA concentration, C, over the range of 0.01 to 1 mM with a regression relation of J (mA cm^{-2}) = 0.33766 × C (mM) + 0.04538 (with a correlation coefficient of 0.9974). Furthermore, potentiostatic amperometry of the $Fe_{30}Pt_{70}$-NP electrode in PBS solutions is conducted at low AA concentrations (0.01-0.3 mM). Figure 4.3b shows the amperometry response of the $Fe_{30}Pt_{70}$-NP electrode at +0.5 V to successive additions of five aliquots of 5, 10 and 20 μL of 50 mM AA to a 10 mM PBS solution. After each injection, the solution is gently stirred for one minute before the current measurement, during which the solution is kept quiescent. Evidently, successive addition of AA aliquots results in stepwise increase of anodic current. As expected, we also obtain a good linear relationship between the current response and low AA concentration (Figure 4.3b, inset).

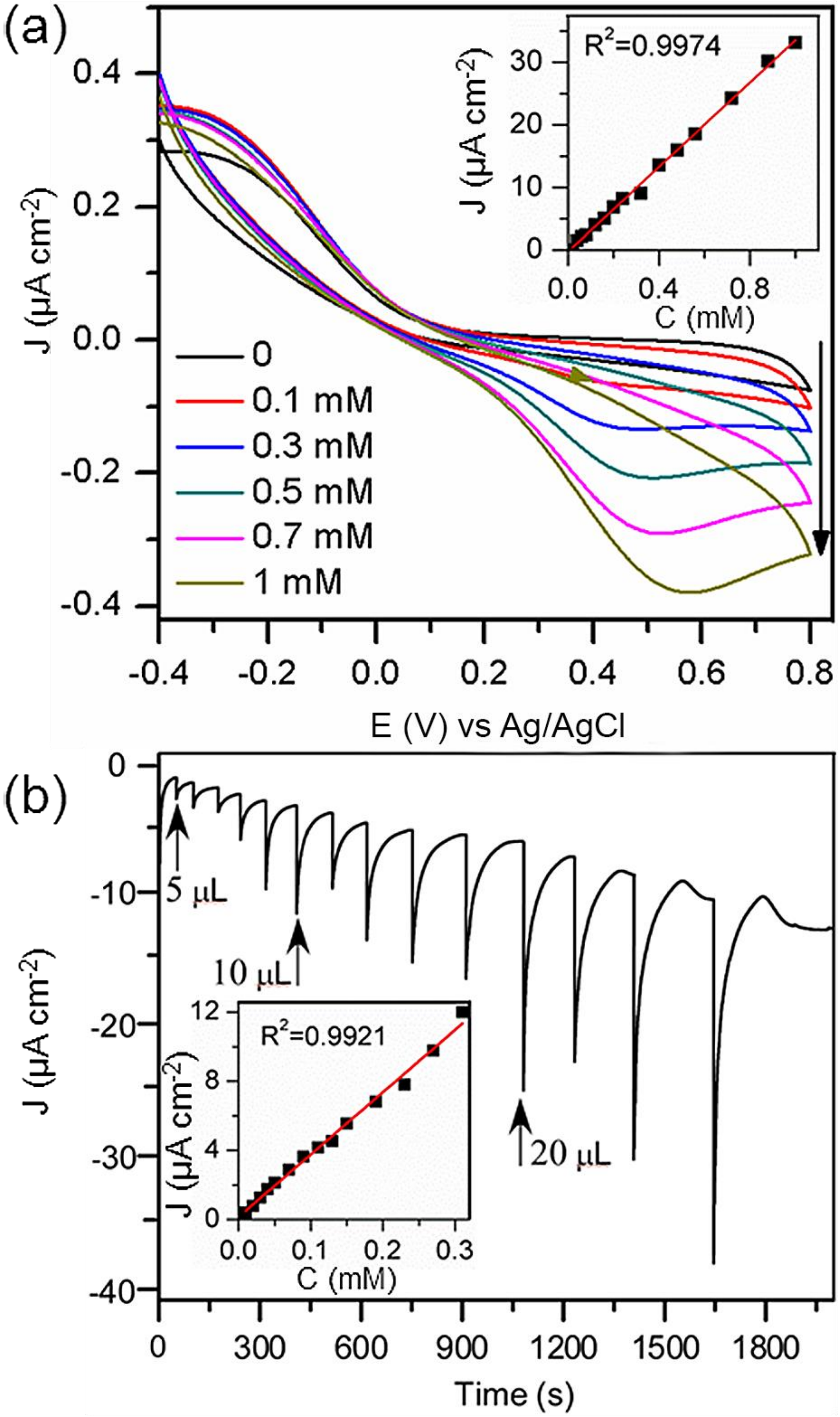

Figure 4.3 (a) Cyclic voltammetry of the $Fe_{30}Pt_{70}$ NP electrode (with a scan rate of 50 mV s^{-1}) in the absence and presence of different Vitamin C concentrations in a 10 mM PBS solution. (b) Corresponding amperometric response to successive addition of five aliquots of 5, 10 and 20 μL of a stock solution of 50 mM AA to a 10 mM PBS solution. The linear relationships between the peak current density at 0.5 V and the concentration over different ranges are shown in the respective insets.

4.3.3 Interference study

The coexistence of biomolecules such as dopamine, citric acid, uric acid and glucose introduces serious interferences to the electrochemical detection of AA, which hinders the practical application of the biosensor. In order to minimize the common interference signals, in the present work we use metallic nanostructures as the catalysts in order to reduce the over-potential of AA oxidation. The current responses of $Fe_{30}Pt_{70}$ NPs to successive additions of AA are investigated using different applied potentials from 0 to 0.6 V (not shown). The best potential that gives the largest current response is found to be +0.5 V (vs Ag/AgCl). However, at this potential the common electro-active species such as dopamine and citric acid also exhibit sizable current signals similar to that for AA, indicating strong interferences from these biomolecules toward AA determination. At 30% of the value found at +0.5 V, a good current response is also obtained for 0 V (vs Ag/AgCl). Amperometric responses of $Fe_{30}Pt_{70}$ NPs recorded at 0 V to successive additions of equal aliquots of AA and other biomolecules, including dopamine (DA), citric acid (CA), uric acid (UA), glucose (G), and NaCl, all with the same concentration of 20 μM, are compared with those of Pt NPs in Figure 4.4a. The solution is stirred after each aliquot injection to obtain a homogeneous concentration. Both $Fe_{30}Pt_{0}$ NPs and Pt NPs show a notable current response to the addition of AA, with the response for $Fe_{30}Pt_{0}$ NPs being three times that for Pt NPs. Figure 4.4b summarizes the relative responses of both $Fe_{30}Pt_{0}$ NPs and Pt NPs to the additions of AA, DA, CA, UA, G, and NaCl, all normalized to the respective AA current responses. Evidently, all five species introduce current responses comparable to that AA for Pt NPs, with the ordering: DA > CA > UA > NaCl > G. In contrast, UA, G and NaCl do not show any response for $Fe_{30}Pt_{70}$ NPs, while DA and CA only exhibit relatively weak signals (less than 15% that of AA signal). The present result therefore shows that $Fe_{30}Pt_{70}$ NPs are much more selective as an AA sensor than Pt NPs.

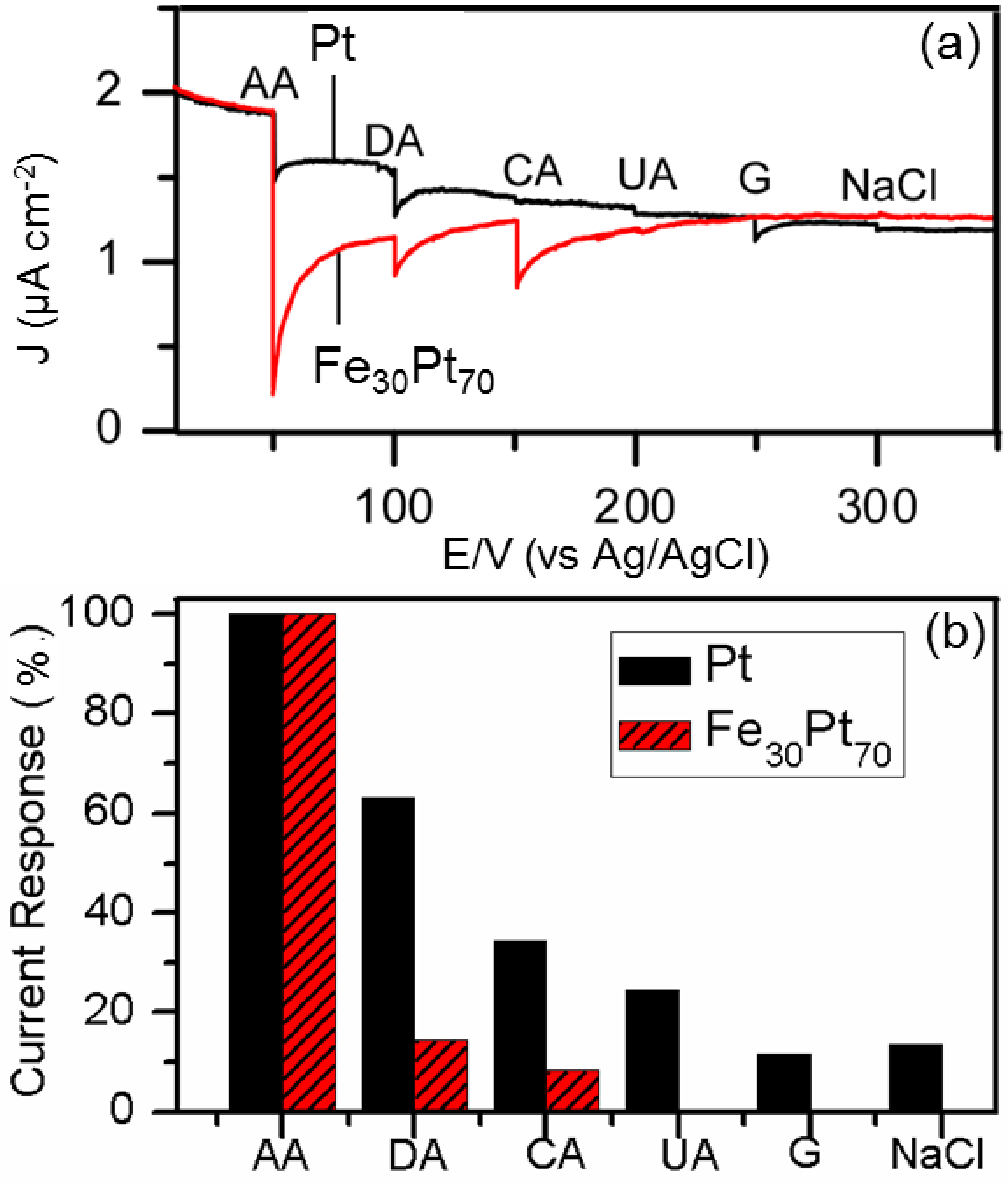

Figure 4.4 (a) Amperometry of Fe$_{30}$Pt$_{70}$ NPs and Pt NPs at an applied potential of 0 V (vs Ag/AgCl) by successive additions of 1 mM ascorbic acid (AA), dopamine (DA), citric Acid (CA), uric Acid (UA), glucose (G), and NaCl to 10 mM PBS to obtain a final concentration of 20 µM for all species; and (b) the corresponding relative current responses normalized to the AA current response.

4.3.4 Sensor optimization

In order to obtain the best sensor performance, we increase the electro-active surface area of the electrode. This can be achieved by optimizing the NP loading onto the substrate by tuning the deposition time (to obtain the maximum NP number density) and/or increasing the surface area of the substrate (from flat Si(100) to Si nanowires). Of the FePt alloy NPs studied in the present work, the best current response to AA detection is obtained by $Fe_{30}Pt_{70}$ alloy NPs, following the order: $Fe_{30}Pt_{70} > Fe_{25}Pt_{75} > Fe_{35}Pt_{65}$. Using the electrolyte solution for producing the $Fe_{30}Pt_{70}$ alloy NPs at the optimized deposition potential (–1.1 V vs Ag/AgCl), we vary the deposition time from 3 s to 600 s. Increasing deposition time leads to larger NPs with a higher number density (i.e. a larger surface coverage), thereby increasing the electro-active area, until a monolayer film of NPs is eventually reached at 600 s. The current response to 1 mM AA increases with increasing surface coverage and reaches a maximum at the 300 s deposition time (not shown). Further increase in the deposition time causes the NPs to merge into a film, reduce the electro-active surface, and gradually decrease the current response. To increase the Si surface area for depositing the NPs, we prepare Si nanowires by chemical etching of the Si(100) substrate in a 5M HF and 0.02 M $AgNO_3$ solution at room temperature for 10 minutes and followed by dipping in a HNO_3:H_2O (3:1) solution for 30 minutes (to remove the Ag deposits).[212,213] Figure 4.5a shows the typical morphology of the resulting Si nanowires, with significantly increased surface area than the flat Si(100) surface. We then deposit $Fe_{30}Pt_{70}$ alloy NPs at –1.1 V (vs Ag/AgCl) for 300 s on the Si nanowires. Evidently, these alloy NPs appear to cover at least the top halves of the nanowires, as shown in Figure 4.5b, leading to significant increase in the NP loading on the substrate. Using the Si nanowires loaded with $Fe_{30}Pt_{70}$ NPs as the electrode, we observe over five-fold increase in the current response, compared to that found for flat Si electrode. Furthermore, we perform amperometry for a series of solutions with different AA concentrations at 0 V (vs Ag/AgCl), at which applied potential the least interference from other species has been observed. The current density has reached a steady-state value in less than 5 s in all solutions (Figure 4.5c). These steady-state current densities are found to increase linearly with increasing concentration, which provides a calibration curve for this $Fe_{30}Pt_{70}$ NPs/Si-nanowire sensor (Figure 4.5c, inset). The sensitivity of this sensor is estimated to be 4.347 mA cm^{-2} mM^{-1}, and a detection limit of 0.1 μM is obtained from 3σ/S, where σ is the standard deviation of 10 blank measurements and S is the slope of the calibration curve. The resulting sensitivity is therefore over 10 times higher than the best-performance sensor materials reported to date (as summarized in Table 4.1), including $K_2UO_2[Fe(CN)_6]$-modified Pd/Al electrode (122.3 μA cm^{-2} mM^{-1}),[202] Pd NP composites (570 μA cm^{-2} mM^{-1})[192] and Pd nanowires (166.5 μA cm^{-2} mM^{-1}).[196]

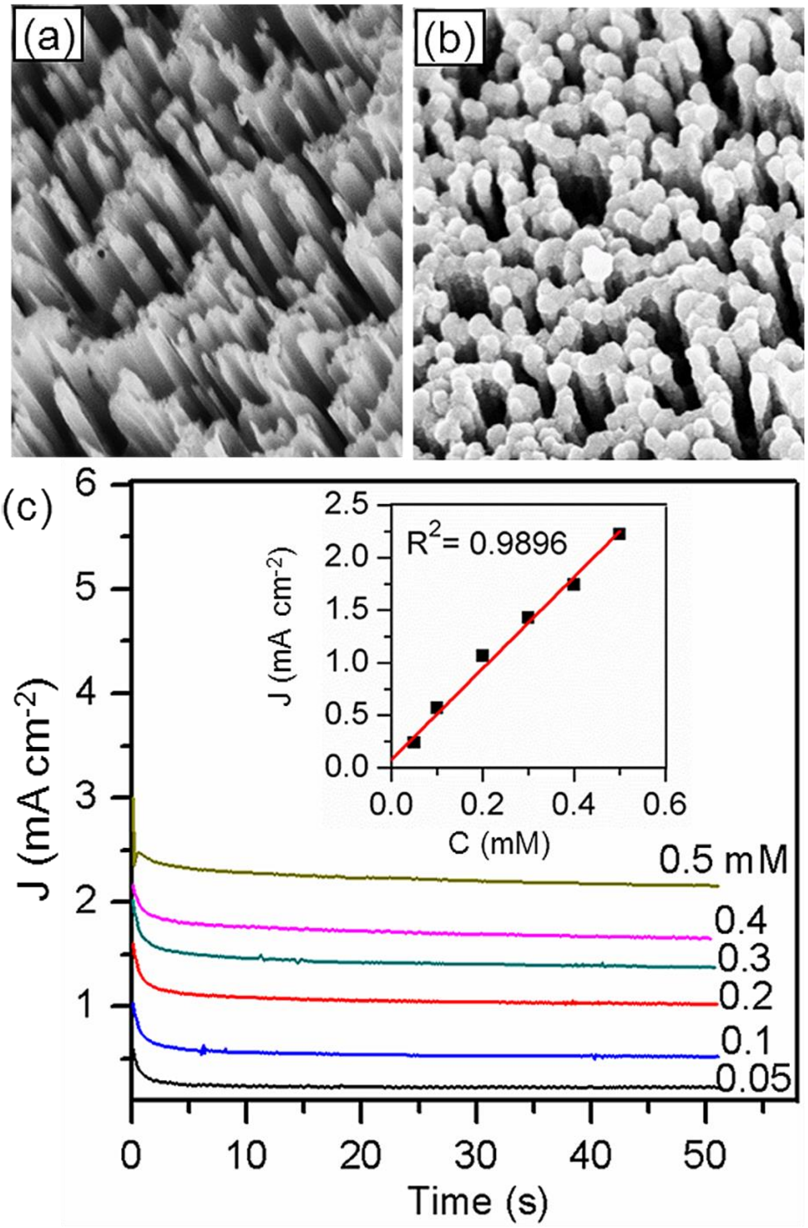

Figure 4.5 SEM images of Si nanowires (a) before and (b) after $Fe_{30}Pt_{70}$ NPs deposition, and (c) amperometry response of $Fe_{30}Pt_{70}$ NPs/Si-nanowires electrode in solutions with different AA concentrations (C) at an applied potential of 0 V (vs Ag/AgCl). Inset shows the linear relationship of the steady-state current density to the concentration.

Table 4.1 Comparison of the working potential, linear range, sensitivity and detection limit of the $Fe_{30}Pt_{70}$ NPs/Si-nanowires electrode with other electrodes for the electro-oxidation of ascorbic acid.

Electrode	**Applied Potential (**V) (vs Ag/AgCl)	**Linear Range (**μM)	**Sensitivity (μA mM^{-1}** cm^{-2}**)**	**Detection Limit** (μM)	**Ref.**
Over-oxidized polypyrrole and Pd nanoparticle composites	0	1-520	570	1	192
Pd nanowires	0	25-900	166.5	0.2	196
$K_2UO_2[Fe(CN)_6]$-modified Pd/Al electrode	0.3 (SCE)	1-50	122.3	0.5	202
Ferricyanide mediator/ polyelectrolyte–calcium carbonate microspheres	0.27	1-2143	4.5	0.7	214
Multiwall carbon nanotube–silica network–Au nanoparticles	~ 0.46	1000-5000	8.59	Not reported	215
Graphene nanosheets on pyrolysed photoresist film	~ 0.35	400-6000	18.5	120	216
Polyacrylic acid-coated multiwall carbon nanotubes	~ –0.1	100-1000	26	49.8	217
CoNSal modified electrode	~ 0.25	1-100	4.2	0.7	218
$Fe_{30}Pt_{70}$ alloy NPs on Si nanowire electrode	0	10-1000	4347	0.1	This work

4.3.5 Electro-oxidation Model

To verify the relative near-surface composition of the FePt alloy NPs, we also analyse their chemical-state compositions by XPS after brief (20 s) Ar sputtering the respective NP samples (to remove the carbonaceous layer due to ambient handling in air). Figure 4.6a compares the XPS spectra of the Fe 2p and Pt 4f regions for pristine Fe, pristine Pt, and the three

FePt alloy NPs. Evidently, pristine Pt NPs and all three FePt alloy NPs all exhibit Pt $4f_{7/2}$ ($4f_{5/2}$) features at essentially the same binding energy of 71.0 eV (74.3 eV), within the instrumental accuracy of 0.1 eV. For the pristine Fe NPs, two Fe $2p_{3/2}$ features at 707.0 eV and near 711 eV can be attributed to metallic Fe and Fe oxides, respectively. In contrast, the FePt alloy NPs all exhibit only the metallic feature at 0.4 eV higher binding energy, except for $Fe_{35}Pt_{65}$ NPs which has an additional oxide feature near 711 eV. The observed chemical shifts indicate changes in the electronic structures of the FePt alloy NPs from that of pristine Fe NPs. This is in good agreement with the in-situ EXAFS data obtained for Pt alloys by Mukerjee, et al.,[219] which shows more d-band vacancies for the Pt alloys than Pt metal. It should be noted the chemical stability of the FePt NPs catalysts has also been investigated by XPS before and after AA detection. No degradation or change in surface composition has been observed.

The increase in the d-band vacancies in the FePt alloy NPs has been used to account for the observed enhancement in the electroactivity of FePt alloy NPs compared to that of Pt NPs. Because Fe has more 5d vacancies than Pt, the replacement of Pt by Fe in a FePt alloy generally increases the d vacancies (relative to pristine Pt), which affects the electron affinities of the Pt atoms in the alloys. Following the mechanism of electro-oxidation of AA on Pt electrode proposed by Casella[220,221]and Karabinas et al.,[222] an increase in the electron affinities of the alloy would enhance the adsorption of deprotonated AA adspecies ($C_6H_6O_6^{2-}$), which subsequently lead to oxidation of the adsorbed AA radical. Figure 4.6b shows a schematic diagram of the AA anionic radical formation and its adsorption to the surface of the alloy NPs. The radical then loses an electron and desorbs from the surface. Alloying is believed to increase the adsorption rate and therefore enhance the electron detection.

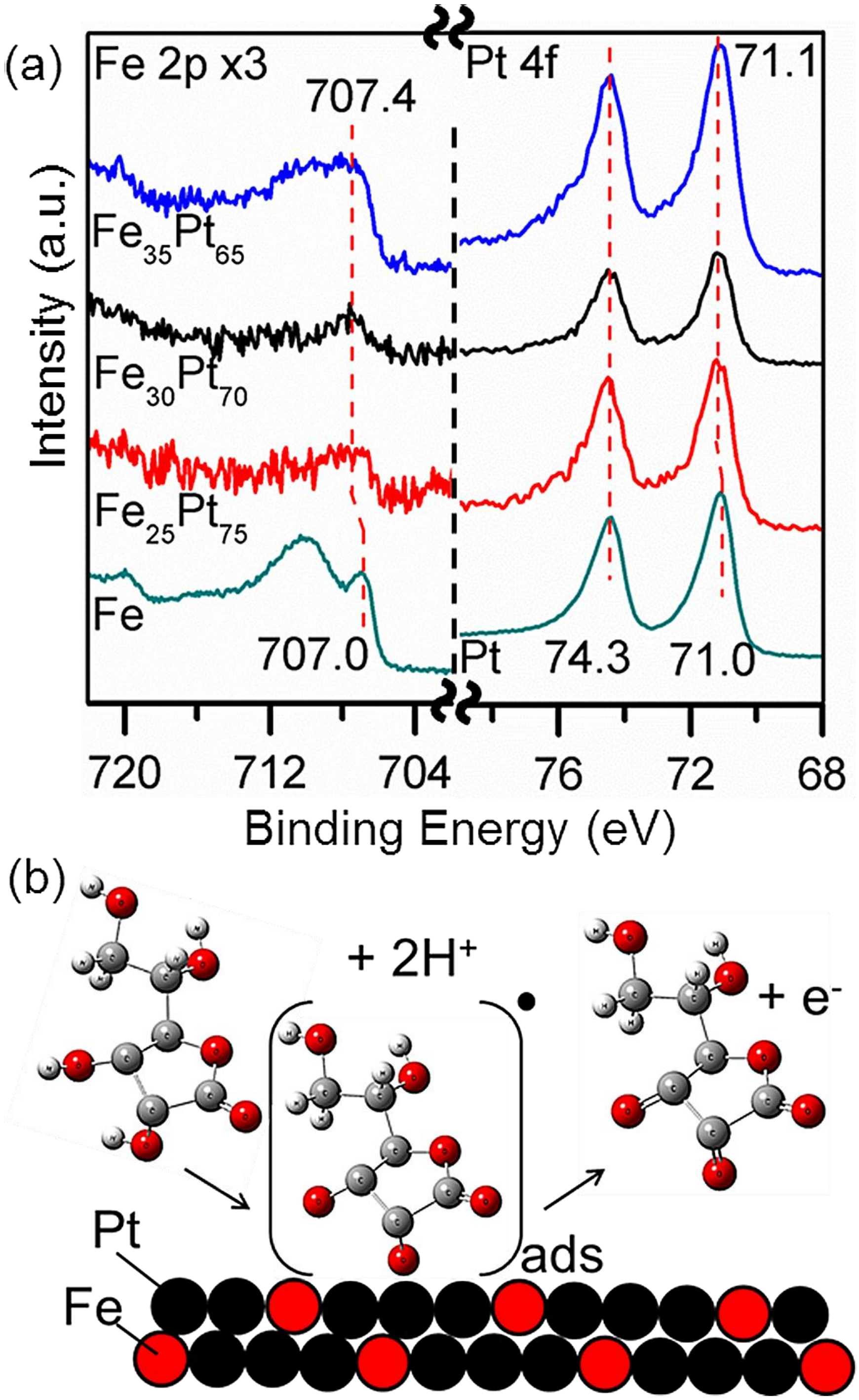

Figure 4.6 (a) XPS spectra of the Fe 2p and Pt 4f regions for pristine Fe, pristine Pt, and the $Fe_{25}Pt_{75}$, $Fe_{30}Pt_{70}$, $Fe_{35}Pt_{65}$ NPs, and (b) a schematic model of AA electro-oxidation on the FePt NP surface.

4.4 Summary

In summary, FePt alloy NPs with three different compositions have been obtained on Si substrate by electrodeposition. These NPs have been tested for electro-oxidation of AA and all alloy compositions show higher electrocatalytic activity than pristine Pt NPs. By effectively reducing the over-potential for AA oxidation, these alloy NPs are significantly more selective to AA detection related to other common interference species, including dopamine, citric acid, uric acid, glucose, and NaCl. Increasing electroactive surface area of the substrate by replacing flat Si substrate with Si nanowires enhances the current response five-fold. Higher d-vacancies of FePt relative to Pt have been used to account for the observed enhancement in the electroactivity of FePt alloy NPs. The present FePt alloy NPs can therefore provide superior materials for a fast-response AA sensor with high sensitivity, wide linear detection range and low detection limit in a neutral pH operating environment.

Chapter 5

Bimetallic Nanoparticles for Arsenic Detection

5.1 Introduction

Arsenic (As) is a widely distributed element in nature, as the 20th most abundant mineral in the earth's crust and the 12th most abundant mineral in the human body. Arsenic occures in organic and inorganic species with oxidation states of −3, +3, and +5.[223,224] Inorganic As is more toxic than organic As, while arsenite (As with a +3 oxidation state) is more toxic than arsenate (As with a +5 oxidation state).[225] According to the World Health Organization[226] and the US Environmental Protection Agency,[227] the acceptable level for maximum As contamination in drinking water is 10 ppb. Drinking water with a higher level of As contamination will cause adverse health effects, including hyperkeratosis on the palm or feet, fatigue, cancer of the bladder, and genotoxic and mutagenic effects.[228] Analytical techniques capable of determining ppb or sub-ppb level of As are therefore very important for this critical public health threat.[229,230] Electrochemical techniques, particularly stripping voltammetry, are very attractive because of their unique capability for high selectivity for As(III), rapid analysis, and low-cost instrumentation. They also offer high sensitivity and very low limit of detection comparable to those found in more expensive techniques, such as atomic absorption and inductively coupled plasma spectrometry.[231,232] Furthermore, the generation of very toxic $AsH_3(g)$ as required in most of these latter techniques is not necessary in electrochemical techniques.[233]

Metallic films and nanomaterials have been used as sensing materials for electrochemical analysis of trace metal ions including Hg, Cd, Sb, Pb, Fe, and Cu,[234–237] the detection of As in contaminated water with these electrochemical methods has become more popular.[238–242] Bimetallic nanostructured materials, alloy or core-shell nanoparticles (NPs), have attracted much recent attention because of their novel catalytic, magnetic, and optical properties, which could offer significant additional advantages over those of their constituent single-metallic materials. While studies on the sensing properties of bimetallic NPs have been recently reported,[243–245] very few have focused on trace metal detection by electrodes modified by bimetallic or alloy NPs.[246,247] For instance, Gong et al. used Au-Pt inorganic-organic hybrid nanocomposite-modified glassy carbon electrode to detect Hg(II) with high sensitivity that is not affected by intereference from other metal ions.[246] Lan et al. employed Au-Pd NP modified glassy carbon electrode to determine As(III) and reported a detection limit of 0.25 ppb at pH 4.5.[247] However, no systematic study on the detection of metal ions by using different bimetallic NPs has been reported. Driven by the need for low-cost catalysts and sensors, the study of bimetallic NPs, including inexpensive materials such as Fe, has become a very important research area. Since most of the electrodes, employ noble metals (Au and Pt), with and without modification, mixing these noble metals with a low-cost element will not only reduce the production cost but also introduce new properties or enhance in sensing properties not found in single-metal materials. Here, we report the synthesis of FeM NPs (where M is a noble metal: Pt, Pd, Au) and determine their structural and electrochemical properties. We also evaluate and compare their sensing performance for As(III) with those of AuPt NPs (involving two noble metals), Au, Pd, and Pt pristine NPs (single noble metals). Using anodic stripping voltammetry, we compare the sensitivity and limit of detection of different bimetallic NPs for As(III) detection, and obtain the best sensitivity and limit of detection for FePt NPs. We also investigate the interference of Cu(II) ions, which is one of the most serious problems in arsenic detection for these NPs.

5.2 Materials and Methods

5.2.1 Materials

The chemicals (all analytical grades): $FeCl_2$, $FeCl_3$, $H_2PtCl_6•xH_2O$, $AuCl_3$, $PdCl_2$, and $CuCl_2+2H_2O$ were purchased from Sigma-Aldrich and used as delivered. The phosphate buffer saline solution (PBS, 0.1 M Na_2HPO_4-NaH_2PO_4-KCl, pH 7.2) was prepared by dissolving PBS tablets (Sigma) in filtered deionized water (18 MΩ cm). Acetate buffer solutions with the desired pH were obtained by mixing appropriate portions of 0.1 M acetic acid and 0.1 M sodium acetate. The Si substrates (15×2.5 mm2, 0.4 mm thick) were cut from an one-side-polished Si(100) wafer (p-type, B-doped, with a resistivity of 0.01-0.02 Ω-cm) purchased from Siegert Wafer GmbH. Arsenic stock solution was obtained by dissolving 0.95 g As_2O_3 in 10 mL NaOH (1 M) and diluting the solution to 100 mL final volume. The pH of the resulting solution was 6 and the concentration of As(III) was 0.048 M.

5.2.2 Fabrication of Electrodes

The Si(100) substrates were cleaned by using the RCA method[83] and H-terminated by dipping in an aqueous HF (2%) solution. They were used as the working electrodes for both NP deposition and sensor application. The as-prepared working electrodes were dried and stored in a N_2 atmosphere at room temperature when not in use. Pristine (i.e. single-metal) and bimetallic NPs were prepared by potentiostatic amperometry (except for the Pt and FePt NPs) on a Si substrate in a deoxygenated electrolyte containing different reagent salts and supporting electrolytes. FeAu and AuPt NPs were electrodeposited for 30 s from solutions of 1 mM $AuCl_3$ mixed with 10 mM $FeCl_3$ and 1 mM H_2PtCl_6, respectively, in 0.1 M $NaClO_4$ electrolyte, while Au NPs were prepared in the AuCl3 solution without any added Fe or Pt solution. The applied potentials were –0.8 V for Au and AuPt and –1.2 V for FeAu. Pd and FePd NPs were deposited at –1.4 V for 30 s from solutions of 0.5 mM PdCl2 without and with 5 mM $FeCl_2$, respectively, in 3 M KCl electrolyte. Pt and FePt NPs were obtained from solutions of 1 mM H_2PtCl_6 without and with 1 mM $FeCl_2$, respectively, in a 0.2 M H_3BO_3 electrolyte by using chronoamperometry with a high potential of –1.1 V and a low potential of –1.6 V and a pulse width of 10 s. The appropriate applied potential (all vs Ag/AgCl) and deposition time were chosen by variation of both parameters and optimized to produce uniform coverage of near-monosized NPs. After the deposition, the samples were washed by filtered deionized water (18 MΩ cm) and stored in a N_2 atmosphere at room temperature until use. This method has the advantage of producing NPs with a uniform spatial distribution without agglomeration, which therefore provides the maximal exposed surface for electro-catalysis without additional step(s).

5.2.3 Characterizations

An electrochemical station (CH Instruments 660A) was employed for synthesis and electrochemical analysis, using a three-electrode cell with the NPs deposited on the Si substrate as the working electrode, and a Pt wire and standard Ag/AgCl electrode as the respective counter and reference electrodes. The background current was recorded for all sweep rates and appropriately removed in calculating the peak currents. The analyte solution was purged with N_2 for 20 minutes before recording the voltammograms. The surface morphology of the NPs was characterized by field-emission scanning electron microscopy (SEM) in a Zeiss Ultra Plus microscope, and their crystal structures were determined by glancing-incidence X-ray diffraction (XRD) at an incidence angle of 0.5° in a PANalytical X'Pert Pro MRD diffractometer with Cu Kα (1.542 Å) radiation. Chemical-state composition was analyzed by X-ray photoelectron spectroscopy (XPS) as a function of Ar ion sputtering time in a Thermo-VG Scientific ESCALab

250 Microprobe, equipped with a monochromatic Al Kα X-ray source (1486.6 eV).

5.3 Results and discussion

5.3.1 Morphology and composition of bimetallic NP electrodes

The SEM images in Figure 5.1 show that the NPs so obtained generally have a spherical shape with a narrow size distribution and an average size under 100 nm: AuPt (40 nm), FePt (100 nm), FePd (20 nm), FeAu (20 nm), Pd (20 nm), Au (30 nm). We also obtained pristine Pt NPs (not shown). As these Pt NPs were found to have two different size distributions and they were not very homogeneous, we have therefore not examined them further for the present sensing application. For the largest NP obtained here, the FePt NPs appear to have a rough surface and consist of grains that are a few nanometers in size. It should be noted that the conditions used to prepare the NP samples (shown in Figure 5.1) were determined in separate experiments for each NP sample on Si substrates. For instance, AuPt NPs were obtained by potentiostatic amperometry at –0.8 V for 30 s deposition time. Applying a higher potential for the same deposition time did not change the number density nor the size of the NPs, but the deposition became increasingly disrupted due to H_2 evolution. Deposition for a longer time would result in larger NPs with more agglomeration. FeAu and FePd NPs were deposited for 30 s at –1.2 V and –1.4 V, respectively. These bimetallic NPs required a more negative applied potential than that for AuPt NPs, in order for deposition to occur. The applied potential could be made even more negative to –1.6 V, but did not lead to very homogenous deposits, with NPs becoming more distorted in shape and more widely distributed in size.

The relative composition of each sample has been estimated by energy-dispersive X-ray analysis. AuPt NPs are found to correspond to $Au_{45}Pt_{55}$, i.e. with 45% Au and 55% Pt, which is similar to the ratio of their composition in the electrolyte. In contrast, the compositions of FeM (M=Pt, Pd, Au) NPs are relatively different from their respective compositions in the electrolytes. We obtain $Fe_{70}Pd_{30}$, $Fe_{40}Pt_{60}$, and $Fe_{10}Au_{90}$ for the compositions of the respective FeM NPs. The relative Au and Pt contents in these FeM NPs are much more than the relative compositions in their respective electrolytes, because their reduction potentials are lower than that for Fe, and their adsorption and reduction rates are therefore much higher than those for Fe[248,249] at the relatively large negative applied potential of –1.4 V (vs Ag/AgCl). For Pd deposition, the number of free ions is reduced in the electrolyte because of the tendency of Pd to stay in the complex form of K_2PdCl_4.

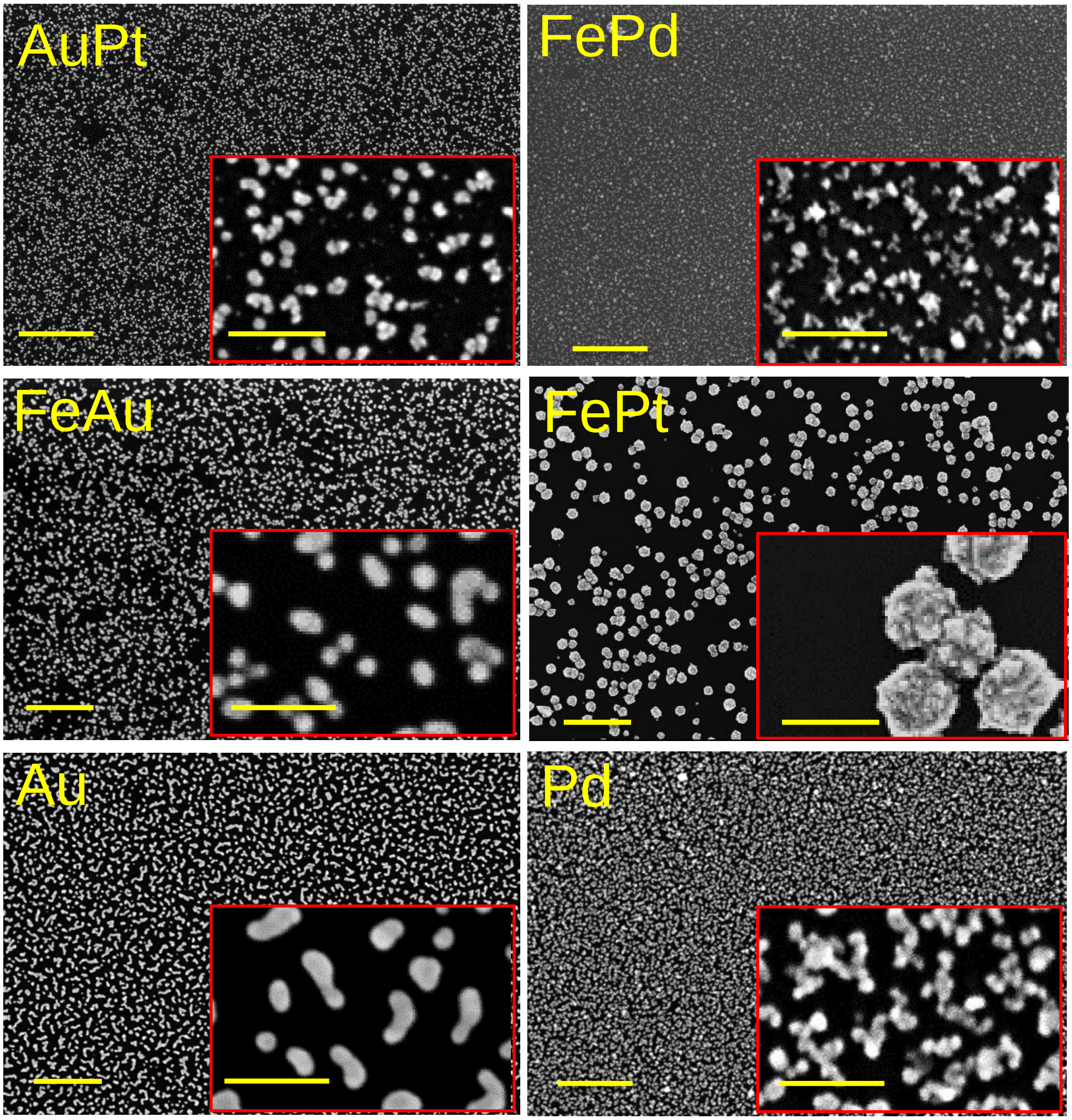

Figure 5.1 SEM images of $Au_{45}Pt_{55}$, $Fe_{70}Pd_{30}$, $Fe_{40}Pt_{60}$, $Fe_{10}Au_{90}$ bimetallic NPs and pristine Au and Pd NPs and their higher magnification images in the insets, with scale bars of 500 nm and 100 nm, respectively.

Figure 5.2a shows the corresponding XRD patterns for FePt, AuPt, FeAu, Au, FePd and Pd NPs along with the reference patterns for Pt (PDF00-004-0802) and Fe metals (PDF01-085-1410). As the region of 2-theta = 50-60° contains mainly diffraction features of the Si(100) substrate, this region is therefore not shown. Comparison of the patterns for bimetallic NPs with the pristine metal patterns reveals discernible shifts toward higher 2-theta values for FePt and AuPt NPs than the respective Pt and Au patterns, which indicates lattice expansion as a result of alloy formation. No peak corresponding to pristine Fe in these FePt or FeAu NPs is observed in their respective patterns, which shows that these FePt or FeAu NPs are single phase. The FeAu and FePd patterns exhibit no obvious shift and they only appear slightly more crystalline, when compared with those of their respective pristine Au and Pd NPs. To confirm alloy formation and the absence of segregated Fe or Au or Pd NPs or domains inside the NPs, we collect XPS spectra of the Fe 2p and Au 4f regions for FeAu NPs and of the Fe 2p and Pd 3d regions for FePd NPs. To identify the peak locations and the corresponding chemical shifts, we have fitted the spectra with Gaussian-Lorentzian lineshapes after appropriate correction with the Shirley background. To remove the carbonaceous layer commonly found due to sample handling in air, we performed Ar sputtering of the as-prepared samples for 10 s. We also removed the oxide part of NPs by sputtering for additional 10 s, which allowed us to study the metallic part of the NPs. Figure 5.2b shows the resulting chemical-state compositions for typical FeAu and FePd NPs after 10 s and 20 s of sputtering. Compared to the pristine Fe XPS features (not shown here), the Fe $2p_{3/2}$ peaks at 707.3 eV has a discernible shift of 0.3 eV toward higher binding energies for both FeAu and FePd NPs. While no obvious difference in the Au $4f_{7/2}$ peak position for the FeAu NPs from the pristine Au is observed, the metallic Pd $3d_{5/2}$ peak for the FePd NPs exhibits a 0.4 eV shift to a higher binding energy. The corresponding Fe $2p_{3/2}$ peaks near 710.4 eV for FePd NPs and 710.1 eV for FeAu NPs are related to the Fe oxides, while the Pd $3d_{5/2}$ peak at 337.0 eV corresponds to Pd silicide. These chemical shifts from the binding energies of the pristine NPs further confirm alloy formation.

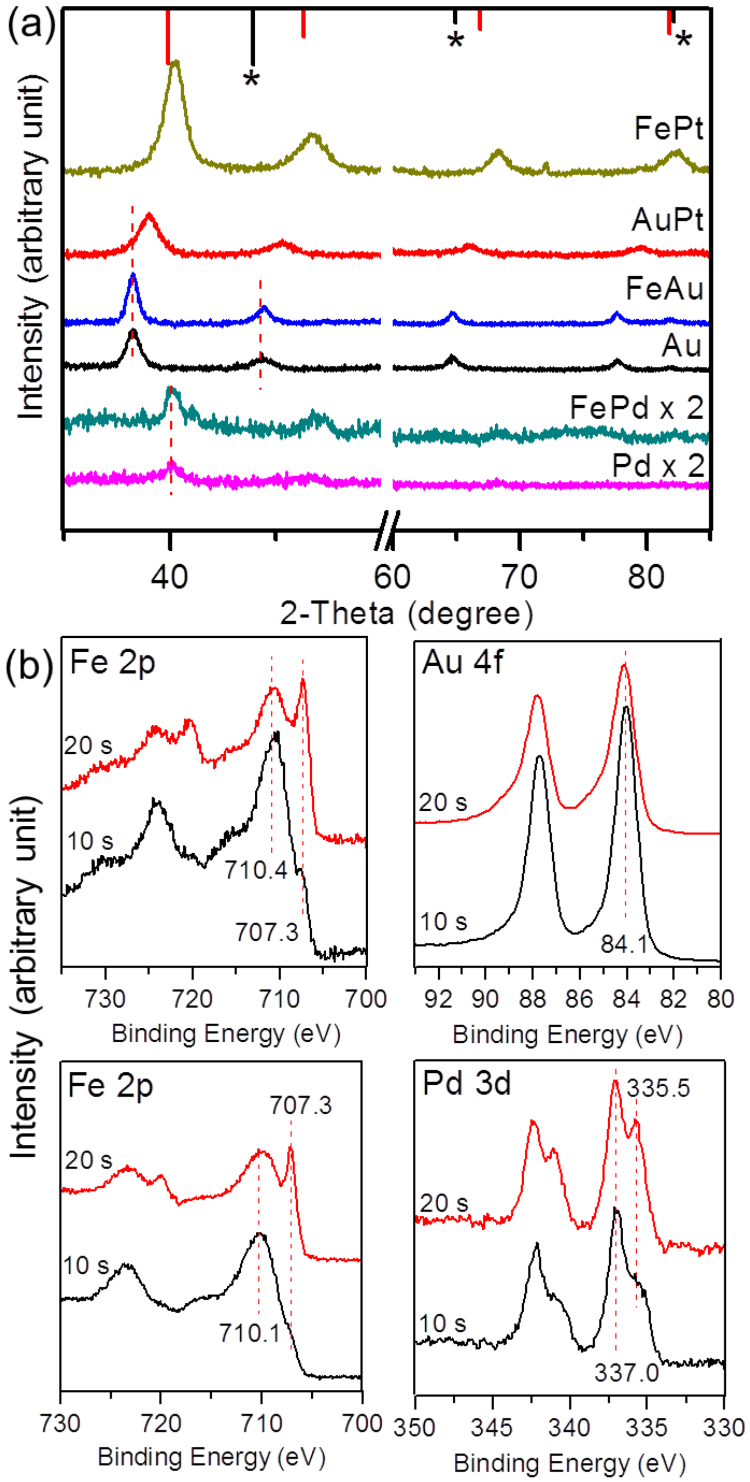

Figure 5.2 (a) X-ray diffraction patterns of FePt, AuPt, FeAu, and FePd NPs, compared with those of pristine Au and Pd NPs. Reference patterns for Pt (PDF2: 00-004-0802) and Fe (PDF2: 01-085-1410) are indicated on top by lines and lines with stars, respectively. (b) XPS spectra of Fe 2p and Au 4f regions for FeAu nanoparticles (upper panels) and of Fe 2p and Pd 3d regions for FePd nanoparticles (lower panels), after 10s and 20 s of Ar^+ sputtering.

5.3.2 Electrochemical behaviors of bimetallic-NPs/Si electrodes

To investigate electrochemical sensing using the as-prepared bimetallic-NPs-coated Si electrode, cyclic voltammetry (CV) was carried out in quiescent solutions in a PBS solution with and without arsenic at a scan rate of 50 mV s^{-1}. The electrode was vigorously rinsed with deionized water after each measurement. The CV curves from –0.5 V to +0.6 V of the AuPt, FePt, FePd, FeAu, Pd, and Au NPs/Si electrodes with and without 1 mM As in a 10 mM PBS solution are shown in Figure 5.3.

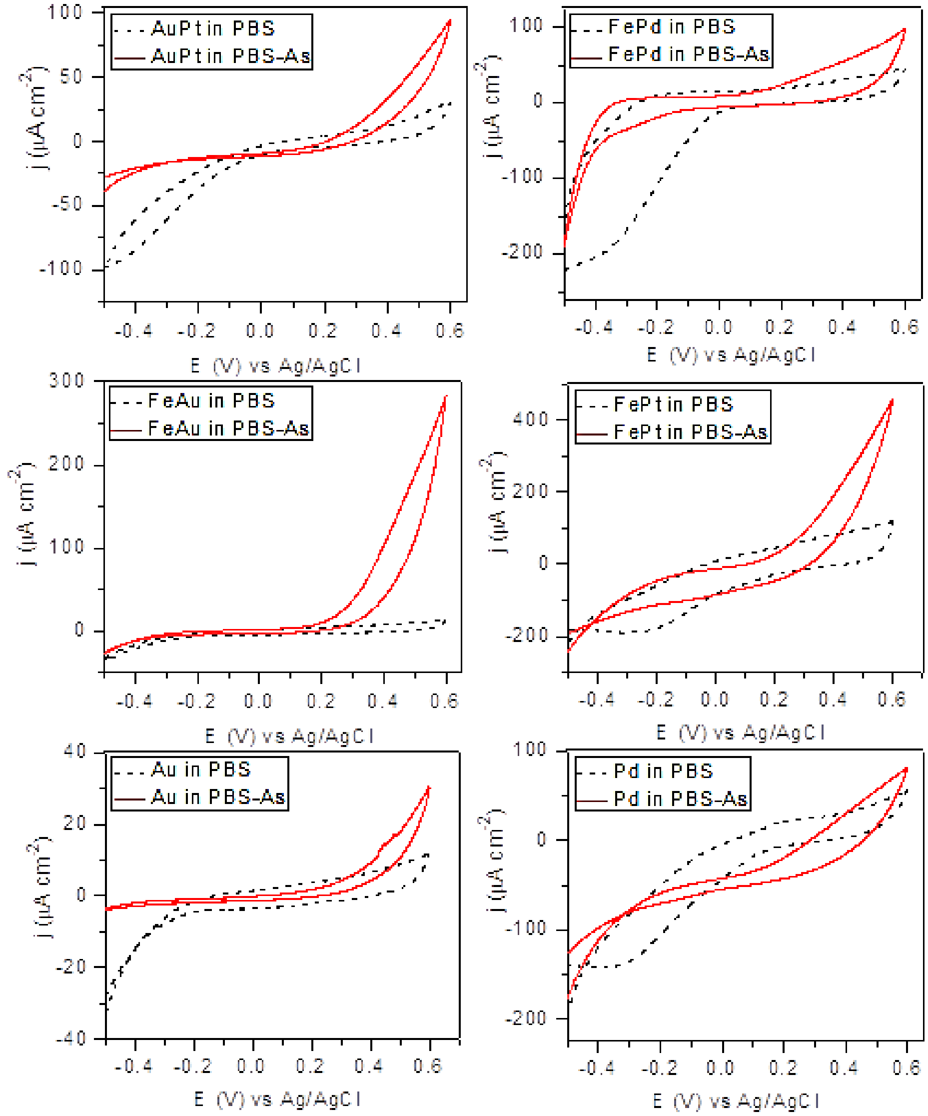

Figure 5.3 Cyclic voltammograms of AuPt, FePd, FeAu, FePt, Au and Pd NP-coated Si electrodes, all in a 10 mM PBS solution without (dashed lines) and with 1 mM As (III) (solid lines). Scan rate is 50 mV s^{-1}.

The scans are limited to below 0.7 V to prevent the oxidation of NP surfaces. The bare Si electrode was also used but found to exhibit no current response in the presence of As, and so is not shown in Figure 5.3. In the pristine PBS solution (i.e. without As addition), all NPs/Si electrodes except for the Au and FeAu NPs show a peak near – 0.3 V. This peak disappears in the presence of As in the solution, which corresponds to oxidation of As(0) to As(III). Furthermore, a rise in current density at 0.6 V can be observed when As is added to the solution, which can be attributed to oxidation of As(III) to As(V) at potential above 0.6 V. For the FeAu NPs/Si electrode, no obvious peak corresponding to oxidation of As(0) to As(III) is observed but the current signal for As(III) oxidation to As(V) is notable. In Figure 5.4, we compare the current signals obtained from all the electrodes in the presence of As in the solution. The current rise near 0.6 V is found to be the largest for FePt NPs followed by FeAu NPs, but the reduction in current at – 0.3 V is the largest for FePd NPs.

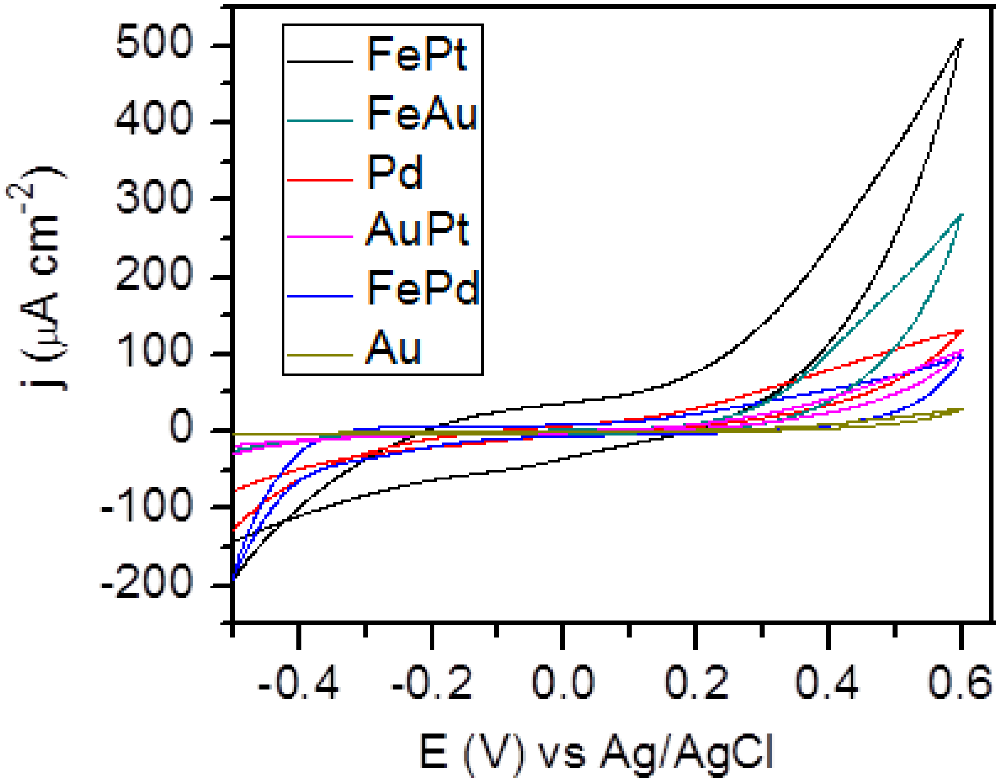

Figure 5.4 Cyclic voltammograms of FePt, FeAu, Pd, AuPt, FePd, and Au NPs-coated Si electrodes (from top to bottom at 0.6 V) in 10 mM PBS and 1 mM As solution. Scan rate is 50 mV s^{-1}.

To study the effects of different electrolytes and the pH of the electrolyte on the sensing properties, aqueous solutions of 1 mM As in various media with different pH were prepared and used for CV studies. We have chosen FePt and FeAu NPs-coated Si electrodes that exhibit the best primary responses and compare the corresponding oxidation currents of As(III) to As(V) in PBS (with pH 7) and acetate buffer solutions with pH 5 (Acetic-5) and pH 6 (Acetic-6) in Figure 5.5. Evidently, both FePt and FeAu NPs show similar CV profiles in PBS and acetate buffer solutions in the absence of As, with two weak peaks near –0.2 V and +0.1 V in the CV profile of FePt NPs compared to the FeAu NPs profile. In the presence of As(III), the current signal in PBS is higher for both FePt and FeAu NPs than the current signals in both acetate buffers. Lowering the pH in the acetate buffer apparently decreases the current response. For the rest of the experiments, we have therefore chosen PBS as the optimized electrolyte. Clearly, a neutral pH is particularly important for the practical use of the sensor for drinking water.

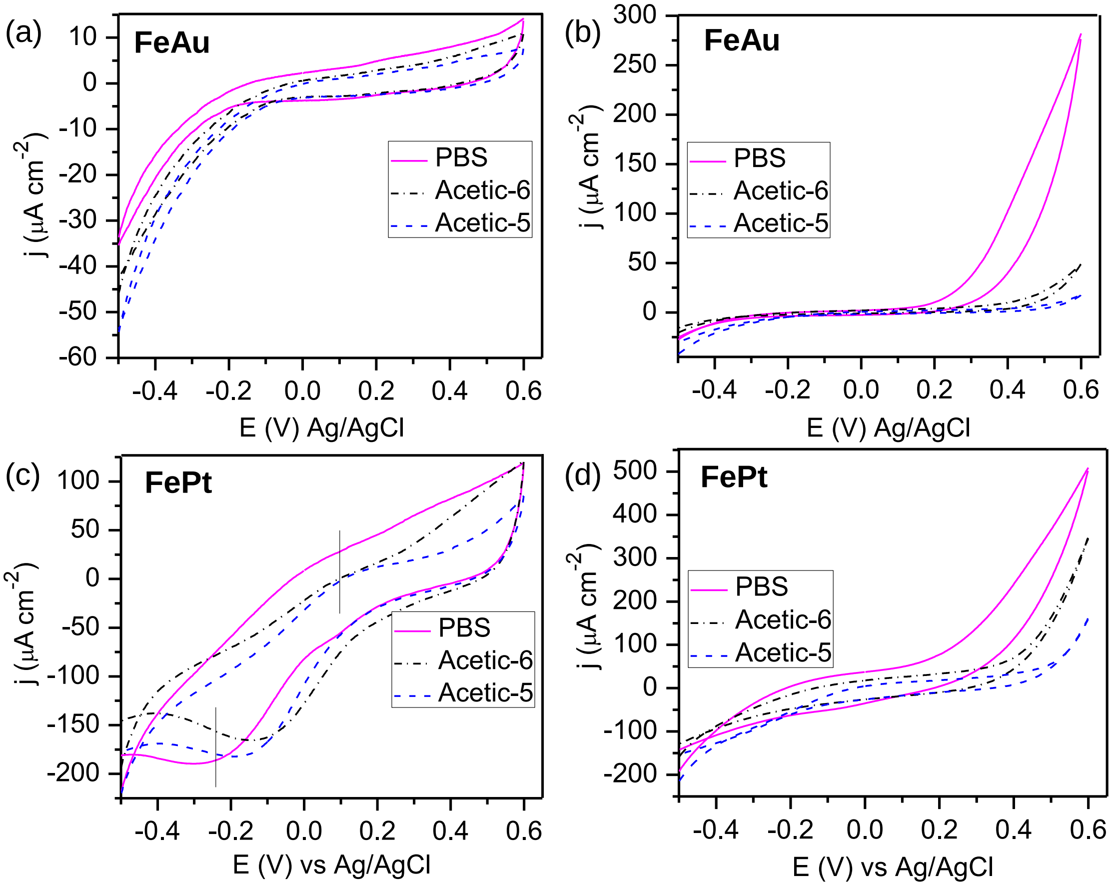

Figure 5.5 Cyclic voltammograms of (a, b) FeAu and (c, d) FePt NPs-coated Si electrodes in 10 mM PBS with pH 7, and in 100 mM acetate buffer solutions with pH 6 (acetic-6) and 5 (acetic-5) (a, c) in the absence and (b, d) presence of As(III). Scan rate is 50 mV s^{-1}.

5.3.3 Anodic stripping voltammetric detection of arsenic

Stripping voltammetric techniques are well known for trace metal analysis providing detection limits comparable to that of very expensive spectroscopic techniques.[223,250,251] The process includes two main steps: electrochemical deposition of trace metals on the electrode (accumulation step), followed by oxidation of the metal back into solution in a linear or pulsed reverse scan (stripping step). Various solutions containing different concentrations of As were prepared and used for these studies. The accumulation step was achieved with the reduction of As ions to metallic As on the electrode, while the stripping step involved the reverse process of oxidation. Square wave voltammetry (SWV) and differential pulse stripping voltammetry (DPSV) were carried out using the FePt, FeAu and FePd NPs-coated Si electrodes. Although the As(III) to As(V) oxidation peaks on the FePt and FeAu NPs are considerably stronger than that for FePd NPs, the oxidation peak for As(0) to As(III) on FePd NPs is larger than those for FePt and FeAu NPs (Figure 5.3). We have therefore carried out SWV and DPSV measurements for these three samples and calculated their limits of detection. After purging with N_2 gas for 20 min, different amounts of As(III) ions were added step by step to the blank test solution. In order to obtain reproducible results, we also applied a constant potential of 0 V (vs Ag/AgCl) for 60 s and stirred rigorously after each stripping step. This also helped to clean and maintain the electrode in its original condition. All electrodes exhibited good stripping signals. Figure 5.6 (upper panels) shows the SWV curves of FePt and FeAu NPs and DPSV curves of FePd NPs in 10 mM PBS with As(III) increasing from 1 to 3, 5, 10 and 15 ppb after background subtraction. For the primary results, SWV and DPSV have been carried out with an accumulation potential of –0.4 V and an accumulation time of 60 s. The solution was stirred throughout the accumulation period, followed by 30 s of equilibrium (rest) time without any stirring before the stripping step. For optimization, we varied the initial scanning potential, accumulation time and pH of the electrolyte. The initial scanning potential is an important parameter because it controls both the peak potential and peak current in the stripping voltammogram. We have carried out SWV for FePt with different initial potentials from –0.5 V to –0.2 V and obtained the peak current for each potential. When the initial potential was set to –0.4 V, the corresponding current signal increased by 37% compared to that obtained with an initial potential of –0.5 V. Decreasing the initial potential to –0.3 V did not change the current signal, but setting the initial potential to –0.2 V produced a current signal almost twice that obtained with –0.5 V. We have therefore chosen

–0.4 V as the optimum initial potential because –0.2 V was too close to the peak potential in the SWV curves, which might introduce a false reading in the current signal. We varied the accumulation time from 20 s to 120 s and found an accumulation time of 60 s to give the optimum response. To determine the best pH for the electrolyte, we prepared three different PBS solutions with pHs of 3.3, 5.5 and 7 and carried out SWV in these electrolytes. The current signals obtained for oxidation of both As(III) to As(V) and As(0) to As(III) were found to be the highest at pH 7 and they became smaller with decreasing pH. The optimum pH value was therefore set to 7, which serendipitously makes this sensor very environment-friendly and reduces the problems associated with operating in a low pH condition. The optimization for DPSV on FePd NPs followed the same approach used for SWV although the data is not presented here. Using the optimized conditions so determined, increasing the As(III) concentration leads to a rise in the current signal for FePt and FePd NPs, while the trend from FeAu NPs is less clear, as shown in Figure 5.6 (upper panels). As shown in Figure 5.6 (lower panels), a linear relationship between the peak current at –0.17 V for FePt, –0.25 V for FeAu, and –0.3 V for FePd and the As(III) concentration in the range of 1-10 ppb is obtained for these NPs. Among these three NPs-coated Si electrodes, FePt NPs exhibit the best limit of detection of 1.2 ppb, which is calculated by $3\sigma/S$, where σ is the standard deviation of 10 blank measurements and S is the slope of the calibration curve. The limits of detection are found to be higher for FeAu (3.8 ppb) and FePd NPs (13.6 ppb). For the FePt NPs with the best (i.e. smallest) limit of detection, the sensitivity of FePt NPs is estimated to be 1.23 μA ppb^{-1}. In Table 5.1, we compare the sensing performance data of the FePt NPs-coated Si electrode with those for other metallic NPs on different electrodes. It should be noted that our electrode employs the Si substrate for NPs deposition, in contrast to other electrodes that use glassy carbon substrates. Despite the lower conductivity of Si relative to glassy carbon, the present electrode offers competitive sensing performance. In addition, an important advantage of the present sensor is the neutral electrolyte environment (with pH 7), in marked contrast to other sensors that require electrolytes with lower pH. This is particularly important for the practical use of sensors targeted for drinking water.

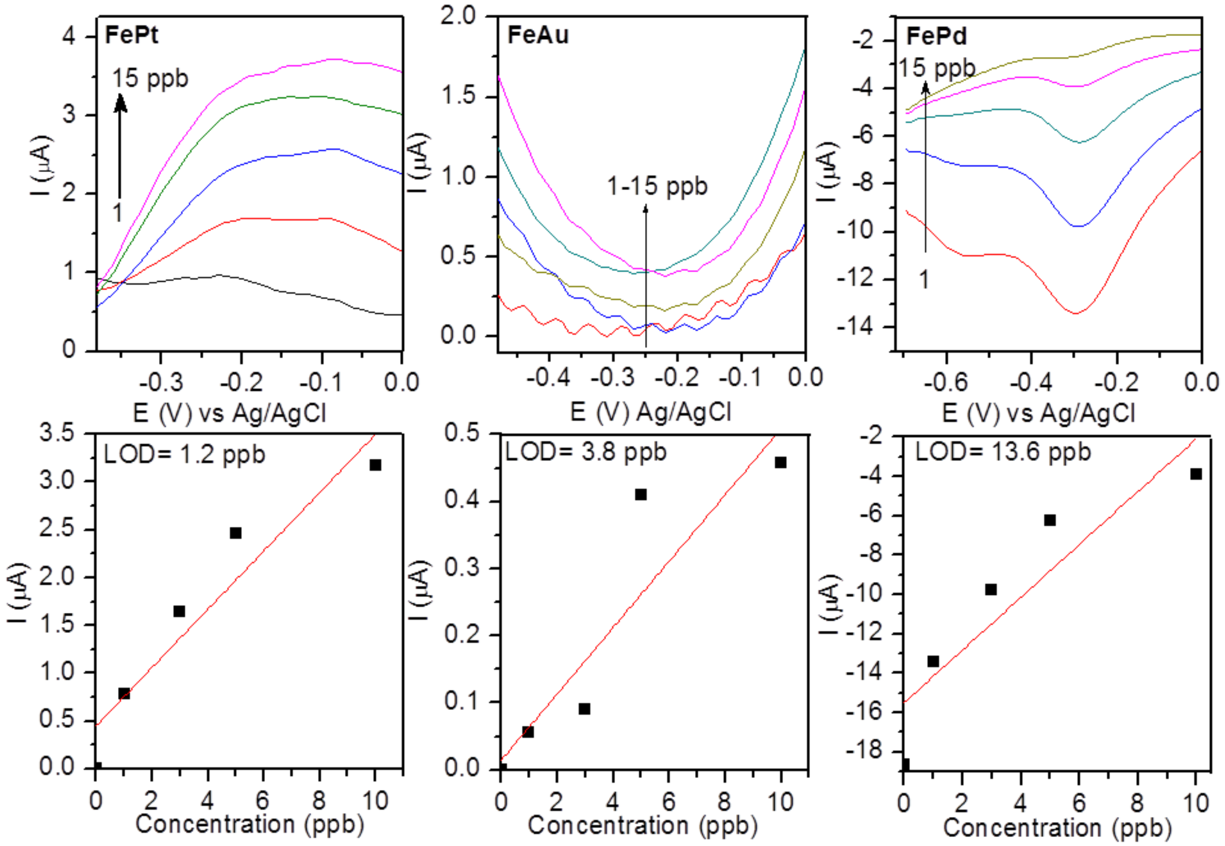

Figure 5.6 (Upper panels) Square wave stripping voltammograms (SWV) of FePt and FeAu NPs and differential pulse stripping voltammetry (DPSV) of FePd NPs in 10 mM PBS for As(III) concentration of 1, 3, 5, 10 and to 15 ppb. (Predisposition condition: –0.4 V, 60 s) (Lower panels) The corresponding linear relationships between the peak currents for FePt (at –0.17 V), FeAu (at –0.25 V), and FePd (at –0.3 V) and the As(III) concentration. The limit of detection (LOD) for each of the lines is also given.

Table 5.1 Comparison of performance for detection of As(III) between the proposed FePt NPs-coated Si sensor with other sensors reported in the literature.

Sensor	Method	Electrolyte	Linear Range (ppb)	Limit of Detection (ppb)	Ref.
Au NPs on glassy carbon electrode	Linear Sweep Voltammetry	1 M HCl	0.38–9	0.0096	239
Au-coated Fe_3O_4 on glassy carbon electrode	SWV	0.1 M PBS (pH 5)	0.01–1	0.00097	252
Au NPs on polyaniline film or glassy carbon electrode	SWV	1 M HCl	610-3050	0.4	253
Pt NPs on glassy carbon electrode	Linear Sweep Voltammetry	0.1 M H_2SO_4	0.075–3.75	2	254
Ag NPs coated carbon nanotubes on glassy carbon electrode	DPSV	1 M HNO_3	10–100	1.20	255
AuPd on glassy carbon electrode	Anodic Stripping Voltammetry	0.1 M Acetate buffer solution	1–25	0.25	247
FePt NPs on Si	SWV	0.01 M PBS (pH 7)	1–10	1.2	This work

5.3.4 Interference and stability studies

Determination of As(III) using anodic stripping voltammetry is known to be susceptible to interferences from various metals.[252,256,257] These interferences arise from either competition for deposition sites on the electrode surface or formation of intermetallic compounds with As during the deposition step.[258,259] Among all the possible interference metals, copper [in the form of Cu(II)] presents the most serious challenge to arsenic detection because its stripping voltage is similar to (and slightly more positive) than the As(III) oxidation voltage. Moreover, Cu can also form intermetallic compounds with As(III) during the deposition process.

Figure 5.7a shows the CV curves obtained in 10 mM PBS with 15 ppb As(III) solution in the absence and presence of 1 mM of $CuCl_2$ representing 170.5 ppm Cu(II). Evidently, a decrease in the current signal for the As(III) to As(V) oxidation at 0.5 V and a small change in the region of As(0) to As(III) oxidation at –0.1 V are observed when the Cu(II) ions are present. Since these changes are rather small, we conduct more detailed examination using DPSV to detect any minute change in As(III) in the presence of Cu(II). DPSV curves were obtained after accumulation time of 60 s at –0.4 V starting from –0.7 V to 0 V in 6 mV increments and with the amplitude (0.05 V), pulse width (0.05 s), sampling width (0.017 V) and pulse period (0.2 s) kept constant. Figure 5.7b shows the corresponding DPSV curves of FePt NPs in the absence and presence of 170.5 ppm Cu(II). No discernible change in the detection region of As(III) (i.e. at – 0.33 V) is found between the curves, after appropriate background subtraction. There is, however, a discernible decrease in current at – 0.11 V in the presence of Cu(II), which can be attributed to Cu oxidation. The present DPSV result therefore shows that Cu(II) oxidation does not interfere with As(III) oxidation, both of which can be detected simultaneously.

For the stability test, we have stored the sensors in a dry box at room temperature for 30 days and repeated the tests. Only 5% decrease was observed in the current signal after 30 days, which shows the remarkable stability of these sensors.

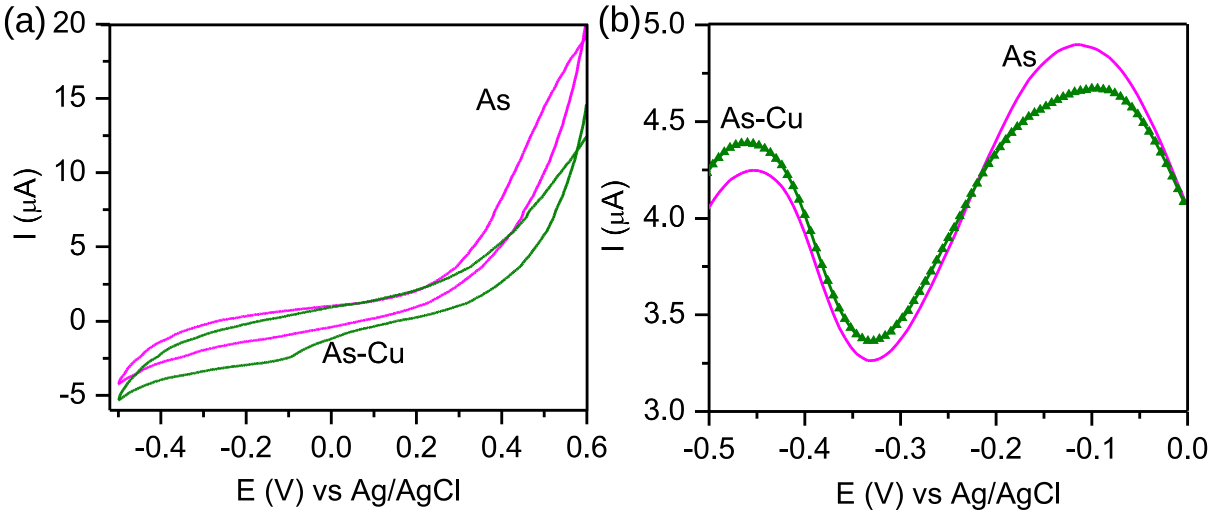

Figure 5.7 (a) Cyclic voltammograms (scan rate 50 mV s^{-1}) and (b) differential pulse stripping voltammograms of FePt NPs in 10 mM PBS and 15 ppb As(III) with and without 170.5 ppm Cu (II).

5.4 Summary

Driven by the need for low-cost catalysts and sensors, the incorporation of inexpensive materials such as Fe into active noble metals promises a new approach of synthesizing the next-generation catalysts. In the present work, we obtain bimetallic AuPt, FePt, FePd, and FeAu NPs by electrochemical deposition from the appropriate solutions on Si(100) substrate. Their morphologies and structures are studied and their electrochemical properties are optimized to obtain the best bimetallic NPs for As(III) detection. Their performance, including the sensitivity and limit of detection, are characterized systematically and compared with those of pristine Au, Pd, and Pt NPs by using very precise anodic stripping voltammetry methods, including square wave voltammetry and differential pulse stripping voltammetry. Among the bimetallic NPs studied here, FePt NPs are found to provide the best performance, with minimal interference from Cu(II) and exhibit long-term stability.

Chapter 6

In-situ Hybridization of Superparamagnetic Iron-Biomolecule Nanoparticles[§§§]

6.1 Introduction

Composite systems of biomolecules and metal nanostructures combine the evolution-optimized molecular recognition capability of biomolecules with the novel optical, electronic, and catalytic properties of nanomaterials. These composite systems are excellent prospects for a new generation of multi-functional bioelectronic devices. In the past decade, substantial progress has been made in the use of biomolecule-nanostructure composites in electrochemical biosensors, electronic nanocircuitry and even nanodevices.[260–263] In conventional approaches, the biomolecules and metal nanostructures are treated as separate entities. Bio-integration into nanostructures could only be obtained by immobilization of biomolecules on the inner and/or outer surfaces of the nanostructures, including polymer matrices, inorganic supports and nanoparticles (NPs).[264–266] Well-established techniques based on physical adsorption, electrostatic binding, specific recognition, and covalent coupling have often been used for immobilization.[267–270] In particular, adsorption of proteins on NPs has been achieved through electrostatic interactions between the partially charged amino acid side groups of the protein and the appropriate component with opposite polarity on the NPs. The latter component could be a functional group of a linker molecule pre-coated on the NPs or a partially charged site on the nanostructure.[271,272] On the other hand, relatively little study on bio-integration into the nanostructure during growth has been made. Such studies can provide fundamental information about the nature of this integration (including bonding, interactions, and growth mechanism), which could lead to a new class of bio-nanomaterials. With many potential applications in biosensor research, food industry, and renewable fuel cells,[273–277] glucose oxidase (GOx, with MW of 160 kDa) is a popular model biomolecule for studying self-organization of nanostructures on biomolecules and of biomolecules on other surfaces. In the limited number of studies on conjugating GOx onto NPs by electrostatic interaction,[278,279] the NPs were synthesized

---

[§§§] This section is made from one of my publications: N. Moghimi, A. D. Donkor, M. Mahapatra, J. P. Thomas, Z. Su, X. Tang, K.T. Leung, J. Am. Chem. Soc., 2014, 136 (29), pp 10478–10485. Copyright (2014) American Chemical Society.

first and GOx were subsequently allowed to interact with the NPs. Even in the earlier work on the co-electrodeposition of GOx and gold NPs,[280,281] separate GOx and pre-grown NPs were used. To date, direct incorporation of biomolecules into the nanostructures during growth remains challenging because the presence of an aqueous medium with a mild pH (as required by the biomolecules) and the need for low growth temperature (preferably below room temperature) are not conducive to nanostructure growth. Although the chelation and complexation of metal ions with GOx have been widely studied, the use of metal ions-GOx complexes directly to synthesize hybrid nanoparticles (HNPs) has not been reported.

The same hybridization approach can also be easily extended to incorporate other biomolecules, even with dramatically different sizes, in these HNPs. The anticancer p53 peptide (p53p, with MW of 1.8 kDa) is a promising drug for most cancers because it can bind to both Mdm2 and MdmX in cancer cells.[282] Almost 50% of cancers are caused by overexpressed Mdm2 and MdmX as they inhibit the tumor suppressor, p53p.[283,284] The attachment of p53p to magnetic NPs that can be delivered to targeted tumor sites would be a breakthrough in anticancer therapeutics.

In this work, we report the successful synthesis of Fe-GOx and Fe-p53p HNPs by using Fe-GOx and Fe-p53p complexes directly as the building blocks, without involving pre-grown Fe NPs followed by biomolecule coating. We further demonstrate that these HNPs consist of Fe nanocrystallites bound together by biomolecules similar to a stone-and-mortar architecture. These Fe-biomolecule complexes are made by adjusting the pH of the aqueous solution to above the isoelectric point of GOx or p53p, in which the negatively charged amino acids on the surface of the biomolecule electrostatically interact with the positive Fe ions. By conducting the co-electrodeposition at 4°C, we produce Fe-GOx and Fe-p53p HNPs that show superparamagnetic properties even when these HNPs are as large as a few hundred nanometers, while preserving the bioactivities of GOx and p53p at the same time. The Fe-GOx HNPs also exhibit remarkable biocompatibility to human hepatoma cells (liver cells). This method of producing size-specific superparamagnetic HNPs has the important advantage of attaining the desired dimension while eliminating the post-functionalization (coating) step to achieve the size needed for practical use of these superparamagnetic NPs. We show that in the present hybridization method GOx not only maintains its enzymatic activities but also acts as a protective shell from oxidation for metallic Fe nanocrystallites. As a further practical demonstration, we also show that p53p remains active after hybridization and can bind to Mdm2, which confirms the generality of the present approach. Isolation of Fe nanocrystallites by GOx or p53p introduces extraordinary magnetic property for large hybrid nanoparticles (i.e. superparamagnetism in large sizes). Electrochemical hybridization of metals with biomolecules therefore offers a novel approach to developing cell-friendly magnetic HNPs with homogeneously distributed magnetic nanocrystallites and biomolecules inside. The present method is however not limited to electrochemical reduction, and Fe-biomolecule complex reduction with any other reducing agent would also be possible. These HNPs promise potential applications not only as magnetic contrast agents but also in targeted slow-release drug delivery systems.

6.2 Materials and Methods

6.2.1 Preparation of the HNPs

Fe-GOx HNPs were prepared by co-electrodeposition of Fe and GOx on a H-terminated Si(100) substrate in a three-electrode cell using an electrochemical workstation (CH Instruments 660A). A silicon chip (15×2.5 mm^2, 0.4 mm thick), precut from a Si(100) wafer (p-type, B-doped, with a resistivity of 0.01-0.02 Ω-cm), was used as the working electrode after it was cleaned using the RCA method[83]. It was then H-terminated by dipping in a 2% aqueous HF solution. A standard Ag/AgCl electrode was used as the reference electrode and a Pt wire as the counter electrode. The electrolyte consisted of 5 mM $FeCl_2$ by dissolving $FeCl_2{\cdot}6H_2O$ salt (Aldrich, 99%) in an aqueous solution with 200 mM boric acid as the supporting electrolyte. The pH of the electrolyte solution was then adjusted to 6.5 with 250 mM NaOH (Aldrich, 99.9%). After deoxygenation with N_2 for 30 minutes, the electrolyte was mixed with GOx from Aspergillus niger (Fulka) to obtain 75 μM GOx in the solution. In this freshly prepared electrolyte solution, electrodeposition was conducted at 4 °C by amperometry potentiostatically at −1.2 V vs Ag/AgCl for an appropriate deposition time. The resulting electrodeposits were washed thoroughly with filtered deionized water (18.2 MΩ•cm) and stored in N_2 at room temperature for further analysis. Fe-p53p HNPs were prepared using the same method described above for Fe-GOx HNPs. The p53p peptide, with the sequence of SQETFSDLWKLLPEN,[285] was chemically synthesized using standard Fmoc solid-phase chemistry[286] at St Jude Children's Research Hospital Peptide Facility. The synthetic peptides were purified by HPLC using a reverse-phase C18 semi-preparative column with an acetonitrile gradient of 10–35%. The purity of the peptides was verified by a reversed-phase analytical HPLC column and the identity of the final products was verified by mass spectral analysis. The isoelectric point of p53p is 4.0, which is similar to that of GOx (4.2). The same concentration of p53p (as that of GOx i.e. 75 μM) was added to a solution of 5 mM $FeCl_2$ with a pH of 6.5. The electrodeposition was also carried out at 4 °C followed by a thorough wash with filtered deionized water and kept at 4 °C for bioactivity tests.

6.2.2 Analysis of the HNPs

The surface morphology of the so-prepared samples of Fe-GOx and Fe-p53p HNPs were characterized by field-emission scanning electron microscopy (SEM) (Zeiss LEO FE-SEM 1530 microscope) and by Helium ion microscopy (HIM) (Zeiss Orion Plus microscope). Multi-cross-sectional imaging was conducted using a Zeiss Auriga focused ion beam (FIB) SEM system. The samples were first coated by a thin carbon layer to protect the top surface from damage due to the sputtering Ga ion beam. Very thin slices of the samples with thickness no larger than 1 μm (containing selected NPs on top of the Si substrate) were cut vertically along the surface normal (i.e., in the depth direction of the substrate). SEM images of the exposed cross sections were then collected by using the backscattered electron detector in order to differentiate elements with different atomic masses based on the image contrast. Subsequent cross-sectional SEM images were collected interleavingly after removing additonal vertical slices (10 nm thick) from the samples. Crystal structures of HNPs were also determined by glancing-incidence X-ray diffraction (XRD) (PANalytical X'Pert Pro MRD diffractometer) with Cu Kα (1.542 Å) radiation at an incidence angle of 0.5°.

Chemical-state composition of the HNPs were analyzed as a function of Ar ion sputtering time by depth-profiling X-ray photoelectron spectroscopy (XPS) (Thermo-VG Scientific ESCALab 250 microprobe), equipped with a monochromatic Al Kα radiation (1486.6 eV) and operated with a typical energy resolution of 0.4-0.5 full width at half-maximum (fwhm). Three-dimensional chemical mapping of the HNPs was conducted by time-of-flight (TOF) secondary ion mass spectrometry (SIMS) (ION-TOF SIMS-5 system), equipped with a 2 m long TOF reflectron analyser and a multichannel detector along with a Bi_3^+ liquid metal analysis ion source and an O_2^+ sputtering ion source. For the kinetics studies, absorption spectra were collected using a Perkin-Elmer Lambda 35 UV-Visible spectrometer equipped with a Labsphere integrating sphere. Magnetic properties were studied in a Quantum Design Dynacool vibrating sample magnetometer (VSM).

6.2.3 Cellular Assay

To test the biocompatibility of the HNPs, cells were cultured on substrates with attached HNPs. Before the cellular assays, the HNPs were sterilized with 70% ethanol. HeLa cells (HeLa, No: CCL-2; ATCC)) were cultured in Dulbecco's modified Eagle's medium with 10% fetal bovine serum and 1% penicillin-streptomycin (ATCC). Cells were maintained in 5% CO_2 in humidity at 37°C. For live cell imaging experiments, $1\text{-}2\times10^4$ cells were seeded on glass cover slips and allowed to attach overnight. The cells were then cultured and observed for several days.

6.2.4 Preparation of Mdm2 and Mdm2-GST

The N-terminal domain of human Mdm2 (i.e., Mdm2), which contains 89 amino acid residues, was prepared through a recombinant DNA technology. The DNA encoding Mdm2 was cloned into pGEX-6p-3 GST-fusion protein expression vector (GE, USA) and transformed into E-coli BL21 (DE3) host strain. Mdm2-GST fusion protein was expressed in soluble form with 0.5 mM IPTG induction at 25 °C. The fusion protein was purified by GST-affinity column and its purity was characterized by SDS-PAGE electrophoresis, indicating a single band.

6.2.5 SIMS Chemical Mapping

In the ION-TOF SIMS-5 system, the Bi^{3+} analysis ion source positioned at 45° to the sample was operated at 30 keV beam energy, with a 0.4 pA beam current and a 100 μs pulse width. Secondary ions were electrostatically directed to the TOF analyser by biasing the sample stage at 2.5 kV with the extraction lens set at 4.5 kV at an opposite polarity. Appropriate secondary ions: Fe^+, $NaNH_2^+$ corresponding to GOx, and Si^+ were collected over a rastered sampling area of 100×100 μm^2 to obtain a 2D map. The sample was then sputtered with O^{2+} (generated from a separate sputtering ion source) to remove the sample layer by layer at a well-defined sputtering rate. The 2D maps were collected interleavingly between the sputtered layers as a function of sputtering depth to obtain the depth profiles and to construct the corresponding 3D images of the Fe, GOx and Si components. It should be noted that due to the destruction layer created by the O^{2+} sputtering, molecular information from the GOx cannot be expected in 3D analyses. Furthermore, given that the ion detection limit of the present TOF SIMS instrument is 10,000 Da, it was not possible to detect intact GOx molecules (160,000 Da). Secondary fragments such as $NaNH^{2+}$ were therefore used to monitor the amount of GOx.

6.3 Results and discussion

Fe-GOx HNPs was prepared at 4 °C by co-electrodeposition of Fe and GOx on a H-terminated Si(100) substrate in a three-electrode cell. The electrolyte solution consisted of 5 mM $FeCl_2$ mixed with an appropriate amount of GOx from asparagines to obtain a concentration of 75 μM GOx in a 200 mM boric acid solution. In order to take advantage of the electrostatic attraction between GOx (with an isoelectric point of 4.2) and Fe^{2+} ions, the solution was maintained at pH 6.5 such that GOx became partially negative. UV-visible spectroscopy was used to monitor the change in the absorption band of GOx (Figure 6.1a). The Fe electrolyte (i.e., Fe^{2+}) exhibits a featureless spectrum with no discernible peaks in the region of interest, while the GOx spectrum shows a strong, sharp absorption peak at 274 nm along with weaker, broader bands at 377 nm and 454 nm, all of which correspond to the oxidized form of flavin groups.[287,288] The Fe-GOx electrolyte, however, exhibits a peak at 273 nm with a shift in the broad bands to 383 nm and 452 nm, respectively.

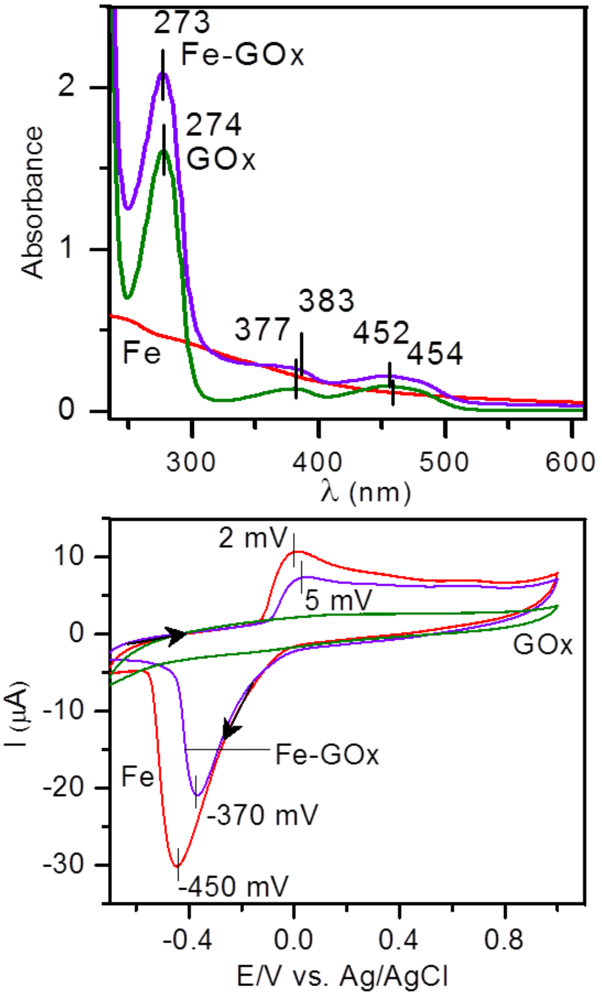

Figure 6.1 (a) UV-Visible spectra and (b) cyclic voltammograms of pristine Fe, pristine GOx, and Fe-GOx electrolytes (all at pH 6.5).

Formation of GOx-Fe complex is possible because of the many functional groups, such as amine, imidazole and sulfhydryl groups, in GOx that could interact with oxidizing mediators. Although both cationic and anionic groups are located on the GOx surface, the enzyme molecule has an essentially negative electrostatic surface potential at pH 6.5 as a result of excess glutamate and aspartate over lysine and arginine.[289,290] The presence of this negative surface potential favours electrostatic complexation of the anionic sites of the enzyme with mediators containing positively charged groups. In an aqueous environment, $FeCl_2$ tends to form $FeOH^+$ monomers,[96,291,292] with a significantly higher ionic mobility than the considerably larger GOx molecule. The resulting $FeOH^+$ could therefore attach to the anionic sites of GOx through a charge-transfer bond.

To further investigate the Fe-GOx complexation, we performed cyclic voltammetry on the Fe-GOx electrolyte (Figure 6.1b), and compare the result with those on the pristine GOx electrolyte and Fe electrolyte in UV experiments (Figure 6.1a). In the absence of GOx, oxidation of Fe^{2+} to Fe^{3+} complex species occurs at an anodic peak potential of 2 mV (vs Ag/AgCl), while reduction occurs at a cathodic potential of –450 mV (vs Ag/AgCl) upon the reverse scan. In the presence of GOx, both anodic and cathodic peak potentials are shifted to more positive values, with the shift in the cathodic peak potential (from –450 mV to –370 mV) found to be discernibly larger than that of the anodic peak potential (from 2 mV to 5 mV). The smaller reduction potential needed for Fe^{3+} to Fe^{2+} in the presence of GOx confirms the complex formation of the Fe species that changes the reduction potential, in good accord with our UV-Visible spectroscopic results. A decrease in the corresponding current density is also observed, which can be attributed to the slower diffusion of $FeOH^+$ when bound to a large and slowly moving GOx molecule. In general, the concentrations of the redox species and the number of electrons involved in the reactions control their diffusion coefficients and the resulting current densities.[293] As these voltammograms were obtained under the same experimental conditions, the observed difference in the current density is attributed to the difference in diffusion coefficients. The diffusion coefficient for $FeOH^+$ is expected to be smaller upon binding with GOx. A similar observation has been reported for the $[Fe^{II}(phen)_3]^{2+}$ when bounded to GOx and to DNA.[294,295]

Using the Fe-GOx complexes as our precursors, we synthesized the HNPs. In a freshly prepared Fe-GOx electrolyte solution, homogenous spherical NPs were deposited on the H-terminated Si substrate by amperometry at −1.2 V (vs Ag/AgCl). These NPs exhibit a remarkably narrow size distribution, with the average size easily controllable from 30 nm to 3.5 μm by varying the respective deposition time from 10 s to 60 minutes (Figure 6.2).

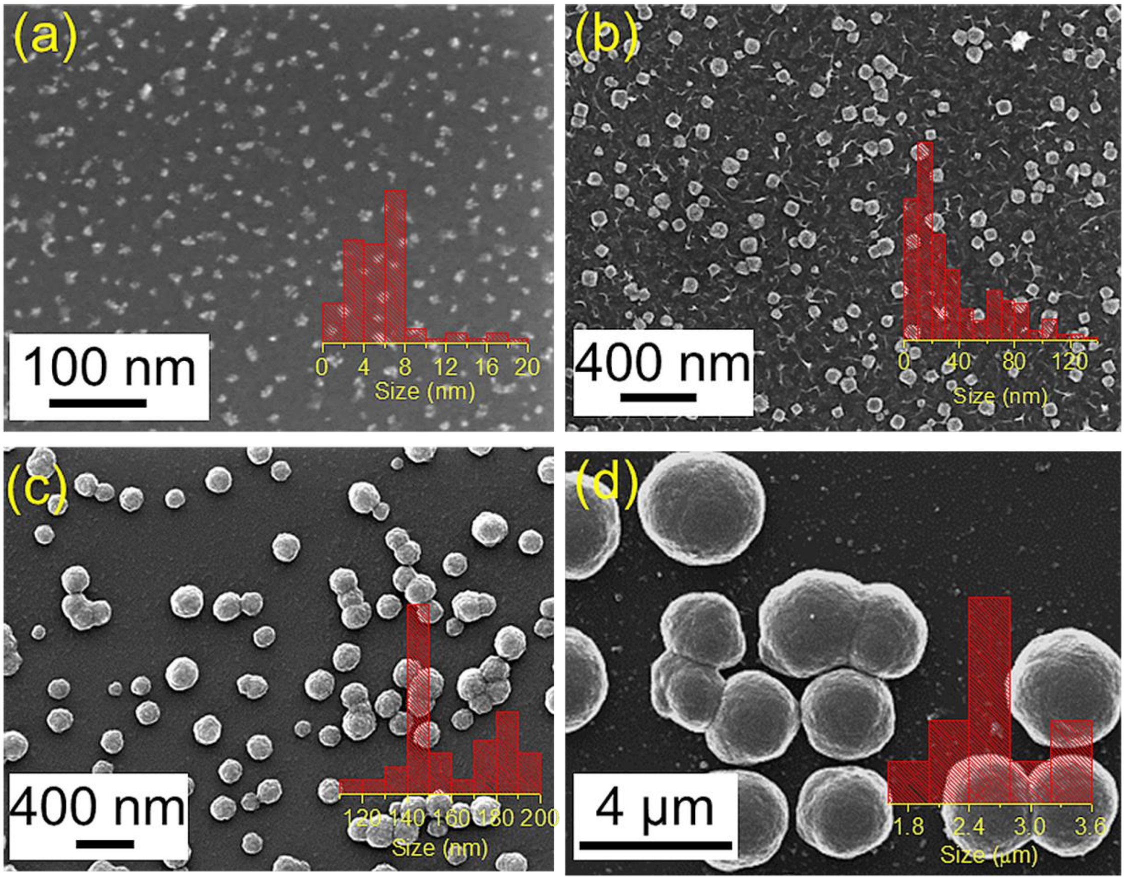

Figure 6.2 SEM images of Fe-GOx hybrid nanoparticles obtained by (a) 10 s, (b) 30 s, (c) 120 s, and (d) 60 min deposition. The corresponding average sizes are 30, 100, 170, and 3,500 nm, respectively.

Figure 6.3a shows a typical HIM image of Fe-GOx HNPs obtained by a 30 minute deposition. Furthermore, these nanograins are made up of nanocrystallites of 18 nm dia. in size (Figure 6.3b), as estimated by applying the Scherrer analysis to the Fe(110) diffraction peak in the corresponding X-ray diffraction pattern (Figure 6.3d). The features in the XRD pattern (Figure 6.3d) correspond to the bcc phase of metallic Fe (PDF2 006-0696).

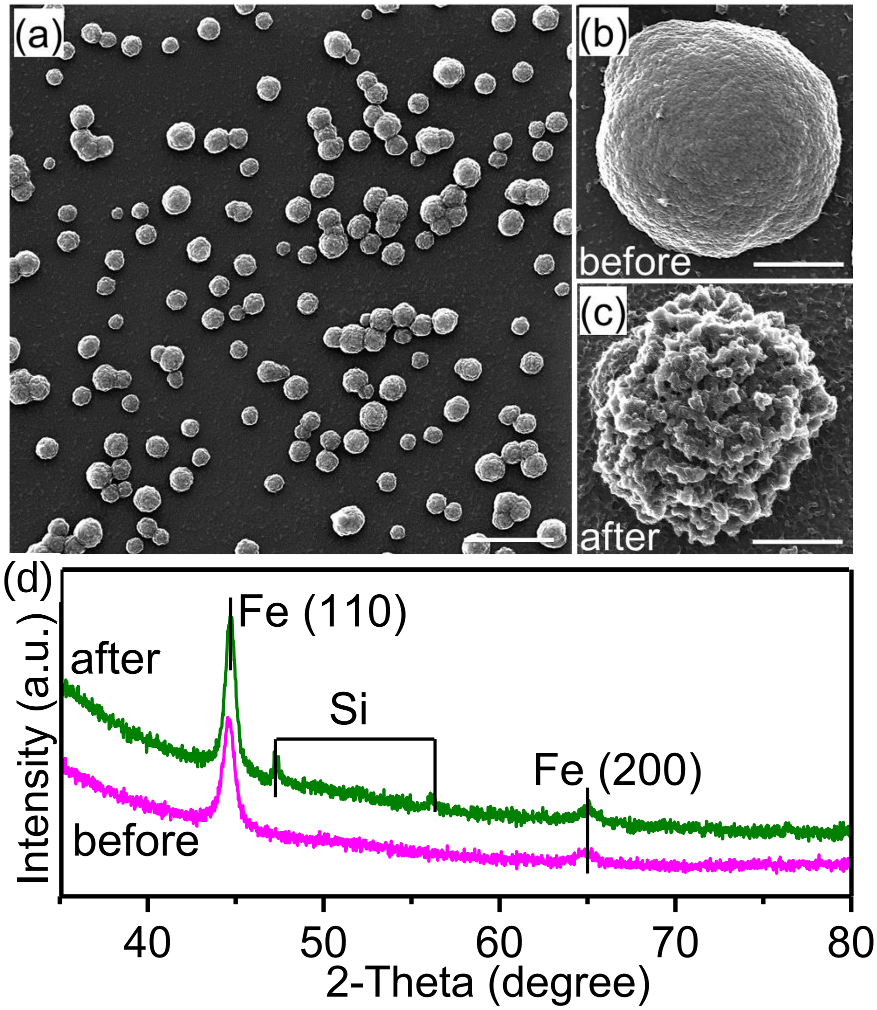

Figure 6.3 HIM images of Fe-GOx hybrid nanoparticles (a) and (b) before and (c) after the activity test, and (d) their corresponding glancing incidence XRD patterns before (bottom curve) and after the activity test (top curve). Scale bars represent 5 μm in (a) and 1 μm in (b) and (c).

To confirm the activity of GOx after electrodeposition, we used a glucose spectrometric assay to monitor the production of H_2O_2 by detecting quinoneimine dye with the details as following:

Absorption kinetics was studied by using a Perkin-Elmer Lambda 35 UV-Visible spectrometer equipped with a Labsphere integrating sphere. The activity of the enzyme was obtained by the small modification made in the popular glucose assay used for measuring the amount of glucose extracted from plants. The method is based on the following enzymatic reaction of glucose oxidase that converts glucose to gluconate:

$$\beta\text{–D-glucose} + O_2 + H_2O \xrightarrow{(GOx)} \text{D–glucono–}\delta\text{–lactone} + H_2O_2$$

An appropriate peroxidase (POD) reaction is then used to convert the resulting H_2O_2 to a dye that can be detected and measured easily by absorption spectroscopy in the visible region:

$$2H_2O_2 + \rho\text{–hydroxybenzoic acid} + 4\text{–aminoantipyrine} \xrightarrow{(POD)} \text{quinoneimine dye} + 4H_2O$$

where the quinoneimine dye formed in the above reaction exhibits absorption maximum at 510 nm. (Figure 6.4) For a known constant amount of glucose, the activity of glucose oxidase can be defined by the rate of dye formation, which corresponds to the slope of the absorbance vs time plot and can be obtained by monitoring the absorbance at 510 nm with respect to time. In our measurement, the sample did not show any activity for the first few minutes due to the time needed for the dye molecules to disperse into the region of the cuvette exposed to the radiation.

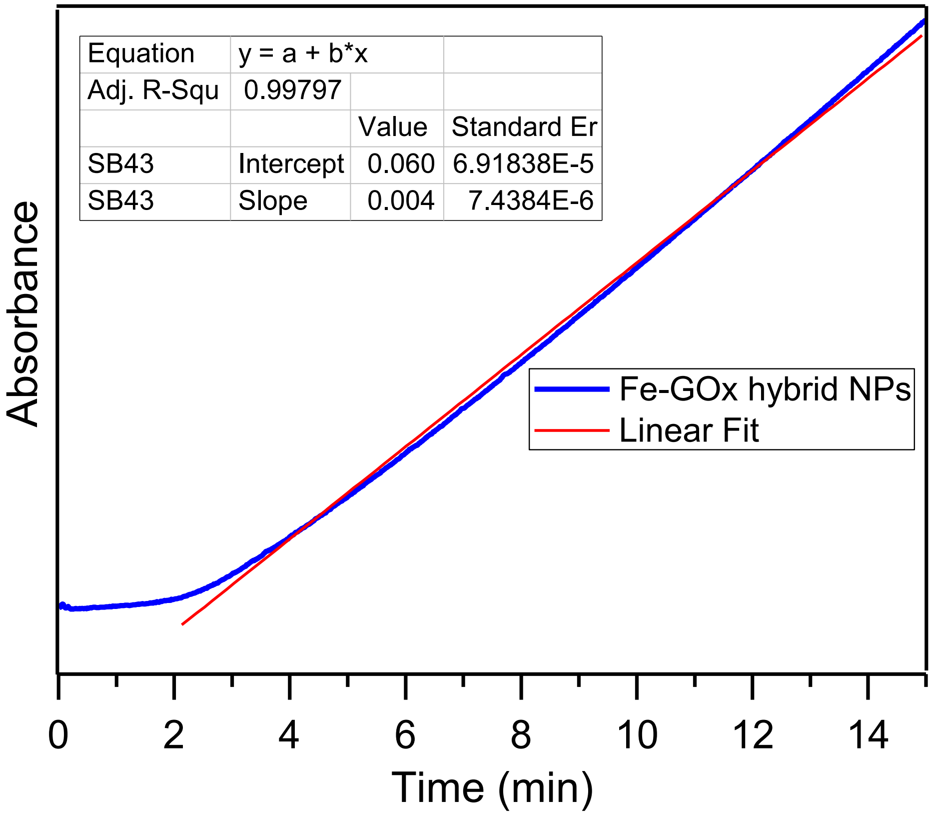

Figure 6.4 Absorbance of the feature at 510 nm for a glucose assay as a function of time, used for the activity test of Fe-GOx hybrid nanoparticles.

The characteristic absorption band of the dye at 510 nm is found to become more intense over 15 min, which indicates that GOx remains bioactive upon hybridization into the NPs. After the bioactivity test, the sample was washed thoroughly with filtered deionized water, which also makes the porous structure of the HNPs more obvious (Figure 6.3c). The appearance of the porous structure suggests diffusion of glucose into the Fe-GOx HNPs to reach the active sites of GOx, which causes the nanograins to cluster into larger grains resulting in a more porous appearance for the NPs. The average nanocrystallite size also increases from 18 nm to 24 nm as estimated from their respective XRD patterns (Figure 6.3d). This suggests the presence of GOx in the deeper layers of NPs and not just on the surface. It should be noted that the XRD features obtained after the activity test also correspond to the bcc phase of metallic Fe. We also soaked the Fe-GOx HNPs in H_2O_2 overnight. No increase in porosity or grain clustering was observed, which confirms that such an increase in porosity is caused by glucose reaction with HNPs, thereby validating the unique activity of the HNP. No increase in porosity was observed upon the glucose activity test on the pristine Fe NP sample (i.e. without GOx).

The presence of nanosized grains throughout a HNP can also be observed in the tomography images obtained by using the multi-cross-sectional imaging technique in a FIB-SEM.[296,297] This technique allows us to observe nanostructures buried within the bulk with a spatial resolution of 10 nm. The SEM image obtained with the back-scattered detector in Figure 6.5a shows the top view of two Fe-GOx HNPs, with the lines marking the vertical cut locations for the selected cross-sectional images, shown in Figure 6.5b-f. The black spots inside the NPs correspond to voids and/or elements with lower masses, likely reflecting the locations of GOx, among the brighter Fe nanocrystallites. From the series of cross-sectional images, it is evident that the observed HNPs consist of very small Fe subunits of nanocrystallites separated by voids and/or organic materials. The fairly uniform distribution of these GOx locations observed inside the nanoparticles leads us to propose a “stone-and-mortar” model for the hybrid nanoparticle, shown schematically in Figure 6.5g. In this model, individual nanograins (in a Fe-GOx HNP) consist of Fe nanocrystallites “sticking” together by GOx molecules. Inside a nanograin, GOx could serve as the substrate, providing nucleation sites for Fe crystallization, which could proceed by reduction of $FeOH^+$ ions adsorbed on the GOx substrate through its interaction with the partially negative amino acid components (e.g. glutamate and asparatate) of the GOx. $FeOH^+$ ions undergo adsorption onto the GOx followed by reduction to metallic Fe, i.e. $FeOH^+(ads) + H^+ + 2e^- \rightarrow Fe + H_2O$. However, to distinguish between an actual void and an organic intermediate layer would require additional analysis by a complementary method, such as three-dimensional chemical imaging provided by the SIMS technique.

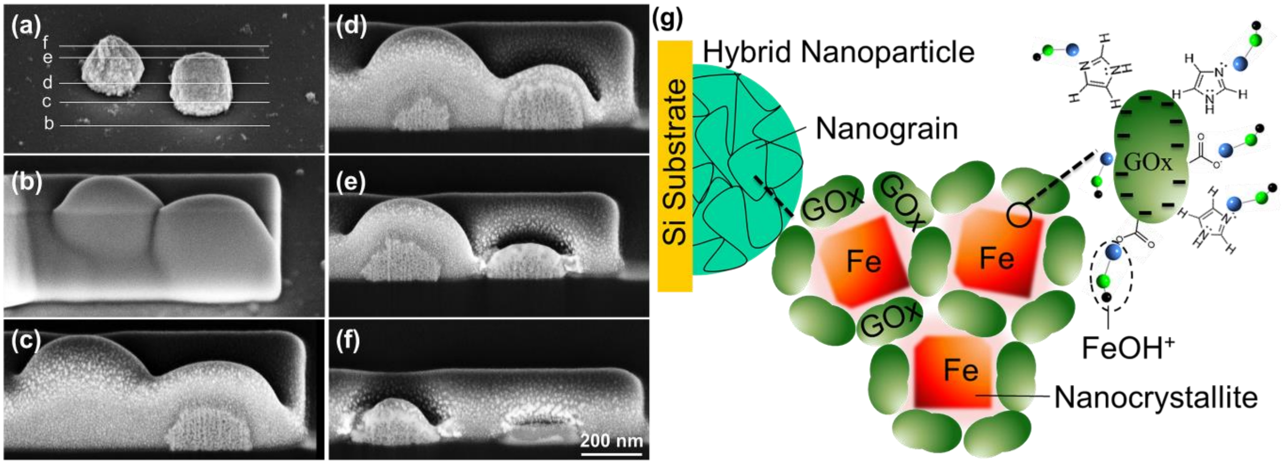

Figure 6.5 Back-scattered electron SEM images of (a) the top view of two Fe-GOx hybrid nanoparticles (HNPs) before cross-sectional imaging, and (b-f) cross-sectional views of selected vertical cuts at the locations marked in (a). (g) Schematic "stone-and-mortar" model for Fe-GOx HNPs electrodeposited on a Si substrate.

One possible configuration for the hybridization of Fe and GOx is that the NPs consist of nanocrystallites individually covered by GOx. In this configuration, it should be possible to observe the GOx inside the NP even when all the GOx molecules on the surface of the NP are removed. To confirm the presence of GOx along with Fe inside the HNPs, we conduct 3D chemical imaging by TOF-SIMS. This method enables us to probe the composition of the bulk materials at different depth, which makes possible studies not just of 3D composition of biomaterials but also of diffusion of a component into a semiconductor material.[75,298] We have chosen relatively large HNPs (2.5 μm) for this experiment in order to increase the accuracy of the characterization, but the results are expected to be similar for all sizes. A 300×300 μm^2 area of the sample was pre-cleaned with O^{2+} sputtering for 5 s before imaging. The secondary ions were mass-separated in a 2 m long TOF reflectron analyser, and the appropriate secondary ions Fe^+, $NaNH^{2+}$ for GOx, and Si^+ were collected over a rastered sampling area of 100×100 μm^2 to obtain a 2D map. The sample was then sputtered with O_2^+ to remove the sample layer-by-layer at a well-defined sputtering rate. The 2D maps were collected interleavingly between the sputtered layers as a function of sputtering depth to obtain the depth profiles and to construct the corresponding 3D images of the Fe, GOx and Si components. Figure 6.6a shows the 3D images obtained for three component ions and their overlap (total) for a typical sample of HNPs. The presence of the enzyme component only on the Fe component (i.e. nanoparticle) and not on the bare surface of the Si substrate can clearly be seen in the corresponding topmost 2D maps shown in Figure 6.7.

We also show as insets in Figure 6.6a a magnified view of a selected area of the topmost 2D maps marked by a small square in Figure 6.6a, top rightmost panel. Figure 6.6b shows the YZ cross sections of the respective 3D images in Figure 6.6a for a selected X position. Evidently, the concurrence of component intensities at the same location shown in Figure 6.6b further confirms the presence of both Fe and GOx throughout the NPs, indicating their hybrid nature. The YZ cross-sectional maps are plotted with an extended Z scale to better illustrate the details in the depth direction. The similar decreasing trends found for the Fe and GOx components with depth are also clearly observed in the corresponding depth profiles shown in Figure 6.8.

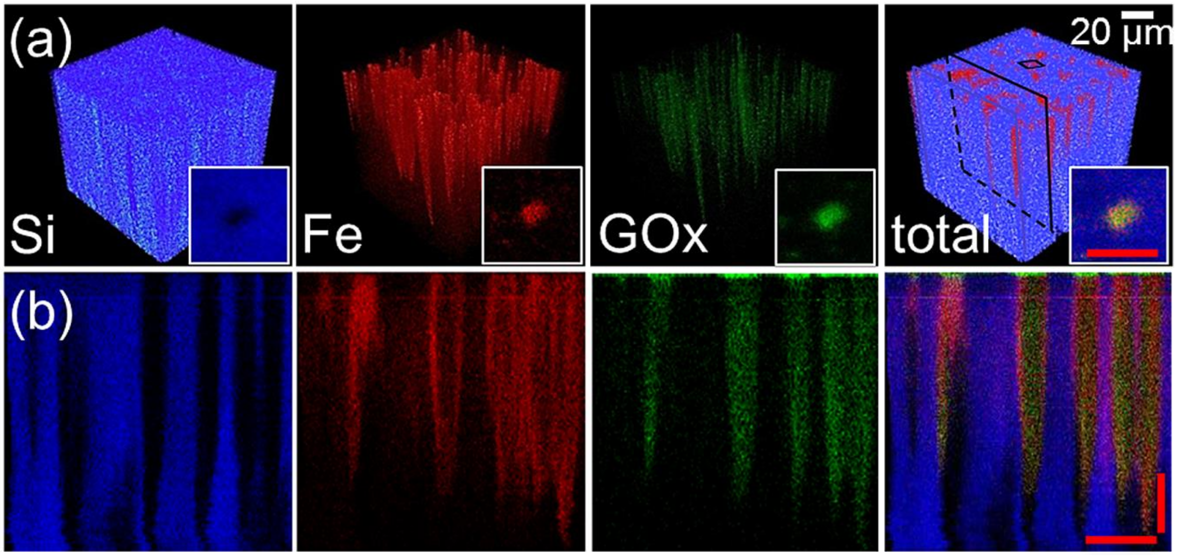

Figure 6.6 (a) TOF-SIMS 3D images of Si^+ (blue), Fe^+ (red), and $NaNH^{2+}$ (corresponding to GOx; green), and their overlap (total) for Fe-GOx hybrid nanoparticles (HNPs) on a 100×100 μm^2 area of the sample, with the insets depicting their corresponding topmost 2D maps of a selected Fe-GOx HNP in this sampling area (marked by small square in top rightmost panel). The scale bar for the insets is 2 μm. (b) Selected YZ cross sections of the corresponding 3D images of Fe-GOx HNPs (at an X location as marked in the image cube in (a), top rightmost panel). The horizontal (Y) and vertical (Z) scale bars correspond to 2 μm and 200 nm, respectively.

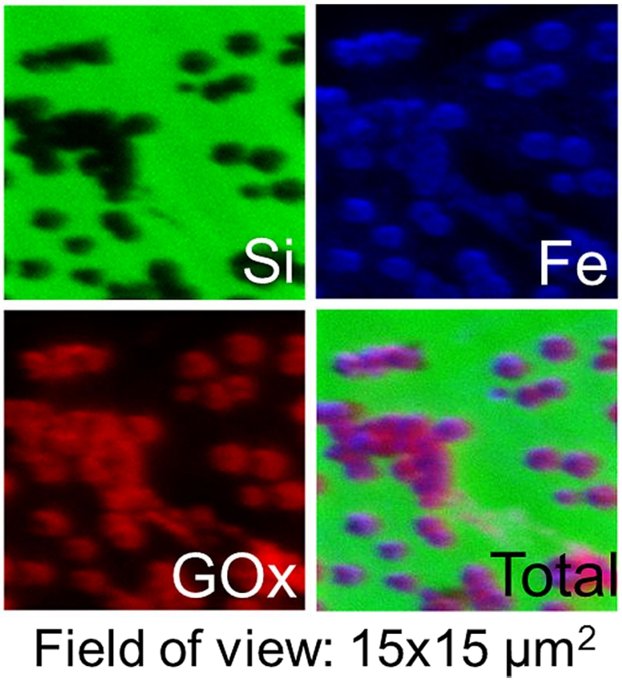

Figure 6.7 TOF-SIMS 2D images of Si^+, Fe^+, and $NaNH^{2+}$ (corresponding to GOx), and their summed image of Fe-GOx hybrid nanoparticles on a 15×15 μm^2 field of view of the substrate. It is obvious that GOx only presents on the Fe NPs and not on the entire Si substrate.

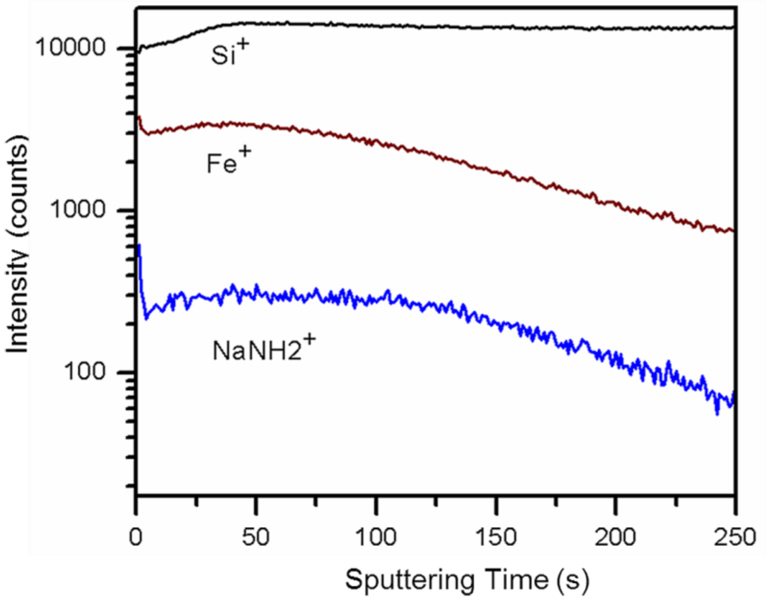

Figure 6.8 TOF-SIMS depth-profiles of Fe-GOx hybrid nanoparticles. The similar decreasing trends found for the Fe and GOx ($NaNH_2^+$) components show the intermixed nature of the hybrid nanoparticles.

The depth-profile XPS data shown in Figure 6.9 provides collaborative support for our SIMS observation. For the as-prepared sample, the C 1s peaks at 284.8 eV, 286.2 eV, and 288.4 eV can be attributed, respectively, to the C–H, C–O, and C=O components of the amino acid side chains of the polypeptide backbone of GOx.[299,300] Similarly, the N 1s features at 398.9 eV and 400.2 eV correspond to the NH_2 and NHC=O components,[301,302] respectively. Upon sputtering for 110 s, dramatic reductions in the intensities of these C 1s and N 1s components are observed. Additional C 1s feature found at 283.3 eV and N 1s feature at 397.3 eV can be assigned to C–Fe[303] and N–Fe features,[74] respectively, indicating the interaction between GOx and Fe nanocrystallites. After 290 s of sputtering, the Fe $2p_{3/2}$ peak at 710.0 eV and the shoulder emerged at 707.1 eV can be attributed to Fe oxides and metallic Fe, respectively.[74] From our sputtering rate, we estimate that this initial sputtering corresponds to the removal of a 4-5 nm thick layer of material, consistent with one monolayer of physisorbed GOx (uniformly distributed on both the HNPs and Si substrate). Continued sputtering for over 650 s reveals that the relative-intensity reductions of the C–Fe and N–Fe features parallel those of the other C and N components of GOx and of the metallic Fe. The similar trends found in the intensity reductions, along with the presence of N and C even after extended Ar sputtering (into the deeper layers), provide strong support for the intermixing of GOx with Fe nanocrystallites inside the HNP.

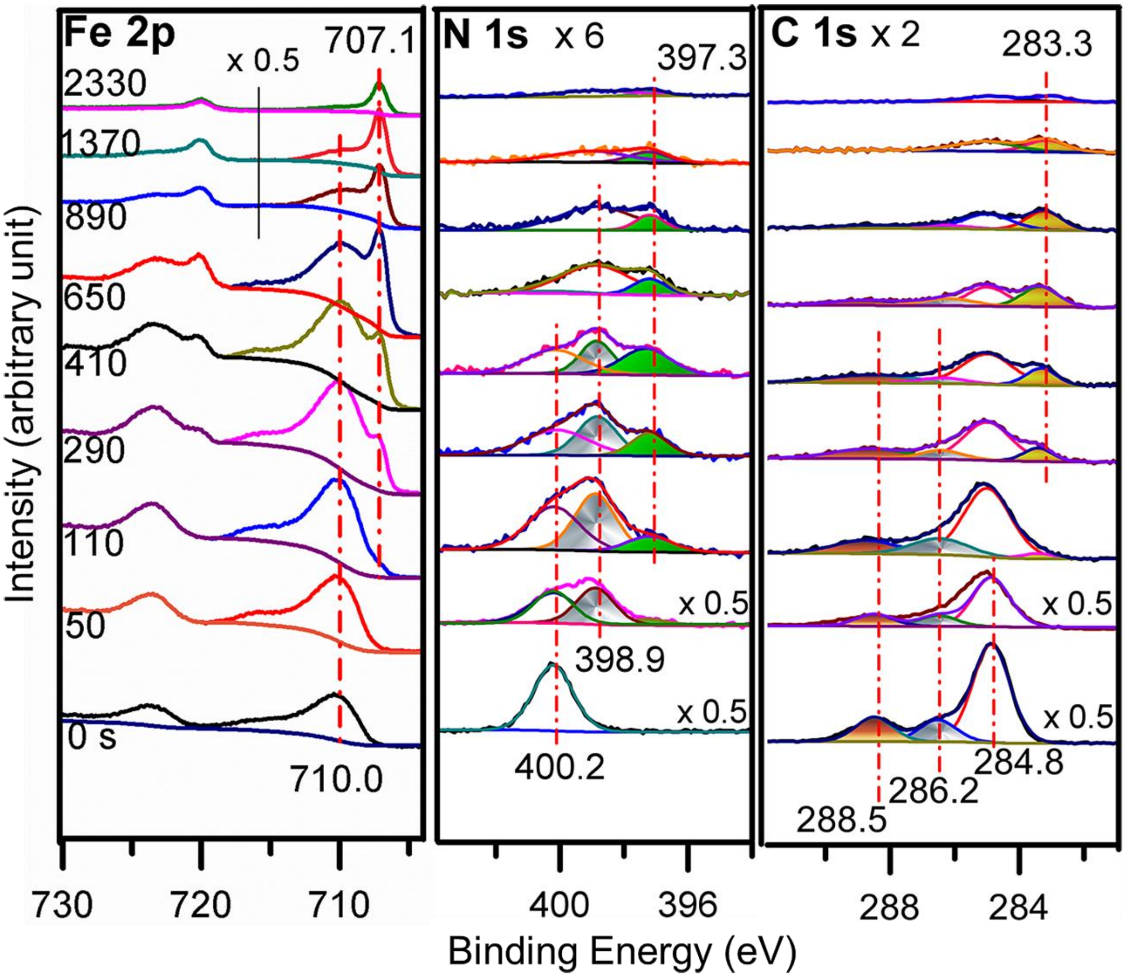

Figure 6.9 Depth-profiling XPS spectra of Fe 2p, N 1s, and C 1s regions for the as-prepared Fe-GOx hybrid nanoparticles and upon Ar sputtering for 50, 110, 290, 410, 650, 890, 1370, and 2330 s.

To further investigate the nature of the Fe–C and Fe–N bonds found between GOx and Fe before formation of the HNP and the role of these bonds in the evolution of the HNP, we prepared drop-cast thin films of electrolytes containing GOx with $FeCl_2$ (Fe-GOx electrolyte) and without $FeCl_2$ (GOx electrolyte) before amperometry. Their C 1s and N 1s spectra are compared with those of HNPs (after 290 s of sputtering) in Figure 6.10. (It should be noted that a brief sputtering was used to remove any surface carbonaceous layer often found due to sample handling in air.) Evidently, the drop-cast film of the Fe-GOx electrolyte exhibits all the C 1s and N 1s features as those of the GOx electrolyte, but with additional C 1s peak at 283.3 eV and N 1s peak at 397.3 eV. The similar relative intensities of the common C 1s and N 1s features for the GOx electrolyte to those found for Fe-GOx electrolyte indicate that the GOx molecules interact with Fe without dissociation. The observed additional features for the Fe-GOx electrolyte are found at the same binding energy locations as the respective features in the Fe-GOx HNPs, which indicates that the HNPs contain Fe-GOx complexes as their building blocks (before nanocrystallite formation). The differences in the relative intensities of the C 1s and N 1s features for Fe-GOx HNPs from those for the drop-cast film of Fe-GOx electrolyte suggest that there are more GOx interactions with Fe involving the NHC=O group and C–O group in the HNPs than the drop-cast film.

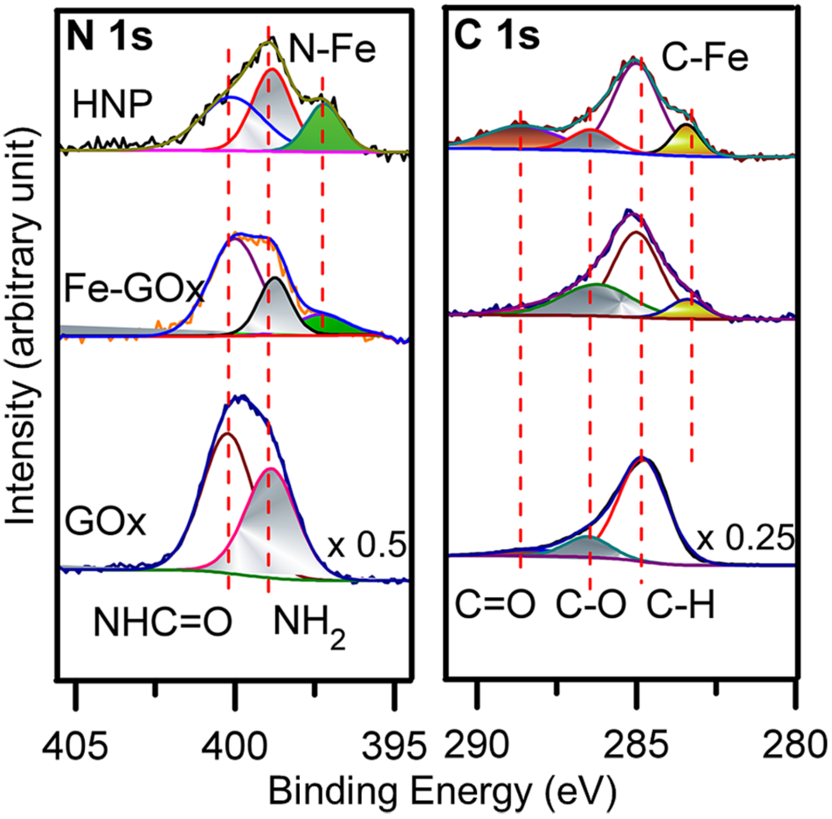

Figure 6.10 XPS spectra of N 1s and C 1s regions for drop-cast films of pristine GOx and of Fe-GOx electrolytes, and for Fe-GOx hybrid nanoparticles (HNPs), all after 290 s sputtering.

In order to investigate the biocompatibility of the Fe-GOx HNPs, we studied the effect of HNPs on cell proliferation. To be safe for use in the human body, Fe oxides usually need to be coated with a biocompatible shell. These shells are mainly polymeric materials that should be water soluble and non-cytotoxic. However, in addition to adding an extra step to the synthesis, the main drawback of polymeric coating is their poor long-term chemical stability of the inorganic core.[304–307] We therefore have not used any coating in the present experiment. In particular, we used the Fe-GOx NPs directly deposited on an ITO-glass substrate and evaluated their effects on HeLa cells. In the present experiment, we employed ITO-glass instead of H-Si as the conductive substrate in order to obtain optical images of the samples. It should be noted that the respective SEM images show no difference in the morphologies of HNPs deposited on ITO-glass and H-Si substrates. HeLa cells were seeded on ITO-glass substrates with the pre-deposited Fe-GOx HNPs, and cell growth was then monitored by bright-field optical microscopy for 5 days (Figure 6.11a). Some parts of the samples were scratched to remove the HNP cell seeding, and these were used as the control so as to allow comparison with the areas with HNPs. As shown in Figure 6.11b, cell seeding density, morphology, and growth appear to be similar in the bright regions (without HNPs) and in the darker areas (with HNPs). In other words, the cells are able to grow on the substrates coated with the Fe-GOx HNPs as on substrates without the Fe-GOx HNPs.

Furthermore, in order to metabolically quantify the amount of active cells after exposure to Fe-GOx HNPs, we performed MTT (3-[4,5-dimethyl-2-thiazol]-2,5-diphenyl-2H-tetrazolium bromide) reduction experiments involving more delicate cells. Human hepatoma cells (Liver, PLC/PRF/5, ATCC No: CRL-8024) were cultured in Eagle's Minimum Essential Medium (EMEM) American Type Culture Collection (ATCC) with 10% fetal bovine serum and 1% penicillin-streptomycin. The cells were maintained in 5% CO_2 in humidity at 37 ºC. Before incubating the cells on the substrates, each substrate has been sterilized by first immersing in 70% ethanol thrice (10 minutes each), followed by PBS rinse. The substrates were subsequently irradiated with UV light for 2 hours before use. Liver cells (10,000 cells) were then seeded onto each substrate in a 12-well plate and incubated for 24 hours at 37 ºC. We employed the procedure for the MTT assay as outlined by the supplier (Sigma/Aldrich). Figure 6.11c depicts the results from the MTT assay, which has been performed in triplicates. Our results show quantitatively the cell population and activity on the three substrates coated with Fe-GOx HNPs compared to that on a plain ITO-glass used as the control. Only a slight difference is observed, indicating that these Fe-GOx HNPs are cell-safe and have no obvious detrimental effect on viability and cell growth.

Figure 6.11d shows the magnetization curve of the Fe-GOx HNPs (with an average size of 400 nm) as determined by using a VSM. Evidently, the lack of hysteresis, along with the observed 90 emu/g saturation magnetization, indicates that the Fe-GOx HNPs exhibit superparamagnetic behavior. Due to the metallic nature of Fe in Fe-GOx HNPs, the saturation magnetization has a much larger value than the reported values for superparamagnetic iron oxide NPs in the literature.[308,309] The high saturation magnetization is especially important for NPs when they are used as a contrast agent for MRI application. It should be noted that the size of the superparamagnetic NPs cannot exceed 10 nm for Fe oxide and 20 nm for Fe.[310–312] However, for in-vivo applications, magnetic NPs should have an appropriate size of 10-100 nm to maintain longer circulation times, because NPs smaller than 10 nm are removed by renal clearance.[313] For this reason, they are usually coated with a (polymer or organic) shell to obtain the desired size.[308] The present superparamagnetic Fe-GOx HNPs are therefore quite remarkable because the size of superparamagnetic HNPs can be easily controlled during the co-electrodeposition, thereby allowing us to eliminate the extra coating step. Since the present HNPs are much larger than the superparamagnetic NP size regime, the observed behavior supports our structural model shown schematically in Figure 6.5g. In other words, if the nanograins were just surface-functionalized by the GOx (i.e., without any hybridization), then the nanocrystallites inside a nanograin are not isolated from one another by the GOx. In this case, the NP should exhibit ferromagnetic and not the observed superparamagnetic behaviour.

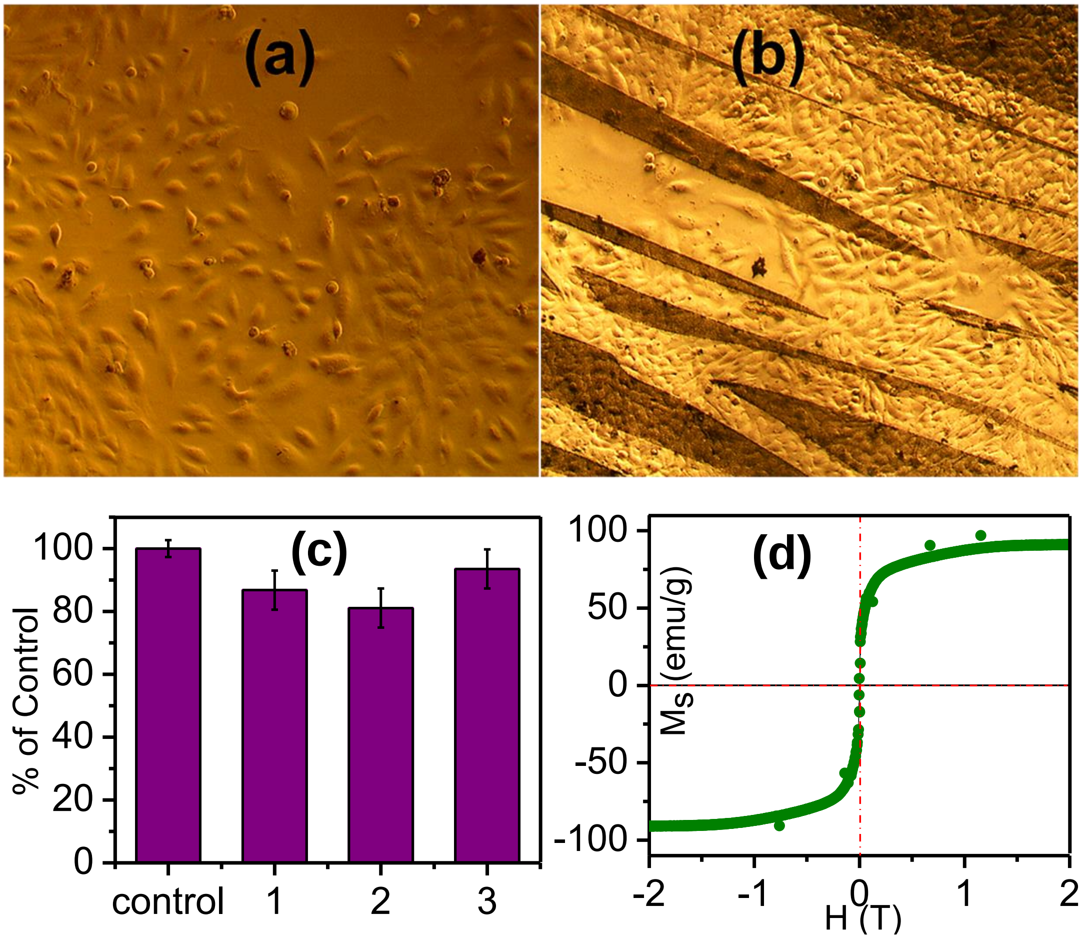

Figure 6.11 Optical images of HeLa cells grown on ITO–glass substrate coated with Fe-GOx hybrid nanoparticles (HNPs), 400 nm in average size, after 5 days: (a) without and (b) with sample scratching. (c) MTT data quantifying consistently high viability of human hepatoma cells after 5 days of culturing on three separate ITO-glass substrates coated with Fe-GOx HNPs in relative to control (cultured on a plain ITO-glass substrate). (d) Magnetization curve of the Fe-GOx HNPs (with an average size of 400 nm).

To demonstrate the general applicability of the present approach to other biomolecules even with different sizes and the application of HNPs to targeted drug delivery, we prepared Fe-p53p HNPs at 4 °C by co-electrodeposition of Fe and p53p on a H-terminated Si(100) substrate in a three-electrode cell. (It should be noted that p53p is approximately 100 times smaller than GOx.) The electrolyte solution consisted of 5 mM $FeCl_2$ and 75 μM p53p and 200 mM boric acid. The pH was adjusted to 6.5 before adding p53p to the solution. Deposition was carried out at –1.2 V vs Ag/AgCl for different amounts of deposition time. Figure 6.12a shows the SEM image of typical Fe-p53p HNPs after 600 s deposition. The corresponding XRD pattern (Figure 6.12b) shows metallic Fe with an average grain size of 22 nm, which accounts for the observed rough surfaces of HNPs in the SEM image. Similar to Fe-GOx HNPs, these Fe-p53p HNPs also exhibit superparamagnetic behaviour with 60 emu/g saturation magnetization and no hysteresis (Figure 6.12c). The depth-profiling XPS spectra for the N 1s and C 1s regions in Figure 6.12d indicate the presence of N–Fe and C–Fe features at 397.3 eV and 283.3 eV, respectively. The emergence of these features only upon longer sputtering time (1400 s) confirms the intermixing of Fe with p53p in the core (i.e. sub-surface) region and the hybrid nature of NPs. To verify that the p53p in the HNP does not change after hybridization and preserves its bioactivity, we examine p53p-Mdm2 bonding ability. For this purpose, we incubated pristine Fe NPs and Fe-p53p HNPs in the solution of Mdm2-GST for 4 hours. We then washed both samples thoroughly with deionized water. The SEM images obtained after incubation show extra materials on top of Fe-p53p HNPs but not on pristine Fe NPs, which confirms the attachment of Mdm2 to p53p and therefore the bioactivity of p53p in the HNP (Figure 6.13).

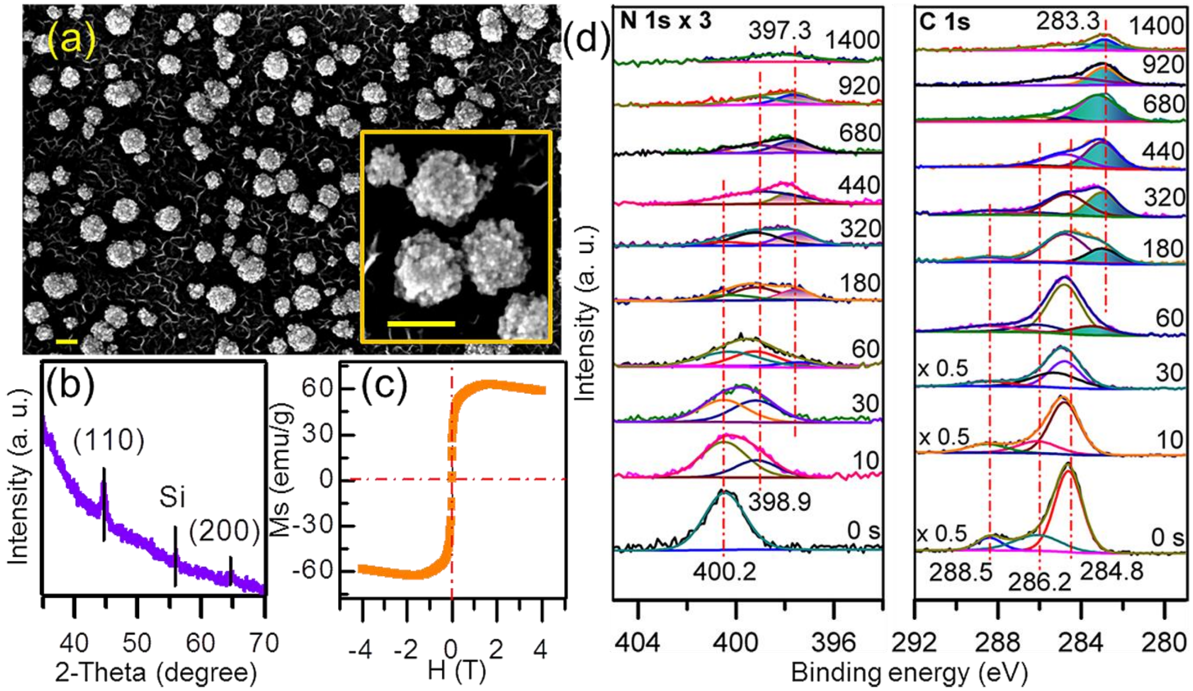

Figure 6.12 (a) SEM images (scale bars are 200 nm), (b) XRD pattern, (c) hysteresis loop, (d) depth-profiling XPS spectra of N 1s and C 1s regions of Fe-p53p HNPs obtained after 600 s deposition.

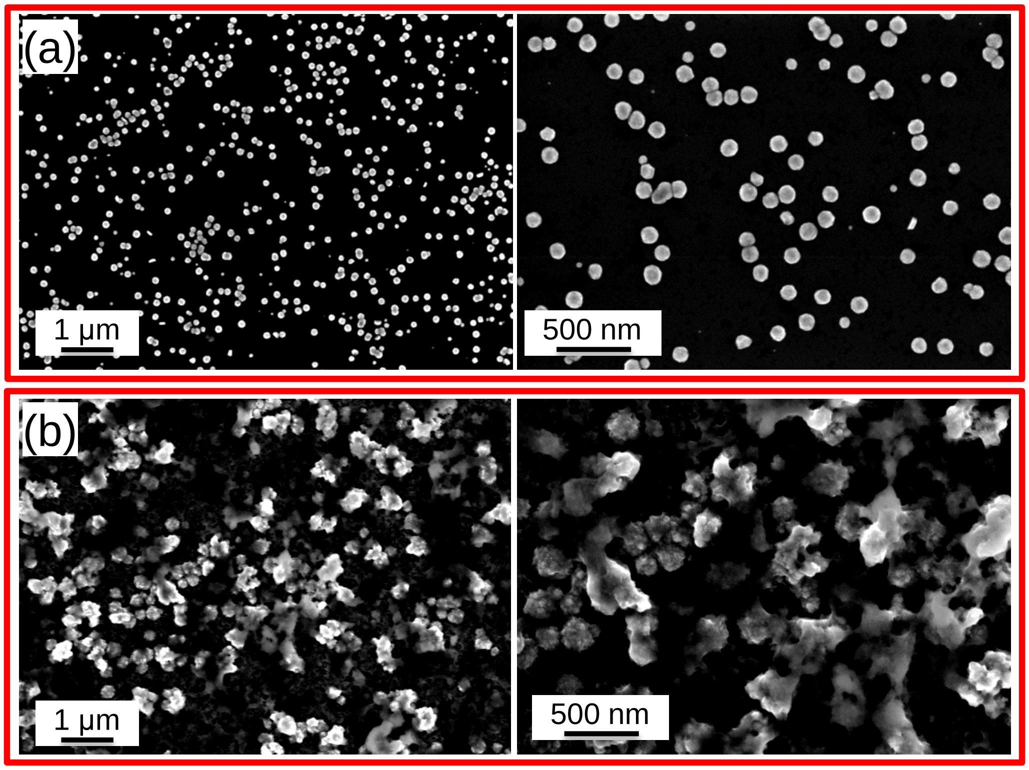

Figure 6.13 SEM images of (a) pristine Fe NPs and (b) Fe-p53p HNPs after incubation in Mdm2-GST solution.

6.4 Summary

In summary, Fe-GOx and Fe-p53p HNPs have been successfully obtained by electrodeposition of Fe-GOx and Fe-p53p complexes directly as the building blocks of the nanograins at 4 °C. We propose a “stone-and-mortar” architecture for the HNP, in which GOx or p53p molecules behave as the mortar to keep the Fe nanocrystallites together. HIM and FIB-SEM multi cross-sectional studies both show the nanograins interconnected to one another by the GOx or p53p molecules in the HNPs. Furthermore, both TOF-SIMS and depth-profiling XPS results further confirm the intermixed nature of the Fe-biomolecule NPs, in which the biomolecules are incorporated throughout the HNP without affecting their bioactivity. Of special interest is that hybridization of Fe-GOx and Fe-p53p HNPs is obtained by complex formation of Fe with the biomolecule (GOx or p53p) before deposition onto the substrate and the growth is maintained by these Fe-biomolecule complexes as the building blocks. Furthermore, these HNPs are found to be superparamagnetic and could be made with different desired sizes. As demonstrated by their apparent lack of a detrimental effect on cell growth, their biocompatibility, together with their strong magnetic properties, make these HNPs promising agents for MRI and targeted drug delivery systems. These HNPs can be easily harvested from the substrate and dispersed in an aqueous solution by sonication. Incorporating two different biomolecules with very different sizes confirms the general applicability of the present synthetic approach. The present method of incorporating bioactive molecules into magnetic (and non-magnetic) nanostructures is therefore not limited to GOx or p53p. Hybridization of GOx as a water-soluble enzyme and p53p as an anticancer peptide with magnetic nanostructures therefore offers an effective immobilization method to enable their use not only as reusable sensors and magnetic contrast agents, but also to greatly improve drug delivery and recovery systems.

Chapter 7

Concluding Remarks and Outlook

7.1 Summary

The goal of the present research is to design-and-build new materials with novel properties by hybridization of two or more components for sensing and bio-applications. These components could be two (or three) metals, or one metal with one organic or biomolecule, or one metal with one metal oxide. I have developed a fast, facile electrochemical method to synthesize metallic nanoparticles on conductive surfaces with excellent control of their shape and areal density. This method has been applied successfully to synthesize bimetallic or trimetallic nanoparticles. In the first part of this work (Chapter 3), a series of detailed studies on the synthesis and growth of FeNi as a bimetallic system with different compositions was presented. The effects of experimental parameters on the composition, shape and size of nanoparticles have been investigated. Some properties arising from combination of two metals, including air stability of the nanoparticles and enhanced sensing properties (toward detection of 4-aminophenol, a pharmaceutical waste product), are discussed. Differences in the magnetic properties of nanoparticles with the same composition but different shapes are also demonstrated. The companion computer modelling study provides support for our experimental observations. This work also illustrates the power of large-scale VASP calculations in simulating the structure-property relation in nanomaterials. I extended this one-pot approach to synthesize bimetallic nanoparticles of Fe-M (M = Au, Pt, Pd, Ni, Co, Cr) on silicon substrates (Chapters 4 and 5). The goal here is to use these bimetallic nanoparticles to introduce additional selectivity and reactivity towards different biomolecules. The studies demonstrate synergistic properties arising from the components of the hybrid composites, with particular focus on biosensing applications illustrating the enhancement of vitamin C detection by FePt nanoparticles and as an arsenic sensor based on FePt, FeAu and FePd nanoparticles. The role of different shapes of the same type of nanoparticles in the sensing properties is also presented.

In the latter part of the present work (Chapter 6), I introduced a novel electrochemical approach for in-situ embedding (i.e. encapsulating) biomolecules during nanostructure growth, without the risk of denaturation by manipulating the growth at a low deposition temperature (near 0°C). This study demonstrated hybridization of Fe with biomolecules of different size, including the enzyme glucose oxidase (Fe-GOx) and an anticancer peptide (Fe-p53d). It is important to point out that this approach is general, allowing hybridization to be applied to virtually any positively charged metal ion and partially negative protein. In-vitro toxicity assessment of Fe-GOx HNPs has also been performed and showed no adverse effect, while Fe-p53p HNPs were found to selectively bind to cancer cells. Furthermore, p53p and GOx act as protective shells, preventing oxidation, for metallic Fe nanocrystallites. This study further illustrated the remarkable superparamagnetic properties of these unique nanoparticles in the large-size regime (30 to 3500 nm). In addition, this study showed that Fe-p53p HNPs can selectively bind to Mdm2 and MdmX, which are over-expressed in nearly 50% of cancers and can therefore inhibit p53p anticancer activity, providing a promising anticancer therapeutic and imaging agent. For Fe-GOx HNPs, our results showed that these hybrid nanoparticles exhibit no detrimental effects on cell growth of very delicate cells (such as human hepatoma cells), which make them excellent, bio-friendly material for use as magnetic resonance contrast agents requiring cell-friendly magnetic nanoparticles.

7.2 Conclusions and New Findings

This thesis presents the successful synthesis of hybrid nanoparticles including bimetallic FeM nanoparticles (M=Ni, Pt, Au, Pd) and Fe-biomolecule (biomolecule=glucose oxidase, p53p protein) using electrochemical deposition method. The growth mechanism of bimetallic nanoparticles, formation of different shapes, surface crystalline facets and shape dependent properties have been investigated by performing extensive characterization on these nanoparticles. The results of these studies show promises in controlling the size and shape of hybrid nanoparticles, while the effect of composition on the shape, shape-dependent magnetic properties and chemical sensing performance are also studied systematically. For the Fe-biomolecules study, the biocompatibility and magnetic properties are also investigated and the hybrid NPs are found to be good candidates for magnetic resonance imaging (MRI) agents or drug delivery vehicles. The present study provides the following new, significant findings:

7.2.1 A simple synthetic hybridization method for shape-controlled nanoalloys

We show that a simple room-temperature technique can be used to synthesize FeNi alloy nanoparticles of well-defined shapes and narrow size distributions without the use of surfactants.

This approach makes use of co-electrochemical deposition in electrolytes of well-controlled compositions and can be generalized to other bimetallic alloy systems, including FeCo, FeZn, and NiCo. We observed the shape evolution of NPs from concave nanocubes to truncated nanospheres by changing their composition. The formation of FeNi concave nanocubes is an unexpected but very interesting result because such a shape is well known to be thermodynamically unfavorable. We correlate the evolution of the crystal structures of these alloy nanoparticles with the change in the particle shape and illustrate the importance of the "guest" crystal structure in modifying the final morphology of a "host" lattice.

We also developed our method for making concave nanocubes and nanocages. We prepare bimetallic FeNi concave nanocubes with high Miller index planes through controlled triggering of different growth kinetics of Fe and Ni. To date, concave nanostructures could only be made by using surfactants or galvanic replacements, which were limited to noble metals. For non-noble metals, it has not been possible to make concave nanostructures with these methods due to their inherently high reactivity. By manipulating the growth kinetics involving a bimetallic system, we show here that it is indeed possible to produce FeNi concave nanocubes using a one-step, surfactant-free method. In the second step, we fabricate mono-dispersed concave nanocages by taking advantage of the higher activity of the high-index planes in a material-independent electroleaching process. Metallic nanocages have been traditionally prepared by first depositing thin shells of a metal on polymer or silica beads and then followed by removal of the beads by calcination or wet chemical etching, or by galvanic replacement reaction involving a less reactive metal. These methods suffer from the rather limited material options difficulties in removing the colloidal templates, poorly defined composition, and unwanted coupling in dealloying. The present synthesis method of cage-like nanostructures is material-independent and can be extended to any concave systems because etching is driven by the high activity of the high-index planes located at the cavity.

Another important achievement using the aforementioned method is that we could synthesize FeNi alloy nanoparticles with same composition but different shapes. Bimetallic systems especially FeNi has been subjected to many studies because of their interesting properties, but very few reports on the shape-dependent magnetic properties of bimetallic nanosystems have been published, presumably because there is virtually no synthesis method that could produce nanoparticles with same composition but different shape was available. Here, we have successfully used a simple electrochemical method to obtain, for the first time, both FeNi concave cube and cuboctahedron nanoparticles with the same composition. High-resolution XPS analysis on these samples not only shows highly homogenous alloy NPs but also uncovers two new binding energy references for FeNi nanoalloys – Fe 2p at 707 eV and Ni 2p at 852.9 eV.

7.2.2 Improvements in properties by hybridization

Remarkable air stability and different magnetic properties: We have tested our FeNi nanoparticles and observed a remarkable resistance of these nanoparticles to oxidation in air. Our detailed depth-profiling XPS and TEM-EDX studies of FeNi nanocubes and nanospheres have identified the presence of 5-6 nm thin oxide shells, which accounts for the protection against oxidation. Of special interest is that the oxide shell is produced in-situ during the formation of the FeNi alloy nanoparticles, therefore eliminating an extra step in introducing this important property. We also study the shape-dependent magnetic properties of bimetallic materials system with a single composition experimentally for the first time. We investigate the dependence of magnetic properties as a function of the different two-phase combinations of two phases in FeNi NPs. By taking advantage of the unique nanoscale properties, we synthesized $Fe_{63}Ni_{37}$ alloy NPs in the mixed-phase region (i.e. coexistence of fcc and bcc phase) with two distinct shapes, for which the combination of fcc and bcc phases is different. This two-phase combination in effect causes the different NP shape observed, which can be used as a new parameter for tuning the magnetic property of alloys with a single composition. For both bulk and nanosize, magnetic properties of bimetallic alloys (including FeNi) with a specific composition but a different combination of bcc and fcc phases have not yet been reported. Certainly, these studies are very challenging in theory and experiment primarily, it has not been possible to make alloys with different two-phase combinations using a single method until now. We have obtained two different combinations of fcc + bcc phases for different shape nanoparticles. We have used VASP calculations to illustrate for the first time the important role of the two-phase combination in the magnetic properties of FeNi alloys in the mixed phase region of their phase diagram.

We also expand our hybridization method for synthesis of FeM (M=Au, Pt, Pd) and Fe-biomolecule (biomolecule=glucose oxidase, p53p protein) NPs and show the versatility of the method in obtaining different hybrid systems.

Enhancement in chemical sensitivity and selectivity: Hybridization is introduced to fabricate novel active nanomaterials for label-free sensing applications in monitoring toxins in water and pharmaceutical wastes and vitamin C. With the high-index facets exposed, the FeNi concave nanocubes and nanocages offer 10- and 100-fold, respectively, higher activities toward the electro-detection of 4-aminophenol than cuboctahedrons (with the convex surfaces). It should be noted that 4-aminophenol is an important organic compound that can be used for E. coli detection and as an intermediate or degradation product in synthesis of paracetamol in the pharmaceutical industry.

We also observed enhancement of the sensing properties for detection of vitamin C by FePt NPs compared to Pt NPs. FePt NPs were synthesized with three different compositions on Si substrate. Their sensing properties have been investigated and found to exhibit an enhanced sensitivity and selectivity toward vitamin C in comparison to Pt NPs. Alloying leads to reduction in the over-potential for vitamin C oxidation and greatly enhances the selectivity of FePt NPs to VC detection even in the presence of other common interference species, including dopamine, citric acid, uric acid, glucose, and NaCl.

In addition, we performed a systematic study of bimetallic FeM (M=Pt, Au, Pd) NPs for detecting ultra-low amounts of arsenic in neutral pH and with minimal interference from Cu(II). The synergistic effects resulting from alloy formation lead to better performance for the Fe-noble metal NPs (Au, Pt, Pd) compared to pristine noble metal NPs (without Fe alloying). Using precise measurement techniques capable of determining ppb levels, such as anodic stripping voltammetry, we determine and compare the sensitivities and limits of detection of the aforementioned bimetallic NPs for As(III) detection. We also show that As detection using these bimetallic NPs is not affected by interference of Cu(II) ions, as one of the most serious problems in arsenic detection. Unlike most of the non-enzymatic sensors that operate in highly acidic or basic environment, vitamin C and arsenic sensors not only could work at neutral pH but also show significantly enhanced sensitivity, detection limit, linear response range and a higher signal-to-noise performance.

7.2.3 A breakthrough impact on making and understanding a new class of hybrid bionanomaterials

The versatility of the new method for hybridization of organic-inorganic structures has been demonstrated by choosing two very different biomolecules in terms of structure and size. The functionality of the new hybrid nanostructures has also been illustrated by their biocompatibility and binding to cancer cells. It should be noted that the bioapplication of these hybrid nanoparticles are discussed here only as a potential but definitely not an exclusive application of these nanoparticles. This work has led to a novel and general method used for hybridization of two different species involving a biomolecule and an inorganic material.

New hybrid material and new hybridization method: Hybrid materials are very important in medicine and energy conversion applications because they not only maintain their original properties but also introduce new synergetic properties. Fe-biomolecule (p53p and GOx) hybrid nanoparticles are obtained for the first time by electrochemical deposition of Fe-p53p/GOx complexes, which are pre-formed in the electrolyte by pH adjustment and used as the building blocks for the hybrid nanoparticles. We have chosen an anticancer peptide (p53p) and an enzyme (GOx) as model molecules to demonstrate the versatility of the method towards different types of biomolecules with vastly different sizes (1.8 kDa vs 160 kDa). It is important to point out that this approach is general, allowing hybridization to be applied to virtually any positively charged metal ions and partially negative proteins. In vitro toxicity assessment of Fe-GOx HNPs showed no adverse effect and Fe-p53p HNPs were shown to selectively bind to cancer cells. Furthermore, p53p and GOx act as a protective shell from oxidation for the metallic Fe nanocrystallites.

3D characterization by multi-cross-sectional FIB-SEM and SIMS chemical imaging: We confirm the nature of the hybrid nanoparticles by detailed characterization using advanced 3D methods, including SIMS chemical imaging and multi-cross-sectional FIB-SEM analysis. We show that these characterization tools are essential for proper characterization of integrated nanostructures with multiple components.

Superparamagnetism of nanoparticles in the large-size regime: Hybridization of p53p/GOx with Fe introduces superparamagnetic behavior for the Fe-biomolecule hybrid nanoparticles in the large-size regime (30 to 3500 nm), which is a big challenge. Isolation of Fe nanocrystallites (18 nm) by the biomolecule accounts for this extraordinary property of these much bigger hybrid nanoparticles. It should be noted that the Fe nanocrystallites consist primarily of metallic Fe (i.e. not iron oxide), which gives rise to large saturation magnetization, making these hybrid nanoparticles important for applications requiring strong magnetic properties. As the size of the Fe-GOx hybrid nanoparticles can be easily controlled, the present technique can therefore be used to make superparamagnetic nanoparticles of a specific desirable size.

Targeted drug delivery and magnetic resonance imaging contrast agents with cell-friendly hybrid nanoparticles: Fe-p53p HNPs can selectively bind to Mdm2 and MdmX, which are over-expressed in nearly 50% of cancers and inhibit p53p anticancer activity, providing a promising anticancer therapeutic and imaging agent. In vitro toxicity assessment showed that Fe-P53 HNPs selectively bind to Mdm2 after hybridization. For Fe-GOx HNPs, we showed that these hybrid nanoparticles exhibit no detrimental effects on cell growth of very delicate cells (i.e. human hepatoma cells), which make them bio-friendly and excellent material as a magnetic resonance contrast agents requiring cell-friendly magnetic nanoparticles. The present work not only introduces the strategy of direct incorporation of two components (metal and biomolecule) into a hybrid structure, but also demonstrates their new application as targeted drug delivery and magnetic resonance imaging contrast agents.

7.3 Future Work

In this thesis, we demonstrated that the electrochemical technique is a powerful method for synthesis of bimetallic and hybrid nanoparticles. In particular, bimetallic FeM (M=Ni, Au, Pt, Pd) nanoparticles have been synthesized. A further step would be is to use the same method to synthesize different combinations of metals and trimetallic nanoparticles. Alloys of Co and Cr are good candidates because of their interesting magnetic properties and their air stability and acid resistance when produced in the alloy form. We have showed that by changing the composition of FeNi NPs we can control their final shape at room temperature. We also showed that by changing the synthesis temperature from room temperature to 4 C, we can obtain different shape with the same composition. These studies can be extended by examining the effects of different electrolytes on the synthesis, shape and composition of bimetallic NPs. We have also shown that FeNi NPs containing 65% Fe contain in grains with both fcc and bcc phases present. The ratios of these phases were different for different shapes and we have investigated the role of mixing these phases on controlling the magnetic properties of bulk FeNi alloys by VASP calculations (Chapter 3). Experimental confirmation of these results will be of great interest and could be achieved by making bulk FeNi alloys (or other bimetallic systems) with different ratios of the two phases or by synthesis of these NPs with same shape but different phase combinations.

Another important future project will be the investigation of the chemical sensing properties and performance of these bimetallic nanoparticles. Indeed, we have already performed a few primary experiments involving the use of FeNi NPs toward detection of 4-aminophenol (Chapter 3) but more work is needed to design and build a commercial sensor based on these bimetallic NPs. We have also showed that concave nanocages can be produced by electroleaching of concave nanocubes driven by the high activity of the high-index planes located at the cavity. We introduced a controlled electroleaching process by applying cyclic voltammetric waves from –0.1 V to 0.5 V (vs Ag/AgCl) in a 10 mB PBS solution with pH = 3. By controlling the number of CV scans, we could increase the concavity and eventually hollow out the interior of the nanocubes, producing concave nanocages. These nanocages have been found to exhibit much higher activities toward the detection of 4-aminopehol (used as a test molecule). The same method can be used to synthesize other hollow structures for sensing application and for other application including drug carriers that need more surface area for drug loading.

Investigation of the sensing properties of hybrid NPs led to the design of a vitamic C sensor based on FePt NP electrodes (Chapter 4). FePt NPs with three different compositions were fabricated by a single-step electrodeposition method. These spatially well-separated nanoparticles consist of 7-9 nm grains exhibit mixed alloy composition and have a significiantly enhanced for vitamin C in comparison to Pt NPs. We could increase the sensitivity of the sensor even more by increasing the electroactive area of the electrode by replacing our flat Si substrate with a Si-nanowires substrate. Si nanowires can be prepared by chemical etching of the Si(100) substrate in a 5M HF and 0.02 M $AgNO_3$ solution at room temperature for 10 minutes and followed by dipping in a HNO_3:H_2O (3:1) solution for 30 minutes (to remove the Ag deposits).[212,213] To further enhance sensing properties, the next step would be the synthesis of different Fe-Pt nanostructures (e.g. nanotubes or nanowires) or coating FePt NPs on carbon nanotubes or other conductive substrate with high active surface area instead of Si.

We have also showed the synergetic effect of alloying in bimetallic NPs for enhanced arsenic sensing performance in Chapter 5. We have prepared bimetallic FePt, FeAu, FePd and AuPt NPs with narrow size distributions and uniform spatial densities on Si substrate and studied their sensing properties to detect ultra-low amounts of arsenic systematically. FePt has showed the best performance among these NPs. Of special interest here is removal of arsenic from drinking water after its detection. Usually oxide NPs are used for this purpose. One future project will involve the synthesis of hybrid NPs that can do both tasks (detection and remediation) at the same time. In a preliminary study, we have attempted to synthesize Au and Pt decorated FeOOH NPs, containing many pores in the oxide nanostructure. The results are not presented in this thesis, because a more complete study is needed to optimize the nanostructure and to fully develop the simultaneous sensing and removal procedure.

The results obtained for hybridization of Fe-biomolecules (Chapter 6) have opened up new prospects for designing new bio-nanomaterials. We have shown that our hybridization method can be used not only for different metal-metal hybrid NPs but also for metal-biomolecule NPs (e.g. Fe-biomolecules in Chapter 6). We demonstrated the biocompatibility of the NPs obtained by this method along with their extraordinary superparamagnetic property in large size regime. The next step in this area is to incorporate a drug molecule (e.g. a cancer killing drug) to the hybrid NPs. This can be done by making metal-drug hybrid NPs or integration of the drug molecule into as-prepared hybrid NPs and use the latter as a linker for this attachment. In this way, it will allow us to evaluate the drug transport by hybrid NPs to the tumor site and test the drug release on the site of interest. The feasibility of magnetic-field guided delivery using these superparamagnetic hybrid NPs as the drug carriers will be of particular interest.

Finally, one of the most important subjects in this research area is the biocompatibility of hybrid NPs and their toxicity to human body. We have demonstrated the biocompatibility of Fe-glucose oxidase and Fe-p53p NPs by in-vitro toxicity and selective cancer cell binding studies in Chapter 6. If a drug attached to these NPs or any other hybrid NPs is synthesized, proper biocompatibility test must to be done. Animal testing would be a good choice to test their circulation time and removal by renal clearance. To increase the drug loading capacity, we would fabricate three-dimensional magnetic superstructures using these nanoparticles as the building blocks. The drug carrier size could be made between 10 nm and100 nm in order to maintain longer circulation times because nanoparticles smaller than 10 nm are easily removed by renal clearance. On the other hand, in order to increase the drug loading capacity, the drug carrying constituents should be small. The proposed drug-carrying three-dimensional superstructures will be designed to break apart into bionanoparticles (with size less than 10 nm to allow them clear from the kidney) upon reaching the targeted (tumor) sites of interest. Much work remains to be done in this fascinating world of nanoscience and nanotechnology.

Appendix A

Permissions

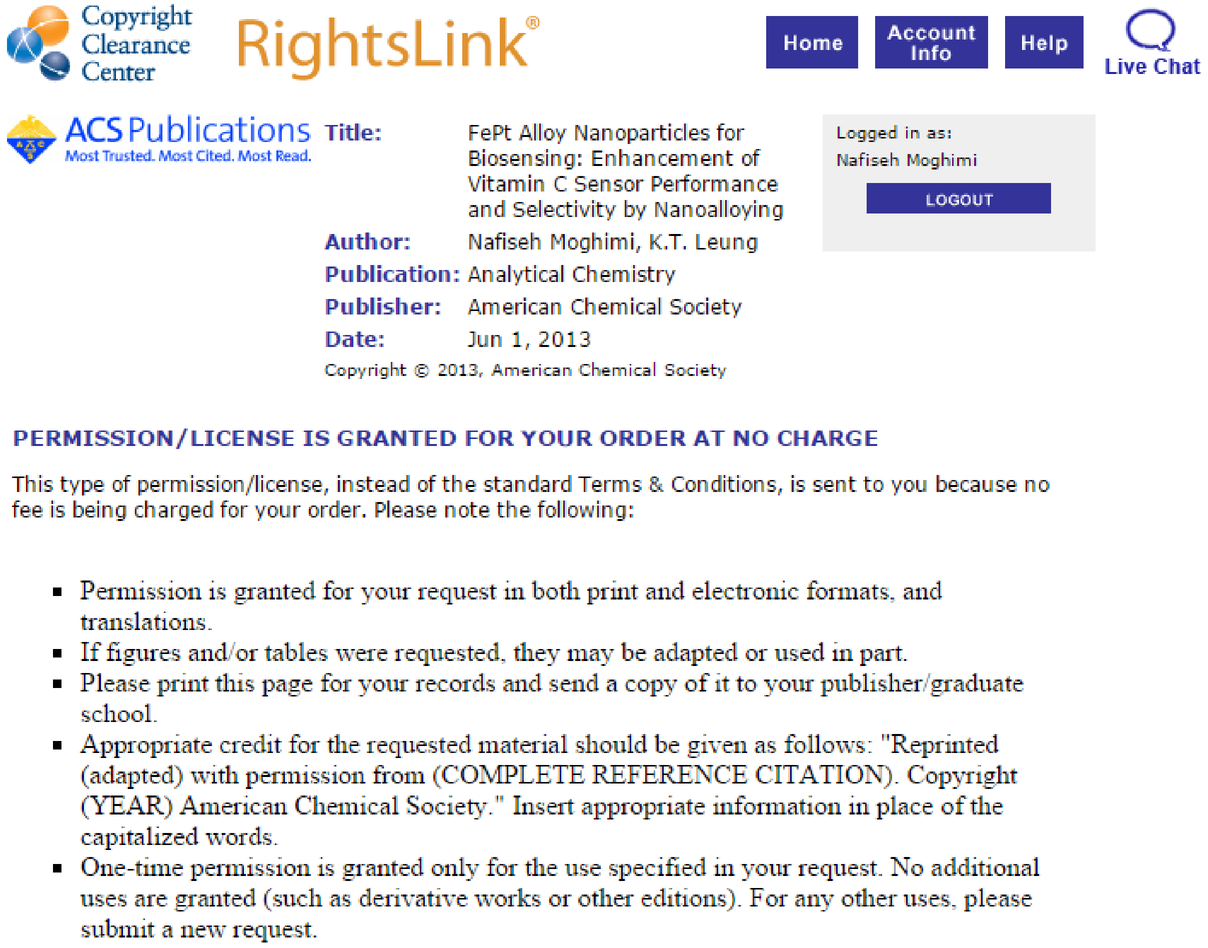

Title: FePt Alloy Nanoparticles for Biosensing: Enhancement of Vitamin C Sensor Performance and Selectivity by Nanoalloying

Author: Nafiseh Moghimi, K.T. Leung

Publication: Analytical Chemistry

Publisher: American Chemical Society

Date: Jun 1, 2013

Copyright © 2013, American Chemical Society

Logged in as:
Nafiseh Moghimi

PERMISSION/LICENSE IS GRANTED FOR YOUR ORDER AT NO CHARGE

This type of permission/license, instead of the standard Terms & Conditions, is sent to you because no fee is being charged for your order. Please note the following:

- Permission is granted for your request in both print and electronic formats, and translations.
- If figures and/or tables were requested, they may be adapted or used in part.
- Please print this page for your records and send a copy of it to your publisher/graduate school.
- Appropriate credit for the requested material should be given as follows: "Reprinted (adapted) with permission from (COMPLETE REFERENCE CITATION). Copyright (YEAR) American Chemical Society." Insert appropriate information in place of the capitalized words.
- One-time permission is granted only for the use specified in your request. No additional uses are granted (such as derivative works or other editions). For any other uses, please submit a new request.

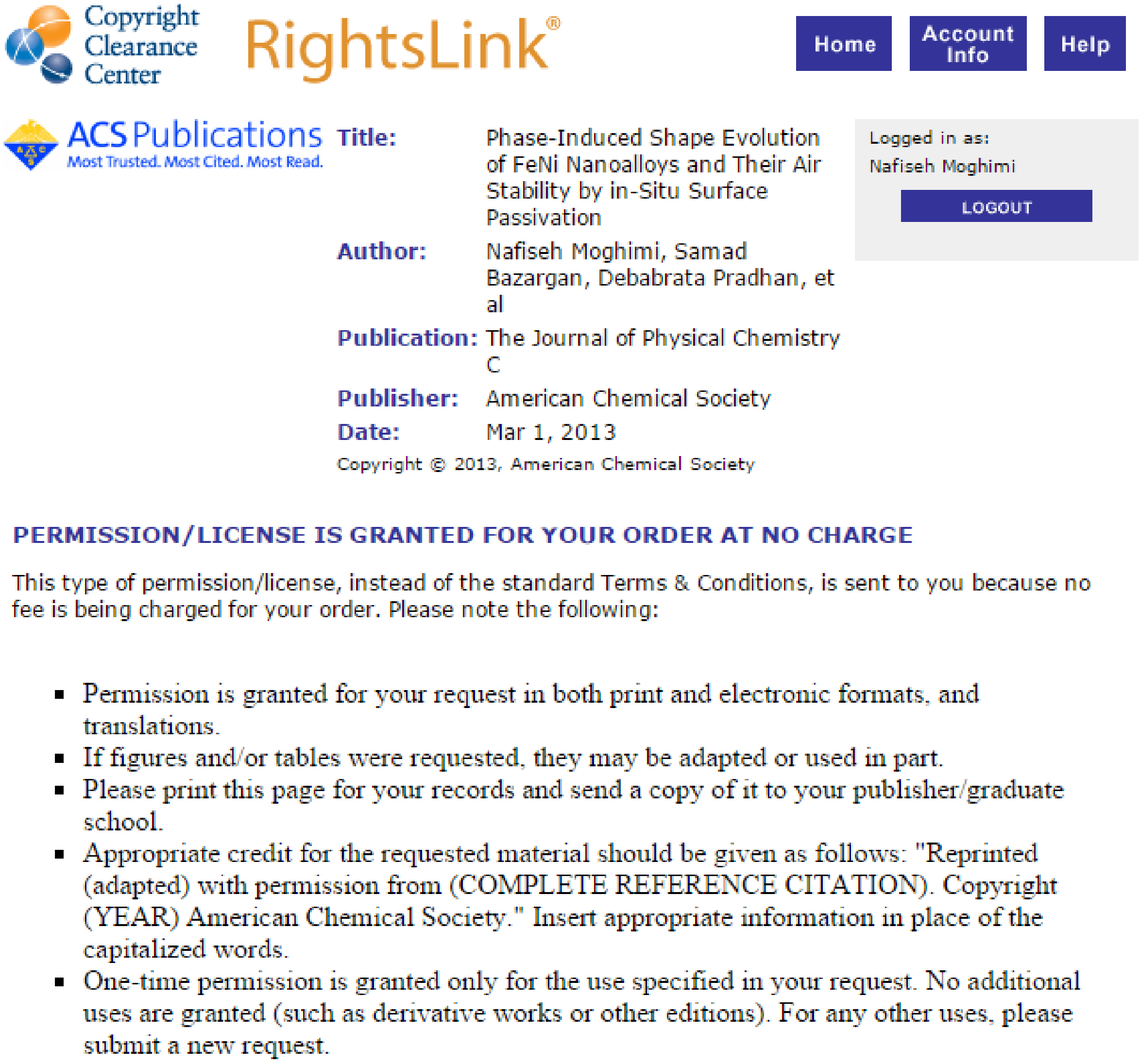

Title: Phase-Induced Shape Evolution of FeNi Nanoalloys and Their Air Stability by in-Situ Surface Passivation

Author: Nafiseh Moghimi, Samad Bazargan, Debabrata Pradhan, et al

Publication: The Journal of Physical Chemistry C

Publisher: American Chemical Society

Date: Mar 1, 2013

Copyright © 2013, American Chemical Society

Logged in as:
Nafiseh Moghimi

PERMISSION/LICENSE IS GRANTED FOR YOUR ORDER AT NO CHARGE

This type of permission/license, instead of the standard Terms & Conditions, is sent to you because no fee is being charged for your order. Please note the following:

- Permission is granted for your request in both print and electronic formats, and translations.
- If figures and/or tables were requested, they may be adapted or used in part.
- Please print this page for your records and send a copy of it to your publisher/graduate school.
- Appropriate credit for the requested material should be given as follows: "Reprinted (adapted) with permission from (COMPLETE REFERENCE CITATION). Copyright (YEAR) American Chemical Society." Insert appropriate information in place of the capitalized words.
- One-time permission is granted only for the use specified in your request. No additional uses are granted (such as derivative works or other editions). For any other uses, please submit a new request.

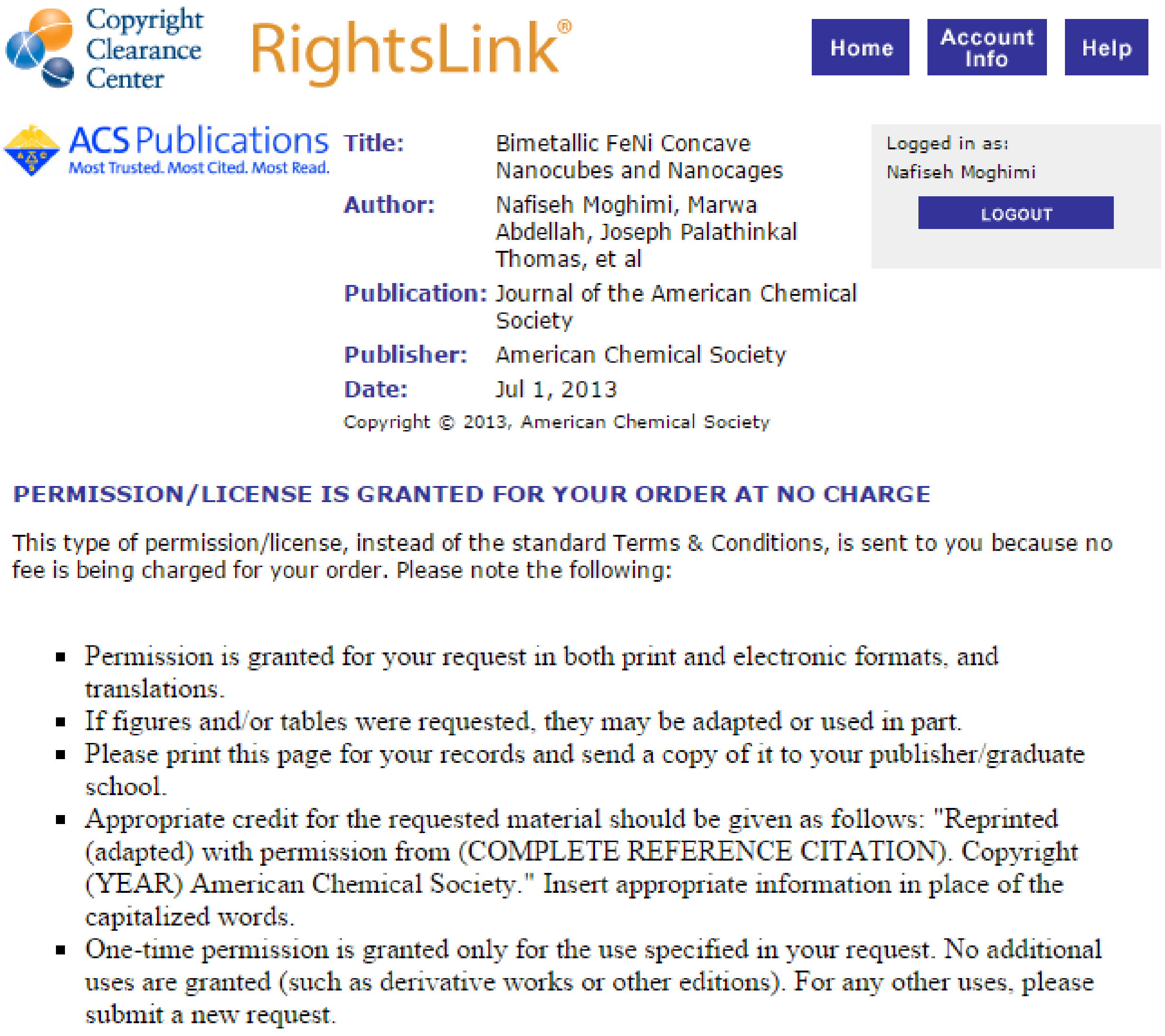

Title: Bimetallic FeNi Concave Nanocubes and Nanocages

Author: Nafiseh Moghimi, Marwa Abdellah, Joseph Palathinkal Thomas, et al

Publication: Journal of the American Chemical Society

Publisher: American Chemical Society

Date: Jul 1, 2013

Copyright © 2013, American Chemical Society

Logged in as:
Nafiseh Moghimi

PERMISSION/LICENSE IS GRANTED FOR YOUR ORDER AT NO CHARGE

This type of permission/license, instead of the standard Terms & Conditions, is sent to you because no fee is being charged for your order. Please note the following:

- Permission is granted for your request in both print and electronic formats, and translations.
- If figures and/or tables were requested, they may be adapted or used in part.
- Please print this page for your records and send a copy of it to your publisher/graduate school.
- Appropriate credit for the requested material should be given as follows: "Reprinted (adapted) with permission from (COMPLETE REFERENCE CITATION). Copyright (YEAR) American Chemical Society." Insert appropriate information in place of the capitalized words.
- One-time permission is granted only for the use specified in your request. No additional uses are granted (such as derivative works or other editions). For any other uses, please submit a new request.

Title: In Situ Hybridization of Superparamagnetic Iron-Biomolecule Nanoparticles

Author: Nafiseh Moghimi, Apraku David Donkor, Mamata Mohapatra, et al

Publication: Journal of the American Chemical Society

Publisher: American Chemical Society

Date: Jul 1, 2014

Copyright © 2014, American Chemical Society

Logged in as:
Nafiseh Moghimi

PERMISSION/LICENSE IS GRANTED FOR YOUR ORDER AT NO CHARGE

This type of permission/license, instead of the standard Terms & Conditions, is sent to you because no fee is being charged for your order. Please note the following:

- Permission is granted for your request in both print and electronic formats, and translations.
- If figures and/or tables were requested, they may be adapted or used in part.
- Please print this page for your records and send a copy of it to your publisher/graduate school.
- Appropriate credit for the requested material should be given as follows: "Reprinted (adapted) with permission from (COMPLETE REFERENCE CITATION). Copyright (YEAR) American Chemical Society." Insert appropriate information in place of the capitalized words.
- One-time permission is granted only for the use specified in your request. No additional uses are granted (such as derivative works or other editions). For any other uses, please submit a new request.

Figure 1.1:

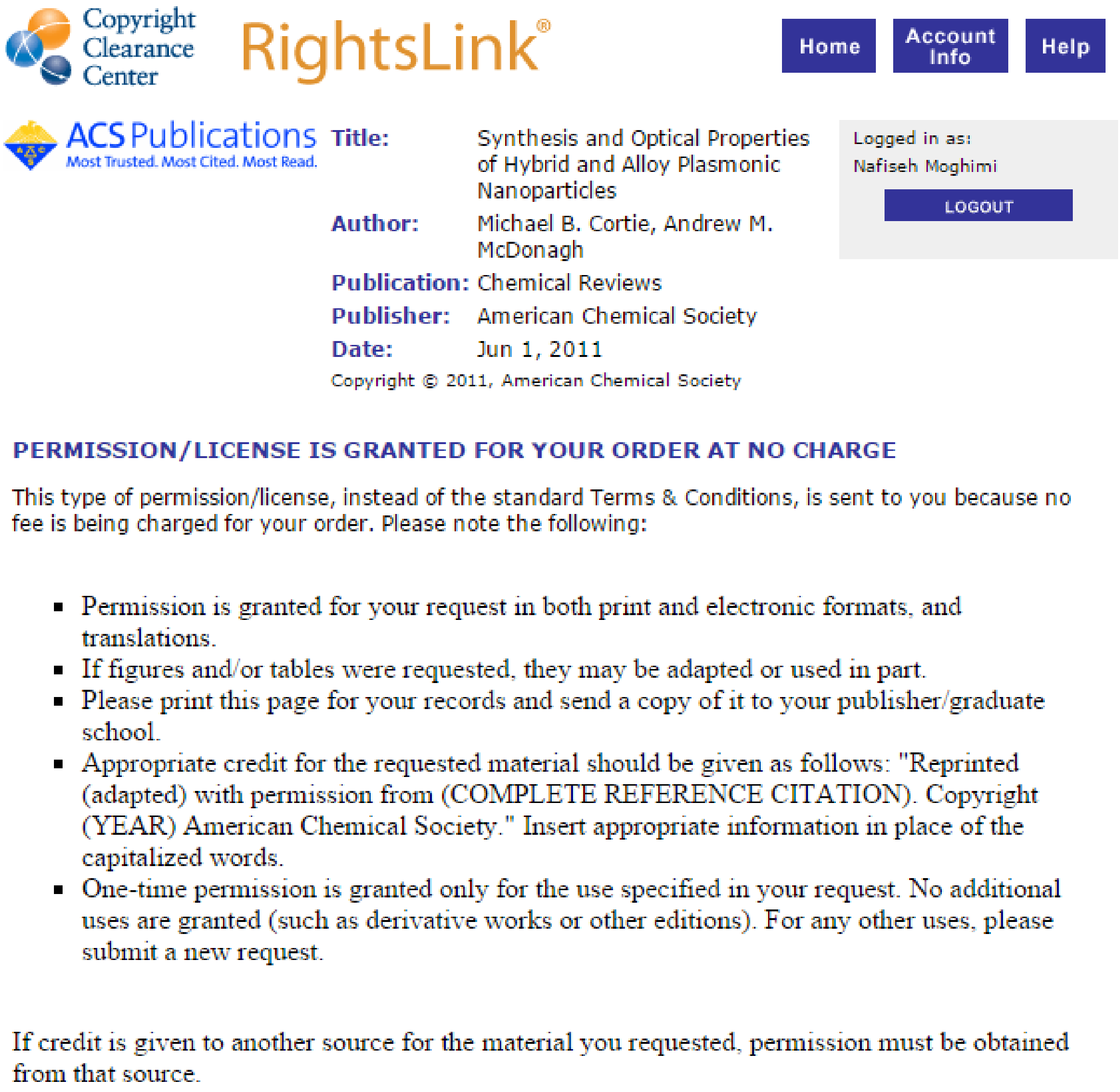

Title: Synthesis and Optical Properties of Hybrid and Alloy Plasmonic Nanoparticles

Author: Michael B. Cortie, Andrew M. McDonagh

Publication: Chemical Reviews

Publisher: American Chemical Society

Date: Jun 1, 2011

Copyright © 2011, American Chemical Society

Logged in as:
Nafiseh Moghimi

PERMISSION/LICENSE IS GRANTED FOR YOUR ORDER AT NO CHARGE

This type of permission/license, instead of the standard Terms & Conditions, is sent to you because no fee is being charged for your order. Please note the following:

- Permission is granted for your request in both print and electronic formats, and translations.
- If figures and/or tables were requested, they may be adapted or used in part.
- Please print this page for your records and send a copy of it to your publisher/graduate school.
- Appropriate credit for the requested material should be given as follows: "Reprinted (adapted) with permission from (COMPLETE REFERENCE CITATION). Copyright (YEAR) American Chemical Society." Insert appropriate information in place of the capitalized words.
- One-time permission is granted only for the use specified in your request. No additional uses are granted (such as derivative works or other editions). For any other uses, please submit a new request.

If credit is given to another source for the material you requested, permission must be obtained from that source.

Figure 1.2:

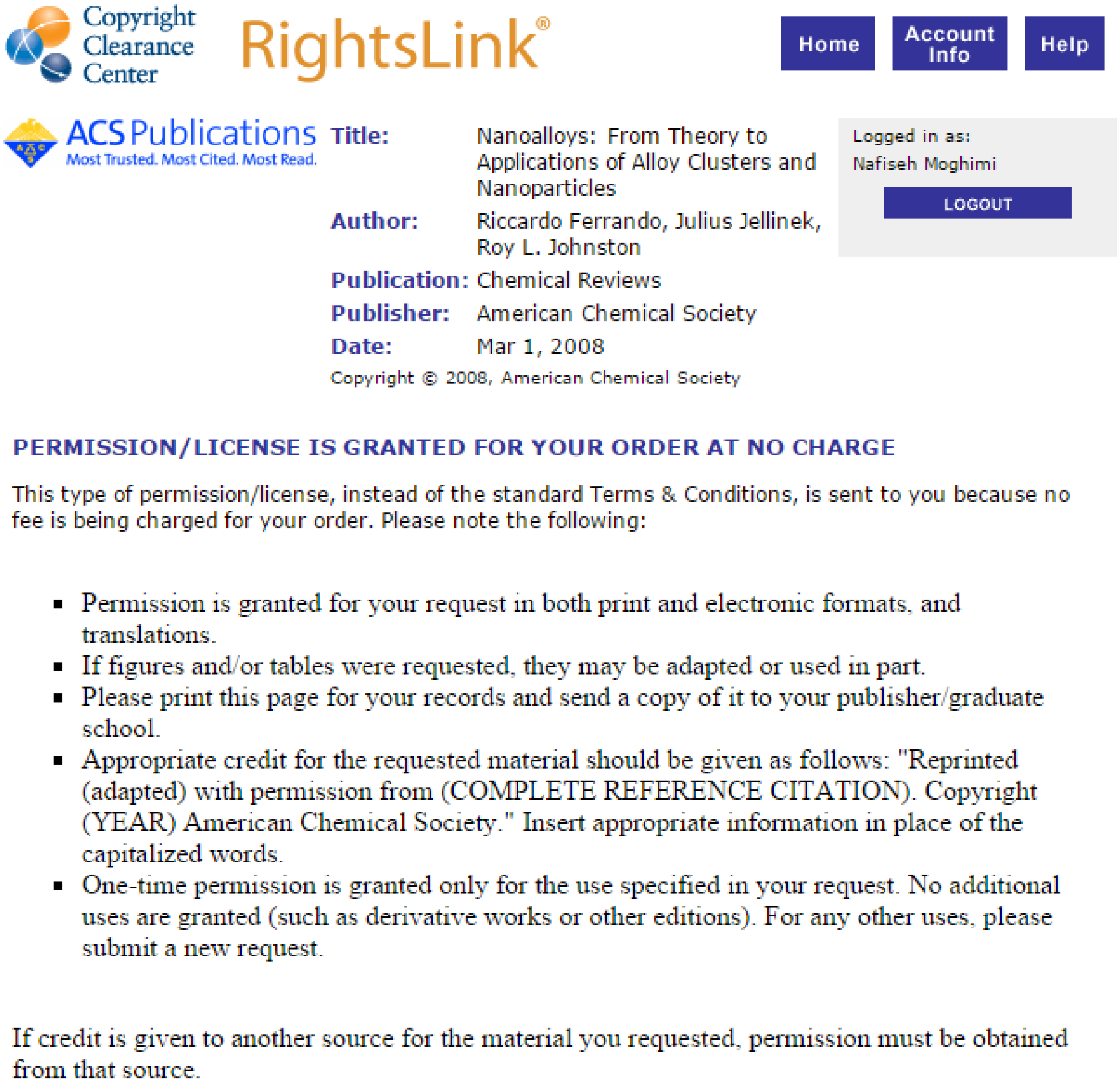

Title:	Nanoalloys: From Theory to Applications of Alloy Clusters and Nanoparticles
Author:	Riccardo Ferrando, Julius Jellinek, Roy L. Johnston
Publication:	Chemical Reviews
Publisher:	American Chemical Society
Date:	Mar 1, 2008

Logged in as:
Nafiseh Moghimi

PERMISSION/LICENSE IS GRANTED FOR YOUR ORDER AT NO CHARGE

This type of permission/license, instead of the standard Terms & Conditions, is sent to you because no fee is being charged for your order. Please note the following:

- Permission is granted for your request in both print and electronic formats, and translations.
- If figures and/or tables were requested, they may be adapted or used in part.
- Please print this page for your records and send a copy of it to your publisher/graduate school.
- Appropriate credit for the requested material should be given as follows: "Reprinted (adapted) with permission from (COMPLETE REFERENCE CITATION). Copyright (YEAR) American Chemical Society." Insert appropriate information in place of the capitalized words.
- One-time permission is granted only for the use specified in your request. No additional uses are granted (such as derivative works or other editions). For any other uses, please submit a new request.

If credit is given to another source for the material you requested, permission must be obtained from that source.

Figure 1.3:

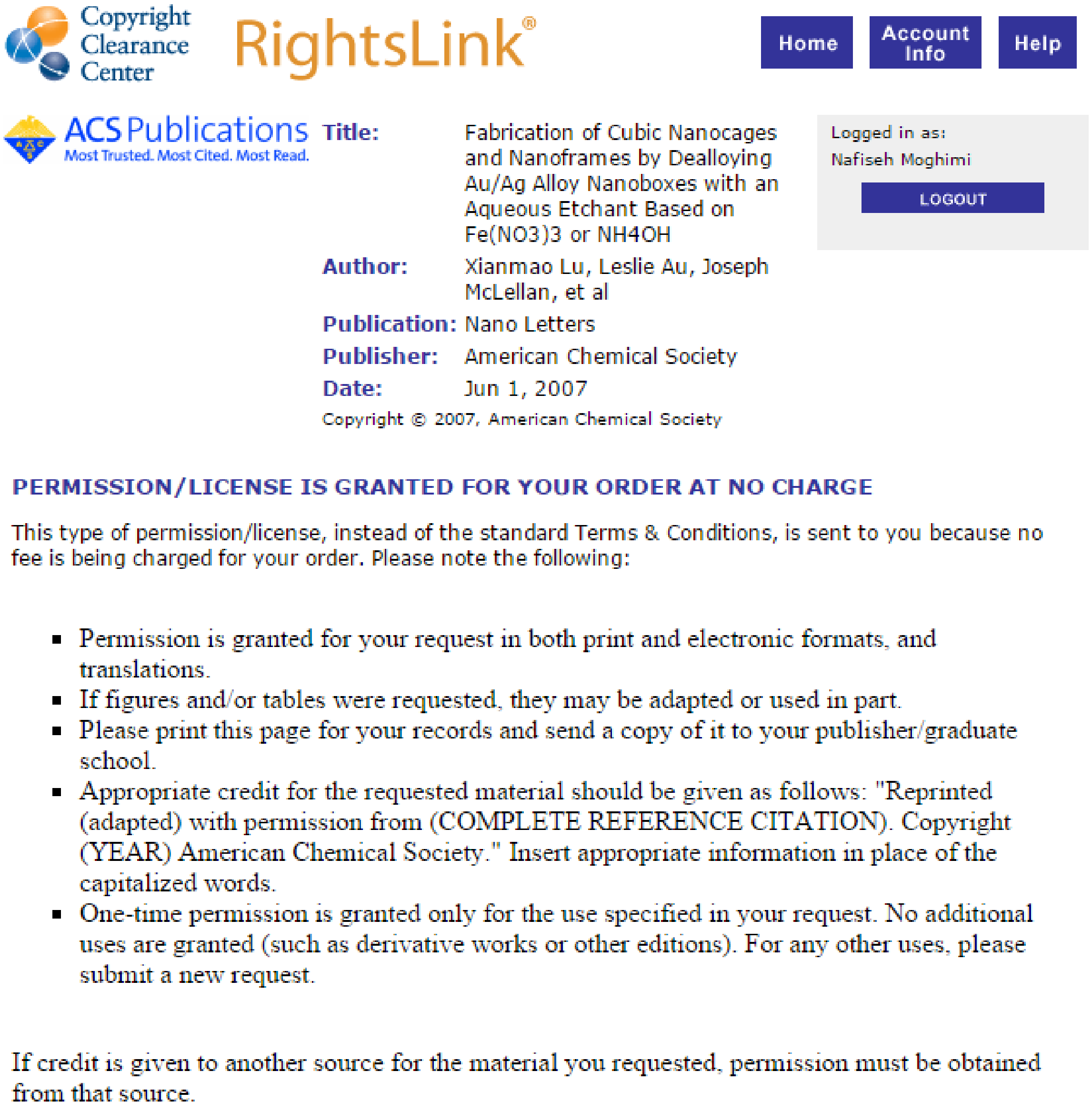

Title:	Fabrication of Cubic Nanocages and Nanoframes by Dealloying Au/Ag Alloy Nanoboxes with an Aqueous Etchant Based on Fe(NO3)3 or NH4OH
Author:	Xianmao Lu, Leslie Au, Joseph McLellan, et al
Publication:	Nano Letters
Publisher:	American Chemical Society
Date:	Jun 1, 2007

Copyright © 2007, American Chemical Society

Logged in as:
Nafiseh Moghimi

PERMISSION/LICENSE IS GRANTED FOR YOUR ORDER AT NO CHARGE

This type of permission/license, instead of the standard Terms & Conditions, is sent to you because no fee is being charged for your order. Please note the following:

- Permission is granted for your request in both print and electronic formats, and translations.
- If figures and/or tables were requested, they may be adapted or used in part.
- Please print this page for your records and send a copy of it to your publisher/graduate school.
- Appropriate credit for the requested material should be given as follows: "Reprinted (adapted) with permission from (COMPLETE REFERENCE CITATION). Copyright (YEAR) American Chemical Society." Insert appropriate information in place of the capitalized words.
- One-time permission is granted only for the use specified in your request. No additional uses are granted (such as derivative works or other editions). For any other uses, please submit a new request.

If credit is given to another source for the material you requested, permission must be obtained from that source.

Figure 1.4:

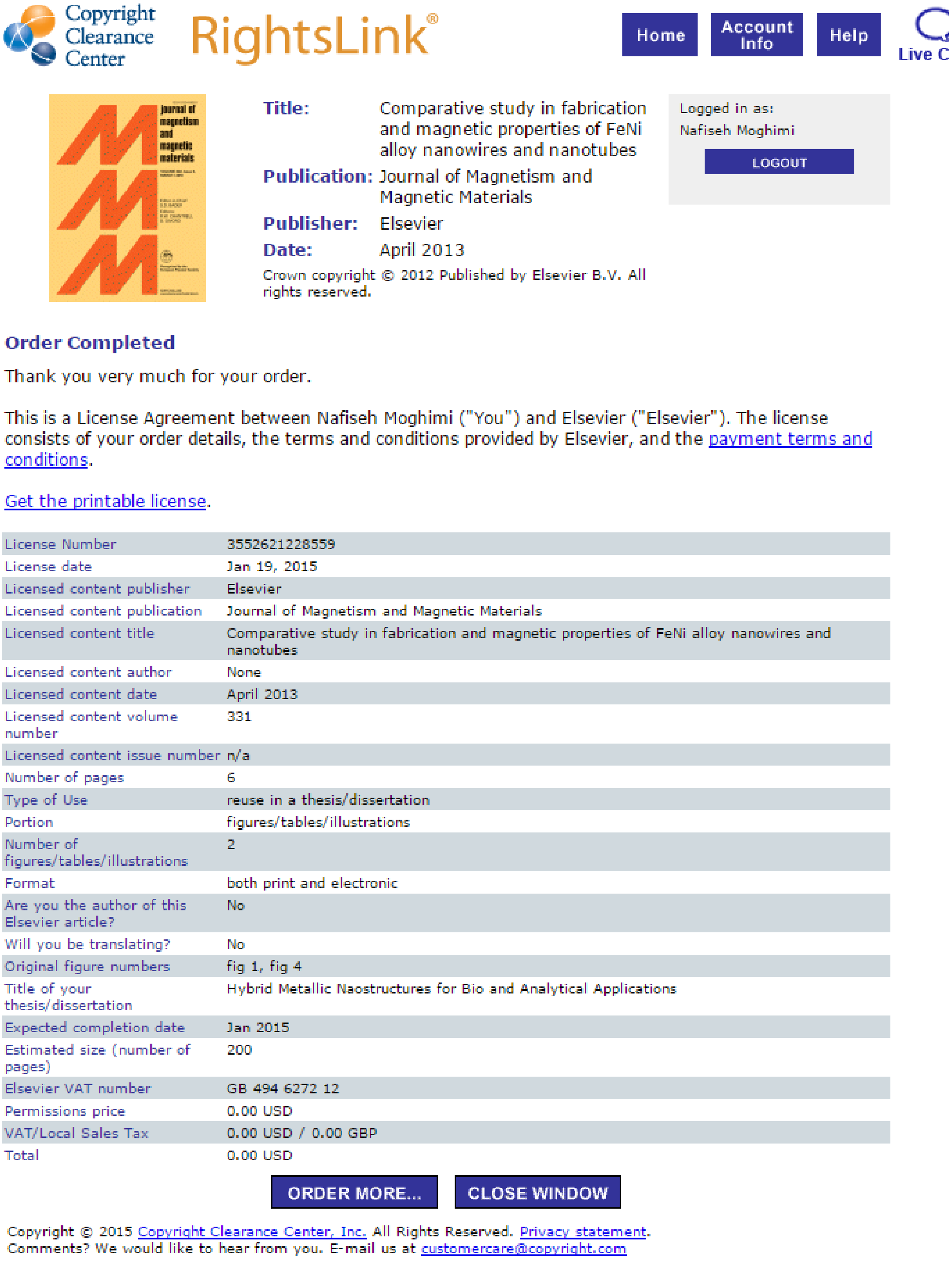

Title: Comparative study in fabrication and magnetic properties of FeNi alloy nanowires and nanotubes

Publication: Journal of Magnetism and Magnetic Materials

Publisher: Elsevier

Date: April 2013

Crown copyright © 2012 Published by Elsevier B.V. All rights reserved.

Logged in as:
Nafiseh Moghimi

Order Completed

Thank you very much for your order.

This is a License Agreement between Nafiseh Moghimi ("You") and Elsevier ("Elsevier"). The license consists of your order details, the terms and conditions provided by Elsevier, and the payment terms and conditions.

Get the printable license.

License Number	3552621228559
License date	Jan 19, 2015
Licensed content publisher	Elsevier
Licensed content publication	Journal of Magnetism and Magnetic Materials
Licensed content title	Comparative study in fabrication and magnetic properties of FeNi alloy nanowires and nanotubes
Licensed content author	None
Licensed content date	April 2013
Licensed content volume number	331
Licensed content issue number	n/a
Number of pages	6
Type of Use	reuse in a thesis/dissertation
Portion	figures/tables/illustrations
Number of figures/tables/illustrations	2
Format	both print and electronic
Are you the author of this Elsevier article?	No
Will you be translating?	No
Original figure numbers	fig 1, fig 4
Title of your thesis/dissertation	Hybrid Metallic Naostructures for Bio and Analytical Applications
Expected completion date	Jan 2015
Estimated size (number of pages)	200
Elsevier VAT number	GB 494 6272 12
Permissions price	0.00 USD
VAT/Local Sales Tax	0.00 USD / 0.00 GBP
Total	0.00 USD

Copyright © 2015 Copyright Clearance Center, Inc. All Rights Reserved. Privacy statement.
Comments? We would like to hear from you. E-mail us at customercare@copyright.com

Figure 1.5:

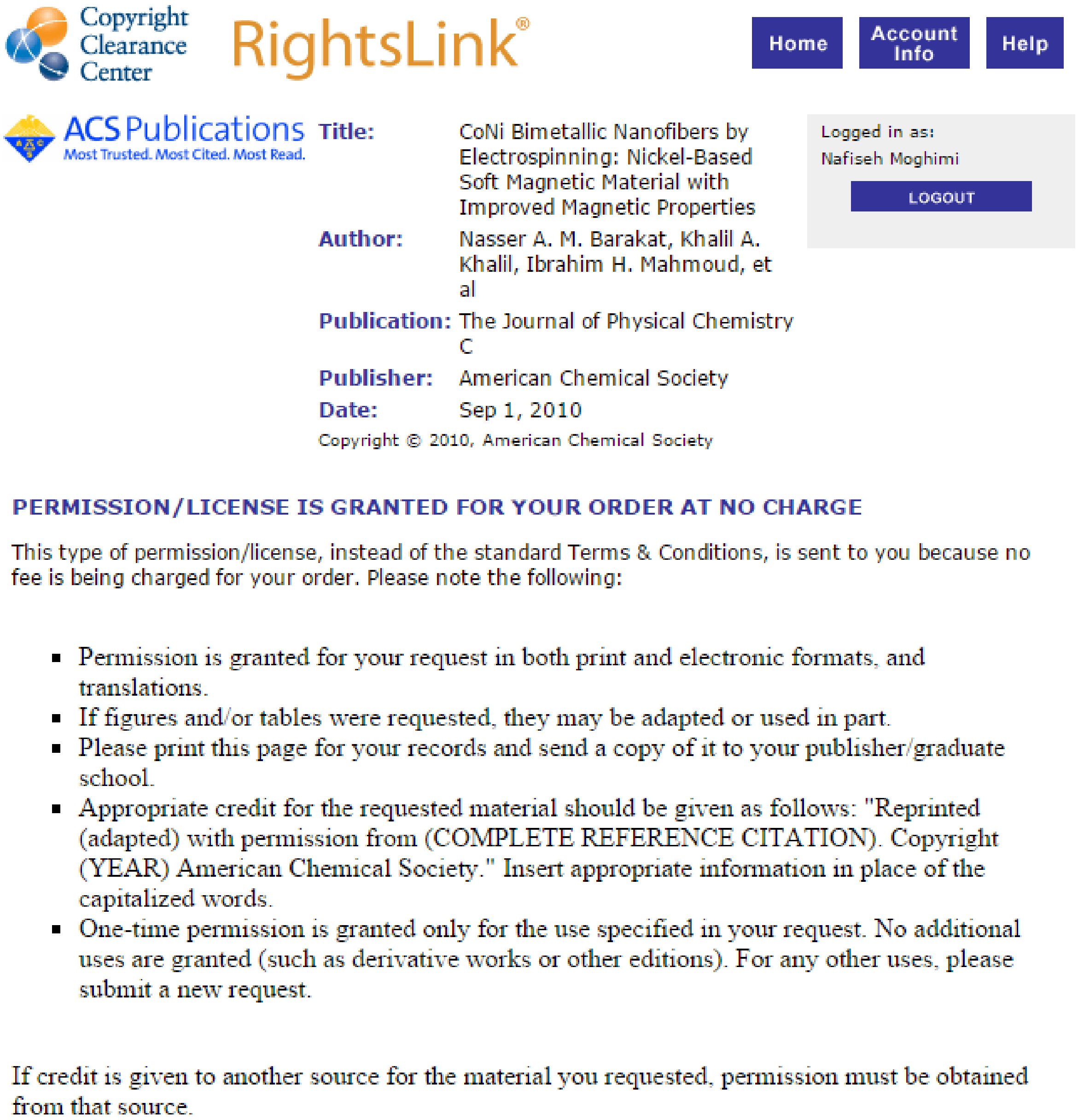

Title: CoNi Bimetallic Nanofibers by Electrospinning: Nickel-Based Soft Magnetic Material with Improved Magnetic Properties

Author: Nasser A. M. Barakat, Khalil A. Khalil, Ibrahim H. Mahmoud, et al

Publication: The Journal of Physical Chemistry C

Publisher: American Chemical Society

Date: Sep 1, 2010

Copyright © 2010, American Chemical Society

Logged in as:
Nafiseh Moghimi

PERMISSION/LICENSE IS GRANTED FOR YOUR ORDER AT NO CHARGE

This type of permission/license, instead of the standard Terms & Conditions, is sent to you because no fee is being charged for your order. Please note the following:

- Permission is granted for your request in both print and electronic formats, and translations.
- If figures and/or tables were requested, they may be adapted or used in part.
- Please print this page for your records and send a copy of it to your publisher/graduate school.
- Appropriate credit for the requested material should be given as follows: "Reprinted (adapted) with permission from (COMPLETE REFERENCE CITATION). Copyright (YEAR) American Chemical Society." Insert appropriate information in place of the capitalized words.
- One-time permission is granted only for the use specified in your request. No additional uses are granted (such as derivative works or other editions). For any other uses, please submit a new request.

If credit is given to another source for the material you requested, permission must be obtained from that source.

Figure 1.6:

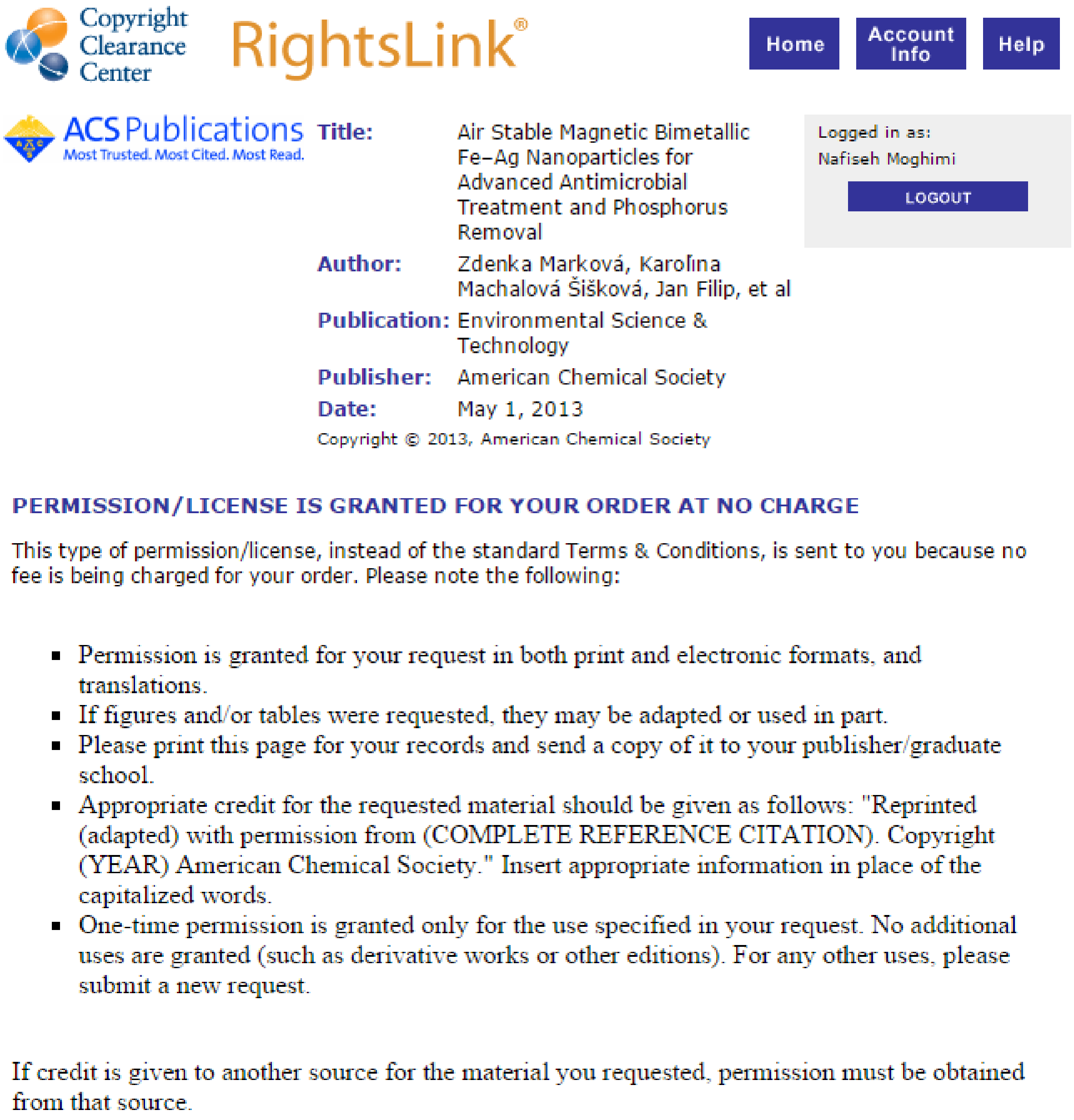

Title: Air Stable Magnetic Bimetallic Fe–Ag Nanoparticles for Advanced Antimicrobial Treatment and Phosphorus Removal

Author: Zdenka Marková, Karolína Machalová Šišková, Jan Filip, et al

Publication: Environmental Science & Technology

Publisher: American Chemical Society

Date: May 1, 2013

Copyright © 2013, American Chemical Society

Logged in as:
Nafiseh Moghimi

PERMISSION/LICENSE IS GRANTED FOR YOUR ORDER AT NO CHARGE

This type of permission/license, instead of the standard Terms & Conditions, is sent to you because no fee is being charged for your order. Please note the following:

- Permission is granted for your request in both print and electronic formats, and translations.
- If figures and/or tables were requested, they may be adapted or used in part.
- Please print this page for your records and send a copy of it to your publisher/graduate school.
- Appropriate credit for the requested material should be given as follows: "Reprinted (adapted) with permission from (COMPLETE REFERENCE CITATION). Copyright (YEAR) American Chemical Society." Insert appropriate information in place of the capitalized words.
- One-time permission is granted only for the use specified in your request. No additional uses are granted (such as derivative works or other editions). For any other uses, please submit a new request.

If credit is given to another source for the material you requested, permission must be obtained from that source.

Bibliography

(1) Singh, A. K.; Xu, Q. Synergistic Catalysis over Bimetallic Alloy Nanoparticles. *ChemCatChem* **2013**, *5*, 652–676.

(2) Soriaga, M. P. Surface Coordination Chemistry of Monometallic and Bimetallic Electrocatalysts. *Chem. Rev.* **1990**, *90*, 771–793.

(3) Yim, W.-L.; Klüner, T. Understanding of Adsorption and Catalytic Properties of Bimetallic Pt−Co Alloy Surfaces from First Principles: Insight from Disordered Alloy Surfaces. *J. Phys. Chem. C* **2010**, *114*, 7141–7152.

(4) Polshettiwar, V.; Luque, R.; Fihri, A.; Zhu, H.; Bouhrara, M.; Basset, J.-M. Magnetically Recoverable Nanocatalysts. *Chem. Rev.* **2011**, *111*, 3036–3075.

(5) Derosa, P. A.; Seminario, J. M.; Balbuena, P. B. Properties of Small Bimetallic Ni−Cu Clusters. *J. Phys. Chem. A* **2001**, *105*, 7917–7925.

(6) Li, G.-R.; Zhang, Z.-S.; Su, C.-Y.; Tong, Y.-X. Electrochemical Synthesis of Tb−Co Alloy Nanoparticle Aggregates and Their Magnetic Properties. *J. Phys. Chem. C* **2009**, *113*, 1227–1234.

(7) Rosi, N. L.; Giljohann, D. A.; Thaxton, C. S.; Lytton-Jean, A. K. R.; Han, M. S.; Mirkin, C. A. Oligonucleotide-Modified Gold Nanoparticles for Intracellular Gene Regulation. *Science* **2006**, *312*, 1027–1030.

(8) Tessier, P. M.; Velev, O. D.; Kalambur, A. T.; Rabolt, J. F.; Lenhoff, A. M.; Kaler, E. W. Assembly of Gold Nanostructured Films Templated by Colloidal Crystals and Use in Surface-Enhanced Raman Spectroscopy. *J. Am. Chem. Soc.* **2000**, *122*, 9554–9555.

(9) Ferrando, R.; Jellinek, J.; Johnston, R. L. Nanoalloys: From Theory to Applications of Alloy Clusters and Nanoparticles. *Chem. Rev.* **2008**, *108*, 845–910.

(10) Cortie, M. B.; McDonagh, A. M. Synthesis and Optical Properties of Hybrid and Alloy Plasmonic Nanoparticles. *Chem. Rev.* **2011**, *111*, 3713–3735.

(11) Costi, R.; Saunders, A. E.; Banin, U. Colloidal Hybrid Nanostructures: A New Type of Functional Materials. *Angew. Chem. Int. Ed. Engl.* **2010**, *49*, 4878–4897.

(12) Katz, E.; Willner, I. Integrated Nanoparticle-Biomolecule Hybrid Systems: Synthesis, Properties, and Applications. *Angew. Chem. Int. Ed. Engl.* **2004**, *43*, 6042–6108.

(13) Cozzoli, P. D.; Pellegrino, T.; Manna, L. Synthesis, Properties and Perspectives of Hybrid Nanocrystal Structures. *Chem. Soc. Rev.* **2006**, *35*, 1195–1208.

(14) Zeng, H.; Sun, S. Syntheses, Properties, and Potential Applications of Multicomponent Magnetic Nanoparticles. *Adv. Funct. Mater.* **2008**, *18*, 391–400.

(15) Krenke, T.; Duman, E.; Acet, M.; Wassermann, E. F.; Moya, X.; Mañosa, L.; Planes, A. Inverse Magnetocaloric Effect in Ferromagnetic Ni-Mn-Sn Alloys. *Nat. Mater.* **2005**, *4*, 450–454.

(16) Jiang, H.-L.; Xu, Q. Recent Progress in Synergistic Catalysis over Heterometallic Nanoparticles. *J. Mater. Chem.* **2011**, *21*, 13705.

(17) Ferrer, D.; Torres-Castro, A.; Gao, X.; Sepulveda-Guzman, S.; Ortiz-Mendez, U.; Jose-Yacaman, M. Three-Layer Core/Shell Structure in Au−Pd Bimetallic Nanoparticles. *Nano Lett.* **2007**, *7*, 1701–1705.

(18) Fromen, M. C.; Morillo, J.; Casanove, M. J.; Lecante, P. Structure and Chemical Order in Co–Rh Nanoparticles. *Europhys. Lett.* **2006**, *73*, 885–891.

(19) Baletto, F.; Mottet, C.; Ferrando, R. Growth of Three-Shell Onionlike Bimetallic Nanoparticles. *Phys. Rev. Lett.* **2003**, *90*, 135504.

(20) Schrick, B.; Blough, J. L.; Jones, A. D.; Mallouk, T. E. . Hydrodechlorination of Trichloroethylene to Hydrocarbons Using Bimetallic Nickel−Iron Nanoparticles. *Chem. Mater.* **2002**, *14*, 5140–5147.

(21) Hansgen, D. A.; Vlachos, D. G.; Chen, J. G. Using First Principles to Predict Bimetallic Catalysts for the Ammonia Decomposition Reaction. *Nat. Chem.* **2010**, *2*, 484–489.

(22) Ji, X.; Lee, K. T.; Holden, R.; Zhang, L.; Zhang, J.; Botton, G. A.; Couillard, M.; Nazar, L. F. Nanocrystalline Intermetallics on Mesoporous Carbon for Direct Formic Acid Fuel Cell Anodes. *Nat. Chem.* **2010**, *2*, 286–293.

(23) Kobayashi, H.; Yamauchi, M.; Kitagawa, H.; Kubota, Y. Atomic-Level Pd-Pt Alloying and Largely Enhanced Hydrogen-Storage Capacity in Bimetallic Nanoparticles Reconstructed from Core/Shell Structure by a Process of Hydrogen Absorption/Desorption. *J. Am. Chem. Soc.* **2010**, *132*, 5576–5577.

(24) Studt, F.; Abild-Pedersen, F.; Bligaard, T.; Sørensen, R. Z.; Christensen, C. H.; Nørskov, J. K. Identification of Non-Precious Metal Alloy Catalysts for Selective

Hydrogenation of Acetylene. *Science* **2008**, *320*, 1320–1322.

(25) Tee, Y.; Grulke, E.; Bhattacharyya, D. Role of Ni/Fe Nanoparticle Composition on the Degradation of Trichloroethylene from Water. **2005**, 7062–7070.

(26) Teng, X.; Yang, H. Synthesis and Electrocatalytic Property of Cubic and Spherical Nanoparticles of Cobalt Platinum Alloys. *Front. Chem. Eng. China* **2010**, *4*, 45–51.

(27) Toshima, N.; Yonezawa, T. Bimetallic Nanoparticles-Novel Materials for Chemical and Physical Applications. *New J. Chem.* **1998**, 1179–1201.

(28) Faraday, M. The Bakerian Lecture: Experimental Relations of Gold (and Other Metals) to Light. *Philos. Trans. R. Soc. London* **1857**, *147*, 145–181.

(29) Turkevich, J.; Cooper Stevenson, P.; Hillier, J. A Study of the Nucleation and Growth Processes in the Synthesis of Colloidal Gold. *Discuss. Faraday Soc.* **1951**, 55–75.

(30) Turkevich, J.; Cooper Stevenson, P.; Hillier, J. A Study of the Nucleation and Growth Processes in the Synthesis of Colloidal Gold. *Discuss. Faraday Soc.* **1951**, 55–75.

(31) Burda, C.; Chen, X.; Narayanan, R.; El-Sayed, M. A. Chemistry and Properties of Nanocrystals of Different Shapes. *Chem. Rev.* **2005**, *105*, 1025–1102.

(32) Liu, J.; Maaroof, A. I.; Wieczorek, L.; Cortie, M. B. Fabrication of Hollow Metal "Nanocaps" and Their Red-Shifted Optical Absorption Spectra. *Adv. Mater.* **2005**, *17*, 1276–1281.

(33) Park, J.; Joo, J.; Kwon, S. G.; Jang, Y.; Hyeon, T. Synthesis of Monodisperse Spherical Nanocrystals. *Angew. Chem. Int. Ed. Engl.* **2007**, *46*, 4630–4660.

(34) Cozzoli, P. D.; Pellegrino, T.; Manna, L. Synthesis, Properties and Perspectives of Hybrid Nanocrystal Structures. *Chem. Soc. Rev.* **2006**, *35*, 1195–1208.

(35) Mokari, T.; Aharoni, A.; Popov, I.; Banin, U. Diffusion of Gold into InAs Nanocrystals. *Angew. Chem. Int. Ed. Engl.* **2006**, *45*, 8001–8005.

(36) Lu, X.; Au, L.; McLellan, J.; Li, Z.-Y.; Marquez, M.; Xia, Y. Fabrication of Cubic Nanocages and Nanoframes by Dealloying Au/Ag Alloy Nanoboxes with an Aqueous Etchant Based on Fe(NO3)3 or NH4OH. *Nano Lett.* **2007**, *7*, 1764–1769.

(37) Hulteen, J. C. Nanosphere Lithography: A Materials General Fabrication Process for Periodic Particle Array Surfaces. *J. Vac. Sci. Technol. A* **1995**, *13*, 1553.

(38) Wang, Y.; Hernandez, R. M.; Bartlett, D. J.; Bingham, J. M.; Kline, T. R.; Sen, A.; Mallouk, T. E. Bipolar Electrochemical Mechanism for the Propulsion of Catalytic Nanomotors in Hydrogen Peroxide Solutions. *Langmuir* **2006**, *22*, 10451–10456.

(39) Nicewarner-Pena, S. R.; Freeman, R. G.; Reiss, B. D.; He, L.; Pena, D. J.; Walton, I. D.; Cromer, R.; Keating, C. D.; Natan, M. J. Submicrometer Metallic Barcodes. *Science* **2001**, *294*, 137–141.

(40) Belloni, J.; Mostafavi, M.; Remita, H.; Marignier, J.-L.; Delcourt, and M.-O. Radiation-Induced Synthesis of Mono- and Multi-Metallic Clusters and Nanocolloids. *New J. Chem.* **1998**, *22*, 1239–1255.

(41) Mizukoshi, Y.; Fujimoto, T.; Nagata, Y.; Oshima, R.; Maeda, Y. Characterization and Catalytic Activity of Core-Shell Structured Gold/Palladium Bimetallic Nanoparticles Synthesized by the Sonochemical Method. *J. Phys. Chem. B* **2000**, *104*, 6028–6032.

(42) Kan, C.; Cai, W.; I, C.; Zhang, L.; Hofmeister, H. Ultrasonic Synthesis and Optical Properties of Au/Pd Bimetallic Nanoparticles in Ethylene Glycol. *J. Phys. D. Appl. Phys.* **2003**, *1609*, 1609–1614.

(43) Baletto, F.; Ferrando, R.; Fisica, D.; Genova, U. Structural Properties of nanoclusters:Energetic , Thermodynamic, and Kinetic Effects. *Rev. Mod. Pysics* **2005**, *77*, 317–423.

(44) De Heer, W. The Physics of Simple Metal Clusters: Experimental Aspects and Simple Models. *Rev. Mod. Phys.* **1993**, *65*, 611–676.

(45) Binns, C. Nanoclusters Deposited on Surfaces. *Surf. Sci. Rep.* **2001**, *44*, 1–49.

(46) Gaudry, M.; Pellarin, M.; Vialle, J.; Broyer, M. Size Effects in the Optical Properties of Au Ag Embedded Clusters. *Phys. Rev. B* **2000**, *62*, 5179–5185.

(47) Mattei, G.; Maurizio, C.; Mazzoldi, P.; D'Acapito, F.; Battaglin, G.; Cattaruzza, E.; de Julián Fernández, C.; Sada, C. Dynamics of Compositional Evolution of Pd-Cu Alloy Nanoclusters upon Heating in Selected Atmospheres. *Phys. Rev. B* **2005**, *71*, 195418.

(48) Reetz, M. T.; Helbig, W.; Quaiser, S. A. Electrochemical Preparation of Nanostructured Bimetallic Clusters. *Chem. Mater.* **1995**, *7*, 2227–2228.

(49) Kolb, U.; Quaiser, S. A.; Winter, M.; Reetz, M. T. Investigation of Tetraalkylammonium Bromide Stabilized Palladium/Platinum Bimetallic Clusters Using Extended X-Ray Absorption Fine Structure Spectroscopy. *Chem. Mater.* **1996**,

4756, 1889–1894.

(50) Wang, C.-B.; Zhang, W. Synthesizing Nanoscale Iron Particles for Rapid and Complete Dechlorination of TCE and PCBs. *Environ. Sci. Technol.* **1997**, *31*, 2154–2156.

(51) Ban, I.; Drofenik, M.; Makovec, D. The Synthesis of Iron–nickel Alloy Nanoparticles Using a Reverse Micelle Technique. *J. Magn. Magn. Mater.* **2006**, *307*, 250–256.

(52) Wang, H.; Li, J.; Kou, X.; Zhang, L. Synthesis and Characterizations of Size-Controlled FeNi3 Nanoplatelets. *J. Cryst. Growth* **2008**, *310*, 3072–3076.

(53) Chen, Y.; She, H.; Luo, X.; Yue, G.-H.; Mi, W.-B.; Bai, H.-L.; Peng, D.-L. Chemical Synthesis of Monodisperse Fe–Ni Nanoparticles via a Diffusion-Based Approach. *J. Nanosci. Nanotechnol.* **2010**, *10*, 3053–3059.

(54) Lu, B.; Huang, H.; Dong, X. L.; Zhang, X. F.; Lei, J. P.; Sun, J. P.; Dong, C. Influence of Alloy Components on Electromagnetic Characteristics of Core/shell-Type Fe–Ni Nanoparticles. *J. Appl. Phys.* **2008**, *104*, 114313.

(55) Dong, X. L.; Zhang, Z. D.; Zhao, X. G.; Chuang, Y. C. Preparation and Characterization of Ultrafine Fe-Ni Particles. *J. Mater. Res.* **1999**, *109*, 7203–7207.

(56) Suh, Y.; Jang, H.; Chang, H.; Kim, W.; Kim, H. Size-Controlled Synthesis of Fe–Ni Alloy Nanoparticles by Hydrogen Reduction of Metal Chlorides. *Powder Technol.* **2006**, *161*, 196–201.

(57) Vitta, S.; Khuntia, a; Ravikumar, G.; Bahadur, D. Electrical and Magnetic Properties of Nanocrystalline Fe100−xNix Alloys. *J. Magn. Magn. Mater.* **2008**, *320*, 182–189.

(58) Rao, B.; Ramos de Debiaggi, S.; Jena, P. Structure and Magnetic Properties of Fe-Ni Clusters. *Phys. Rev. B* **2001**, *64*, 1–6.

(59) Shen, W.; Huggins, F. E.; Shah, N.; Jacobs, G.; Wang, Y.; Shi, X.; Huffman, G. P. Novel Fe–Ni Nanoparticle Catalyst for the Production of CO- and CO2-Free H2 and Carbon Nanotubes by Dehydrogenation of Methane. *Appl. Catal. A Gen.* **2008**, *351*, 102–110.

(60) Behrens, S.; Bönnemann, H.; Matoussevitch, N.; Gorschinski, A.; Dinjus, E.; Habicht, W.; Bolle, J.; Zinoveva, S.; Palina, N.; Hormes, J.; *et al.* Surface Engineering of Co and FeCo Nanoparticles for Biomedical Application. *J. Phys. Condens. Matter* **2006**, *18*, S2543–S2561.

(61) Zhang, X.; Zhang, H.; Wu, T.; Li, Z.; Zhang, Z.; Sun, H. Comparative Study in Fabrication and Magnetic Properties of FeNi Alloy Nanowires and Nanotubes. *J. Magn. Magn. Mater.* **2013**, *331*, 162–167.

(62) Barakat, N. A. M.; Khalil, K. A.; Mahmoud, I. H.; Kanjwal, M. A.; Sheikh, F. A.; Kim, H. Y. CoNi Bimetallic Nanofibers by Electrospinning: Nickel-Based Soft Magnetic Material with Improved Magnetic Properties. *J. Phys. Chem. C* **2010**, *114*, 15589–15593.

(63) Saha, K.; Agasti, S. S.; Kim, C.; Li, X.; Rotello, V. M. Gold Nanoparticles in Chemical and Biological Sensing. *Chem. Rev.* **2012**, *112*, 2739–2779.

(64) Xiang, D.; Yin, L. Well-Dispersed and Size-Tuned Bimetallic PtFex Nanoparticle Catalysts Supported on Ordered Mesoporous Carbon for Enhanced Electrocatalytic Activity in Direct Methanol Fuel Cells. *J. Mater. Chem.* **2012**, *22*, 9584.

(65) Ding, K.; Liu, L.; Cao, Y.; Yan, X.; Wei, H.; Guo, Z. Formic Acid Oxidation Reaction on a PdxNiy Bimetallic Nanoparticle Catalyst Prepared by a Thermal Decomposition Process Using Ionic Liquids as the Solvent. *Int. J. Hydrogen Energy* **2014**, *39*, 7326–7337.

(66) Kim, J.; Lee, Y.; Sun, S. Structurally Ordered FePt Nanoparticles and Their Enhanced Catalysis for Oxygen Reduction Reaction. *J. Am. Chem. Soc.* **2010**, *132*, 4996–4997.

(67) Markova, Z.; Siskova, K. M.; Filip, J.; Cuda, J.; Kolar, M.; Safarova, K.; Medrik, I.; Zboril, R. Air Stable Magnetic Bimetallic Fe−Ag Nanoparticles for Advanced Antimicrobial Treatment and Phosphorus Removal. *Enviromental Sci. Technol.* **2013**, *47*, 5285–5293.

(68) Liu, Z.; Jackson, G. S.; Eichhorn, B. W. Tuning the CO-Tolerance of Pt-Fe Bimetallic Nanoparticle Electrocatalysts through Architectural Control. *Energy Environ. Sci.* **2011**, *4*, 1900.

(69) Heinze, J. Cyclic Voltammetry-Electrochemical Spectroscopy. *Angew. Chem. Int. Ed. Engl.* **1984**, *23*, 831–918.

(70) Ramaley, L.; Krause, M. S. Theory of Square Wave Voltammetry. *Anal. Chem.* **1969**, *41*, 1362–1365.

(71) Osteryoung, J. G. .; Osteryoung, R. A. Square Wave Voltammetry. *Anal. Chem.* **1985**, *57*, 1–6.

(72) Ward, B.; Notte, J. N. .; Economou, N. P. Helium Ion Microscopy. *Photonics Spectra* **2007**.

(73) Postek, M. T.; Vladar, A. E.; Kramar, J.; Stern, L. A.; Notte, J.; McVey, S.; Seiler, D. G.; Diebold, A. C.; McDonald, R.; Garner, C. M.; *et al.* Helium Ion Microscopy: A New Technique for Semiconductor Metrology and Nanotechnology. *AIP Conf. Proc.* **2007**, *931*, 161–167.

(74) Moulder, J.F. ; Stickle, W.F.; Sobol, P. E. ; B. K. D. *Handbook of X-Ray Photoelectron Spectroscopy*; Chastain, J., Ed.; 2nd ed.; Perkin-Elmer Corp., 1992.

(75) Passarelli, M. K.; Winograd, N. Lipid Imaging with Time-of-Flight Secondary Ion Mass Spectrometry (ToF-SIMS). *Biochim. Biophys. Acta* **2011**, *1811*, 976–990.

(76) Kimura, M. X-Ray Evanescent Diffraction: Application to Metal Surfaces. *Rigaku J.* **1999**, *16*, 25–31.

(77) Wang, C. M.; Baer, D. R.; Amonette, J. E.; Engelhard, M. H.; Qiang, Y.; Antony, J. Morphology and Oxide Shell Structure of Iron Nanoparticles Grown by Sputter-Gas-Aggregation. *Nanotechnology* **2007**, *18*, 255603.

(78) Shavel, A.; Rodríguez-González, B.; Spasova, M.; Farle, M.; Liz-Marzán, L. M. Synthesis and Characterization of Iron/Iron Oxide Core/Shell Nanocubes. *Adv. Funct. Mater.* **2007**, *0*, 1–7.

(79) Ponder, S. M.; Darab, J. G.; Bucher, J.; Caulder, D.; Craig, I.; Davis, L.; Edelstein, N.; Lukens, W.; Nitsche, H.; Rao, L.; *et al.* Surface Chemistry and Electrochemistry of Supported Zerovalent Iron Nanoparticles in the Remediation of Aqueous Metal Contaminants. *Chem. Mater.* **2001**, *13*, 479–486.

(80) Xu, M. H.; Zhong, W.; Qi, X. S.; Au, C. T.; Deng, Y.; Du, Y. W. Highly Stable Fe–Ni Alloy Nanoparticles Encapsulated in Carbon Nanotubes: Synthesis, Structure and Magnetic Properties. *J. Alloys Compd.* **2010**, *495*, 200–204.

(81) Ammar, M.; Mazaleyrat, F.; Bonnet, J. P.; Audebert, P.; Brosseau, A.; Wang, G.; Champion, Y. Synthesis and Characterization of Core–shell Structure Silica-Coated Fe 29.5 Ni 70.5 Nanoparticles. *Nanotechnology* **2007**, *18*, 285606.

(82) Wu, J.; Gross, A.; Yang, H. Shape and Composition-Controlled Platinum Alloy Nanocrystals Using Carbon Monoxide as Reducing Agent. *Nano Lett.* **2011**, *11*, 798–802.

(83) Kern, W. *Handbook Of Semiconductor Wafer Cleaning Technology*; Noyes, P. R., Ed.; NJ, 1993.

(84) Scharifker, B.; Hills, G. Theoretical and Experimental Studies of Multiple Nucleation. *Electrochem. Acta* **1983**, *28*, 879–889.

(85) Zhu, L. H.; Ma, X. M.; Zhao, L. Study on Phase Transformation of Fe-Ni Powders during Mechanical Alloying. *J. Mater. Sci.* **2001**, *36*, 5571–5574.

(86) Valderruten, J. F.; Pérez Alcázar, G. A.; Grenèche, J. M. Mössbauer and X-Ray Study of Mechanically Alloyed Fe–Ni Alloys around the Invar Composition. *J. Phys. Condens. Matter* **2008**, *20*, 485204.

(87) Bradley, A. J, Jay, A. H., and Taylor, A. The Lattice Spacing of Iron-Nickel Alloys. *Philos. Mag.* **1973**, *23*, 155.

(88) Rührnschopf, K.; Borgmann, D.; Wedler, G. Growth of Fe on Si (100) at Room Temperature and Formation of Iron Silicide. *Thin Solid Films* **1996**, *280*, 171–177.

(89) Miedema, A. R. The Electronegativity Parameter for Transition Metals: Heat of Formation and Charge Transfer in Alloys. *J. Less Common Met.* **1973**, *32*, 117–136.

(90) Suzuki, S.; Yanagihara, K.; Hirokawa, K. XPS Study of Oxides Formed on the Surface of High-Purity Iron Exposed to Air. *Surf. Interface Anal.* **2000**, *30*, 372–376.

(91) Li, X.; Zhang, W. Iron Nanoparticles : The Core-Shell Structure and Unique Properties for Ni (II) Sequestration. *Society* **2006**, 4638–4642.

(92) Matlosz, M. Competitive Adsorption Effects in the Electrodeposition of Iron-Nickel Alloys. *J. Electrochem. Soc.* **1993**, *140*, 2272.

(93) Zakharov, A.I.; Narmonev, A.G.; Batirev, I. G. Specification of the Invar Alloys Electronic Structure. *J. Magn. Magn. Mater.* **1984**, *44*, 105–108.

(94) Kinsinger, V.; Dezsi, I.; Steiner, P.; Langouche, G. XPS Investigations of FeSi , FeSi , and Fe Implanted in Si and Ge. *Condens. Matterondensed Matter* **1990**, 4955.

(95) Tersoff, J.; Hamann, D. R. Bonding and Structure of CoSi2 and NiSi2. *Phys. Rev. B* **1983**, *28*, 1168–1170.

(96) Mohapatra, M.; Mohapatra, L.; Anand, S.; Mishra, B. K. One-Pot Synthesis of High Surface Area Nano-Akaganeite Powder and Its Cation Sorption Behavior. *J. Chem.*

Eng. data **2010**, *55*, 1486–1491.

(97) Chung, K.W.; Kho, Y. T.; Kim, K. B. Oxidation Behavior of Nix Fe1-x(OH)2 in Cl-Containing Solution. *Corros. Sci.* **2002**, *44*, 2757–2775.

(98) Nawale, A. B.; Kanhe, N. S.; Patil, K. R.; Bhoraskar, S. V.; Mathe, V. L.; Das, A. K. Magnetic Properties of Thermal Plasma Synthesized Nanocrystalline Nickel Ferrite (NiFe2O4). *J. Alloys Compd.* **2011**, *509*, 4404–4413.

(99) Nishimura, T.; Katayama, H.; Noda, K. Effect of Co and Ni on the Corrosion Behavior of Low Alloy Steels in Wet / Dry Environments. *Corros. Sci.* **2000**, *42*, 1611–1621.

(100) Ullman, F. *Ullman's Encyclopedia of Industrial Chemistry*; John Wiley & Sons, Inc, 1999.

(101) Regalloni, A. E.; Matijevic, E. Formation of Spherical Colloidal Nickel Ferrite Particles as Model Corrosion Products. *Corrosion* **1982**, *38*, 212–218.

(102) Dahms, H.; Croll, I. M. The Anomalous Codeposition of Iron-Nickel Alloys. *J. Electrochem. Soc.* **1965**, *112*, 771–775.

(103) Xia, Y.; Xiong, Y.; Lim, B.; Skrabalak, S. E. Shape-Controlled Synthesis of Metal Nanocrystals: Simple Chemistry Meets Complex Physics? *Angew. Chem. Int. Ed. Engl.* **2009**, *48*, 60–103.

(104) Tao, A. R.; Habas, S.; Yang, P. Shape Control of Colloidal Metal Nanocrystals. *Small* **2008**, *4*, 310–325.

(105) Wang, C.; Daimon, H.; Onodera, T.; Koda, T.; Sun, S. A General Approach to the Size- and Shape-Controlled Synthesis of Platinum Nanoparticles and Their Catalytic Reduction of Oxygen. *Angew. Chem. Int. Ed. Engl.* **2008**, *47*, 3588–3591.

(106) Sun, Y.; Xia, Y. Shape-Controlled Synthesis of Gold and Silver Nanoparticles. *Science (80-.).* **2002**, *298*, 2176–2179.

(107) Zhang, J.; Li, S.; Wu, J.; Schatz, G. C.; Mirkin, C. A. Plasmon-Mediated Synthesis of Silver Triangular Bipyramids. *Angew. Chem. Int. Ed. Engl.* **2009**, *48*, 7787–7791.

(108) Jin, R.; Cao, Y. C.; Hao, E.; Me, G. S.; Schatz, G. C.; Mirkin, C. A. Controlling Anisotropic Nanoparticle Growth through Plasmon Excitation. *Nature* **2003**, *425*, 487–490.

(109) Ming, T.; Feng, W.; Tang, Q.; Wang, F.; Sun, L.; Wang, J.; Yan, C. Growth of Tetrahexahedral Gold Nanocrystals with High-Index Facets. *J. Am. Chem. Soc.* **2009**, *131*, 16350–16351.

(110) Tian, N.; Zhou, Z.-Y.; Sun, S.-G.; Ding, Y.; Wang, Z. L. Synthesis of Tetrahexahedral Platinum Nanocrystals with High-Index Facets and High Electro-Oxidation Activity. *Science* **2007**, *316*, 732–735.

(111) Lu, C.-L.; Prasad, K. S.; Wu, H.-L.; Ho, J. A.; Huang, M. H. Au Nanocube-Directed Fabrication of Au-Pd Core-Shell Nanocrystals with Tetrahexahedral, Concave Octahedral, and Octahedral Structures and Their Electrocatalytic Activity. *J. Am. Chem. Soc.* **2010**, *132*, 14546–14553.

(112) Huang, X.; Tang, S.; Zhang, H.; Zhou, Z.; Zheng, N. Controlled Formation of Concave Tetrahedral/trigonal Bipyramidal Palladium Nanocrystals. *J. Am. Chem. Soc.* **2009**, *131*, 13916–13917.

(113) Zhang, J.; Langille, M. R.; Personick, M. L.; Zhang, K.; Li, S.; Mirkin, C. A. Concave Cubic Gold Nanocrystals with High-Index Facets. *J. Am. Chem. Soc.* **2010**, *132*, 14012–14014.

(114) Ma, Y.; Kuang, Q.; Jiang, Z.; Xie, Z.; Huang, R.; Zheng, L. Synthesis of Trisoctahedral Gold Nanocrystals with Exposed High-Index Facets by a Facile Chemical Method. *Angew. Chem. Int. Ed. Engl.* **2008**, *47*, 8901–8904.

(115) Yu, T.; Kim, D. Y.; Zhang, H.; Xia, Y. Platinum Concave Nanocubes with High-Index Facets and Their Enhanced Activity for Oxygen Reduction Reaction. *Angew. Chem. Int. Ed. Engl.* **2011**, *50*, 2773–2777.

(116) Zhou, Z.-Y.; Tian, N.; Huang, Z.-Z.; Chen, D.-J.; Sun, S.-G. Nanoparticle Catalysts with High Energy Surfaces and Enhanced Activity Synthesized by Electrochemical Method. *Faraday Discuss.* **2008**, *140*, 81–92.

(117) Zhang, H.; Jin, M.; Wang, J.; Li, W.; Camargo, P. H. C.; Kim, M. J.; Yang, D.; Xie, Z.; Xia, Y. Synthesis of Pd-Pt Bimetallic Nanocrystals with a Concave Structure through a Bromide-Induced Galvanic Replacement Reaction. *J. Am. Chem. Soc.* **2011**, *133*, 6078–6089.

(118) Moghimi, N.; Bazargan, S.; Pradhan, D.; Leung, K. T. Phase-Induced Shape Evolution of FeNi Nanoalloys and Their Air Stability by in-Situ Surface Passivation. *J. Phys. Chem. C* **2013**, *117*, 4852–4858.

(119) Choe, S.; Lee, S.; Chang, Y.; Hwang, K.; Khim, J. Rapid Reductive Destruction of Hazardous Organic Compounds by Nanoscale Fe 0. *Chemosphere* **2001**, *42*, 367–372.

(120) Song, H.; Carraway, E. R. Reduction of Chlorinated Ethanes by Nanosized Zero-Valent Iron : Kinetics , Pathways , and Effects of Reaction Conditions. *Environ. Sci. Technol.* **2005**, *39*, 6237–6245.

(121) Hong, Y.; Rheem, Y.; Lai, M.; Cwiertny, D. M.; Walker, S. L.; Myung, N. V. Electrochemical Synthesis of FexNi1−x Nanostructures for Environmental Remediation. *Chem. Eng. J.* **2009**, *151*, 66–72.

(122) Ponder, S. M.; Darab, John G; Mallouk, T. E. Remediation of Cr (VI) and Pb (II) Aqueous Solutions Using Supported , Nanoscale Zero-Valent Iron. *Environ. Sci. Technol.* **2000**, *34*, 2564–2569.

(123) Karnel, S. R.; Manning, B.; Charlet, L.; Choi, H. Removal of Arsenic (III) from Groundwater by Nanoscale Zero-Valent Iron. *Environ. Sci. Technol.* **2005**, *39*, 1291–1298.

(124) Yin, K.-M.; Lin, B.-T. Effects of Boric Acid on the Electrodeposition of Iron, Nickel and Iron-Nickel. *Surf. Coatings Technol.* **1996**, *78*, 205–210.

(125) Vaes, J.; Fransaer, J.; Celis, J.-P. The Role of Metal Hydroxides in NiFe Deposition. *J. Electrochem. Soc.* **2000**, *147*, 3718.

(126) Vitos, L. The Surface Energy of Metals. *Surf. Sci.* **1998**, *411*, 186–202.

(127) Huitink, D.; Kundu, S.; Park, C.; Mallick, B.; Huang, J. Z.; Liang, H. Nanoparticle Shape Evolution Identified through Multivariate Statistics. *J. Phys. Chem. A* **2010**, *114*, 5596–5600.

(128) Pérez, F.; Tryland, I.; Mascini, M.; Fiksdal, L. Rapid Detection of Escherichia Coli in Water by a Culture-Based Amperometric Method. *Anal. Chim. Acta* **2001**, *427*, 149–154.

(129) Fan, Y.; Liu, J.-H.; Yang, C.-P.; Yu, M.; Liu, P. Graphene–polyaniline Composite Film Modified Electrode for Voltammetric Determination of 4-Aminophenol. *Sensors Actuators B Chem.* **2011**, *157*, 669–674.

(130) Shiroma, L. Y.; Santhiago, M.; Gobbi, A. L.; Kubota, L. T. Separation and Electrochemical Detection of Paracetamol and 4-Aminophenol in a Paper-Based Microfluidic Device. *Anal. Chim. Acta* **2012**, *725*, 44–50.

(131) Yin, H.; Ma, Q.; Zhou, Y.; Ai, S.; Zhu, L. Electrochemical Behavior and Voltammetric Determination of 4-Aminophenol Based on Graphene–chitosan Composite Film Modified Glassy Carbon Electrode. *Electrochim. Acta* **2010**, *55*, 7102–7108.

(132) Yang, W. H.; Srolovitz, D. J. Surface Morphology Evolution in Stressed Solids: Surface Diffusion Controlled Crack Initiation. *J. Mech. Phys. Solids* **1994**, *42*, 1551–1574.

(133) Oldenburg, S. J.; Averitt, R. D.; Westcott, S. L.; Halas, N. J. Nanoengineering of Optical Resonances. *Chem. Phys. Lett.* **1998**, *288*, 243–247.

(134) Alia, S. M.; Zhang, G.; Kisailus, D.; Li, D.; Gu, S.; Jensen, K.; Yan, Y. Porous Platinum Nanotubes for Oxygen Reduction and Methanol Oxidation Reactions. *Adv. Funct. Mater.* **2010**, *20*, 3742–3746.

(135) Wang, Y.; Angelatos, A. S.; Caruso, F. Template Synthesis of Nanostructured Materials via Layer-by-Layer Assembly. *Chem. Mater.* **2008**, *20*, 848–858.

(136) Schwartzberg, A. M.; Olson, T. Y.; Talley, C. E.; Zhang, J. Z. Synthesis, Characterization, and Tunable Optical Properties of Hollow Gold Nanospheres. *J. Phys. Chem. B* **2006**, *110*, 19935–19944.

(137) Yang, J.; Lee, J. Y.; Too, H.-P. Core-Shell Ag-Au Nanoparticles from Replacement Reaction in Organic Medium. *J. Phys. Chem. B* **2005**, *109*, 19208–19212.

(138) Vasquez, Y.; Sra, A. K.; Schaak, R. E. One-Pot Synthesis of Hollow Superparamagnetic CoPt Nanospheres. *J. Am. Chem. Soc.* **2005**, *127*, 12504–12505.

(139) Selvakannan, P. R.; Sastry, M. Hollow Gold and Platinum Nanoparticles by a Transmetallation Reaction in an Organic Solution. *Chem. Commun. (Camb).* **2005**, 1684–1686.

(140) Chen, J.; McLellan, J. M.; Siekkinen, A.; Xiong, Y.; Li, Z.-Y.; Xia, Y. Facile Synthesis of Gold-Silver Nanocages with Controllable Pores on the Surface. *J. Am. Chem. Soc.* **2006**, *128*, 14776–14777.

(141) Kijima, T.; Yoshimura, T.; Uota, M.; Ikeda, T.; Fujikawa, D.; Mouri, S.; Uoyama, S. Noble-Metal Nanotubes (Pt, Pd, Ag) from Lyotropic Mixed-Surfactant Liquid-Crystal Templates. *Angew. Chem. Int. Ed. Engl.* **2004**, *43*, 228–232.

(142) Xia, Younan; Li, Weiyang; Cobley, C. M. .; Chen, J.; Xia, Xiaohu; Zhang, Q.; Yang,

Miaoxin; Cho EunChul; Brown, P. K. Gold Nanocages: From Synthesis to Theranostic Applications. *Acc. Chem. Res.* **2011**, *44*, 914–924.

(143) Wei, X.; Zhu, G.; Zhou, J.; Sun, H. Solution Phase Reduction to Fe–Ni Alloy Nanostructures with Tunable Shape and Size. *Mater. Chem. Phys.* **2006**, *100*, 481–485.

(144) Hong, L. B.; Fultz, B. Two-Phase Coexistence in Fe–Ni Alloys Synthesized by Ball Milling. *J. Appl. Phys.* **1996**, *79*, 3946–3955.

(145) Dumpich, G; Wassermann, E.F.; Manns, V.; Keune, W. ; Murayama, S.; Miyako, Y. Structural and Magnetic Properties of Ni(x) Fe(1-X) Evaporated Thin Films. *J. Magn. Magn. Mater.* **1987**, *67*, 55–64.

(146) Sumiyama, K.; Kadono, M.; Nakamura, Y. Metastable Phase in Sputtered Fe-Ni Alloys. *Trans. Japan Inst. Met.* **1983**, *24*, 190–194.

(147) Wu, H.; Cao, Y.; Yuan, P.; Xu, H.; Wei, X. Controlled Synthesis, Structure and Magnetic Properties of Fe1−xNix Alloy Nanoparticles Attached on Carbon Nanotubes. *Chem. Phys. Lett.* **2005**, *406*, 148–153.

(148) Collins, M. F.; Forsyth, J. B. The Magnetic Moment Distribution in Some Transition Metal Alloys. *Philos. Mag.* **1963**, *8*, 401–410.

(149) Li, X. G.; Chiba, A.; Takahashi, S. Preparation and Magnetic Properties of Ultrafine Particles of Fe-Ni Alloys. *J. Magn. Magn. Mater.* **1997**, *170*, 339–345.

(150) Collins, M. F.; Jones, R. V.; Lowde, R. D. On the Magnetic Moments and Degree of Order in Iron-Nickle Alloys. *J. Phys. Scociety Japan* **1962**, *17*, 19–26.

(151) Glaubitz, B.; Buschhorn, S.; Brüssing, F.; Abrudan, R.; Zabel, H. Development of Magnetic Moments in Fe 1 − X Ni X -Alloys. *J. Phys. Condens. Matter* **2011**, *23*, 254210–254219.

(152) Song, Q.; Zhang, Z. J. Shape Control and Associated Magnetic Properties of Spinel Cobalt Ferrite Nanocrystals. *J. Am. Chem. Soc.* **2004**, *126*, 6164–6168.

(153) Gao, G.; Liu, X.; Shi, R.; Zhou, K.; Shi, Y.; Ma, R.; Takayama-Muromachi, E.; Qiu, G. Shape-Controlled Synthesis and Magnetic Properties of Monodisperse Fe 3 O 4 Nanocubes. *Cryst. Growth Des.* **2010**, *10*, 2888–2894.

(154) Moghimi, N.; Abdellah, M.; Thomas, J. P.; Mohapatra, M.; Leung, K. T. Bimetallic

FeNi Concave Nanocubes and Nanocages. *J. Am. Chem. Soc.* **2013**, *135*, 10958–10961.

(155) Bradley, A. J. The Lattice Spacing of Iron-Nickel Alloys. *Philos. Mag.* **1937**, *23*, 545–557.

(156) James, P.; Eriksson, O.; Johansson, B.; Abrikosov, I. Calculated Magnetic Properties of Binary Alloys between Fe, Co, Ni, and Cu. *Phys. Rev. B* **1999**, *59*, 419–430.

(157) Fendle, J. *Nanoparticles and Nanostructured Films: Preparation, Characterization and Applications*; Fendle, J. H., Ed.; WILEY-VCH Verlag GmbH & Co. KGaA: NY, 1998.

(158) Wang, Z. L.; Liu, Y.; Zhang, Z. *Handbook of Nanophase and Nanostructured Materials: Material Systems and Applications I*; Kluwer Academic: Boston, 2003.

(159) Del Bianco, L.; Fiorani, D.; Testa, A.; Bonetti, E.; Savini, L.; Signoretti, S. Magnetothermal Behavior of a Nanoscale Fe/Fe Oxide Granular System. *Phys. Rev. B* **2002**, *66*, 174418.

(160) Thakur, M.; Patra, M.; Majumdar, S.; Giri, S. Influence of Cooling Field on the Magnetic Properties of Ni/NiO Nanostructure. *J. Alloys Compd.* **2009**, *480*, 193–197.

(161) Chia, C. H.; Zakaria, S.; Yusoff, M.; Goh, S. C.; Haw, C. Y.; Ahmadi, S.; Huang, N. M.; Lim, H. N. Size and Crystallinity-Dependent Magnetic Properties of CoFe2O4 Nanocrystals. *Ceram. Int.* **2010**, *36*, 605–609.

(162) Demortière, A.; Panissod, P.; Pichon, B. P.; Pourroy, G.; Guillon, D.; Donnio, B.; Bégin-Colin, S. Size-Dependent Properties of Magnetic Iron Oxide Nanocrystals. *Nanoscale* **2011**, *3*, 225–232.

(163) Kim, K. W.; Yoon, K. S.; Koo, J. H.; Do, Y. H.; Kim, C. O.; Hong, J. P. Influence of Grain Boundaries and Voids on the Saturated Magnetization in Fe3O4 Films at a Low Magnetic Field. *IEEE Trans. Magn.* **2006**, *42*, 1495–1498.

(164) Soo, Y. L.; Wu, T. S.; Wang, C. S.; Chang, S. L.; Lee, H. Y.; Chu, P. P.; Chen, C. Y.; Chou, L. J.; Chan, T. S.; Hsieh, C. A.; *et al.* Thermal Annealing and Grain Boundary Effects on Ferromagnetism in Y2O3:Co Diluted Magnetic Oxide Nanocrystals. *Appl. Phys. Lett.* **2011**, *98*, 031906.

(165) Vestal, C. R.; Zhang, Z. J. Effects of Surface Coordination Chemistry on the Magnetic Properties of MnFe(2)O(4) Spinel Ferrite Nanoparticles. *J. Am. Chem. Soc.* **2003**, *125*,

9828–9833.

(166) Miller, J. S.; Drillon, M. *Magnetism: Molecules to Materials III*; John Wiley & Sons, Inc, 2002; p. 230.

(167) Sun, H.-L.; Shi, H.; Zhao, F.; Qi, L.; Gao, S. Shape-Dependent Magnetic Properties of Low-Dimensional Nanoscale Prussian Blue (PB) Analogue SmFe(CN)6.4H2O. *Chem. Commun. (Camb).* **2005**, 4339–4341.

(168) Dimitrov, A.; Wysin, M. EfFects of Surface Anisotropy on Hysteresis in Fine Magnetic Particles. *Phys. Rev. B* **1994**, *50*, 3077–3084.

(169) Salazar-Alvarez, G.; Qin, J.; Bergmann, I.; Vasilakaki, M.; Trohidou, K. N. .; Ardisson, J. D.; Macedo, W. A. A. .; Mikhaylova, M.; Muhammed, M.; Baro, M. D.; *et al.* Cubic versus Spherical Magnetic Nanoparticles : The Role of. *J. Am. Chem. Soc.* **2008**, *130*, 13234–13239.

(170) Kohn, W.; Sham, L. J. Self-Consistent Equations Including Exchange and Correlation Effects. *Phys. Rev.* **1965**, *140*, 1133–1138.

(171) Kresse, G.; Furthmuller, J. Efficiency of Ab-Initio Total Energy Calculations for Metals and Semiconductors Using a Plane-Wave Basis Set. *Comput. Mater. Sci.* **1996**, *6*, 15–50.

(172) Eckert, J.; Holzer, J. C.; Johnson, W. L. Thermal Stability and Grain Growth Behavior of Mechanically Alloyed Nanocrystalline Fe-Cu Alloys. *J. Appl. Phys.* **1993**, *73*, 131.

(173) Eckert, J.; Holzer, J. C.; Krill, C. E.; Johnson, W. L. Mechanically Driven Alloying and Grain Size Changes in Nanocrystalline Fe-Cu Powders. *J. Appl. Phys.* **1993**, *73*, 2794.

(174) Perdew, J.; Burke, K.; Ernzerhof, M. Generalized Gradient Approximation Made Simple. *Phys. Rev. Lett.* **1996**, *77*, 3865–3868.

(175) Vosko, S. H.; Wilk, L.; Nusair, M. Accurate Spin-Dependent Electron Liquid Correlation Energies for Local Spin Density Calculations: A Critical analysis1. *Can. J. Pysics* **1980**, *58*, 1200–1211.

(176) Crangle, J.; Hallam, G. C. The Magnetization of Face-Centred Cubic and Body-Centred Cubic Iron + Nickel Alloys. *Proc. R. Soc. London. Math. Physicl Sceinces* **1963**, *272*, 119–132.

(177) Kondorsky, E. I. F. J., Fedotov, L. N., Invest. Akad. Nauk., SSSR, 1952, 16, 432; (b) Peschard, M., Rev. Met. 22, 1925, 490, 581, 663.

(178) Gazdik, Z.; Zitka, O.; Petrlova, J.; Adam, V.; Zehnalek, J.; Horna, A.; Reznicek, V.; Beklova, M.; Kizek, R. Determination of Vitamin C (Ascorbic Acid) Using High Performance Liquid Chromatography Coupled with Electrochemical Detection. *Sensors* **2008**, *8*, 7097–7112.

(179) Velíšek, Jan; Cejpek, K. Biosynthesis of Food Constituents : Vitamins . 2 . Water-Soluble Vitamins : Part 1 – a Review. *Czech J. Food Sci.* **2006**, *25*, 49–64.

(180) Levine, Mark and Downing, D. New Concepts in the Biology and Biochemistry of Ascorbic Acid. *J. Nutr. Environ. Med.* **1992**, *3*, 361.

(181) Mesías-García, M.; Guerra-Hernández, E.; García-Villanova, B. Determination of Furan Precursors and Some Thermal Damage Markers in Baby Foods: Ascorbic Acid, Dehydroascorbic Acid, Hydroxymethylfurfural and Furfural. *J. Agric. Food Chem.* **2010**, *58*, 6027–6032.

(182) Qiu, S.; Gao, S.; Xie, L.; Chen, H.; Liu, Q.; Lin, Z.; Qiu, B.; Chen, G. An Ultra-Sensitive Electrochemical Sensor for Ascorbic Acid Based on Click Chemistry. *Analyst* **2011**, *136*, 3962–3966.

(183) Zare, H. R.; Rajabzadeh, N.; Nasirizadeh, N.; Mazloum Ardakani, M. Voltammetric Studies of an Oracet Blue Modified Glassy Carbon Electrode and Its Application for the Simultaneous Determination of Dopamine, Ascorbic Acid and Uric Acid. *J. Electroanal. Chem.* **2006**, *589*, 60–69.

(184) Ensafi, A. A.; Rezaei, B. Flow Injection Analysis Determination of Ascorbic Acid with Spectrofluorimetric Detection. *Anakytical Lett.* **1998**, *31(2)*, 333–342.

(185) Wu, X.; Diao, Y.; Sun, C.; Yang, J.; Wang, Y.; Sun, S. Fluorimetric Determination of Ascorbic Acid with O-Phenylenediamine. *Talanta* **2003**, *59*, 95–99.

(186) Themelis, D. G.; Tzanavaras, P. D.; Kika, F. S. On-Line Dilution Flow Injection Manifold for the Selective Spectrophotometric Determination of Ascorbic Acid Based on the Fe(II)-2,2’-Dipyridyl-2-Pyridylhydrazone Complex Formation. *Talanta* **2001**, *55*, 127–134.

(187) Pereira, A. V.; Fatibello-Filho, O. Flow Injection Spectrophotometric Determination of L-Ascorbic Acid in Pharmaceutical Formulations with on-Line Solid-Phase Reactor Containing Copper (II) Phosphate. *Anal. Chim. Acta* **1998**, *366*, 55–62.

(188) Arya, S. .; Mahajan, M.; Jain, P. Spectrophotometric Determination of Vitamin C with iron(II)-4-(2-Pyridylazo)resorcinol Complex. *Anal. Chim. Acta* **2001**, *427*, 245–251.

(189) Kall, M. a; Andersen, C. Improved Method for Simultaneous Determination of Ascorbic Acid and Dehydroascorbic Acid, Isoascorbic Acid and Dehydroisoascorbic Acid in Food and Biological Samples. *J. Chromatogr. B. Biomed. Sci. Appl.* **1999**, *730*, 101–111.

(190) Lykkesfeldt, J. Determination of Ascorbic Acid and Dehydroascorbic Acid in Biological Samples by High-Performance Liquid Chromatography Using Subtraction Methods: Reliable Reduction with tris[2-Carboxyethyl]phosphine Hydrochloride. *Anal. Biochem.* **2000**, *282*, 89–93.

(191) Ozyürek, M.; Güçlü, K.; Bektaşoğlu, B.; Apak, R. Spectrophotometric Determination of Ascorbic Acid by the Modified CUPRAC Method with Extractive Separation of Flavonoids-La(III) Complexes. *Anal. Chim. Acta* **2007**, *588*, 88–95.

(192) Shi, W.; Liu, C.; Song, Y.; Lin, N.; Zhou, S.; Cai, X. An Ascorbic Acid Amperometric Sensor Using over-Oxidized Polypyrrole and Palladium Nanoparticles Composites. *Biosens. Bioelectron.* **2012**, *38*, 100–106.

(193) Xia, C.; Ning, W. A Novel Bio-Electrochemical Ascorbic Acid Sensor Modified with Cu4(OH)6SO4 Nanorods. *Analyst* **2011**, *136*, 288–292.

(194) Hernandez-Santos, D.; Gonzalez-Garcia, M. B.; Garcìa, A. C. Metal-Nanoparticles Based Electroanalysis. *Electroanalysis* **2002**, *14*, 1225–1235.

(195) He, J. H.; Xu, Q.; Song, Z. R.; Kuang, H. Y. Determination of Ascorbic Acid Based on a Platinum Nanoparticles Modified Au Electrode. *Appl. Mech. Mater.* **2012**, *110-116*, 1732–1735.

(196) Wen, D.; Guo, S.; Dong, S.; Wang, E. Ultrathin Pd Nanowire as a Highly Active Electrode Material for Sensitive and Selective Detection of Ascorbic Acid. *Biosens. Bioelectron.* **2010**, *26*, 1056–1061.

(197) Das, J.; Aziz, M. A.; Yang, H. A Nanocatalyst-Based Assay for Proteins: DNA-Free Ultrasensitive Electrochemical Detection Using Catalytic Reduction of P-Nitrophenol by Gold-Nanoparticle Labels. *J. Am. Chem. Soc.* **2006**, *128*, 16022–16023.

(198) Jia, J.; Wang, B.; Wu, A.; Cheng, G.; Li, Z.; Dong, S. A Method to Construct a Third-Generation Horseradish Peroxidase Biosensor : Self-Assembling Gold Nanoparticles to Three-Dimensional Sol-Gel Network. *Anal. Chem.* **2002**, *74*, 2217–2223.

(199) Satheesh Babu, T. G.; Varadarajan, D.; Murugan, G.; Ramachandran, T.; Nair, B. G. Gold Nanoparticle–polypyrrole Composite Modified TiO2 Nanotube Array Electrode for the Amperometric Sensing of Ascorbic Acid. *J. Appl. Electrochem.* **2012**, *42*, 427–434.

(200) Morais, A.; Silveira, G.; Villis, P. C. M.; Maroneze, C. M.; Gushikem, Y.; Pissetti, F. L.; Lucho, A. M. S. Gold Nanoparticles on a Thiol-Functionalized Silica Network for Ascorbic Acid Electrochemical Detection in Presence of Dopamine and Uric Acid. *J. Solid State Electrochem.* **2012**, *16*, 2957–2966.

(201) Ghoreishi, S. M.; Behpour, M.; Saeidinejad, F. Electrochemical Determination of Tryptophan, Uric Acid and Ascorbic Acid at a Gold Nanoparticles Modified Carbon Paste Electrode. *Anal. Methods* **2012**, *4*, 2447.

(202) Pournaghi-Azar, M. Â.; Dastangoo, H.; Fadakar, R. Differentiation of Detection of Ascorbic Acid and Dehydroascorbic Acid Using Hydrodynamic Amperometry and Anodic Stripping Voltammetry on Modified Aluminum Electrodes. *Electroanalysis* **2010**, *22*, 229–235.

(203) Claussen, J. C.; Kumar, A.; Jaroch, D. B.; Khawaja, M. H.; Hibbard, A. B.; Porterfield, D. M.; Fisher, T. S. Nanostructuring Platinum Nanoparticles on Multilayered Graphene Petal Nanosheets for Electrochemical Biosensing. *Adv. Funct. Mater.* **2012**, *22*, 3399–3405.

(204) Bo, X.; Ndamanisha, J. C.; Bai, J.; Guo, L. Nonenzymatic Amperometric Sensor of Hydrogen Peroxide and Glucose Based on Pt Nanoparticles/ordered Mesoporous Carbon Nanocomposite. *Talanta* **2010**, *82*, 85–91.

(205) Su, C.; Zhang, C.; Lu, G.; Ma, C. Nonenzymatic Electrochemical Glucose Sensor Based on Pt Nanoparticles/Mesoporous Carbon Matrix. *Electroanalysis* **2010**, *22*, 1901–1905.

(206) Zhu, N.; Chang, Z.; He, P.; Fang, Y. Electrochemical DNA Biosensors Based on Platinum Nanoparticles Combined Carbon Nanotubes. *Anal. Chim. Acta* **2005**, *545*, 21–26.

(207) Dey, R. S.; Raj, C. R. Development of an Amperometric Cholesterol Biosensor Based on Graphene−Pt Nanoparticle Hybrid Material. *J. Phys. Chem. C* **2010**, *114*, 21427–21433.

(208) Gilbert, J. A.; Kariuki, N. N.; Subbaraman, R.; Kropf, A. J.; Smith, M. C.; Holby, E. F.; Morgan, D.; and Myers, D. J. In Situ Anomalous Small-Angle X-Ray Scattering

Studies of Platinum Nanoparticles Fuel Cell Electrocatalyst Degradation. *J. Am. Chem. Soc.* **2012**, 14823–14833.

(209) Wang, C.; Daimon, H.; Sun, S. Dumbbell-like Pt-Fe3O4 Nanoparticles and Their Enhanced Catalysis for Oxygen Reduction Reaction. *Nano Lett.* **2009**, *9*, 1493–1496.

(210) Aravind, S. S. J.; Ramaprabhu, S. Pt Nanoparticle-Dispersed Graphene-Wrapped MWNT Composites As Oxygen Reduction Reaction Electrocatalyst in Proton Exchange Membrane Fuel Cell. *Appl. Mater. Interfaces* **2012**, *4*, 3805–3810.

(211) Sheng, W.; Chen, S.; Vescovo, E.; Shao-Horn, Y. Size Influence on the Oxygen Reduction Reaction Activity and Instability of Supported Pt Nanoparticles. *J. Electrochem. Soc.* **2012**, *159*, B96–B103.

(212) Peng, K.; Xu, Y.; Wu, Y.; Yan, Y.; Lee, S.-T.; Zhu, J. Aligned Single-Crystalline Si Nanowire Arrays for Photovoltaic Applications. *Small* **2005**, *1*, 1062–1067.

(213) Chen, C.-Y.; Wu, C.-S.; Chou, C.-J.; Yen, T.-J. Morphological Control of Single-Crystalline Silicon Nanowire Arrays near Room Temperature. *Adv. Mater.* **2008**, *20*, 3811–3815.

(214) Li, F.; Tang, C.; Liu, S.; Ma, G. Development of an Electrochemical Ascorbic Acid Sensor Based on the Incorporation of a Ferricyanide Mediator with a Polyelectrolyte–calcium Carbonate Microsphere. *Electrochim. Acta* **2010**, *55*, 838–843.

(215) Ragupathy, D.; Gopalan, A. I.; Lee, K.-P. Electrocatalytic Oxidation and Determination of Ascorbic Acid in the Presence of Dopamine at Multiwalled Carbon Nanotube–silica Network–gold Nanoparticles Based Nanohybrid Modified Electrode. *Sensors Actuators B Chem.* **2010**, *143*, 696–703.

(216) Keeley, G. P.; O'Neill, A.; McEvoy, N.; Peltekis, N.; Coleman, J. N.; Duesberg, G. S. Electrochemical Ascorbic Acid Sensor Based on DMF-Exfoliated Graphene. *J. Mater. Chem.* **2010**, *20*, 7864–7869.

(217) Huang, S.-H.; Liao, H.-H.; Chen, D.-H. Simultaneous Determination of Norepinephrine, Uric Acid, and Ascorbic Acid at a Screen Printed Carbon Electrode Modified with Polyacrylic Acid-Coated Multi-Wall Carbon Nanotubes. *Biosens. Bioelectron.* **2010**, *25*, 2351–2355.

(218) Shahrokhian, S.; Zaremehrjardi, H. Cobalt Salophen-Modified Carbon-Paste Electrode Incorporating a Cationic Surfactant for Simultaneous Voltammetric Detection of Ascorbic Acid and Dopamine. *Sensors Actuators B Chem.* **2007**, *121*, 530–537.

(219) Mukerjee, S.; Srinivasan, S.; Soriaga, M. P.; Mcbreen, J. Role of Structural and Electronic Properties of Pt and Pt Alloys on Electrocatalysis of Oxygen Reduction. *J. Electrocemical Soc.* **1995**, *142*, 1409–1422.

(220) Casella, I. G. Electrooxidation of Ascorbic Acid on the Dispersed Platinum Glassy Carbon Electrode and Its Amperometric Determination in Flow Injection Analysis. *Electroanalysis* **1996**, *8*, 128–134.

(221) Zidan, M.; Tee, T. W.; Abdullah, A. H.; Zainal, Z. Electrochemical Oxidation of Ascorbic Acid Mediated by Bi 2 O 3 Microparticles Modified Glassy Carbon Electrode. *Int. J. Electrochem. Sci.* **2011**, *6*, 289–300.

(222) Karabinas, Pantelis; Jannakoudakis, D. Kinetic Parameters and Mechanism of the Electrochemical Oxidation of L-Ascorbic Acid on Platinum Electrodes in Acid Solutions. *J. Electroanal. Chem.* **1984**, *160*, 159–167.

(223) Mays, Douglas, E.; Hussam, A. Voltammetric Methods for Determination and Speciation of Inorganic Arsenic in the Environment--a Review. *Anal. Chim. Acta* **2009**, *646*, 6–16.

(224) Chouhan, S.; Flora, S. J. S. Arsenic and Fluoride: Two Major Ground Water Pollutants. *Indian J. Exp. Biol.* **2010**, *48*, 666–678.

(225) Yokel, R. a; Lasley, S. M.; Dorman, D. C. The Speciation of Metals in Mammals Influences Their Toxicokinetics and Toxicodynamics and Therefore Human Health Risk Assessment. *J. Toxicol. Environ. Health. B. Crit. Rev.* **2006**, *9*, 63–85.

(226) World Heaalth Organization, Arsenic in Drinking Water, Fact Sheet No 372, http://www.who.int/mediacentre/factsheets/fs372/en/index.html.

(227) P. Mushak. Natural Resources Defence Council Http://www.nrdc.org/water/drinking/arsenic/aolinx.asp, 2000.

(228) Mandal, B. K.; Suzuki, K. T. Arsenic Round the World: A Review. *Talanta* **2002**, *58*, 201–235.

(229) Chakraborti, D.; Rahman, M. M.; Paul, K.; Chowdhury, U. K.; Sengupta, M. K.; Lodh, D.; Chanda, C. R.; Saha, K. C.; Mukherjee, S. C. Arsenic Calamity in the Indian Subcontinent What Lessons Have Been Learned? *Talanta* **2002**, *58*, 3–22.

(230) Smedley, P. L.; Kinniburgh, D. G. A Review of the Source, Behaviour and Distribution of Arsenic in Natural Waters. *Appl. Geochemistry* **2002**, *17*, 517–568.

(231) Manisankar, P.; Vedhi, C.; Selvanathan, G.; Arumugam, P. Differential Pulse Stripping Voltammetric Determination of Heavy Metals Simultaneously Using New Polymer Modified Glassy Carbon Electrodes. *Microchim. Acta* **2008**, *163*, 289–295.

(232) Muñoz, E.; Palmero, S. Analysis and Speciation of Arsenic by Stripping Potentiometry: A Review. *Talanta* **2005**, *65*, 613–620.

(233) Hussam, A; Alauddin, M.; Khan, A. H.; Rasul, S. B.; Munir, K. M. Evaluation of Arsine Generation in Arsenic Field Kit. *Environ. Sci. Technol.* **1999**, *33*, 3686–3688.

(234) Aragay, G.; Pons, J.; Merkoçi, A. Recent Trends in Macro-, Micro-, and Nanomaterial-Based Tools and Strategies for Heavy-Metal Detection. *Chem. Rev.* **2011**, *111*, 3433–3458.

(235) Pinilla Gil, E.; Ostapczuk, P. Potentiometric Stripping Determination of mercury(II), selenium(IV), copper(II) and lead(II) at a Gold Film Electrode in Water Samples. *Anal. Chim. Acta* **1994**, *293*, 55–65.

(236) Mandil, A.; Idrissi, L.; Amine, A. Stripping Voltammetric Determination of mercury(II) and lead(II) Using Screen-Printed Electrodes Modified with Gold Films, and Metal Ion Preconcentration with Thiol-Modified Magnetic Particles. *Microchim. Acta* **2010**, *170*, 299–305.

(237) Zong, P.; Nagaosa, Y. Determination of antimony(III) and (V) in Natural Water by Cathodic Stripping Voltammetry with in-Situ Plated Bismuth Film Electrode. *Microchim. Acta* **2009**, *166*, 139–144.

(238) Baron, R.; Šljukić, B.; Salter, C.; Crossley, a.; Compton, R. G. Electrochemical Detection of Arsenic on a Gold Nanoparticle Array. *Russ. J. Phys. Chem. A* **2007**, *81*, 1443–1447.

(239) Dai, X.; Nekrassova, O.; Hyde, M. E.; Compton, R. G. Anodic Stripping Voltammetry of arsenic(III) Using Gold Nanoparticle-Modified Electrodes. *Anal. Chem.* **2004**, *76*, 5924–5929.

(240) Sanllorente-Méndez, S.; Domínguez-Renedo, O.; Arcos-Martínez, M. J. Determination of Arsenic(III) Using Platinum Nanoparticle-Modified Screen-Printed Carbon-Based Electrodes. *Electroanalysis* **2009**, *21*, 635–639.

(241) Dai, X.; Compton, R. G. Direct Electrodeposition of Gold Nanoparticles onto Indium Tin Oxide Film Coated Glass: Application to the Detection of arsenic(III). *Anal. Sci.* **2006**, *22*, 567–570.

(242) Xu, H.; Zeng, L.; Xing, S.; Shi, G.; Chen, J.; Xian, Y.; Jin, L. Highly Ordered Platinum-Nanotube Arrays for Oxidative Determination of Trace arsenic(III). *Electrochem. commun.* **2008**, *10*, 1893–1896.

(243) Li, W.; Kuai, L.; Qin, Q.; Geng, B. Ag–Au Bimetallic Nanostructures: Co-Reduction Synthesis and Their Component-Dependent Performance for Enzyme-Free H2O2 Sensing. *J. Mater. Chem. A* **2013**, *1*, 7111.

(244) Liu, S.; Zhang, C.; Yuan, L.; Bao, J.; Tu, W.; Han, M.; Dai, Z. Component-Controlled Synthesis of Small-Sized Pd-Ag Bimetallic Alloy Nanocrystals and Their Application in a Non-Enzymatic Glucose Biosensor. *Part. Part. Syst. Charact.* **2013**, *30*, 549–556.

(245) Yan, J.; Liu, S.; Zhang, Z.; He, G.; Zhou, P.; Liang, H.; Tian, L.; Zhou, X.; Jiang, H. Simultaneous Electrochemical Detection of Ascorbic Acid, Dopamine and Uric Acid Based on Graphene Anchored with Pd-Pt Nanoparticles. *Colloids Surf. B. Biointerfaces* **2013**, *111C*, 392–397.

(246) Gong, J.; Zhou, T.; Song, D.; Zhang, L.; Hu, X. Stripping Voltammetric Detection of mercury(II) Based on a Bimetallic Au-Pt Inorganic-Organic Hybrid Nanocomposite Modified Glassy Carbon Electrode. *Anal. Chem.* **2010**, *82*, 567–573.

(247) Lan, Y.; Luo, H.; Ren, X.; Wang, Y.; Liu, Y. Anodic Stripping Voltammetric Determination of arsenic(III) Using a Glassy Carbon Electrode Modified with Gold-Palladium Bimetallic Nanoparticles. *Microchim. Acta* **2012**, *178*, 153–161.

(248) Oskam, G.; Long, J. G.; Natarajan, a; Searson, P. C. Electrochemical Deposition of Metals onto Silicon. *J. Phys. D. Appl. Phys.* **1998**, *31*, 1927–1949.

(249) Papadimitriou, S.; Tegou, a.; Pavlidou, E.; Armyanov, S.; Valova, E.; Kokkinidis, G.; Sotiropoulos, S. Preparation and Characterisation of Platinum- and Gold-Coated Copper, Iron, Cobalt and Nickel Deposits on Glassy Carbon Substrates. *Electrochim. Acta* **2008**, *53*, 6559–6567.

(250) Edwards, C. A. *Anodic Stripping Voltammetry: A Review*; Volume 22.; Stevenage Laboratory, 1976.

(251) Simm, A. O.; Banks, C. E.; Compton, R. G. Sonically Assisted Electroanalytical Detection of Ultratrace Arsenic. *Anal. Chem.* **2004**, *76*, 5051–5055.

(252) Cui, H.; Yang, W.; Li, X.; Zhao, H.; Yuan, Z. An Electrochemical Sensor Based on a Magnetic Fe3O4 Nanoparticles and Gold Nanoparticles Modified Electrode for Sensitive Determination of Trace Amounts of Arsenic(iii). *Anal. Methods* **2012**, *4*,

4176.

(253) Chowdhury, A.; Ferdousi, S.; Islam, M. M.; Okajima, T. Arsenic Detection by Nanogold / Conducting-Polymer- Modified Glassy Carbon Electrodes. *Appl. Polym. Sci.* **2007**, *104*, 1306–1311.

(254) Dai, X.; Compton, R. G. Detection of As(III) via Oxidation to As(V) Using Platinum Nanoparticle Modified Glassy Carbon Electrodes: Arsenic Detection without Interference from Copper. *Analyst* **2006**, *131*, 516–521.

(255) Prakash, S.; Chakrabarty, T.; Singh, A. K.; Shahi, V. K. Silver Nanoparticles Built-in Chitosan Modified Glassy Carbon Electrode for Anodic Stripping Analysis of As(III) and Its Removal from Water. *Electrochim. Acta* **2012**, *72*, 157–164.

(256) Cavicchioli, A.; La-Scalea, M. A.; Gutz, I. G. R. Analysis and Speciation of Traces of Arsenic in Environmental, Food and Industrial Samples by Voltammetry: A Review. *Electroanalysis* **2004**, *16*, 697–711.

(257) Jena, B. K.; Raj, C. R. Gold Nanoelectrode Ensembles for the Simultaneous Electrochemical Detection of Ultratrace Arsenic, Mercury, and Copper. *Anal. Chem.* **2008**, *80*, 4836–4844.

(258) Feeney, R.; Kounaves, S. On-Site Analysis of Arsenic in Groundwater Using a Microfabricated Gold Ultramicroelectrode Array. *Anal. Chem.* **2000**, *72*, 2222–2228.

(259) Feeney, R.; Kounaves, S. P. Voltammetric Measurement of Arsenic in Natural Waters. *Talanta* **2002**, *58*, 23–31.

(260) Katz, E.; Willner, I. Integrated Nanoparticle-Biomolecule Hybrid Systems: Synthesis, Properties, and Applications. *Angew. Chem. Int. Ed. Engl.* **2004**, *43*, 6042–6108.

(261) Niemeyer, C. M. Nanoparticles, Protein, and Nucleic Acids: Biotechnology Meets Materials Science. *Angew. Chem. Int. Ed. Engl.* **2001**, *40*, 4128–4158.

(262) Katz, E.; Sheeney-Haj-Ichia, L.; Willner, I. Magneto-Switchable Electrocatalytic and Bioelectrocatalytic Transformations. *Chemistry* **2002**, *8*, 4138–4148.

(263) Mornet, S.; Vekris, A.; Bonnet, J.; Duguet, E.; Grasset, F.; Choy, J. H.; Portier, J. DNA – Magnetite Nanocomposite Materials. *Matterials Lett.* **2000**, *42*, 183–188.

(264) Indira, T. K.; Lakshmi, P. K. Magnetic Nanoparticles – A Review. *Int. J. Pharm. Sci. Nanotechnol.* **2010**, *3*, 1035–1042.

(265) Yu, C.-C.; Kuo, Y.-Y.; Liang, C.-F.; Chien, W.-T.; Wu, H.-T.; Chang, T.-C.; Jan, F.-D.; Lin, C.-C. Site-Specific Immobilization of Enzymes on Magnetic Nanoparticles and Their Use in Organic Synthesis. *Bioconjug. Chem.* **2012**, *23*, 714–724.

(266) Ansari, S. A.; Husain, Q. Potential Applications of Enzymes Immobilized On/in Nano Materials: A Review. *Biotechnol. Adv.* **2012**, *30*, 512–523.

(267) Saraswati, T. E.; Ogino, A.; Nagatsu, M. Plasma-Activated Immobilization of Biomolecules onto Graphite-Encapsulated Magnetic Nanoparticles. *Carbon N. Y.* **2012**, *50*, 1253–1261.

(268) Xing, Z.-C.; Chang, Y.; Kang, I.-K. Immobilization of Biomolecules on the Surface of Inorganic Nanoparticles for Biomedical Applications. *Sci. Technol. Adv. Mater.* **2010**, *11*, 014101.

(269) Kandimalla, V.; Tripathi, V.; Ju, H. Immobilization of Biomolecules in Sol–Gels: Biological and Analytical Applications. *Crit. Rev. Anal. Chem.* **2006**, *36*, 73–106.

(270) Rendl, M.; Bönisch, A.; Mader, A.; Schuh, K.; Prucker, O.; Brandstetter, T.; Rühe, J. Simple One-Step Process for Immobilization of Biomolecules on Polymer Substrates Based on Surface-Attached Polymer Networks. *Langmuir* **2011**, *27*, 6116–6123.

(271) Ricci, F.; Palleschi, G. Sensor and Biosensor Preparation, Optimisation and Applications of Prussian Blue Modified Electrodes. *Biosens. Bioelectron.* **2005**, *21*, 389–407.

(272) Luo, X.-L.; Xu, J.-J.; Du, Y.; Chen, H.-Y. A Glucose Biosensor Based on Chitosan-Glucose Oxidase-Gold Nanoparticles Biocomposite Formed by One-Step Electrodeposition. *Anal. Biochem.* **2004**, *334*, 284–289.

(273) Shi, L.; Xiao, Y.; Willner, I. Electrical Contacting of Glucose Oxidase by DNA-Templated Polyaniline Wires on Surfaces. *Electrochem. commun.* **2004**, *6*, 1057–1060.

(274) Wang, J. Electrochemical Glucose Biosensors. *Chem. Rev.* **2008**, *108*, 814–825.

(275) Toghill, K. E.; Compton, R. G. Electrochemical Non-Enzymatic Glucose Sensors : A Perspective and an Evaluation. *Int. J. Electrochem. Sci.* **2010**, *5*, 1246–1301.

(276) Ivnitski, D.; Branch, B.; Atanassov, P.; Apblett, C. Glucose Oxidase Anode for Biofuel Cell Based on Direct Electron Transfer. *Electrochem. commun.* **2006**, *8*, 1204–1210.

(277) Holzapfel, W. H.; Geisen, R.; Schillinger, U. Biological Preservation of Foods with Reference to Protective Cultures, Bacteriocins and Food-Grade Enzymes. *Int. J. Food Microbiol.* **1995**, *24*, 343–362.

(278) Ma, Z.; Ding, T. Bioconjugates of Glucose Oxidase and Gold Nanorods Based on Electrostatic Interaction with Enhanced Thermostability. *Nanoscale Res. Lett.* **2009**, *4*, 1236–1240.

(279) Wei, A.; Sun, X. W.; Wang, J. X.; Lei, Y.; Cai, X. P.; Li, C. M.; Dong, Z. L.; Huang, W. Enzymatic Glucose Biosensor Based on ZnO Nanorod Array Grown by Hydrothermal Decomposition. *Appl. Phys. Lett.* **2006**, *89*, 123902.

(280) Bharathi, S.; Nogami, M. A Glucose Biosensor Based on Electrodeposited Biocomposites of Gold Nanoparticles and Glucose Oxidase Enzyme. *Analyst* **2001**, *126*, 1919–1922.

(281) Crumbliss, A. L.; Perine, S. C.; Stonehuerner, J.; Tubergen, K. R.; Zhao, J.; Henkens, R. W.; O'Daly, J. P. Colloidal Gold as a Biocompatible Immobilization Matrix Suitable for the Fabrication of Enzyme Electrodes by Electrodeposition. *Biotechnol. Bioeng.* **1992**, *40*, 483–490.

(282) Baek, S.; Kutchukian, P. S.; Verdine, G. L.; Huber, R.; Holak, T. a; Lee, K. W.; Popowicz, G. M. Structure of the Stapled p53 Peptide Bound to Mdm2. *J. Am. Chem. Soc.* **2012**, *134*, 103–106.

(283) Wade, M.; Li, Y.-C.; Wahl, G. M. MDM2, MDMX and p53 in Oncogenesis and Cancer Therapy. *Nat. Rev. Cancer* **2013**, *13*, 83–96.

(284) Saha, M. N.; Qiu, L.; Chang, H. Targeting p53 by Small Molecules in Hematological Malignancies. *J. Hematol. Oncol.* **2013**, *6*, 23.

(285) Pazgier, M.; Liu, M.; Zou, G.; Yuan, W.; Li, C.; Li, C.; Li, J.; Monbo, J.; Zella, D.; Tarasov, S. G.; *et al.* Structural Basis for High-Affinity Peptide Inhibition of p53 Interactions with MDM2 and MDMX. *Proc. Natl. Acad. Sci. U. S. A.* **2009**, *106*, 4665–4670.

(286) Merrifield, R. B. Solid Phase Peptide Synthesis. I. The Synthesis of a Tetrapeptide. *J. Am. Chem. Soc.* **1963**, *85*, 2149–2154.

(287) Stoscheck, C. M. Quantitation of Protein. *Methods Enzymol.* **1990**, *182*, 50–68.

(288) Zhou, K.; Zhu, Y.; Yang, X.; Li, C. Electrocatalytic Oxidation of Glucose by the

Glucose Oxidase Immobilized in Graphene-Au-Nafion Biocomposite. *Electroanalysis* **2010**, *22*, 259–264.

(289) Lvov, Y.; Katsuhiko, A.; Ichinose, I.; Kunitake, T. Assembly of Multicomponent Protein Films by Means of Electrostatic Layer-by-Layer Adsorption. *J. Am. Chem. Soc.* **1995**, *117*, 6117–6123.

(290) Hodak, J.; Etchenique, R.; Calvo, E. J.; Singhal, K.; Bartlett, P. N. Layer-by-Layer Self-Assembly of Glucose Oxidase with a Poly(allylamine)ferrocene Redox Mediator. *Langmuir* **1997**, *13*, 2708–2716.

(291) Liu, L.; Kou, H.-Z.; Mo, W.; Liu, H.; Wang, Y. Surfactant-Assisted Synthesis of Alpha-Fe2O3 Nanotubes and Nanorods with Shape-Dependent Magnetic Properties. *J. Phys. Chem. B* **2006**, *110*, 15218–15223.

(292) Boily, Jean-Francois; Lutzenkirchen, Johannes; Balmes, Olivier; Beattie, James; Sjoberg, S. Modeling Proton Binding at the Goethite (a-FeOOH)– Water Interface. *Colloid and Surfaces* **2006**, *179*, 11–27.

(293) Hamann, C. H. *Electrochemistry*; 2nd ed.; WILEY-VCH Verlag GmbH & Co. KGaA: New York, 2007.

(294) Morikawa, M.; Kimizula, N.; Yoshihara, M.; Endo, T. New Colorimetric Detection of Glucose by Means of Electron-Accepting Triggered by Electron Transfer from Glucose Oxidase. *Chem. A Eur. J.* **2002**, *8*, 5580–5584.

(295) Carter, M. T.; Rodriguez, M.; Bard, A. J. Voltammetric Studies of the Interaction of Metal Chelates with DNA. 2. Tris-Chelated Complexes of Cobalt (III) and Iron (II) with 1,10-Phenanthroline and 2,2’-Bipyridine. *J. Am. Chem. Soc.* **1989**, *111*, 8901–8911.

(296) Inkson, B. .; Mulvihill, M.; Möbus, G. 3D Determination of Grain Shape in a FeAl-Based Nanocomposite by 3D FIB Tomography. *Scr. Mater.* **2001**, *45*, 753–758.

(297) Schaffer, M.; Wagner, J.; Schaffer, B.; Schmied, M.; Mulders, H. Automated Three-Dimensional X-Ray Analysis Using a Dual-Beam FIB. *Ultramicroscopy* **2007**, *107*, 587–597.

(298) Hill, R.; Blenkinsopp, P.; Thompson, S.; Vickerman, J.; Fletcher, J. S. A New Time-of-Flight SIMS Instrument for 3D Imaging and Analysis. *Surf. Interface Anal.* **2011**, *43*, 506–509.

(299) De Benedetto, G. E.; Malitesta, C.; Zambonin, C. G. Electroanalytical/X-Ray Photoelectron Spectroscopy Investigation on Glucose Oxidase Adsorbed on Platinum. *J. Chem. Soc. Faraday Trans.* **1994**, *90*, 1495–1499.

(300) Guiomar, A. J.; Guthrie, J. T.; Evans, S. D. Use of Mixed Self-Assembled Monolayers in a Study of the Effect of the Microenvironment on Immobilized Glucose Oxidase. *Langmuir* **1999**, *15*, 1198–1207.

(301) Jagst, E. *Surface Functional Group Characterization Using Chemical Derivatization X-Ray Photoelectron Spectroscopy (CD-XPS)*; 2011.

(302) Liu, X. Enzymatic Activity of Glucose Oxidase Covalently Wired via Viologen to Electrically Conductive Polypyrrole Films. *Biosens. Bioelectron.* **2004**, *19*, 823–834.

(303) Bonnet, F.; Ropital, F.; Lecour, P.; Espinat, D.; Huiban, Y.; Gengembre, L.; Berthier, Y.; Marcus, P. Study of the Oxide/carbide Transition on Iron Surfaces during Catalytic Coke Formation. *Surf. Interface Anal.* **2002**, *34*, 418–422.

(304) Mahmoudi, M.; Laurent, S.; Shokrgozar, M. a; Hosseinkhani, M. Toxicity Evaluations of Superparamagnetic Iron Oxide Nanoparticles: Cell “Vision” versus Physicochemical Properties of Nanoparticles. *ACS Nano* **2011**, *5*, 7263–7276.

(305) Mahmoudi, M.; Hofmann, H.; Rothen-Rutishauser, B.; Petri-Fink, A. Assessing the in Vitro and in Vivo Toxicity of Superparamagnetic Iron Oxide Nanoparticles. *Chem. Rev.* **2012**, *112*, 2323–2338.

(306) Shi, S.-F.; Jia, J.-F.; Guo, X.-K.; Zhao, Y.-P.; Chen, D.-S.; Guo, Y.-Y.; Cheng, T.; Zhang, X.-L. Biocompatibility of Chitosan-Coated Iron Oxide Nanoparticles with Osteoblast Cells. *Int. J. Nanomedicine* **2012**, *7*, 5593–5602.

(307) Babiuch, K.; Wyrwa, R.; Wagner, K.; Seemann, T.; Hoeppener, S.; Becer, C. R.; Linke, R.; Gottschaldt, M.; Weisser, J.; Schnabelrauch, M.; *et al.* Functionalized, Biocompatible Coating for Superparamagnetic Nanoparticles by Controlled Polymerization of a Thioglycosidic Monomer. *Biomacromolecules* **2011**, *12*, 681–691.

(308) Gupta, A. K.; Gupta, M. Synthesis and Surface Engineering of Iron Oxide Nanoparticles for Biomedical Applications. *Biomaterials* **2005**, *26*, 3995–4021.

(309) Cheraghipour, E. Citrate Capped Superparamagnetic Iron Oxide Nanoparticles Used for Hyperthermia Therapy. *J. Biomed. Sci. Eng.* **2012**, *05*, 715–719.

(310) Jeun, M.; Lee, S.; Kyeong Kang, J.; Tomitaka, A.; Wook Kang, K.; Il Kim, Y.;

Takemura, Y.; Chung, K.-W.; Kwak, J.; Bae, S. Physical Limits of Pure Superparamagnetic Fe3O4 Nanoparticles for a Local Hyperthermia Agent in Nanomedicine. *Appl. Phys. Lett.* **2012**, *100*, 092406.

(311) Tartaj, P.; Serna, C. J. Synthesis of Monodisperse Superparamagnetic Fe/silica Nanospherical Composites. *J. Am. Chem. Soc.* **2003**, *125*, 15754–15755.

(312) Joseyphus, R.J.; Matsumoto, T.; Sato, Y.; Jeyadevan, B.; Tohji, K. Role of Polyol on the Formation of Fe Particles. *J. Magn. Magn. Mater.* **2007**, *310*, 2393.

(313) Wahajuddin; Arora, S. Superparamagnetic Iron Oxide Nanoparticles: Magnetic Nanoplatforms as Drug Carriers. *Int. J. Nanomedicine* **2012**, *7*, 3445–3471.